

# Shear-induced alignment in block copolymer solutions

## DISSERTATION

zur Erlangung des akademischen Grades eines  
Doktors der Naturwissenschaften (Dr. rer. nat.)  
im Fach Chemie der Fakultät für Biologie, Chemie und Geowissenschaften  
der Universität Bayreuth

vorgelegt von  
**Gabi Cantea**  
Geboren in Tandarei/Rumänien

Bayreuth, 2005

Die vorliegende Arbeit wurde in der Zeit von October 2001 bis October 2005 in Bayreuth an den Lehrstühlen Makromolekulare Chemie II unter der Betreuung von Herrn Prof. Dr. Volker Abetz angefertigt.

Promotionsgesuch eingereicht am: 14.10.2005

Prüfungsausschuß:

Prof. Dr. Volker Abetz (Erstgutachter)

*Meiner Familie*

Knowledge may give weight, but accomplishments give lustre, and many more people see than weigh.

**-Herodotus-**

# Table of Contents

<b>1. Introduction.....</b>	<b>1</b>
<b>1.1. Microphase Separation of Block Copolymers.....</b>	<b>4</b>
1.1.1. Theoretical background for Microphase Separation in Block Copolymers.....	4
1.1.2. Order-Disorder Transition Temperature ( $T_{ODT}$ ) in Block Copolymers.....	11
1.1.3. Blends of Block Copolymers.....	14
<b>1.2. Alignment of Block Copolymer Morphologies.....</b>	<b>16</b>
1.2.1. Alignment by Mechanical Field – Shear Alignment.....	16
1.2.1.1. Unidirectional Shear.....	16
1.2.1.2. Large Amplitude Oscillatory Shear.....	17
1.2.2. Alignment by Electric Field.....	22
1.2.2.1. Electric Field combined with Birefringence Method.....	23
<b>2. Methods.....</b>	<b>26</b>
<b>2.1. Synthesis.....</b>	<b>26</b>
2.1.1. Anionic Polymerization.....	26
2.1.2. Basics of Anionic Polymerization.....	27
<b>2.2. Characterization.....</b>	<b>28</b>
2.2.1. Transmission Electron Microscopy (TEM).....	28
2.2.1.1. Fundamentals of Transmission Electron Microscopy.....	28
2.2.1.2. Staining of Polymer Samples.....	30
2.2.1.3. Radiation Damage.....	31
2.2.2. Small-Angle X-Ray Scattering (SAXS).....	32
2.2.2.1. Principles of Scattering.....	32
2.2.2.2. Small-Angle X-Ray Scattering on Microphase-Separated Block Copolymers..	34
2.2.2.3. Setup of Synchrotron-SAXS Beamline (ID02A, ESRF, Grenoble).....	38
2.2.3. Dynamic-Mechanical Analysis.....	39
2.2.3.1. Fundamentals of Dynamic-Mechanical Analysis.....	39
2.2.3.2. Viscoelastic Behavior of Polymeric Systems.....	41
2.2.3.3. Mechanical Models of Viscoelastic Behavior.....	44
2.2.3.4. The Glass Transition Temperature.....	49
2.2.3.5. The Time-Temperature Superposition Principle and its Application to Linear Viscoelasticity.....	52
2.2.4. Rheo-optic Method Combined with LAOS. Definition of Alignment Regime.....	54
2.2.5. Setup ( Optical Analysis Module).....	57
2.2.6. Polarization.....	59
2.2.7. Refractive Index, Anisotropy, Birefringence.....	61
2.2.8. Intrinsic and Form Birefringence.....	62
2.2.9. Stress Optical Rule (SOR).....	63
<b>2.3. Experimental Section.....</b>	<b>65</b>
2.3.1. Synthesis of polystyrene- <i>b</i> -poly( <i>t</i> -butyl methacrylate).....	65
2.3.2. Synthesis of polystyrene- <i>b</i> -polybutadiene- <i>b</i> -poly(methyl methacrylate) $S_{37}B_{14}M_{49}^{37}$ and $S_{34}B_{19}M_{47}^{65}$ .....	68

2.3.3. Hydrogenation of $S_{37}B_{14}M_{49}^{37}$ and $S_{34}B_{19}M_{47}^{65}$ .....	69
<b>3. Morphological transitions in block copolymer solutions with a selective solvent</b>	
<b>3.1. Introduction.....</b>	<b>73</b>
3.1.1. Sample preparation.....	74
<b>3.2. Measurement of dynamic mechanical properties.....</b>	<b>75</b>
3.2.1. Determination of order-disorder transition temperature ( $T_{ODT}$ ) from <i>temperature sweep</i> tests.....	75
3.2.2. Determination of order-disorder transition temperature ( $T_{ODT}$ ) from <i>frequency sweep</i> tests.....	84
3.2.3. Determination of order-disorder transition temperature ( $T_{ODT}$ ) using plots of <i>log G'</i> versus <i>log G'</i> .....	89
3.2.4. Determination of order-disorder transition temperature ( $T_{ODT}$ ) using <i>log /<math>\eta^*</math>/</i> versus <i>log <math>\omega</math></i> .....	95
3.2.5. Time-temperature superposition principle applied to block copolymer solutions.....	96
3.2.6. Comparison of experimental $T_{ODT}$ with theoretical predictions.....	104
<b>3.3. Conclusion.....</b>	<b>107</b>
<b>4. In Situ Monitoring of Domain Orientation in Block Copolymers Solutions by Large Amplitude Oscillatory Shear (LAOS)</b>	
<b>4.1. Introduction.....</b>	<b>109</b>
<b>4.2. Results and Discussion.....</b>	<b>110</b>
4.2.1. Rheological and SAXS investigations of $S_{50}T_{50}^{100}$ and $S_{33}B_{33}T_{34}^{160}$ solutions.....	110
4.2.2. Alignment of high molecular weight polystyrene-b-poly( <i>t</i> -butyl methacrylate) $S_{50}T_{50}^{100}$ solution.....	117
4.2.3. Alignment of high molecular $S_{33}B_{33}T_{34}^{160}$ weight triblock terpolymer solution.....	125
4.2.4. Alignment of non-centrosymmetric blend $S_{33}B_{33}T_{34}^{160} : S_{50}T_{50}^{100} = 60:40$ in solution.....	129
4.2.5. Theoretical estimation of birefringence in diluted diblock copolymer $S_{50}T_{50}^{100}$ in DOP.....	134
<b>4.3. Conclusion.....</b>	<b>137</b>
<b>5. Weak Segregated Systems (Lamellae-Cylinder Morphology) in LAOS and Steady Mode</b>	
<b>5.1. Introduction.....</b>	<b>139</b>
<b>5.2. Results and Discussion.....</b>	<b>140</b>
5.2.1. Alignment of $S_{37}B_{14}M_{49}^{37}$ and $S_{34}B_{19}M_{47}^{65}$ .....	140
5.2.2. Alignment of $S_{37}EB_{14}M_{49}^{37}$ and $S_{34}EB_{19}M_{47}^{65}$ .....	163

5.2.3. Validity of SOR for a Block Copolymer in Weak Segregation Limit.....	167
<b>5.3. Conclusion.....</b>	<b>171</b>
<b>6. In situ rheo-SAXS of a Block Copolymer Solution with lamellar morphology in Couette geometry</b>	
<b>6.1. Introduction.....</b>	<b>172</b>
<b>6.2. The monitored alignment in block copolymer solution of 25 wt-% <math>S_{33}B_{33}T_{34}^{160}</math> triblock terpolymer in DOP.....</b>	<b>172</b>
6.2.1. Dynamic-mechanical characterization of the block copolymer solution with 25 wt-% $S_{33}B_{33}T_{34}^{160}$ .....	172
6.2.2. The alignment kinetics of the block copolymer solution of 25 wt-% $S_{33}B_{33}T_{34}^{160}$ in oscillatory mode.....	174
6.2.3. The alignment kinetics of block copolymer solution 25 wt-% $S_{33}B_{33}T_{34}^{160}$ in steady mode.....	186
<b>6.3. Conclusion.....</b>	<b>194</b>
<b>7. In Situ Rheo-SAXS of a Block Copolymer Solution with Cylindrical Morphology in Couette geometry</b>	
<b>7.1. Introduction.....</b>	<b>195</b>
<b>7.2. The monitored alignment in block copolymer solution 30 wt-% <math>S_{34}B_{19}M_{47}^{65}</math> triblock terpolymer.....</b>	<b>195</b>
7.2.1. A preliminary SAXS investigation of block copolymer solution 30 wt-% $S_{34}B_{19}M_{47}^{65}$ .....	195
7.2.2. The alignment kinetics of block copolymer solution 30 wt-% $S_{34}B_{19}M_{47}^{65}$ in oscillatory mode.....	197
7.2.3. The alignment kinetics of block copolymer solution 30 wt-% $S_{34}B_{19}M_{47}^{65}$ in steady mode.....	200
<b>7.3. Conclusion.....</b>	<b>208</b>
<b>8. In situ rheo-SAXS of a solution of <math>S_{34}EB_{19}M_{47}^{65}</math> in DOP in Couette geometry</b>	
<b>8.1. Introduction.....</b>	<b>209</b>
<b>8.2. The monitored alignment of a block copolymer solution of 30 wt-% <math>S_{34}EB_{19}M_{47}^{65}</math> triblock terpolymer in DOP.....</b>	<b>209</b>
8.2.1. A preliminary rheological investigation of block copolymer solution of	

30wt-% S <sub>34</sub> EB <sub>19</sub> M <sub>47</sub> <sup>65</sup> .....	209
8.2.2. The alignment kinetics of the block copolymer solution of 30 wt-% S <sub>34</sub> EB <sub>19</sub> M <sub>47</sub> <sup>65</sup> in steady mode.....	210
<b>8.3. Conclusion.....</b>	<b>222</b>
<b>9. Summary/Zusammenfassung.....</b>	<b>224</b>

## 1. Introduction

Due to the continuously increasing interest in nanotechnology, materials like block copolymers which may form ordered structures on a nanometer scale are attracting more and more attention. Block copolymers as well as their blends with homopolymers or other block copolymers can be used to pattern surfaces or to produce materials in which the nanostructure extends to macroscopic scale. Block copolymers play an important role as templates since they can guide structure formation of inorganic guest molecules in different morphologies with tunable sizes. Block copolymers represent an important class of nanostructured materials because their morphology and dynamics can be systematically controlled by appropriate choice of polymer segments and relative composition. Block copolymers can self-associate into organized structures in a selective solvent, which is good for one part and poor or non-solvent for the other part. The solvent-phobicity difference of the blocks is the driving force for the segregation leading to the ordered nanopatterns.

In general, block copolymer systems can offer various different nanoscale templates such as three dimensional (3D) cubic packings of spherical units, two-dimensional (2D) hexagonal packings of cylindrical units, one-dimensional (1D) periodic lamellar systems, and 3D bicontinuous cubic morphologies. These morphologies usually show grain-like structures. For some potential applications it is, however, necessary to have an uniform orientation in a sample on a large scale, i.e. instead of a grain-like structure a single crystal-like alignment is desirable. Examples for such applications could be photonic crystals, membranes, or lithography, where the orientation of the morphology must be controlled in order to obtain the correct properties. Formation of supramolecular structures can be affected by the fabrication process such as thermal annealing, solvent swelling and by use of external fields.

The macroscopic alignment of block copolymers nanostructured materials is presented in this thesis. The multigrain structure with a random orientation is characteristic of unoriented block copolymers. To achieve an aligned state an external field needs to be applied to an isotropic microstructure and as a result the growth of an anisotropic state is encountered. A mechanical field has been applied to block copolymers and the alignment has been monitored *in situ* through two different pathways: *rheooptical* and *rheo-SAXS* as powerful and efficient tools.

Previously, many studies regarding the mechanical alignment were made on block copolymers melts<sup>1,2,3,4</sup> with low molecular weight and only few reports<sup>5,6,7</sup> concerning the mechanical alignment from solutions.<sup>8</sup> Application of a large amplitude oscillatory shear (LAOS) field (well in the nonlinear viscoelastic regime) results in the macroscopic orientation

of grains through the elimination of interfaces perpendicular to the shear direction and reorientation of the domains along the shear direction. During LAOS the magnitude of the complex shear modulus is a decreasing function of time, and the magnitude of this decrease depends of temperature, frequency, strain amplitude and distance from the order-to-disorder transition.

In order to achieve macroscopically alignment in block copolymer solutions with high molecular weight and different morphologies, *a priori* thermodynamically investigation of the diblock copolymer solutions by rheological means allowed the knowledge about alignment parameters (temperature, frequency) which has been made in the first part of this work. Additionally, from the rheological characterization of diblock copolymer polystyrene-*b*-poly(*t*-butyl methacrylate) as solutions at different concentrations, the resulted order-disorder transition temperatures within an applied dilution approximation theory allowed developing of an expression for the interaction parameter, which have been never reported for such system.

Subsequently, the alignment of a symmetrically diblock copolymer polystyrene-*b*-poly(*t*-butyl methacrylate) has been successful performed by applying LAOS simultaneously with a monitored birefringence. While the diblock copolymer solution showed a selective alignment (only perpendicular over a wide range of frequencies and strain amplitudes), instead the triblock terpolymer polystyrene-*b*-polybutadiene-*b*-poly(*t*-butyl methacrylate) showed a parallel alignment at large time scale through the monitored birefringence and a perpendicular one at small time scale through a 2D scattering pattern. By applying LAOS the monitored alignment within two different methods such as birefringence and SAXS was in a good agreement since the alignment via birefringence method underwent through an intermediate perpendicular state before reaching the final parallel state.

The triblock terpolymer polystyrene-*b*-polybutadiene-*b*-poly(methyl methacrylate) with a cylindrical microstructure (polybutadiene block forms cylinder at the lamellar interface of polystyrene and poly(methyl methacrylate) lamellae) has been aligned by using rheo-optical method in oscillatory shear and by in situ rheo-SAXS in steady mode. While the monitored birefringence in oscillatory mode did not show any clear dependence within alignment parameters (temperature, frequency, and strain amplitude), instead the rheo-SAXS experiments proved a morphological transition from cylindrical toward a spherical microstructure in oscillatory mode. Moreover, in steady shear mode has been induced a well developed hexagonal array from an initially body centred cubic microstructure.

The solution of a “knitting pattern” such as polystyrene-*b*-poly(ethylene-co-butylene)-*b*-poly(methyl methacrylate) has been subjected to rheo-SAXS in steady mode and a supramolecular columnar structure was detected at a certain shear rate. Thus, the rheo-optical method was a sensitive tool in detection of alignment kinetics for the lamellar microstructure whereas the rheo-SAXS besides macroscopically characterization of the lamellar state, represents a powerful tool for detection of morphological changes taking place in asymmetrically structures. For the macroscopically aligned structure a quantification of the alignment has been made through an calculated order parameter,  $P_2$ .

## 1.1 Microphase Separation in Block Copolymers

### 1.1.1 Theoretical Background for Microphase Separation in Block Copolymers

$AB$  block copolymer melts have received considerable attention because immiscibility between  $A$  and  $B$  blocks induces self-assembly into various ordered microstructures.<sup>9,10</sup> In the high temperature disordered phase (DIS),  $A$  and  $B$  blocks mix homogeneously, but as the temperature is lowered (the Flory-Huggins  $\chi$  parameter is increased), they separate on a microscopic scale forming  $A$ - and  $B$ -rich domains separated by an extensive amount of internal interface. Various geometries of these domains occur depending, to a large degree, on the spontaneous mean curvature of the internal interface, which is produced by a mismatch in entropic stretching energy of the  $A$  and  $B$  blocks.<sup>9,11</sup> The simplest phases which these systems display are the lamellar phase in which the two monomers separate into  $A$ -rich and  $B$ -rich lamellae, the hexagonal phase in which the minority component forms cylinders which pack into a hexagonal array, and the cubic phase in which the minority component forms spheres arranged in a body centered cubic structure.<sup>12</sup> A gyroid phase has been observed as well in  $AB$  block copolymer melts in which the minority component forms two three-coordination lattices which interpenetrate and are mirror images of one another. This phase is understood theoretically<sup>13</sup> and is expected to be stable.

The structures of the different thermodynamically stable microphases for  $AB$  diblock copolymers are presented in Figure 1-1.

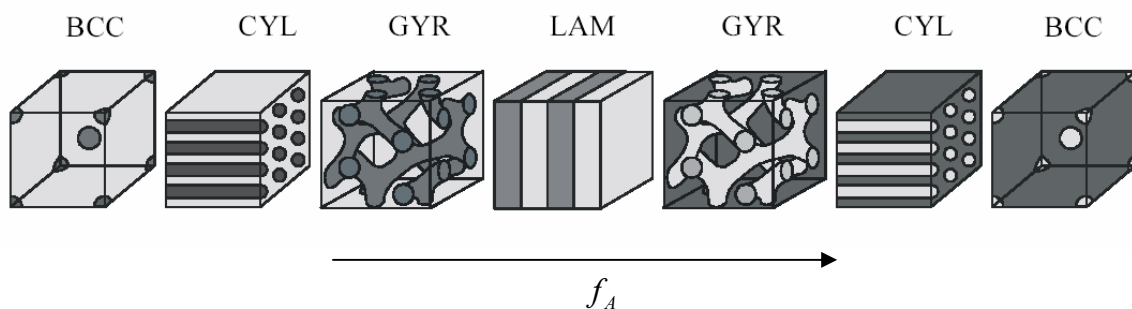


**Figure 1-1.** Equilibrium morphologies in  $AB$  diblock copolymers versus of volume fraction of component  $A$ ,  $f_A$ .

BCC: spheres, arranged on a body centered cubic lattice

CYL: cylinders, arranged on a hexagonal lattice

GYR: gyroid, bicontinuous phase

LAM: lamellar structure

There have also been numerous observations of an ordered, bicontinuous, double diamond phase<sup>14,15,16,17,18,19</sup> in which the minority component forms two separate interpenetrating diamond lattices, but there is some doubt regarding its stability in the diblock system. A monocontinuous catenoid lamellar phase, in which the minority component lamellae are perforated by holes arranged hexagonally within the layers has been observed,<sup>14,20,21,22,23</sup> as well as a bicontinuous catenoid lamellar phase.<sup>15</sup>

In general, the theoretical study of diblock copolymer melts has been based upon a single, standard, Gaussian model.<sup>24,25,26,27</sup> In this model, each molecule of the melt is composed of  $N$  segments of which a fraction  $f$  forms the  $A$  block and the rest forms the  $B$  block. For convenience,  $A$  and  $B$  segments are usually defined to have equal volumes. This simplified model for block copolymer melts retains the three most important ingredients: entropic chain stretching, incompressibility, and immiscibility between unlike segments.

Besides the volume fraction of the block copolymer components, the Flory-Huggins interaction parameter,  $\chi$ , plays an important role for the description of the phase separation of block copolymers. Especially in the strong segregation theory of the formation of complex morphologies, the surface tension,  $\gamma$ , which is proportional to  $\sqrt{\chi}$ , is used as a parameter for the miscibility of the different segments (equation 1-1).

$$\gamma_{ij} \propto \sqrt{\chi_{ij}} \quad (1-1)$$

$\gamma_{ij}$ : surface tension between the segments  $i$  and  $j$  of a block copolymer

$\chi_{ij}$ : Flory – Huggins – interaction parameter between the segments  $i$  and  $j$  of a block copolymer

The Flory-Huggins interaction parameter is derived from experiments or can be calculated from the solubility parameters of both components,  $i$  or  $j$  using the van-Laar-Hildebrand equation (1-2):

$$\chi_{ij} = \frac{V}{RT} \cdot (\delta_i - \delta_j)^2 \quad (1-2)$$

$\delta_{ij}$  solubility parameter for the segments  $i$  and  $j$  of a block copolymer,  $[(cal / cm^3)]^{1/2}$

$V$  molar segment volume, calculated by the mean value of the molar volume of the both segments ( $i$  and  $j$ ), which are derived from the molar mass of the repeating unit and density,  $[cm^3 / mol]$

$R$  universal gas constant  $8.3144 [J \cdot K \cdot mol^{-1}]$

$T$  temperature  $[K]$

The product  $\chi N$  is the quantity that controls the degree of segregation between  $A$  and  $B$  blocks. Typically, segregation is categorized into three regimes: weak, intermediate, and strong. Because there are no well-defined criteria for separating these regimes, they are usually discussed in vague terms. As an example in Figure 1-2 is examined the lamellar phase of a symmetric ( $f = 0.5$ ) diblock and plot the profile for the  $A$  - segment density  $\phi_A(r)$  at several degrees of segregation.

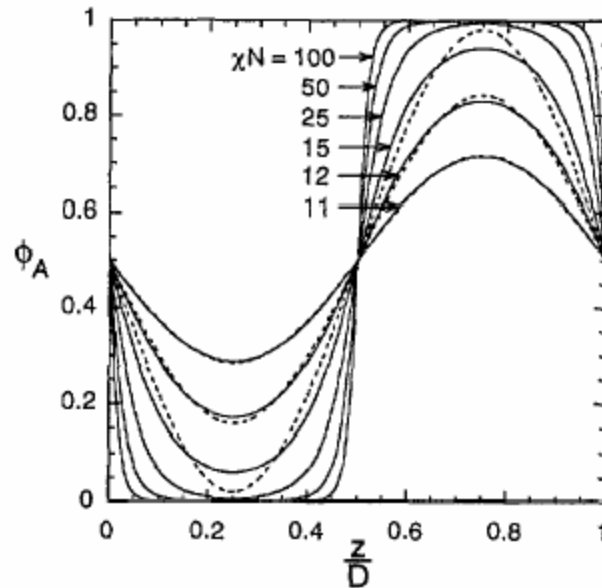


**Figure 1-2.**  $A$ -segment profiles over one period of the lamellar phase of a symmetric ( $f = 0.5$ ) diblock melt for  $\chi N = 11, 12, 15, 25, 50,$  and  $100$ . Dashed lines denote first-harmonic approximations for the profiles at  $\chi N = 11, 12,$  and  $15$ .<sup>28</sup>

The weak segregation regime occurs when the profile is sinusoidal or, in general, when the profile is well approximated by its first Fourier component. The dashed lines in Figure 1-2 show the first-harmonic approximation for the weaker segregated cases. Based on that the weak to intermediate crossover occurs at  $\chi N \sim 12$ , not much above the mean-field critical point at  $\chi N \sim 10.495$  and the strong-segregation regime occurs at  $\chi N \sim 50$ . The strong-segregation theory (*SST*) requires the  $A$  and  $B$  blocks to be strongly segregated, strongly stretched and the internal interfaces to be narrow.

Many interpret the segregation regimes on the basis of how the lamellar spacing,  $D$ , and the interfacial width,  $w$ , vary with  $N$ . In the disordered phase at  $f = 0.5$ , the characteristic length scale ( $D$ ) is  $2\pi/q^* = 1.318aN^{1/2}$ , where  $a$  is Kuhn length,  $q^*$  is the wavevector at which the structure function attains its maximum.<sup>12</sup> This  $N^{1/2}$  scaling should be associated

with the absence of segregation.<sup>29</sup> Often it is assumed that this scaling continues into the weak segregation regime. With further increase of the product  $\chi N$ , the weak segregation limit (*WSL*) is reached where the "disorder to order" phase transition (*ODT*) is observed. The individual domains in the ordered microstructures are enriched with one component, indicated by an approximately sinusoidal composition profile for both components (Figure 1-3).

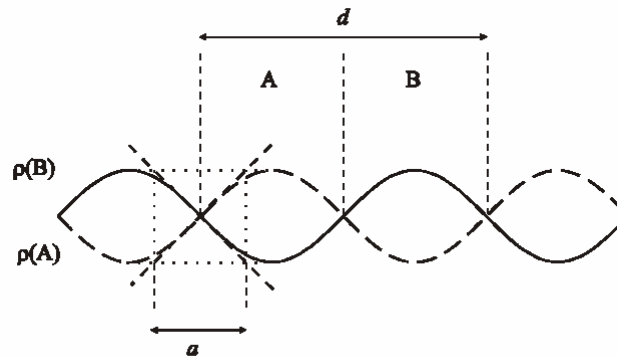


**Figure 1-3.** Sinusoidal composition profile for phase-separated *AB* diblock copolymers in the weak segregation limit (*WSL*).<sup>10</sup>

*d* - length of repeating unit in the composition profile

*a* - thickness of the shared interface of the two components

$\rho(A)$ ,  $\rho(B)$  - density profile of the components *A* and *B* in the different phases

Diblock copolymers belonging to the regime of the strong segregation limit (*SSL*) show a strong incompatibility of the two segments, which is indicated by a large value of  $\chi$ . Even for small *N* phase separation occurs, the interphases between the domains are narrow and nearly pure *A* and *B* microdomains are obtained as illustrated in Figure 1-4.

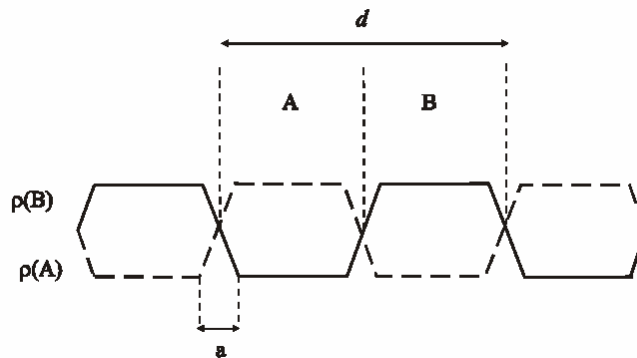


**Figure 1-4.** Characteristic composition profile in the case of strong segregation limits (*SSL*).<sup>10</sup>

$d$  - length of repeating unit in the composition profile

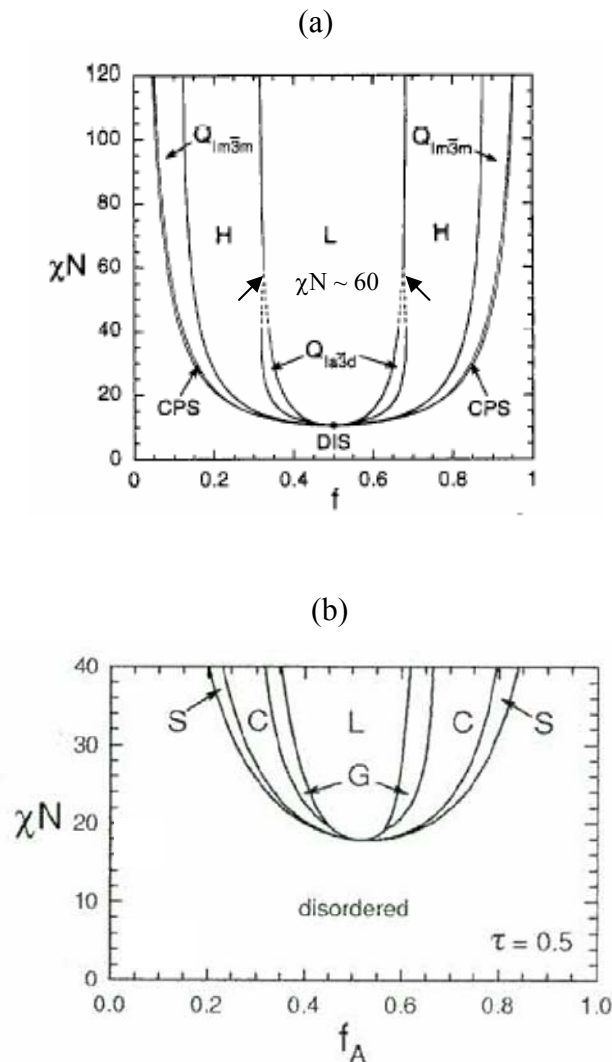
$a$  - thickness of the shared interface of the two components

$\rho(A)$ ,  $\rho(B)$  - density profile of the components  $A$  and  $B$  in the different phases

At strong segregations,  $D$  begins to scale with an exponent of  $(2/3)$  of the degree of polymerization, consistent with experiment<sup>30</sup> and with *SST* result<sup>31</sup>, following the expression:

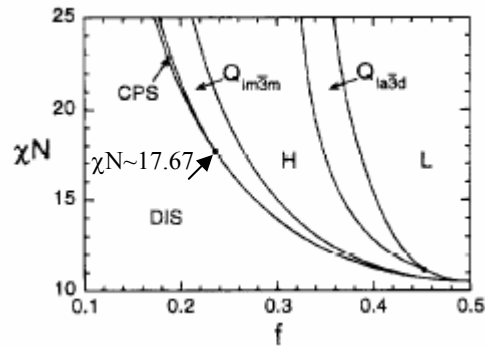
$$\frac{D}{aN^{1/2}} = 2 \left( \frac{8}{3\pi^4} \right)^{1/6} (\chi N)^{1/6} \quad (1-3)$$

Matsen and Bates<sup>28</sup> combined the two limiting cases of *WSL* and *SSL* using the self-consistent field theory developed by Helfand and Wasserman.<sup>32</sup> A mean-field phase diagrams for conformationally symmetric diblock and asymmetric triblock copolymer melts using the standard Gaussian polymer model are presented in Figure 1-5.



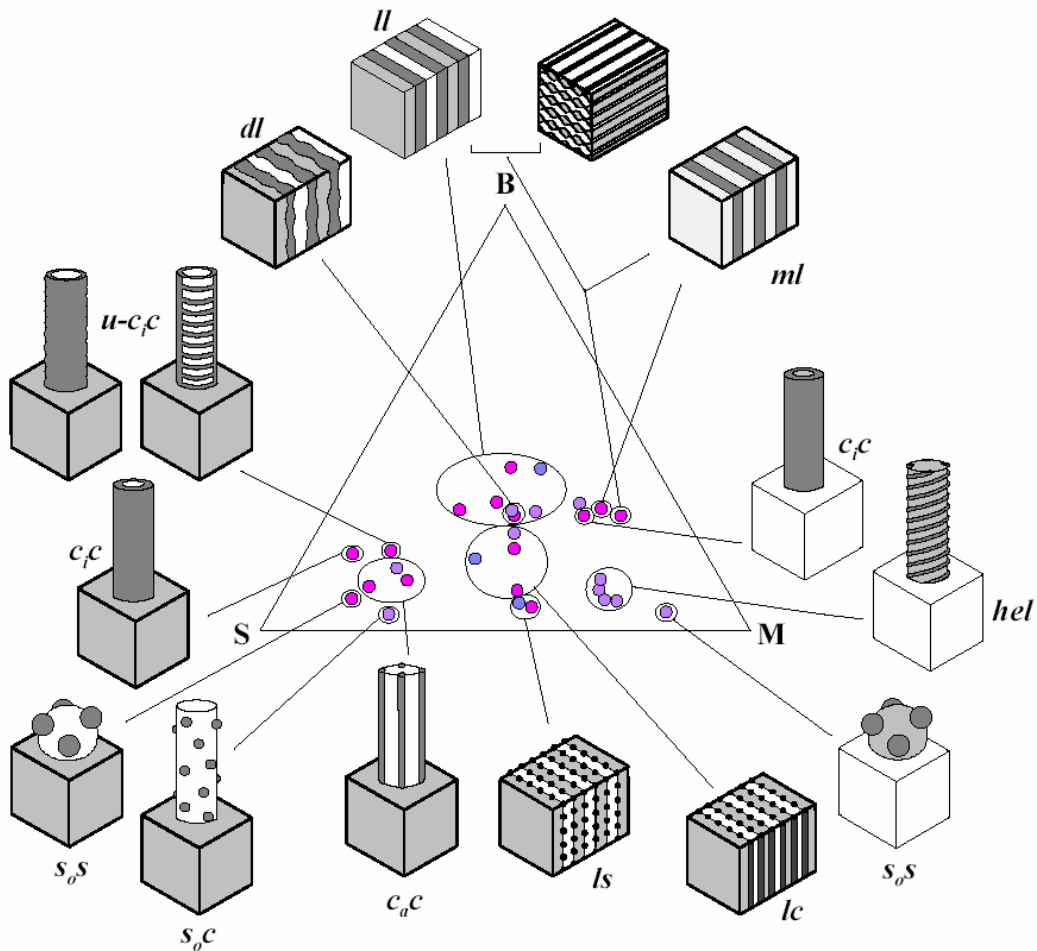
**Figure 1-5.** Mean-field phase diagram for conformationally symmetric melts  $AB$  in the strong segregation limit (*SSL*) calculated by Matsen et al<sup>28</sup> (Figure 1-5a) and for asymmetric

$ABA$  triblock copolymer melts in the intermediate-segregation regime<sup>33</sup> (Figure 1-5b) where  $\tau$  represents the asymmetry parameter : L – lamellar microphase; H - hexagonal microphase;  $Q_{Ia\bar{3}d}$  - bicontinuous  $Ia\bar{3}d$  cubic, gyroid (G);  $Q_{Im\bar{3}m}$  - body-centered cubic microphase (bcc), CPS - close-packed spheres; DIS - disordered;  $f$  - volume fraction of block  $A$  from diblock copolymer  $AB$ . Dashed lines (Figure 1-5a) denote extrapolated phase boundaries, and the dot denotes the mean-field critical point.



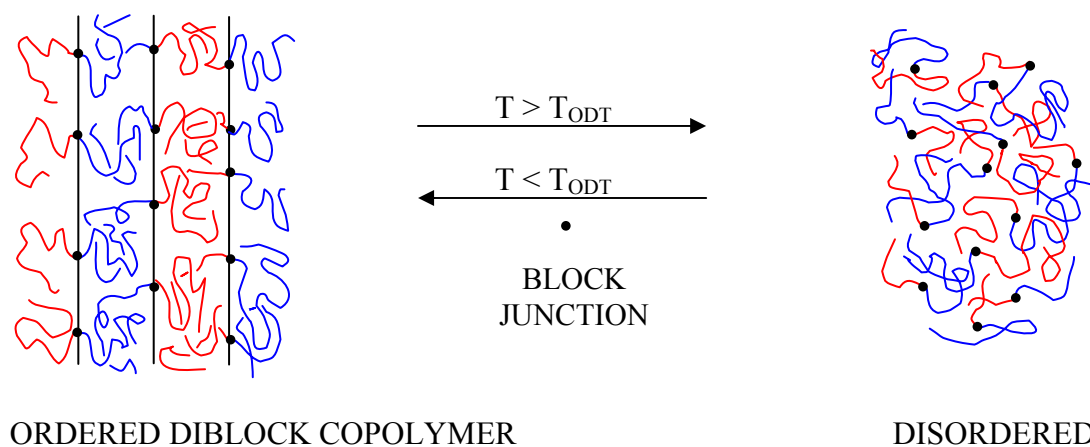
**Figure 1-6.** Phase diagram for diblock copolymers in the weak segregation limit ( $WSL$ ) calculated by Leibler.<sup>12</sup> The  $DIS + CPS + Q_{Im\bar{3}m}$  and  $H + Q_{Ia\bar{3}d} + L$  triple points are denoted with dots;  $f$  - volume fraction of component  $A$  in the diblock copolymer.

There are narrow regions of stability along the order-disorder transition for the CPS phase (Figure 1-5), extending toward the strong-segregation limit from  $DIS + CPS + Q_{Im\bar{3}m}$  triple points at  $\chi N \sim 17.67$  (Figure 1-6). While the regions of stability for the classical ordered phase  $L$ ,  $H$ ,  $Q_{Im\bar{3}m}$  grow with increasing  $\chi N$ , the region of stability for the bicontinuous  $Q_{Ia\bar{3}d}$  phase decreases monotonically beyond  $\chi N \sim 18$ . Initially, the region  $Q_{Ia\bar{3}d}$  narrows gradually, but this becomes more rapid as  $\chi N$  increases.



**Figure 1-7.** Ternary phase diagram of *SBM* triblock terpolymers. Polystyrene (PS) – grey; Polybutadiene (PB) – black; Poly(methyl methacrylate) – white (stained with  $OsO_4$ ).<sup>34,35</sup>

In the case of *ABC* triblock terpolymers, besides *AB* contacts, an important role play *AC* and *BC* interactions. Mogi *et al.*<sup>36,37,38</sup> and Stadler *et al.*<sup>34,35,39</sup> have done pioneering work on *ABC* triblock terpolymers. An example of ternary phase diagram of polystyrene-*block*-polybutadiene-*block*-poly(methyl methacrylate) (*SBM*) is shown in Figure 1-7.

1.1.2 Order-Disorder Transition Temperature ( $T_{ODT}$ ) in Block Copolymers

**Figure 1-8.** Schematic illustration of ordered (lamellar) and disordered  $AB$  diblock copolymer.

The most important thermodynamic feature in block copolymer phase behavior is the order-disorder transition ( $ODT$ ) which separates regions characterized by broken translational and orientational symmetry from the isotropic state (Figure 1-8). The ordered, or microphase-separated, state refers to the periodically arranged spherical, cylindrical, lamellar structures<sup>40</sup>, while the disordered state is spatially homogeneous. These two thermodynamic regimes are separated by the order-disorder transition ( $ODT$ ). As already investigated by Rosedale<sup>41</sup>, the rheological properties around  $ODT$ , taking into account the influence of composition fluctuations, confirms the first-order nature of this transition for nearly symmetric samples. This first-order phase transition can be identified in a variety of ways.

Using rheological measurements to investigate  $ODT$ 's in block copolymers, two types of rheological experiments are usually conducted: (a) a dynamic temperature sweep experiment under isochronal conditions and (b) a dynamic frequency sweep experiment at various temperatures. The easiest method for determining  $T_{ODT}$  is via a low-frequency isochronal viscoelastic measurement.<sup>41,42,43,44</sup> The isochronal test involves measuring the elastic modulus at a constant frequency over a selected range of temperatures while heating the sample near the microphase separation transition. Accurate determination of  $T_{ODT}$  requires the acquisition of dynamical mechanical data well below a critical frequency,  $\omega_c$ . The critical frequencies for  $G'$ ,  $\omega_c'$  and for  $G''$ ,  $\omega_c''$  have been established making use of the time-temperature

superposition principle. In order to observe a significant jump in  $G'$  and  $G''$  at  $T_{ODT}$ , experiments must be conducted well below  $\omega_c'$  and  $\omega_c''$ , respectively. The order-disorder transition determined from the discontinuity in isochronal plots of the elastic modulus and dynamic viscosity versus temperature, was found to be coincident with the identification of two branches in the dynamic moduli below a critical reduced frequency,  $\omega_c$ , as follows:  $G' \sim \omega^2$  and  $G'' \sim \omega$  at  $T > T_{ODT}$  and  $G' \sim G'' \sim \omega^{0.5}$  for a lamellar system at  $T < T_{ODT}$ . The gap between these two distinct branches occurs at  $T_{ODT}$  and increases in size with decreasing reduced frequency. Order and disorder are also reflected in the frequency domain through isothermal measurements. Here the effects of fluctuations<sup>45</sup> in the disordered state,  $T > T_{ODT}$ , could be misinterpreted as evidence of order, leading to estimated transition temperatures that are significantly higher than the actual value. The weakly first-order transition  $ODT$  is driven by fluctuations<sup>26</sup>, which become apparent at temperatures well above and below  $T_{ODT}$ .

Small-angle neutron scattering study of a partially deuterated diblock copolymer demonstrates the central role of fluctuations in inducing the weak first-order microphase separation transition.<sup>42</sup> The failure of time-temperature superposition<sup>46,47</sup> above and below  $T_{ODT}$  is a direct manifestation of these fluctuations, which respond to changes in temperature different than do the classical viscoelastic responses. Because these fluctuation effects reflect a collective response from many polymer chains, they appear at frequencies well below the single-chain terminal frequency, whereas can be assumed the proportionality between frequency and inverse relaxation time ( $\tau_d$ ),  $\omega \approx \tau_d^{-1}$ .

Han and Kim<sup>48</sup> have proposed an alternative method for interpreting dynamic mechanical data in order to establish  $T_{ODT}$  in block copolymers. Their approach relies on the Cole-Cole plot ( $G'(\omega)$  versus  $G''(\omega)$ ) which eliminates the nonrigorous use of time-temperature superposition. Han and Kim interpret as an evidence of the microphase separation transition,  $T_{ODT}$ , a departure from temperature independence in a logarithmic plot  $G'$  versus  $G''$ . Some investigators<sup>41,49</sup> have interpreted the parallel feature of  $\log G'$  vs  $\log G''$  plot having a slope of 2, as being the signature for thermal fluctuations effects in the disordered state near the  $T_{ODT}$  of a block copolymer. As reported by Hashimoto and Han<sup>50</sup>, the plot  $\log G'$  vs  $\log G''$  has been used to determine order-order transition ( $T_{OOT}$ ) in the case of asymmetric polystyrene-b-polyisoprene-b-polystyrene (Vector 4111), as being the threshold temperature at which the plot  $\log G'$  vs  $\log G''$  in the terminal region begins to exhibit a negative slope. The  $T_{OOT}$  result

from the plot  $\log G' \text{ vs } \log G''$  was confirmed by SAXS experiment, thus it might conclude that this plot can be used as well to determine the order-order transition of a block copolymer.

When using the dynamic temperature sweep experiment under isochronal conditions, Bates and co-workers<sup>20,21,22,23,51</sup> determined the order-order transition temperature ( $T_{OOT}$ ) of a block copolymer by identifying the temperature at which  $G'$  goes through a minimum. For PEE-PEP diblock copolymers investigated by Almdal et al.<sup>20,21,22,23</sup> and SI diblock copolymers investigated by Khandpur et al.<sup>51</sup> various ordered phases were observed as manifested by multiple minima in  $G'$  with respect to temperature.

The location of the microphase separation transition,  $T_{ODT}$ , is predicted to depend of the composition,  $f$ , the Flory-Huggins interaction parameter,  $\chi$ , and the degree of polymerization,  $N$ .<sup>12</sup> For a symmetric diblock copolymer ( $f = 0.50$ )

$$(\chi N)_{ODT} = 10.5 + 41.0 \bar{N}^{-1/3} \quad (1-6)$$

with

$$\bar{N} = (a^6 / v^2) N$$

where  $a$  and  $v$  are the statistical segment length and volume, respectively. The constant term from eq 1-6 corresponds to the Leibler's prediction, while the term containing  $\bar{N}^{-1/3}$  is a fluctuation correction.<sup>26</sup> As the temperature approaches  $T_{ODT}$ , the concentration fluctuation amplitude increases significantly, above  $T_{ODT}$  there is no pattern established and the system behaves as a liquid. Fredrickson and co-workers have developed a theory for the low-frequency rheological properties of block copolymers near the  $ODT$  which incorporates fluctuation effects. For the symmetric block copolymer at the  $ODT$

$$\left. \frac{\delta G'(\omega)}{G_0'(\omega)} \right|_{\omega \rightarrow 0} = \frac{0.1 N_e \bar{N}^{1/3}}{N} \quad \text{and} \quad \left. \frac{\delta G''(\omega)}{G_0''(\omega)} \right|_{\omega \rightarrow 0} = \frac{0.4 N_e}{N}$$

where  $G_0'(\omega)$  and  $G_0''(\omega)$  are fluctuation free dynamic moduli,  $\delta$  refers to the fluctuation contribution,  $\omega \rightarrow 0$  specifies the terminal flow regime, and  $N_e$  is the entanglement degree of polymerization.

The  $ODT$  can also be identified using small-angle scattering measurements, with either macroscopically isotropic or oriented specimens. Both the peak intensity and shape, but not  $q^*$ , are affected by the degree of long-ranged order. A convenient approach is to monitor the width of the principal ( $q^*$ ) reflection as a function of temperature in an isotropic sample.<sup>52,53</sup> Heating through the first-order  $ODT$  leads to a discontinuous broadening of the peak since the correlation length drops precipitously with disordering. Fluctuation effects also influence  $I(q^*)$ , and these should not be misinterpreted as evidence for the  $ODT$ .

Previous investigators using scattering results have defined the *ODT* temperature as the temperature at which data first deviates from linearity upon decreasing temperature when plotted as  $1/I_m$  versus  $1/T$ <sup>54,55</sup>;  $I_m$  is the maximum peak intensity and  $T$  is the absolute temperature. A linear decrease of  $1/I_m$  with  $1/T$  is predicted for the disordered state, and deviation from linearity is associated with the onset of microphase separation. Fluctuation effects have been found to be important for scattering experiments near the *ODT* by Bates et al.<sup>42</sup> Additionally the obtained information from the plot  $1/I_m$  versus  $1/T$  is combined with a plot of the domain spacing,  $D$  versus temperature,  $T$ , in which the *ODT* is defined as the temperature at which the domain spacing becomes constant. The domain spacing,  $D$  or correlation length,  $L_C$ , have been found to decrease slightly with increasing temperature and not an abrupt transition.<sup>56</sup>

An alternative to determine the  $T_{ODT}$  from scattering data is based on a qualitative observation made by Roe et al.<sup>57</sup> and involves evaluation of the shape of the scattering patterns. Roe et al. noted that as the temperature of the block copolymer is increased, the second and higher order peaks disappear, the intensity of the main peak decreases, and broadening of the main peak is encountered.

### 1.1.3 Blends of Block Copolymers

An additional pathway toward controlling the morphology is blending of block copolymers with different relative compositions. The first work<sup>58</sup> in the field of mixing block copolymers was done by Hadziioannou and Skoulios on styrene/isoprene di- and triblock copolymers. Blends of binary block copolymers<sup>59,60,61,19</sup> composed of two chemically different monomers have received special attention suggesting that such blends offer an alternative route to generate a desired morphology. Blends of lamellar ABC triblock terpolymers with AC diblock copolymers have been studied as well, and a periodic non-centrosymmetric superlattice<sup>62</sup> was generated. Such non-centrosymmetric materials become interesting due to their properties such as inherent polarization, piezo- or pyroelectricity. While by blending of polystyrene-*b*-polybutadiene-*b*-poly(methyl methacrylate) (SBM) with polystyrene-*b*-poly(methyl methacrylate)(SM) either macrophase separation or a cylindrical superlattice<sup>63</sup> was found, in the blend of polystyrene-*b*-polybutadiene-*b*-poly(*t*-butyl methacrylate) (SBT) with polystyrene-*b*-poly(*t*-butyl methacrylate) (ST) a non-centrosymmetric<sup>62</sup> periodic lamellar superlattice was obtained (equimolar blend 60% SBT and 40%ST).

Besides the composition of block copolymers, their relative amounts and their molecular weights together with the choice of solvent is important for the structure formation in block copolymer blends. In a blend the selectivity of the solvent can lead to microphase separation, for example the blend of SBT and ST cast from toluene shows macrophase separation because toluene favors polybutadiene and thus ST precipitates first. In the case of using chloroform for SBT and ST the macrophase separation is avoided due to the less selectivity of chloroform for the different blocks and the non-centrosymmetric superlattice is obtained.

Blends of ternary triblock copolymers and homopolymers or random copolymers were investigated by Lescanec et al.<sup>64</sup> namely they investigated the polystyrene-b-polyisoprene-b-poly(2-vinyl pyridine) (SIVP) mixed with homopolystyrene and a small amount of added homopolymer was shown to have a pronounced effect on the morphology of the SIVP/S blends.

An example of blends of a ternary triblock terpolymer with a random copolymer and a homopolymer is polystyrene-b-poly(ethylene-co-butylene)-b-poly(methyl methacrylate) (SEBM) with poly(2,6-dimethyl-1,4-phenylene ether) (PPE) and poly(styrene-co-acrylonitrile) (SAN). PPE/SAN blends are of commercial interest and in order to stabilise a highly dispersed morphology of 20% PPE in 80% SAN blends, SEBM lamellar triblock copolymers have been used.<sup>65</sup> While the SEBM forms lamellae morphology (ll) in the pure state, blending with PPE and SAN leads to a lamellae-spherical morphology (ls) due to the selective swelling of the S domain by PPE and a swelling of M domain by SAN, leading to an increase of the relative volume fractions of the endblocks with respect to the EB middle block.

Blends of ABC and ADC triblock terpolymers were considered as well, where the block D differs by a polymer analogous modification of the middle block, B. For example blending of  $S_{33}B_{34}M_{33}^{153}$  lamellae and  $S_{43}B_{14}M_{43}^{102}$  lamellae-cylinders (lc) with their homologous hydrogenated  $S_{33}EB_{34}M_{33}^{153}$  (ll) and  $S_{43}EB_{14}M_{43}^{102}$  (lc) a macrophase separation is observed.<sup>66</sup>

Blends of ternary triblock terpolymers give access to a variety of morphologies which have been unknown for pure triblock terpolymers. A mixing at the molecular level occurs in blends of block copolymers within a simultaneous microphase separation leading to superlattices.

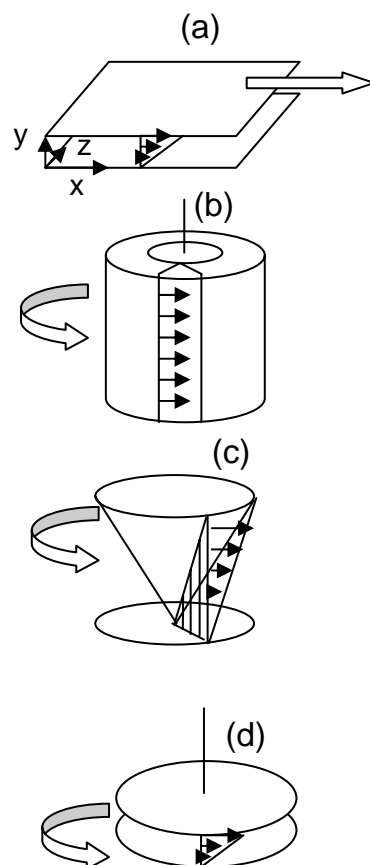
## 1.2 Alignment of Block Copolymer Morphologies

### 1.2.1 Alignment by Mechanical Field – Shear Alignment

The ordered structures provided from block copolymers can be used to pattern surfaces or produce materials in which the order of the nanostructure extends to macroscopic scale. The morphology and dynamics of block copolymers can be systematically controlled by choice of the polymer segments and their relative length. Under the influence of external fields the ordered structures of block copolymers can be aligned toward "single-crystal" materials. Mechanical<sup>1,67,68,69,70</sup> and electrical fields have been the most useful to induce alignment of randomly oriented microdomains from a block copolymer morphology. Keller and co-workers<sup>71,72</sup> were the first to report on the complex dynamics in block copolymers subjected to external mechanical fields. Due to the phenomenon *flow alignment*, macroscopic orientation is induced in ordered block copolymers with an initially random distribution of grain orientations. Shear flow is capable of inducing different orientation states in the same material, depending on alignment conditions (temperature, oscillatory shear flow frequency, strain, shear rate, etc). Macroscopic alignment has been achieved in materials subjected to extrusion, oscillatory<sup>70,69,73,74,75,76,77</sup> and steady shear<sup>78</sup>. Mostly the studies of flow alignment dynamics have been performed on symmetric polystyrene-polyisoprene (PS-PI) diblock copolymers, either in the melt<sup>79,80,3,4,81,1,2,82,83,83,84,85</sup> or in solution.<sup>5,6,7</sup>

#### 1.2.1.1. Unidirectional Shear<sup>86</sup>

The simplest way of generating steady simple shear is to place one material between a fixed plate and another plate moving at constant velocity. If the inertial edge effects can be neglected, then the flow is homogeneous and some examples of such geometries for drag flows are illustrated in the Scheme 1-1. The viscoelastic liquids are capable of steady-state shearing deformation at a constant strain rate,  $\dot{\gamma}$ . The stress during steady flow (sufficiently slow to ensure linear behavior) is:  $\sigma = \dot{\gamma}\eta_0$  where  $\eta_0$  is the viscosity corresponding to vanishing shear rate. In a stress relaxation experiment if the flow is abruptly stopped, the stress will gradually decrease and could be given by:  $\sigma(t) = \dot{\gamma} \int_t^\infty G(t) dt$ , with  $G(t)$  - relaxation modulus.



**Scheme 1-1.** Common shear flow geometries: (a) sliding plates; (b) couette flow; (c) cone and plate; (d) parallel disk.

### 1.2.1.2. Large Amplitude Oscillatory Shear

The linear spectrum of polymer melts or polymer solutions is normally determined in small amplitude oscillatory shear. At low strains the material response is approximately linear. At larger strains, such as Large Amplitude Oscillatory Shear (LAOS) nonlinear effects do play an important role. The earliest LAOS experiments have been already done 50 years ago.<sup>87</sup> Since oscillatory shear testing allows the strain amplitude and the time scale to be varied independently, large amplitude oscillatory shear represents an interesting method for studying nonlinear viscoelasticity in polymeric liquids. Because oscillatory shear does not involve any sudden jumps in the speed or position, it is relatively easy flow to generate. Oscillatory shear is a uniform simple shear deformation in which the shear strain is

$$\gamma(t) = \gamma_0 \sin(\omega t) \quad (1-7)$$

and the shear rate is

$$\dot{\gamma} = \gamma_0 \omega \cos(\omega t) \quad (1-8)$$

where  $\gamma_0$  is the shear strain amplitude and  $\omega$  is the angular frequency. The experimental evidence confirms the shear-stress response to oscillatory shear is also sinusoidal, when  $\gamma_0 \ll 1$

$$\sigma(t) = \sigma_0 \sin(\omega t + \delta) \quad (1-9)$$

where  $\delta(\omega)$  is called the mechanical loss angle and the amplitude ratio,  $\sigma_0 / \gamma_0$  is the dynamic modulus:

$$G_d \equiv \sigma_0 / \gamma_0 \quad (1-10)$$

At small strains  $G_d$  and  $\delta(\omega)$  depend upon frequency only, and not on  $\gamma_0$ . Since  $\sigma_0$  is proportional to  $\gamma_0$ , this behavior is called linear viscoelasticity. In terms of the storage and loss moduli, linear properties are reported:

$$G' \equiv \sigma_0 / \gamma_0 \cos \delta \quad (1-11)$$

and

$$G'' \equiv \sigma_0 / \gamma_0 \sin \delta \quad (1-12)$$

This small strain behavior is described by the theory of viscoelasticity, which can be expressed in terms of the Boltzmann superposition principle:

$$\sigma(t) = \int_{-\infty}^t G(t-t') \dot{\gamma}(t') dt' \quad (1-13)$$

where  $\sigma$  is the stress tensor and  $\dot{\gamma}$  is the rate of deformation tensor. Within the linear theory of viscoelasticity, the response to any deformation history can be calculated if the relaxation modulus,  $G(t)$  is known. By introducing eq 1-8 in eq 1-13, the following expression is obtained:

$$\sigma(t) = \gamma_0 \omega \int_{-\infty}^t G(t-t') \cos(\omega t') dt' \quad (1-14)$$

Thus, the behavior in small-amplitude oscillatory shear for the storage and loss moduli can be deduced from the relaxation modulus,  $G(t)$ :

$$G'(\omega) = \omega \int_0^{\infty} G(t) \sin(\omega t) dt \quad (1-15a)$$

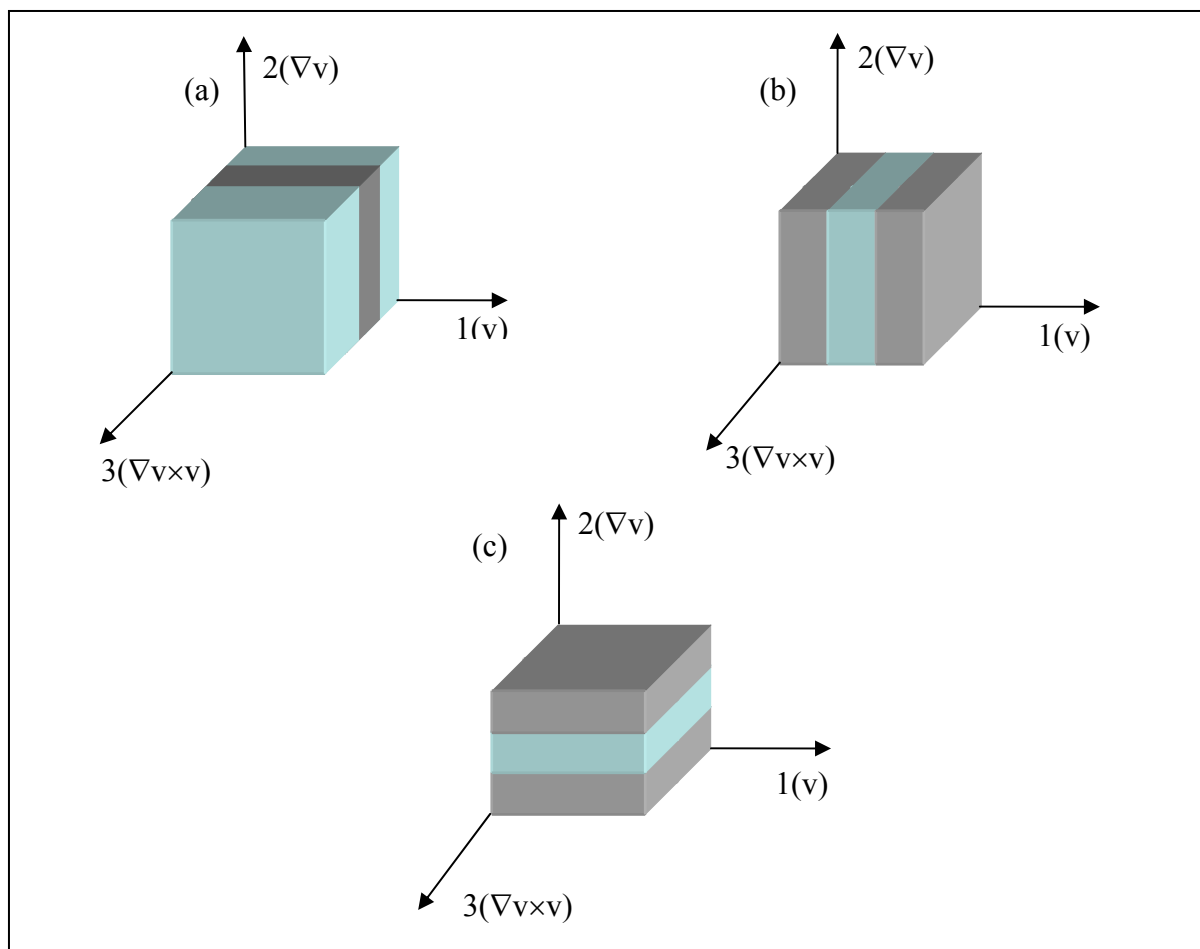
$$G''(\omega) = \omega \int_0^{\infty} G(t) \cos(\omega t) dt \quad (1-15b)$$

However, for most polymeric liquids, the stress response in large-amplitude oscillatory shear is not sinusoidal. This is why the property definitions for linear behavior,  $|G^*|$  and  $\delta$  are not meaningful for a nonlinear viscoelastic response.

Cone-plate geometry has been used to measure large-amplitude oscillatory shear properties. MacSporran and Spiers<sup>88</sup> used a Weissenberg rheogoniometer to characterize

polymer solutions in large amplitude oscillatory shear with cone-plate flow. For low viscosity liquids, centripetal acceleration causes sample outflow while for polymer melts LAOS experiments are very difficult for strain amplitudes  $\gamma_0 > 1$  using cone-plate flow. Hence, cone-plate flow is not a useful technique for polymer melts when  $\gamma_0 > 1$ . In parallel-disk flow, shear strain amplitude is proportional to radial distance from the center and thus there is a heterogeneous flow field. Some of the most successful attempts to measure large-amplitude oscillatory shear properties have employed concentric cylinder rheometers. Onogi and co-workers<sup>89</sup> used concentric cylinders for nonsinusoidal oscillatory shear measurements on polymer solutions and suspensions for shear-strain amplitudes below unity. Dealy and co-workers<sup>90</sup> have used concentric cylinders to molten plastics and the Weissenberg effect has been encountered at strains above 10.

In terms of induced macroscopically alignment in block copolymers, LAOS experiments mostly done for polystyrene-polydiene melts have proved the efficiency of this technique toward obtaining aligned states. Ex situ (SAXS, TEM) and in situ (birefringence, SANS, SAXS) methods have been used to characterize the final aligned state after using large amplitude oscillatory shear. In situ methods are preferable because they offer superior time resolution and opportunity to investigate the alignment kinetics. Off-line SAXS on shear-aligned samples provides the possible orientations in the three coordinate planes defined by the shear geometry in use. A detailed analysis has been made by Chen and Kornfield<sup>67,70</sup> on the SI diblock copolymer melt which combines in-situ rheo-optical measurements and ex-situ structural characterization by electron microscopy and X-ray scattering. As a result a three-dimensional map summarizes the results on the selection on alignment directions (parallel or perpendicular) in correlation with the following parameters: temperature, frequency and strain amplitude. Three regimes of behavior in PS-PI lamellar diblock copolymers have been distinguished: perpendicular and parallel by two distinct pathways (perpendicular or transverse). A schematic representation of the possible type of alignment induced in a lamellar diblock copolymer melt within the defined axes is shown in the Scheme 1-2.



**Scheme 1-2.** Schematic representation of the type of alignment induced in lamellar diblock copolymer melt by applying LAOS: (a) perpendicular; (b) transverse; (c) parallel. The cartesian axes are defined as following:  $1(v)$ -flow direction;  $2(\nabla v)$ -gradient velocity;  $3(\nabla \times v)$ -vorticity.

Rheo-optical studies showed that all three types of alignment trajectories start with a fast process that transforms the initial isotropic melt to an anisotropic melt, followed by a slow process which defines the final stable orientation (either parallel or perpendicular). A priori investigation of the viscoelastic behavior is required before performing the alignment procedure, because the master curve reveals the critical regime of frequency where the system is homogeneous and the frequency where starts the disordering state. Moreover, an order-disorder transition temperature is necessary to be known according to the further alignment protocol. Within the critical frequency,  $\omega_c'$ , there have been defined the regions with the corresponding type of alignment: (1)  $\omega < \omega_c'$ , perpendicular alignment; (2)  $\omega \geq \omega_c'$ , parallel alignment; (3)  $\omega \gg \omega_c'$ , parallel alignment. In general, in PS-PI parallel alignment (layer normals parallel to velocity gradient) has been induced at high frequency, due to the

viscoelastic contrast between rigid polystyrene and rubbery polyisoprene. Patel et al<sup>3</sup> have introduced the concept of *viscoelastic contrast* to explain parallel alignment at higher frequencies,  $\omega \gg \omega_c'$  for the PS-PI diblock. If there is considerable difference in the mechanical properties between the two types of layers, the modulus of the parallel state is lower than that of the perpendicular state, which may explain the selection of parallel alignment. At low frequency,  $\omega < \omega_c'$ , perpendicular alignment<sup>79,80,3</sup> has been detected as the final aligned state and at a frequency close to  $\omega_c'$ , a flip from perpendicular to parallel alignment by changes in the applied strain amplitude<sup>2</sup> is encountered.

It should be mentioned that the previously investigated SI systems in the melt state had an accessible order-disorder transition temperature ( $T_{ODT}$ ). Intermediate molecular weights of nearly symmetric PS-PI (55K, 58K) under large amplitude oscillatory shear, as well as the entanglement effect, have been studied by Zhang and Wiesner.<sup>73</sup> Using 2D-SAXS and TEM measurements, for the PS-PI with intermediate molecular weights so called "cake orientation" have been found beside parallel orientation similar to the transverse orientation introduced earlier by Kornfield. They conclude that topological constraints which dominate the chain dynamics within the entanglement plateau region of the two blocks are responsible for the transverse orientation, this orientation being not reported in the case of low molecular weight systems. It has been pointed out that the pure transverse orientation may be achieved by adjusting the shear conditions like choosing small strain values and short shearing times, the transverse orientation have been theoretically described by Vinals.<sup>91</sup> Furthermore, transverse orientation of lamellae by extruding an ABABA pentablock copolymer solution has been reported by Lodge<sup>92</sup>, as a rapid and facile means to prepare macroscopic quantities of highly aligned block copolymer microstructures.

Balsara and co-workers have started the first investigations on concentrated solutions of PS-PI block copolymers in a neutral solvent<sup>93,5,6,7</sup>, in order to identify the extend to which concentrated solutions mimic the behavior of PS-PI melts. Small-angle neutron scattering experiments on a polystyrene-polyisoprene diblock copolymer in concentrated dioctyl phthalate solution (65wt %) under Couette shear, have identified that lamellae are oriented mostly parallel to the plane of the shear cell walls<sup>5</sup>, while further investigations by Wang<sup>7</sup> demonstrated two orientations: (1) lamellae parallel to the shearing surfaces and (2) lamellae perpendicular to the shearing surfaces. Flow alignment<sup>69</sup> in a symmetric PS-PI (~80K) diblock copolymer, solution in dioctyl phthalate (DOP) has been studied using flow birefringence and rheology and it was found a similar behavior to that in the PS-PI melts.

Steady and oscillatory shear were performed and high degrees of alignment were achieved in large amplitude oscillatory flow, as a proof that steady shear is more complex. Also, it has been pointed out that *viscoelastic contrast* plays a significant role in the high shear rate/high frequency flow alignment dynamics and there is a strong connection between the degree of perpendicular alignment within enhanced linear moduli at high frequency.

Besides shearing conditions (temperature, frequency, strain amplitude), the material properties (order-disorder transition temperature, glass transition temperature of each block, degree of entanglement) affect the alignment kinetics. Here, it should be reminded the following parameters such as: strength of segregation ( $\sim T/T_{ODT}$ ), the chain mobility ( $(T/T_g)_A$ ,  $(T/T_g)_B$ ,  $(M/M_e)_A$ ,  $(M/M_e)_B$ ) and the viscoelastic contrast between layers ( $T_{g,A}/T_{g,B}$ ) which may help to understand the alignment kinetics of an AB diblock copolymer.

### 1.2.2. Alignment by electric field

In addition to mechanical fields, another pathway toward induced aligned block copolymers morphologies is due to the electric field. Electric field alignment is interesting because the driving force for alignment is much simpler than that induced by flow and besides that offers means of orienting block copolymers in ways not possible by flow methods. Electric fields provide a weaker aligning force, but offer the advantage of local alignment control, and the alignment is possible due to the differences in the dielectric constants of the blocks ( $\Delta\epsilon$ ). It has been shown that lamellar and cylindrical microdomain structures in polystyrene-*b*-poly(methyl methacrylate) thin films could be oriented by a dc electric field.<sup>94,95,96,97</sup> In a cylindrical morphology under an electric field the cylinders orient along the field vector resulting in a single monodomain.

Also, the microdomain alignment of an ABC triblock terpolymer during solvent casting in the presence of an external dc electric field has been already investigated.<sup>98</sup> In comparison to melt alignment the method of using block copolymers as solutions is applicable for high molecular weight block copolymers which cannot be aligned in the melt. The aligning force of an electric field is smaller for block copolymer solutions than for melts due to an effective reduction of the difference in the dielectric constants of the blocks  $\Delta\epsilon$  by the solvent. Specifically, the polystyrene-*b*-poly(hydroxyethyl methacrylate)-*b*-poly(methyl methacrylate) (PS-*b*-PHEMA-*b*-PMMA) triblock terpolymer with a molecular weight of  $M_n=82K$  and as 30 vol.-% solutions in chloroform has been aligned under an electric dc field of 1.8 kV/mm with lamellae parallel to the electric field vector. To quantify the induced alignment under an

electric field, the order parameter  $P_2$  is calculated by integrating the scattering intensity from  $\varphi = 0^\circ$  to  $360^\circ$ :

$$P_2 = \frac{3\langle \cos^2 \varphi \rangle - 1}{2} \quad (1-16)$$

with

$$\langle \cos^2 \varphi \rangle = \frac{\int_0^{2\pi} (I_q(\varphi) \cdot \cos^2(\varphi) |\sin(\varphi)|) d\varphi}{\int_0^{2\pi} (I_q(\varphi) \cdot |\sin(\varphi)|) d\varphi} \quad (1-17)$$

The  $P_2$  values range from 0 to 1 and  $P_2 = 1$  corresponding to perfect lamellar alignment with the normals of lamellae perpendicular to the electrodes surfaces. When the lamellae are oriented along field direction ( $\varphi = 90^\circ$ )  $P_2$  ranges from 0 to -0.5 with  $P_2 = -0.5$  corresponding to the case where all lamellae are aligned parallel to the field. The  $P_2$  values of 1 and -0.5 represent the range for order parameter which describes perfect alignment. It has been shown as well in the alignment induced by electric field that an important parameter is the degree of segregation, illustrated through the value of the interaction parameter,  $\chi$ . For the weakly segregated systems the mechanism of the orientation process is dominated by the migration of grain boundaries, whereas for the stronger segregated systems the mechanism of orientation is dominated by the rotation of the grains.<sup>99</sup>

### 1.2.2.1. Electric field combined with birefringence method

#### *Electrothermodynamics*

The free energy of a dielectric material in an electric field<sup>95</sup> is written as following:

$$F = F_0 - \frac{1}{8\pi} \int_v \varepsilon(r) |E(r)|^2 d^3r \quad (1-18)$$

$F_0$ : free energy without an electric field

$\varepsilon(r)$ : local dielectric constant

$E(r)$ : electric field

The integration is over the volume of the material,  $v$

Different composition patterns within a block copolymer material and the associated spatially varying local dielectric constant produce different patterns of electric field. The consequence

is a composition pattern dependent electrostatic contribution to the free energy. Following the equation in terms of the free energy, the materials with high dielectric constant are attracted to regions of high field strength, in order to maximize the magnitude of the negative electrostatic contribution.

For microstructures with at least two distinct axes of threefold or greater rotational symmetry, the electric field cannot act to align such microstructures. In this class are the body centered cubic (spherical) and the ordered bicontinuous double-gyroid morphologies.

On the other hand, cylindrical and lamellar morphologies do interact anisotropically with an electric field, for example for a cylindrical morphology the cylindrical axes are parallel to the field.

The free energy expression presented here neglects the contribution to the electric field energy from the alignment and stretching of the chains and the difference of polarizability of these chains in the directions along and perpendicular to the bonds. Such effects were considered in the context of birefringence.

### *Birefringence*

A block copolymer in the ordered state shows form birefringence. The dielectric tensor in a material with uniform morphology is given by:

$$\underline{\underline{\varepsilon}} = \langle \varepsilon \rangle \underline{\underline{I}} - \frac{\beta^2}{\varepsilon_D} \langle \overline{\psi^2} \rangle e_q^\wedge e_q^\wedge \quad (1-19)$$

$\langle \varepsilon \rangle$ : space averaged dielectric constant

$\beta = \frac{\partial \varepsilon}{\partial \psi}$ : measure the sensitivity of the dielectric constant to composition change,  $\psi$

$\langle \overline{\psi^2} \rangle$ : mean square of the composition pattern strength

$\varepsilon_D$ : dielectric constant in the limit of vanishing stationary composition pattern and includes effects of dynamic composition fluctuations

$e_q^\wedge$ : unit wave vector of the lamellar pattern

All dielectric constants and  $\beta$  must be evaluated at the frequency of light when computing birefringence, and so they are different from those used in equations relating to electrothermodynamics (eq 1-18). Equation 1-19 neglects the anisotropy of the dielectric tensor resulting from the alignment, so called intrinsic birefringence. It has been calculated that intrinsic birefringence is about one-third of the form birefringence for the polystyrene-

block-poly(methyl methacrylate) ( $M_n=37K$ ) in the strong segregation limit, instead for the weak segregation the ratio of the intrinsic to form birefringence is about the same.<sup>95</sup> In the case of a sample aligned by an electric field and monitoring the alignment by birefringence method<sup>95</sup>, the effective birefringence for light propagating at an angle  $\alpha$  with respect to field direction  $e_z^{\wedge}$  is then:

$$\Delta n = \Delta n^0 \langle \sqrt{\psi^2} \rangle P_2 \sin^2 \alpha \quad (1-20)$$

$$\Delta n^0 = -\frac{(n_1^2 - n_2^2)^2}{2n_D^3} \quad (1-21)$$

The order parameter follows the expression  $P_2 = \frac{3}{2} \langle \cos^2 \theta \rangle - \frac{1}{2}$  with  $\theta$  the angle between  $e_q^{\wedge}$  and  $e_z^{\wedge}$ . For a macroscopically disordered block copolymer,  $P_2=0$  and decreases during electric field alignment until it reaches a value  $P_2 = -0.5$  corresponding to a maximum alignment. In eq 1-21,  $n_D \sim \sqrt{\varepsilon_D}$  and  $\beta$  is approximated as  $(\varepsilon_1 - \varepsilon_2) \equiv (n_1^2 - n_2^2)$  with the subscripts “1” and “2” referring to the properties of the two pure components of the lamellar diblock copolymer. Eq 1-20 shows that birefringence is proportional to the orientational order parameter,  $P_2$  when the birefringence is simultaneously monitored during applying an electric field.

## 2. Methods

### 2.1 Synthesis

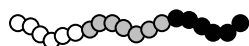
#### 2.1.1 Anionic Polymerization

Living polymerizations provide the methodologies for the preparation of macromolecules with well-defined structures and low degrees of compositional heterogeneity.<sup>100,101</sup> Using these methodologies it is possible to synthesize macromolecular compounds with control of a wide range of compositional and structural parameters including *molecular weight, molecular weight distribution, copolymer composition and microstructure, stereochemistry, branching and chain-end functionality*. Since 1956, Szwarc and co-workers<sup>102,103</sup> have described "living" nature of anionic polymerizations of styrene and diene monomers. The term "living polymers" is used to describe systems in which active centers remain after complete polymerization, so that a new batch of monomer subsequently added will add to the existing chains and increase their degree of polymerization. One of the most important synthetic applications of living polymerizations is the synthesis of block copolymers by sequential monomer addition<sup>104,105</sup>, especially living anionic polymerization provides the best technique for preparation of well-defined block copolymers<sup>106,107</sup>

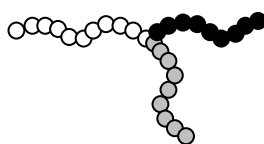
By variation of composition and architecture the following properties can be controlled:

↳ Molecular weight and molecular weight distribution

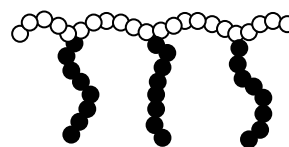
↳ Topology of the polymers



multiblock copolymer



star block copolymer



comb shaped polymer

↳ Sequence of the monomer units



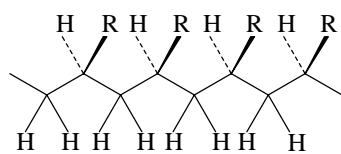
block copolymer



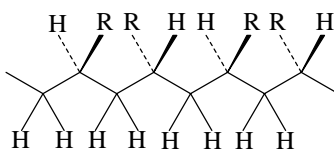
statistical copolymer

↳ End functionalized polymers by a functionalized initiator or end capping of the living chain end<sup>108</sup>

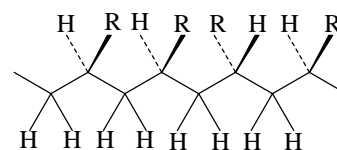
↪ Tacticity for monomers of the type  $\text{CH}_2=\text{CHR}$



isotactic

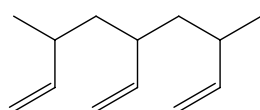


syndiotactic



atactic

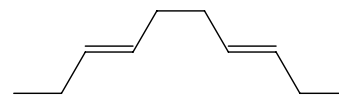
↪ Microstructure of diene-based polymers



1,2-polybutadiene



1,4-cis polybutadiene



1,4-trans polybutadiene

A variety of other mechanistic types of living polymerizations have been developed including *cationic* polymerization<sup>109,110</sup>, *Ziegler-Natta* polymerization<sup>111,112</sup>, *ring-opening metathesis*<sup>113</sup>, *living controlled radical* polymerization (atom transfer radical polymerization, ATRP).<sup>114,115</sup>

### 2.1.2 Basics of anionic polymerization

*Molecular weight distribution.* The molecular weight in a living polymerization can be controlled by the stoichiometry of the reaction and the degree of conversion. In general, it is possible to prepare a polymer with a narrow molecular weight distribution (Poisson distribution) using a living polymerization when the rate of initiation is higher than the rate of propagation.<sup>116</sup> This condition ensures that all of the chains grow simultaneously.

The relationship between the polydispersity and the degree of polymerization for a living polymerization is shown in eq 2-1

$$\frac{X_w}{X_n} = 1 + \frac{X_n}{(X_n + 1)^2} \cong 1 + \frac{1}{X_n} \quad (2-1)$$

where  $X_n$  is the number average degree of polymerization,  $X_w$  is the weight average degree of polymerization,  $X_w / X_n$  is the polydispersity (PDI). The second approximation from eq 2-1 is valid for high molecular weights. Thus, it is predicted that the molecular weight

distribution will decrease with increasing molecular weight for a living polymerization system. From practical point of view it is easier to make higher molecular weight polymers, while lower molecular weight polymers with narrow molecular weight distributions requires careful attention to experimental details.

A living anionic polymerization consists only of initiation and propagation steps, in the absence of termination and chain transfer. As a consequence, the concentration of propagating chains is constant during the course of the reaction and the number average molecular weight depends linearly on the conversion. Thus, for a full conversion the number average degree of polymerization can be written as

$$X_n = \frac{[M]_0}{[I]_0} \quad (2-2)$$

$[M]_0$  : initial concentration of monomer

$[I]_0$  : initial concentration of monofunctional initiator

Efficient mixing throughout the polymerization is required and depropagation must be slow relative to propagation. According to eq 2-1 at sufficiently high degrees of polymerization the PDI is close to unity and under ideal conditions  $X_w / X_n < 1.1$ <sup>117</sup>

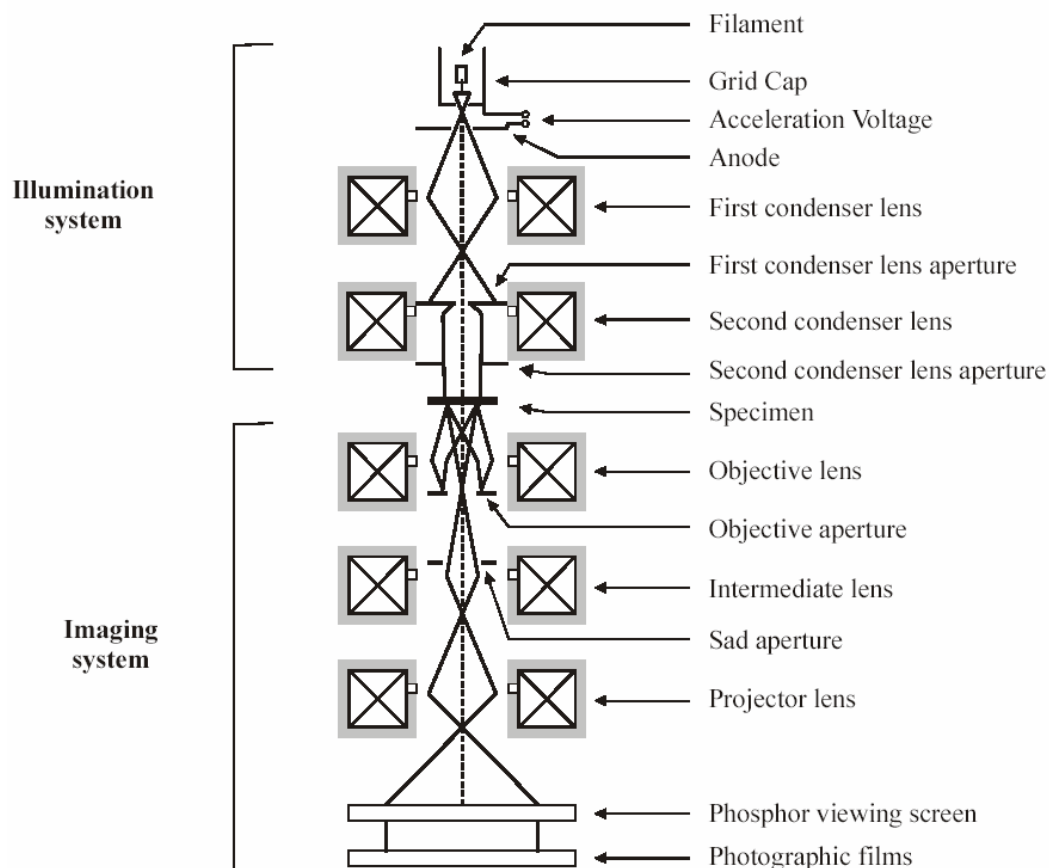
The mechanism of anionic polymerization can be divided in three principal reactions: *initiation*, *propagation* and *termination* of the reaction by addition of a hydrogen transfer agent (e.g. methanol or water).

## 2.2 Characterization

### 2.2.1 Transmission Electron Microscopy (TEM)

#### 2.2.1.1 Fundamentals of Transmission Electron Microscopy<sup>118,119</sup>

Transmission electron microscopy is one of the analytical tools for the investigation of polymer morphologies, especially when studying multiphase polymer morphologies and polymer blends on a nanoscale. The resolution limit in transmission electron microscopy is about 0.1nm using an acceleration voltage of about  $10^4$ - $10^5$  V. A transmission electron microscope can be divided into two parts, the illumination and the imaging systems. A schematic cross-section is given in Scheme 2-1.



**Scheme 2-1.** Schematic cross section of a transmission electron microscope.<sup>118</sup>

The *illumination system* contains the electron gun and the first and second condenser lenses. The electrons are emitted from a V-shaped heated tungsten filament whereas the emitted electron density is controlled by the voltage applied at the filament. The grid cap allows the generation of a spot-shaped electron beam. The emitted electrons are accelerated by a high voltage field toward to the condenser lenses in the illumination system after crossing the anode. The role of the lenses is to regulate the intensity and refocus the electron beam. The resulted intense and parallel beam of monoenergetic electrons interacts with the specimen.

The *imaging system* consists of the *objective lens*, the *intermediate lens* and their corresponding apertures, the *projector lens*, a *phosphor viewing screen* and the *photographic film*. The objective lens and objective aperture from the imaging system can either generate a bright or a dark field image of the specimen. The apertures act as filters for elastically and inelastically scattered or transmitted electrons and are necessary to visualize a phase contrast in the sample. Low-density materials should have less than 100 nm thickness while high-density materials should be less than 20 nm thick. Bright field is the most used mode of transmission electron microscopy imaging, selecting the weakly scattered and transmitted

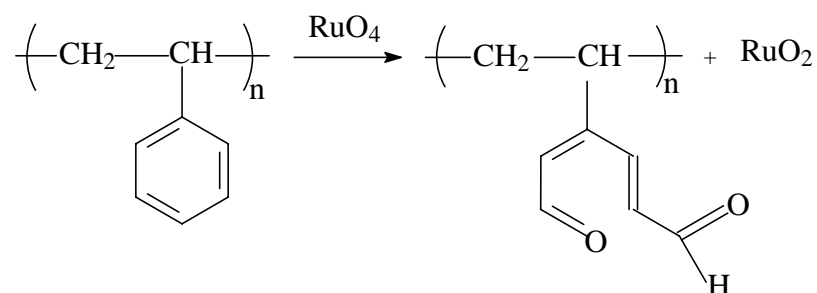
electrons by location of the objective aperture on the optic axis. Dark areas on the image (positive) correspond to strong scattering areas in the specimen.

In this work, TEM images were taken with a Zeiss CEM 902 electron microscope operated at 80 kV or a LEO 922 OMEGA electron microscope operated at 200 kV.

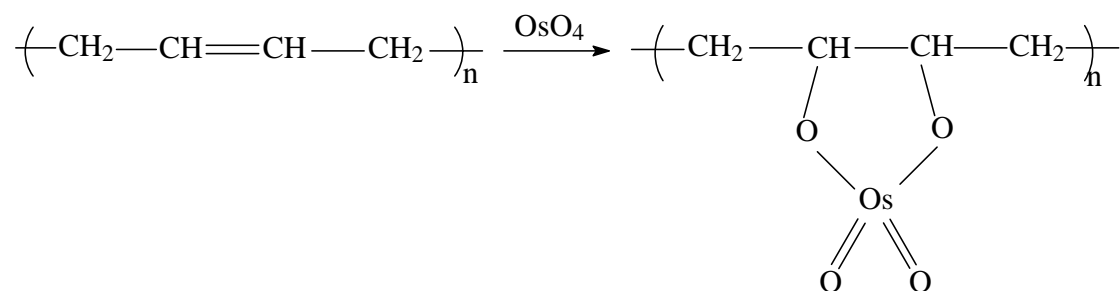
### 2.2.1.2 Staining of Polymer Samples

Due to the similar electron densities of the different components of organic block copolymers (unless they contain blocks with heavier atoms like, for example, Si, Cl or Br) an enhancement of the electron density is necessary. Different methods are available. Staining is one of the most popular technique for contrast enhancement.

The most widely used staining agents are ruthenium tetroxide ( $\text{RuO}_4$ ) and osmium tetroxide ( $\text{OsO}_4$ ) which can react with both aromatic and olefinic double bonds.<sup>120</sup> The reaction of ruthenium tetroxide with aromatic double bonds and osmium tetroxide with olefinic double bonds are shown in Scheme 2-2.



Reaction of  $\text{RuO}_4$  with aromatic double bonds



Reaction of  $\text{OsO}_4$  with olefinic double bonds

**Scheme 2-2.** Reaction of staining agents ( $\text{RuO}_4$ ,  $\text{OsO}_4$ ) with aromatic and olefinic double bonds.

The selectivity of ruthenium tetroxide strongly depends on the staining time and on the concentration of vapor. RuO<sub>4</sub> does not react with ester groups present in polymers, like poly(methyl methacrylate). The interfaces in strongly segregated microphase-separated polymers are stained more strongly by RuO<sub>4</sub> than expected from the corresponding homogeneous phase. This may be explained by an enhanced reactivity of the functional groups due to mechanical tension of the polymer chain at interfaces.

RuO<sub>4</sub> vapor is generated by the reaction of hydrated ruthenium trichloride (RuCl<sub>3</sub>·3H<sub>2</sub>O) and a 15wt.-% aqueous solution of sodium hypochlorite (NaOCl) according to Scheme 2-3.



**Scheme 2-3.** Generation of ruthenium tetroxide (RuO<sub>4</sub>) from ruthenium chloride (RuCl<sub>3</sub>).

An other staining agent is iodine usually used to stain poly(2-vinyl pyridine) by forming a charge-transfer complex with the amino function of the 2-vinyl pyridine.

### 2.2.1.3 Radiation Damage

Due to the high energy electrons of the beam which interact with the specimen possible structural changes may occur by radiation damage. The most commonly used criteria for radiation damage are breaking of covalent bonds, loss of crystallinity or polymerization of the material. An important feature of radiation damage is that, although in a biological or pure organic material up to 70% of the scattering events are inelastic, the damage does not necessarily result in a breaking of covalent bonds. A good example is graphite which is perfectly radiation-stable and is simply composed of carbon-carbon bonds. It is the case in which this energy can be dissipated over many atoms. A polynuclear aromatic species would be expected to be stable since the energy can be spread over the aromatic system.<sup>121</sup> Correspondingly, conjugated molecules should be more stable than aliphatic molecules although polymerization is likely to be a major process. Halogen (particularly chlorine) substituents considerably increase the radiation stability of aromatic systems.<sup>122</sup>

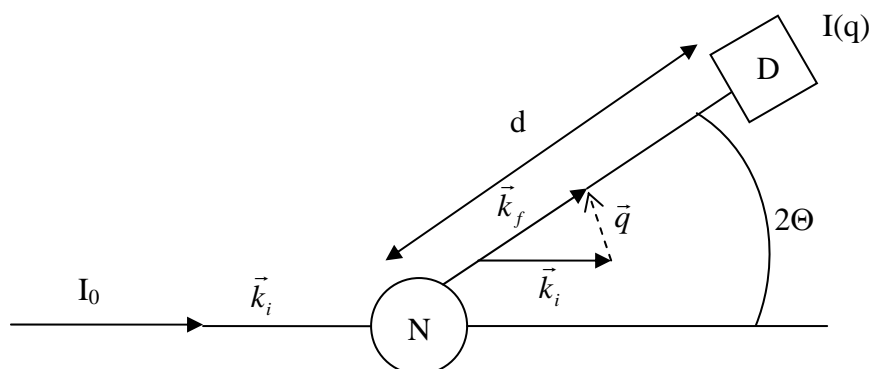
Coating specimens with thin layers of noble metals like gold<sup>121</sup> and cooling the specimen also reduce radiation damage in certain cases.<sup>123</sup> It was shown in block copolymers containing poly(methyl methacrylate) as one block that the apparent micrograph does not reflect the real

dimensions in the specimen, as the thickness of the PMMA-lamella is underestimated from the micrograph.<sup>66</sup>

## 2.2.2 Small Angle X-ray Scattering

### 2.2.2.1 Principles of scattering

Scattering involves "objects" which are of the same size as the wavelength of the radiation. Scattering is a very useful experimental tool for the assessment of the structure of the matter, including polymers. When the interacting "objects" are regularly positioned and when they are of about the same size as the radiation wavelength the scattering phenomenon occurs. Scattering is more diffuse when the objects (e.g. atoms) possess only short-range order. X-rays have wavelengths of about 0.1 nm, making them suitable for studying interatomic distances, e.g. crystal unit cell structures. Visible light ( $\lambda \approx 1 \mu\text{m}$ ) can be used to study larger objects, e.g. spherulites in semicrystalline polymers or polymer molecules in solutions. It is possible to study much larger objects using a certain radiation by recording the scattered intensity at very small angles. Wide-angle X-ray scattering (WAXS) is used for crystallographic work assessing structure with repeating distances typically less than 1 nm, whereas small-angle X-ray scattering is useful for assessing the size of "superstructures", such as the 10-50 nm long period of lamellar stacks in semicrystalline polymers. The thermal neutrons have a wavelength of approximately 0.45 nm and by employing small-angle neutron scattering (SANS), the global molecular dimensions can be assessed. A general experimental setup of a scattering experiment is presented in Scheme 2-4.



**Scheme 2-4.** General setup of a scattering experiment

$I_0$  : intensity of the incident beam

$I(q)$  : intensity of the scattered beam as a function of  $q$

$k$  : wave vector, [ $nm^{-1}$ ]

$d$  : distance between scattering object and detector, [ $nm$ ]

$q$  : scattering vector, [ $nm^{-1}$ ]

$D$  : detector

$N$  : total number of particles

$\Theta$  : Bragg scattering angle, [ $^\circ$ ]

An incident beam of monochromatic radiation with a wavelength  $\lambda$  and an intensity,  $I_0$ , is partly absorbed or scattered by a sample while the rest is transmitted unchanged. The intensity  $I(q)$  of the scattered waves is registered by a detector  $D$  at a distance  $d$  while the direction of observation is varied. The scattering vector,  $q$ , defined as  $q := k_f - k_i$  where  $k_f$  and  $k_i$  denote the wave vectors of the incident and the scattered plane waves, the result of a scattering experiment is usually expressed by giving the "intensity distribution in  $q$ -space",  $I(q)$ . In the majority of scattering experiments on polymers the radiation frequency remains practically unchanged and the wave vectors are equal in their magnitude (eq 2-3).

$$|k_f| \approx |k_i| = \frac{2\pi}{\lambda} \quad (2-3)$$

$k_f$  wave vector of the scattered beam, [ $nm^{-1}$ ]

$k_i$  wave vector of the incident beam, [ $nm^{-1}$ ]

$\lambda$  wavelength, [ $nm$ ]

The scattering vector,  $q$ , is related to the "Bragg scattering angle",  $\Theta$  by eq 2-4.

$$q = |q| = \frac{4\pi \sin \Theta}{\lambda} \quad (2-4)$$

$\Theta$  : Bragg angle, [ $^\circ$ ]

$q$  : scattering vector, [ $nm^{-1}$ ]

In contrast to the coherently scattered X-rays, the incoherently scattered ones result in scattered waves of longer lengths preserving no coherent phase relationship with the incident beam. This behavior can be observed in wide-angle X-ray scattering (WAXS) experiments while in SAXS the former one predominates. For the coherent elastic scattering of radiation at an angle  $2\Theta$  with respect to the incident beam, the intensity  $I(q)$  of the scattered beam is proportional to the square of the amplitude,  $A(q)$  as shown in eq 2-5.

$$I(q) \approx |A(q)|^2 \quad (2-5)$$

$I(q)$  : intensity of the scattered beam

$A(q)$  : amplitude of the scattered beam

The amplitude of the scattered beam,  $A(q)$ , derives from the electron density distribution within the sample as shown in eq 2-6.

$$A(q) = \int_V \rho(r) \exp(iqr) dr \quad (2-6)$$

$A(q)$  : amplitude of the scattered beam

$V$  : scattering volume of the sample, [ $cm^3$ ]

$\rho(r)$  : electron density, [ $C/cm^3$ ]

For materials exhibiting a long range and periodic order, the amplitude can be defined as the product of the so called lattice factor,  $L(q)$ , and the structure factor,  $F(q)$ , following eq 2-7.

$$A(q) = |L(q)| |F(q)| \quad (2-7)$$

$A(q)$  amplitude of the scattered beam

$L(q)$  lattice factor

$F(q)$  structure factor

The most important requirement is a very good collimation of the X-ray beam. There are several methods used: pinhole collimation and slit collimation. Three well-known instruments based on pinhole collimation are the Kiessig camera, the Rigaku Denki camera and the Statton camera. The Kratky camera is a slit camera with excellent collimation which also avoids diaphragm scattering, a problem which is present in the pinhole cameras.

#### 2.2.2.2 Small-angle X-ray scattering on microphase separated block copolymers

Small angle X-ray scattering (SAXS) is the most used technique to study polymer structures on a scale 2-200nm. The transmission electron microscopy allows the investigation of the microphase in local areas of a few micrometers, while SAXS provides the information about bulk properties of the segregated microdomains within the sample. The X-rays scattered from different electrons interfere with each other and generate a diffraction pattern that varies with the scattering angle. Due to the interaction of the beam with the electrons, segments of the block copolymers need to be different in their electron density in order to allow a monitoring of the morphology by SAXS. Otherwise the regularity of the morphology cannot

be detected in form of well-defined intensity maxima in the scattering profile. The electron density can be calculated using the eq 2-8.

$$\rho_{el} = \frac{N_A \rho_i Z_{el}}{m_i} \quad (2-8)$$

$\rho_{el}$  : electron density of component  $i$ , [ $C / cm^3$ ]

$N_A$  : Avogadro's number, [ $mol^{-1}$ ]

$\rho_i$  : density of component  $i$ , [ $g / cm^3$ ]

$Z_{el}$  : number of electrons of component  $i$ , [ $C$ ]

$m_i$  : molar mass of component  $i$ , [ $g / mol$ ]

The scattered intensity pattern arising from a microphase separated block copolymer is similar to the diffraction pattern obtained from a crystalline solid. The Bragg diffraction peaks occur at smaller scattering angles and show a broadening of the peaks due to the diminished regularity as compared to a regular crystalline lattice.<sup>124</sup>

The lattice factor,  $L(q)$  and the structure factor,  $F(q)$  from eq 2-7 must be defined in relation to the specific characteristics of block copolymers compared to crystals.

When the lattice has long range periodicity, the lattice factor,  $L(q)$ , provides information about the spatial distribution of the scattering objects (spheres, cylinders, lamellae) and can be described as a linear array of delta functions for a particular set of lattice planes. The spacing of the delta functions is related to the distance of the lattice by an inverse proportionality.<sup>125</sup> Depending of the type of lattice, only certain peaks can be found corresponding to allowed reflexes of the particular structure. Bragg's equation describes the condition for the interference of the beam scattered at two different planes in the crystal.

$$n\lambda = 2d_{hkl} \sin \Theta \quad (2-9)$$

$\Theta$  : Bragg angle, [ $^\circ$ ]

$n$  : order of the reflex

$d_{hkl}$  : distance between two planes ( $hkl$ ), [ $nm$ ]

Eq. 2-9 together with the definition of the size of the scattering vector (eq. 2-4) determines the spacing  $d_{hkl}$  (eq 2-10) from the diffraction pattern of the crystal.

$$d_{hkl} = \frac{2\pi m}{q} \quad (2-10)$$

The observed values for the spacing can be compared with the characteristic sequences of model lattices and the ratio of the characteristic peaks  $d_{hkl}$  with the first peak  $d_{100}$  (Table 2-1) presents the ratios of Bragg spacings for different spacial arrangements, such as lamellae, hexagonally and tetragonally packed cylinders and body centered cubic (bcc) spheres.

Morphology		Reflex					
		1	2	3	4	5	6
Spheres	$d_{hkl}/d_{100}$	1	0.707	0.577	0.5	0.447	0.408
	$q_{hkl}/q_{100}$	1	$\sqrt{2}$	$\sqrt{3}$	$\sqrt{4}$	$\sqrt{5}$	$\sqrt{6}$
	hkl	110	200	211	220	310	222
Cylinders	$d_{hkl}/d_{100}$	1	0.577	0.5	0.378	0.333	0.289
	$q_{hkl}/q_{100}$	1	$\sqrt{3}$	$\sqrt{4}$	$\sqrt{7}$	$\sqrt{9}$	$\sqrt{12}$
	hkl	100	110	200	210	300	320
Cylinders	$d_{hkl}/d_{100}$	1	0.707	0.5	0.447	0.333	0.316
	$q_{hkl}/q_{100}$	1	$\sqrt{2}$	$\sqrt{4}$	$\sqrt{5}$	$\sqrt{9}$	$\sqrt{10}$
	hkl	100	110	200	210	300	320
Lamellae	$d_{hkl}/d_{100}$	1	0.5	0.333	0.25	0.20	0.167
	$q_{hkl}/q_{100}$	1	2	3	4	5	6
	hkl	100	200	300	400	500	600

**Table 2-1.** Ratios of consecutive Bragg spacings for different models morphologies: body centered cubic (bcc), hexagonally and tetragonally packed cylinders and lamellae.<sup>38,126</sup>

In a hexagonally packed lattice, the distance  $d_{100}$  resulting from the scattering peak  $q_{100}$  corresponds directly to the shortest distance between two parallel neighboring planes (Figure 2-1).

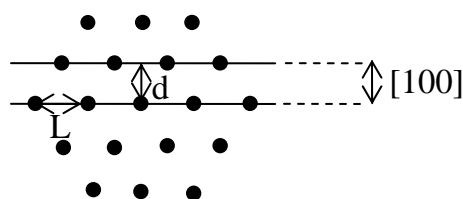


**Figure 2-1.** Cylindrical long period  $L$  and distance  $d$  in a hexagonal lattice.  $L$ -cylindrical long period determined by TEM, shortest distance between two related cylinders, [nm];  $d$ -distance between parallel planes obtained by the reflex  $q_{100}$  for a hexagonal lattice, [nm].

While TEM provides the shortest distance between two cylinders,  $L$ , SAXS provides information about the distance between two neighbored planes. However, once the symmetry of the structure is known as hexagonal, both values are interchangeable by equation 2-11.

$$d_{100} = \frac{\sqrt{3}}{2} L \quad (2-11)$$

$d_{100}$  : distance between two parallel planes,  $[nm]$  (Fig. 2-1)

The structure factor (eq.2-7) depends of the geometric shape of an object and derives from a Fourier transformation of an individual domain structure. For solid spheres, cylinders, and lamellae, the structure factors are rapidly oscillating functions.<sup>127</sup> Spheres can be described by trigonometric functions (eq. 2-12).<sup>128</sup>

$$F_s(q) \propto \frac{\sin qr - \sin qr \cos qr}{(qr)^3} \quad (2-12)$$

$F_s(q)$  : structure factor of a homogeneous sphere

$r$  : radius of the sphere,  $[nm]$

$q$  : scattering vector,  $[nm^{-1}]$

A Bessel function of first order is used to describe the structure factor for cylinders, which have negligible diameters compared to their lengths (eq. 2-13).

$$F_c(q) \propto \frac{J_1(qr)}{qr} \quad (2-13)$$

with

$$J_1(qr) = \sum_{\nu=0}^{\infty} \frac{(-1)^{\nu}}{\nu! \Gamma(\nu+2)} \left( \frac{qr}{2} \right)^{1+2\nu} \quad (2-14)$$

$F_c$  : structure factor of a homogeneous sphere

$r$  : radius of the cylinder,  $[nm]$

$J_1$  : Bessel function of first order

Both functions,  $F_s(q)$  and  $F_c(q)$  strongly depend on the product of the scattering vector,  $q$ , and the radius,  $r$ , of the spheres or cylinders. If the minimum in the function is equal to zero, no diffraction peak will be observed even if it corresponds to a scattering vector, which represents a solution for the delta function of the lattice vector. Thus, the absence of a diffraction peak in an expected sequence may be the result of a weak structure factor.

### 2.2.2.3. Setup of Synchrotron-SAXS Beamline (ID02A, ESRF, Grenoble)

In this work the in-situ Synchrotron SAXS measurements were carried out at the ID02A beamline of the European Synchrotron Radiation Facility (ESRF, Grenoble, France). A schematic depiction of the beamline is shown in Figure 2-2. The typical photon flux obtained at the ID02A is  $10^{13}$  photons/sec, corresponding to twice the full width at half maximum beam size  $(0.2 \text{ mm})^2$  and energy band width  $\Delta E / E = 2 \times 10^{-4}$ . The operating energy range was 12.5 keV, corresponding to a wavelength of 0.1 nm, at which the highest photon flux is obtained.

The detector system with a standard 2-dimensional SAXS camera is housed in a 10 m evacuated flight tube. For most experiments an image intensified CCD detector is used which can handle the full X-ray flux. The CCD is capable of acquiring up to 10 frames of  $1024 \times 1024$  pixels per second and a sequence of 125 frames can be acquired with this time resolution. Prior to data analysis, background scattering was subtracted from the data and corrections were made for spatial distortions and for the detector efficiency.

A Haake rheometer within a Couette geometry aluminium cell has been used and the X-ray beam (cross section:  $200 \mu\text{m}$ ) was going radial and tangential views through the sheared sample.

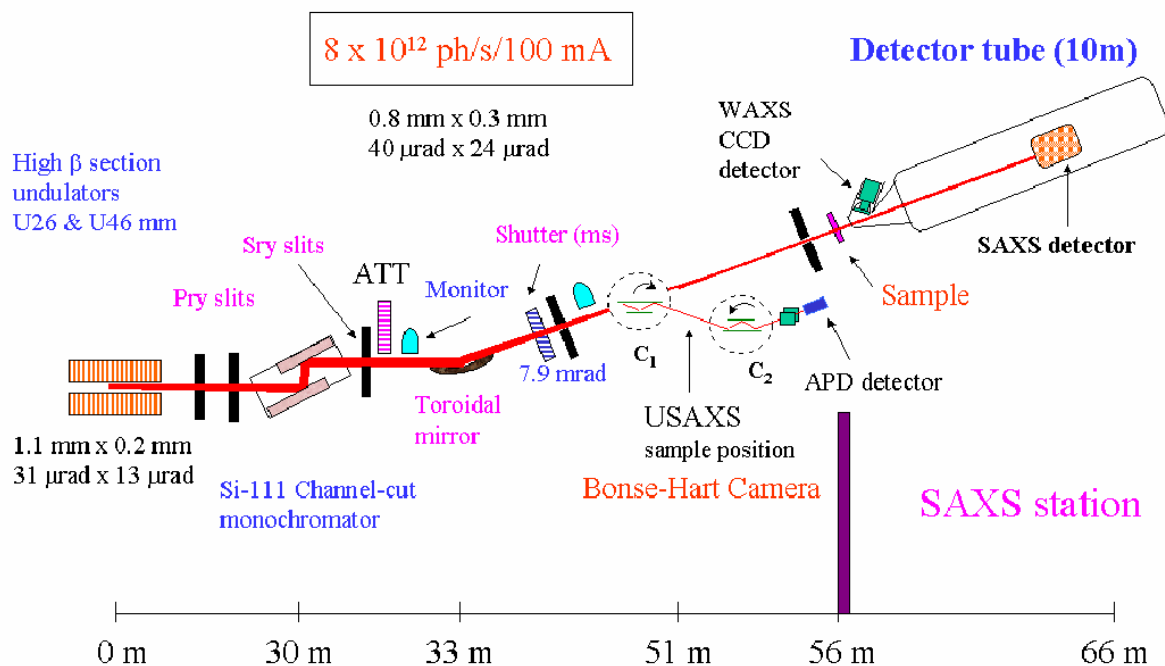


**Figure 2-2.** Setup of ID02A High-Brilliance Beamline at the ESRF, Grenoble (France)

### 2.2.3 Dynamic-Mechanical Analysis

#### 2.2.3.1 Fundamentals of Dynamic-Mechanical Analysis<sup>129</sup>

A polymer may exhibit mechanical behavior characteristic of either an *elastic solid* or a *viscous liquid*. The actual response depends upon temperature, in relation to the glass transition temperature ( $T_g$ ) of the polymer, and upon the time scale of the deformation. The mechanical response of polymeric materials will be intermediate between that of an ideal elastic or viscous liquid, the polymers are viscoelastic. Viscoelastic behavior may be characterized by a variety of techniques that record the time-dependent response of a polymeric solid, melt, or solution to the application of a sinusoidal strain or an electrical voltage. The most commonly used method to measure viscoelastic properties as a function of temperature and time (frequency) is dynamic-mechanical analysis, which records the stress response to an application of a sinusoidal strain. In comparison dielectric methods record the temperature and frequency dependence of the dielectric constant to an oscillatory voltage applied to a sample pressed between two electrodes.

In dynamic mechanical testing, the stress is measured as a function of strain that is some periodic function of time, usually a sine wave. Dynamic-testing instruments are available for operation in several modes of deformation such as tensile, torsion, compression, and shear over a several decades of frequencies.

For a tensile strain that is a sinusoidal function of time,  $t$ , [s] the strain function may be expressed as

$$\varepsilon = \varepsilon^0 \sin(\omega t) \quad (2-15)$$

where  $\varepsilon^0$  is the amplitude of the applied strain and  $\omega$  is the angular frequency of oscillation, in [rad / s]. The angular frequency is related to the frequency,  $f$ , measured in cycles per second (Hz), as  $\omega = 2\pi f$ . The usual range of frequencies for dynamic-mechanical experiments are 0.1 to 110 Hz (0.628 to 691 rad s<sup>-1</sup>).

The stress resulting from the applied sinusoidal strain will also be a sinusoidal function, which may be written as

$$\sigma = \sigma^0 \sin(\omega t + \delta) \quad (2-16)$$

where  $\sigma^0$  is the amplitude of the stress response, in [N / m<sup>2</sup>] and  $\delta$  is the phase angle between the stress and the strain, as illustrated in Figure 2-3.

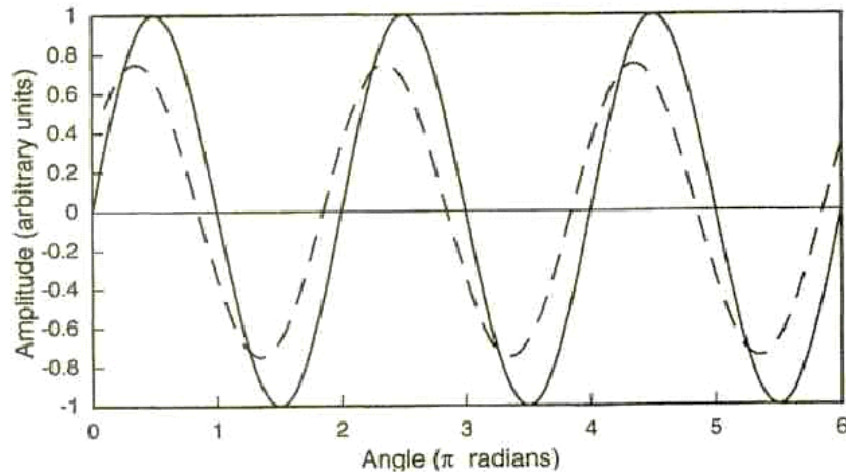


**Figure 2-3.** Representation of an arbitrary strain function (—) and stress response (----) of a viscoelastic material.

In the case of an ideal elastic solid, the stress is always in phase with strain ( $\delta = 0$  in eq 2-16) and by substitution of eq 2-15 into Hook's law is obtained:

$$\sigma = E \cdot \varepsilon = E\varepsilon^0 \sin(\omega t) = \sigma^0 \sin(\omega t) \quad (2-17)$$

where  $\sigma^0$  is the magnitude of the resulting stress function,  $E$  - Young's (tensile) modulus.

The stress of an ideal viscous fluid is always  $90^\circ$  out of phase ( $\delta = \pi/2$ ) with the strain. This can be shown to result from Newton's law of viscosity, given as:

$$\sigma = \eta \left( \frac{d\varepsilon}{dt} \right) \quad (2-18)$$

$$\sigma = \eta \omega \varepsilon^0 \cos(\omega t) = \sigma^0 \sin\left(\omega t + \frac{\pi}{2}\right) \quad (2-19)$$

where  $\eta$  represents the viscosity.

At temperatures below  $T_g$ , polymeric materials behave more as Hookean solids at small deformations, but at higher temperatures their behavior is viscoelastic.

The usual way to report the viscoelastic response of a polymer is by means of a semilogarithmic plot of storage modulus (or  $\tan \delta$ ) as a function of temperature at one or more frequencies. The temperature range may be very broad from liquid nitrogen temperatures (ca.  $-150^\circ\text{C}$ ) to temperatures in the range of  $T_g$  that can be  $200^\circ\text{C}$  or more. The dynamic storage modulus behaves like the tensile (or shear) modulus as a function of temperature. Maxima in loss modulus, or  $\tan \delta$ , occur both at  $T_g$  and at low temperatures, where small-scale molecular motions can occur (secondary relaxations). For the

semicrystalline polymers an additional peak in  $\tan \delta$  corresponding to  $T_m$  (melting temperature) will occur above  $T_g$ . The highest temperature peak is designated the  $\alpha$  relaxation (the glass transition in amorphous polymers and the crystalline-melting transition in semicrystalline polymers), the next highest are the  $\beta$ ,  $\gamma$ ,  $\delta$  relaxations.

### 2.2.3.2 Viscoelastic Behavior of Polymer Systems<sup>130,131</sup>

Polymers show a rheological behavior in between the ideal Newtonian liquid and the ideal Hookean solid. The response changes from solid-like (Hookean) at short shearing times to liquid-like at long shearing times. The history of loading for these viscoelastic materials, which are being characterized by their relaxation shear modulus,  $G(t) = \sigma_{21} / \gamma(t)$ , is thus crucial. It is useful to define the following quantities:

$$\eta_0 = \int_0^{\infty} G(t) dt \quad (2-20)$$

$$J_e^0 = \frac{1}{\eta_0^2} \int_0^{\infty} tG(t) dt \quad (2-21)$$

$$\tau_0 = \frac{\int_0^{\infty} tG(t) dt}{\int_0^{\infty} G(t) dt} = \eta_0 J_e^0 \quad (2-22)$$

where  $\eta_0$  is zero-shear-rate viscosity,  $t$  is the time and  $J_e^0$  is the steady-state recoverable shear compliance, which is obtained from the total recoverable shear strain ( $\gamma_r$ ) at steady state divided by the original applied shear stress ( $\sigma_{21}$ ) in a constant-stress experiment:

$$J_e^0 = \lim_{\sigma_{21} \rightarrow 0; t \rightarrow \infty} \frac{\gamma_r}{\sigma_{21}} \quad (2-23)$$

The steady state viscosity ( $\eta_0$ ) is a measure of the energy dissipated during flow and  $J_e^0$  determines the amount of elastically stored energy. The relaxation time  $\tau_0$ , is a measure of the time required for final equilibration following a step strain. The time-temperature dependence of the shear modulus is illustrated in Figure 2-4 (the  $x$ -axis corresponds to arbitrary temperature scale and time scale from left to right).

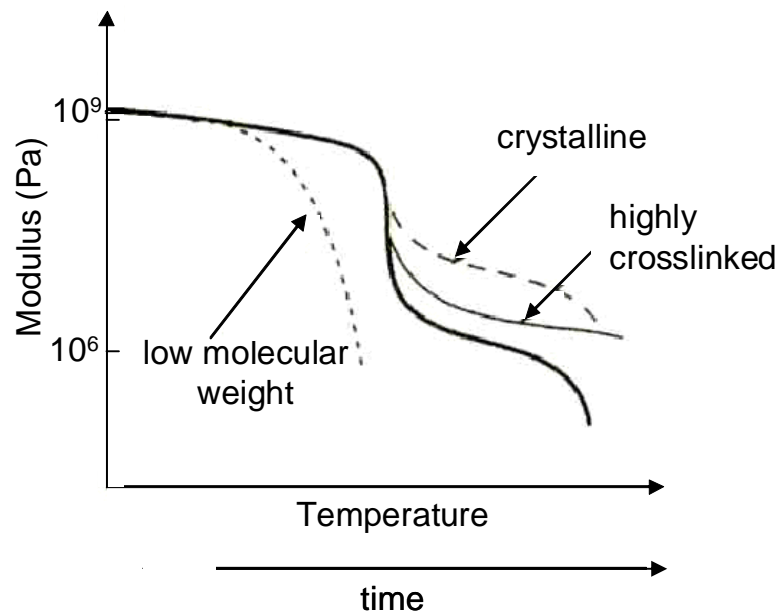


**Figure 2-4.** Schematic diagram showing shear relaxation modulus as a function of temperature and time for amorphous polymers with high and low molecular weight, cross-linked and semicrystalline polymers. The continuous thick line corresponds to high molecular weight polymers.

Moving from short to long times (from low to higher temperatures) in Figure 2-4 four regions of behavior can be distinguished:

1. The response at short times is almost Hookean, the molten polymer behaves like a glassy material, comparable to ordinary window glass at room temperature. The mechanical behavior displayed in this region is called the *glassy state*, regardless of the chemical composition of the specimen. Inorganic and polymeric glasses are very similar in many properties and are often described as being hard, stiff and brittle. The corresponding value of modulus in this region for all polymeric materials as well as low-molecular-weight systems is on the order  $10^9$  N/m<sup>2</sup> or 1 GPa.
2. At longer times the modulus undergoes a gradual transition to a value lower by 3 or 4 orders of magnitude than its glassy value. On this time scale the material has a *leathery consistency*.
3. A more or less pronounced plateau is encountered at longer times. The value of plateau modulus is on the order  $10^6$  N/m<sup>2</sup> and the region is called the *rubbery plateau*. The sample appears elastic in this time frame. The appearance of a rubbery plateau for high molecular weight polymers is the result of the formation of entanglements which prevent slippage at temperatures immediately above  $T_g$  and therefore modulus remains relatively high. The

rubbery plateau modulus,  $G_p$ , is inversely proportional to the molecular weight between entanglements,  $M_e$ , as

$$G_p \propto \frac{\rho RT}{M_e}$$

where  $\rho$  is density,  $[g/cm^3]$ ;  $R$  is universal gas constant,  $[Jmol^{-1}K^{-1}]$ ;  $T$  is temperature,  $[K]$

4. Above  $T_g$ , the entanglements are easily disassociated due to high kinetic energy and the modulus drops. This is an indication of the onset of flow, the material would display viscous flow for very long periods of observation. Here we can cite the analogy between inorganic glass and polymers. The windows in some medieval cathedrals show greater thickness at the bottom than at the top, owing to the slow flow of the glass under the influence of gravity.

The temperature behavior of the modulus of *semicrystalline polymers* is qualitatively similar to that of high-molecular-weight amorphous polymers except that the modulus is typically higher in the secondary plateau due to the reinforcing effect of crystallites dispersed in an amorphous rubbery phase at temperature above  $T_g$  but below  $T_m$ . At  $T_m$ , the crystallites melt and the modulus drops in the viscous-flow region.

The temperature at which the modulus drops from the *glassy* to *rubbery* values is the glass transition temperature ( $T_g$ ).

#### *Understanding the modulus.*

The four regions of behavior shown by the polymers in Figure 2-4 are typical of high molecular weight uncrosslinked polymers. At the molecular level the following explanation is given for each of the four regions:

1. In the glassy state movements of the chain backbone are impossible. The time required for movement of the chain is long and the glassy state is observed when the time of observation is too short for such movements to occur. Alternatively, at low temperatures backbone motion is frozen out. The difference between a crystalline solid and a glassy solid is in the order of the molecular arrangement, not in the magnitude of modulus.
2. In the leathery state a distinct relaxation occurs, the molecules have enough time to go into more relaxed conformations due to their thermal energy.
3. In the rubbery plateau the movement is overcome due to the entanglements. The chains although entangled are still able to move, somehow slipping and sliding past one another.

4. Chemical crosslinks and entanglements differ, the former is permanent, the latter transient. At sufficient time, even the effects of entanglements can be overcome and stationary-state flow is achieved. An increase of temperature facilitates the flow process. For crosslinked polymers the fourth region is not observed and the modulus is observed at equilibrium.

### 2.2.3.3 Mechanical Models of Viscoelastic behavior

An insight into the nature of the viscoelastic properties of polymers can be obtained by analyzing the stress or strain response of mechanical models using an *ideal spring* as the Hookean element and a *dashpot* as the viscous element (dashpot consisting of a piston in a cylinder filled with a Newtonian fluid of viscosity,  $\eta$ ). The elemental models are a series combination of a spring and dashpot, the *Maxwell* element, and a parallel combination of a spring and dashpot, the *Voigt* element, as illustrated in Figure 2-5.

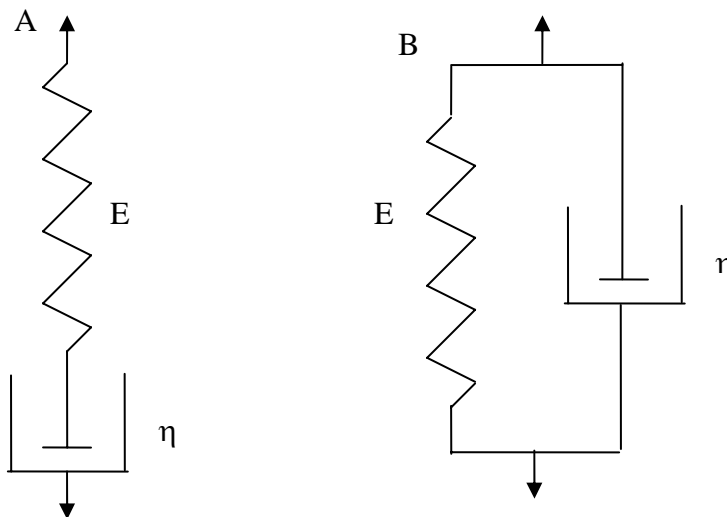


**Figure 2-5.** Maxwell (A) and Voigt (B) elements.

**Maxwell Element.** In the case of a series combination of a spring and dashpot, the total strain is a summation of the individual strains of the spring and dashpot. From Hooke's law ( $\sigma = E\varepsilon$ ), the strain rate of an ideal elastic spring can be written as:

$$\frac{d\varepsilon}{dt} = \left(\frac{1}{E}\right) \frac{d\sigma}{dt} \quad (2-24)$$

while the strain rate for the dashpot is obtained by rearranging Newton's law of viscosity ( $\sigma = \eta \frac{d\varepsilon}{dt}$ ) as:

$$\frac{d\varepsilon}{dt} = \frac{\sigma}{\eta} \quad (2-25)$$

therefore the basic equation for strain rate,  $\left(\frac{d\varepsilon}{dt}\right)$ , in the Maxwell model is the summation of the strain rates for the spring and dashpot (eq 2-24 and eq 2-25) as:

$$\frac{d\varepsilon}{dt} = \left(\frac{1}{E}\right) \frac{d\sigma}{dt} + \frac{\sigma}{\eta} \quad (2-26)$$

The differential equation 2-26 can be solved for stress relaxation, creep, and dynamic response by applying the appropriate stress or strain function.

In a *stress relaxation* experiment, the strain  $\varepsilon_0$  is constant and therefore, the strain rate  $\left(\frac{d\varepsilon}{dt}\right)$  is zero. Eq 2-26 reduces to the first-order ordinary differential equation

$$\left(\frac{1}{E}\right) \frac{d\sigma}{dt} + \frac{\sigma}{\eta} = 0 \quad (2-27)$$

Rearrangement of eq 2-27 and introduction of  $\tau = \frac{\eta}{E}$  gives

$$\frac{d\sigma}{\sigma} = -\left(\frac{1}{\tau}\right) dt \quad (2-28)$$

Integration yields the stress response as

$$\sigma = \sigma_0 \exp\left(-\frac{t}{\tau}\right) \quad (2-29)$$

where  $\sigma_0$  is the instantaneous stress response of the spring. The stress relaxation modulus,  $E_r(t)$ , is then obtained as:

$$E_r(t) = \frac{\sigma}{\varepsilon_0} = \left(\frac{\sigma_0}{\varepsilon_0}\right) \exp\left(\frac{-t}{\tau}\right) = E \exp\left(\frac{-t}{\tau}\right) \quad (2-30)$$

where  $E(= \sigma_0 / \varepsilon_0)$  is the Young's modulus of the spring element.

In a *creep* experiment, a constant stress,  $\sigma_0$ , is applied instantaneously, therefore eq 2-25 reduces to

$$\frac{d\varepsilon}{dt} = \frac{\sigma_0}{\eta} \quad (2-31)$$

Rearrangement and integration of eq 2-31 gives

$$\varepsilon(t) = \left( \frac{\sigma_0}{\eta} \right) t + \varepsilon_0 \quad (2-32)$$

where  $\varepsilon_0$  represents the instantaneous ( $t = 0$ ) strain response of the spring element. The creep compliance function,  $D(t)$ , is then obtained as

$$D(t) = \frac{\varepsilon(t)}{\sigma_0} = \frac{t}{\eta} + \frac{\varepsilon_0}{\sigma_0} = \frac{t}{\eta} + D \quad (2-33)$$

where  $D(= \varepsilon_0 / \sigma_0)$  is the instantaneous compliance (of the spring). An alternative form of eq 2-33 may be obtained by defining the relaxation time,  $\tau$ , as

$$\tau = \frac{\eta}{E} = \eta D \quad (2-34)$$

By substitution the eq 2-34, eq 2-33 becomes

$$\frac{D(t)}{D} = \frac{t}{\tau} + 1 \quad (2-35)$$

To obtain an expression for the *dynamic-mechanical* response, the expression for complex stress,  $\sigma = \sigma^0 \exp(i\omega t)$ , is substituted into the Maxwell equation 2-26 to give

$$\frac{d\varepsilon(t)}{dt} = \left( \frac{\sigma^0}{E} \right) i\omega \exp(i\omega t) + \left( \frac{\sigma^0}{\eta} \right) \exp(i\omega t) \quad (2-36)$$

Integration from time  $t_1$  to  $t_2$  gives

$$\varepsilon(t_2) - \varepsilon(t_1) = \left( \frac{\sigma^0}{E} \right) [\exp(i\omega t_2) - \exp(i\omega t_1)] + \left( \frac{\sigma^0}{\eta i \omega} \right) [\exp(i\omega t_2) - \exp(i\omega t_1)] \quad (2-37)$$

Since the corresponding stress increment can be written as

$$\sigma(t_2) - \sigma(t_1) = \sigma^0 [\exp(i\omega t_2) - \exp(i\omega t_1)] \quad (2-38)$$

division of both sides of eq 2-37 by this expression gives the complex compliance as

$$D^* = D - i \left( \frac{D}{\omega \tau} \right) \quad (2-39)$$

Therefore, the storage compliance ( $D'$ ) obtained from the Maxwell model is the compliance of the spring which is independent of time or frequency

$$D' = D \quad (2-40)$$

while the loss compliance ( $D''$ ) is

$$D'' = \frac{D}{\omega\tau} \quad (2-41)$$

The corresponding expression for complex modulus,  $E^*$ , is obtained by recalling that  $E^*$  is the reciprocal of  $D^*$  as

$$E^* = \frac{1}{D^*} \quad (2-42)$$

Rearranging and using the inverse relation  $E = 1/D$  gives

$$E^* = E' - iE'' = \frac{E(\omega\tau)^2}{1 + (\omega\tau)^2} + i \left[ \frac{E\omega\tau}{1 + (\omega\tau)^2} \right] \quad (2-43)$$

where

$$E' = \frac{E(\omega\tau)^2}{1 + (\omega\tau)^2} \quad (2-44)$$

and

$$E'' = \frac{E\omega\tau}{1 + (\omega\tau)^2} \quad (2-45)$$

From eq 2-44 and eq 2-45 that  $\tan \delta$  for a Maxwell model is

$$\tan \delta = \frac{E''}{E'} = \frac{1}{\omega\tau} \quad (2-46)$$

**Voigt element.** For a parallel combination of a spring and dashpot, the strain on each element must be equal while the *stress is additive*. Therefore the stress follows the relation

$$\sigma = E\varepsilon + \eta \frac{d\varepsilon}{dt} \quad (2-47)$$

Using the expression 2-34 for the relaxation time, the Voigt equation for the creep deformation becomes a linear differential equation:

$$\frac{\sigma_0}{\eta} = \frac{\varepsilon(t)}{\tau} + \frac{d\varepsilon(t)}{dt} \quad (2-48)$$

which can be solved by using an integration factor ( $e^{t/\tau}$ ). Solving for  $\varepsilon(t)$  gives the compliance function as

$$D(t) = D \left[ 1 - \exp\left(\frac{-t}{\tau}\right) \right] \quad (2-49)$$

where  $D = 1/E$ . The response of a Voigt model to *dynamic* strain gives the relationships for the storage and loss compliance as

$$D' = \frac{D}{1 + (\omega\tau)^2} \quad (2-50)$$

$$D'' = \frac{D\omega\tau}{1 + (\omega\tau)^2} \quad (2-51)$$

The forms of these relationships for compliance are the same as those for dynamic moduli (eq 2-44, eq 2-45) given by the Maxwell model.

The most significant limitation of these two models is that they employ only a single relaxation time (eq 2-34). This results in the prediction of only a *single transition* in modulus or compliance, whereas high-molecular-weight polymers exhibit both a glass-to-rubber and rubber-to-liquid transition.

**Multi-element Models.** A parallel combination of multiple Maxwell elements is called Maxwell-Wiechert model. Further improvement in terms of realistic slopes in the transition regions is obtained by adding additional Maxwell elements in the model and therefore providing a distribution of relaxation times as would be expected for a high-molecular-weight polymer with a broad distribution of molecular weights. In general, the stress relaxation modulus of a Maxwell-Wiechert model consisting of  $N$  Maxwell elements can be written:

$$E(t) = \sum_{i=0}^N E_i \exp\left(\frac{-t}{\tau_i}\right) \quad (2-52)$$

**Relaxation and Retardation Spectra.** For an infinite number of Maxwell elements in a Maxwell-Wiechert model, the summation given in eq 2-52 may be replaced by an integral

$$E(t) = \int_0^{\infty} E(\tau) \exp\left(\frac{-t}{\tau}\right) d\tau \quad (2-53)$$

where  $E(\tau)$  is a continuous function of the relaxation times.

$$H(\tau) = \tau E(\tau) \quad (2-54)$$

In the eq 2-54,  $H(\tau)$  is called the *relaxation-time distribution function*.

The substitution of eq 2-54 in eq 2-53 and using  $\ln \tau$  in place of  $\tau$  gives

$$E(t) = \int_{\ln \tau = -\infty}^{\ln \tau = +\infty} H(\tau) \exp\left(\frac{-t}{\tau}\right) d \ln \tau \quad (2-55)$$

An expression for compliance is obtained by considering an infinite number of Voigt elements in series

$$D(t) = \int_{\ln \tau = -\infty}^{\ln \tau = +\infty} L(\tau) \left[ 1 - \exp\left(\frac{-t}{\tau}\right) \right] d \ln \tau \quad (2-56)$$

where  $L(\tau)$  is called the *retardation spectrum function*.

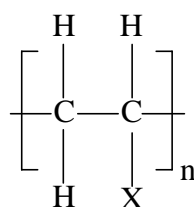
Relaxation and retardation spectra characterize the viscoelastic properties of a polymer at a particular temperature. They can be calculated from one set of experimental data and then be used to predict the viscoelastic response under different experimental conditions. The relaxation-time spectrum can be calculated from the temperature dependence of the dynamic loss modulus and then be used to calculate the temperature dependence of the stress relaxation modulus.

#### 2.2.3.4 The Glass Transition Temperature<sup>132</sup>

When a polymer in its molten state is cooled down two possibilities may happen: the polymer may either *crystallize* or cool down to its *glassy, amorphous state*. The temperature at which the slope in the specific volume-temperature graph changes is referred to as the *glass transition temperature*,  $T_g$ . Cooling past the glass transition temperature is accompanied by a dramatic change in the mechanical properties. The elastic modulus increases by a factor of 1000 when the polymeric liquid is cooled below  $T_g$ . The actual value of  $T_g$  is very dependent on the repeating unit, the molecular architecture and the presence of low molar mass species. It is appropriate to point out that the  $T_g$  value recorded in any given experiment is dependent on the temperature scanning rate.

*Effect of repeating unit structure on the glass transition temperature.*

The class of polymers with the repeating unit  $-\text{CH}_2\text{-CHX}-$ , the question which may arise is the effect of X group on  $T_g$ . If X is a relatively inflexible group then  $T_g$  increases with increasing size of the group (Figure 2-6)



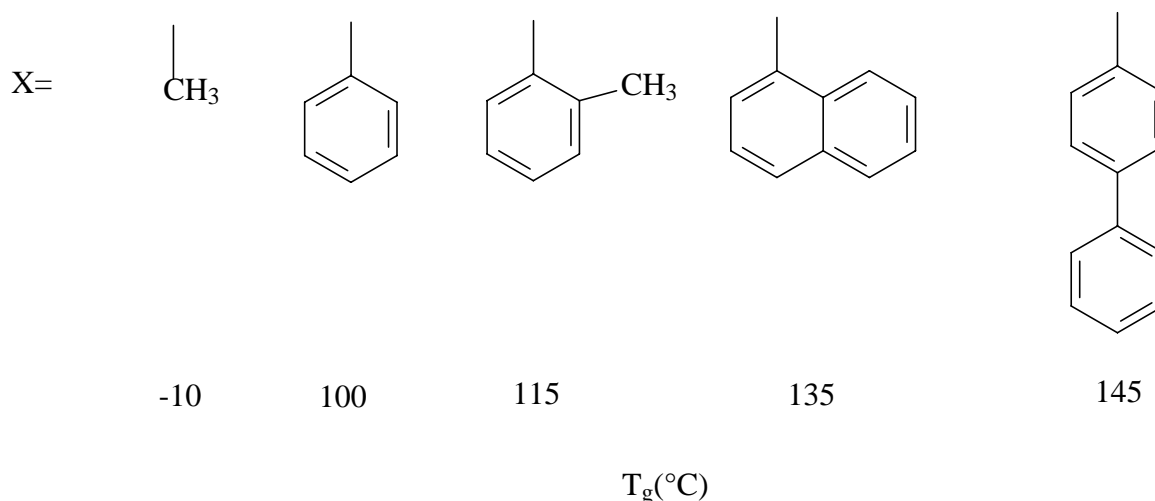


**Figure 2-6.** Glass transition temperatures of different vinyl polymers showing the influence of the size of the pendant group.

The pendant groups pose restrictions of the torsion about  $\sigma$  bonds in the backbone chain, the backbone chain becomes less flexible and this causes the increase in  $T_g$ . Polymers with relatively flexible side chains, e.g. polyacrylates or polymethacrylates, exhibit the opposite behavior with a very pronounced decrease in  $T_g$  with increasing length of the side chain. The dominant effect of the side group is to increase the distance between adjacent backbone chains. Polymers with longer pendant groups may crystallize under certain conditions, which then may lead to an increase in  $T_g$ . As shown in Figure 2-6 the replacement of hydrogen with a methyl group at the  $\alpha$  carbon causes a dramatic increase in  $T_g$ ; the difference in  $T_g$  between polymethacrylates and polyacrylates is about 100°C.

If X is chlorine, the carbon-chlorine bond is polar, thus  $T_g$  increases with increasing polarity. This observation can be generalized to the statement that  $T_g$  generally increases with increasing cohesive energy density (CED) as shown in the equation 2-57.

$$T_g = \frac{2\delta^2}{mR} + C_1 \quad (2-57)$$

where  $\delta^2$  is the CED,  $m$  is a parameter which describes the internal mobility of the groups in a single chain,  $R$  is the gas constant and  $C_1$  is a constant.

Beaman (1953) and Boyer (1954) noticed that both  $T_g$  and the melting point  $T_m$  of crystallizable polymers increased with decreasing chain flexibility and increasing CED and there were established the following empirical correlations:

$$\frac{T_g}{T_m} = \frac{1}{2} \text{ (symmetrical molecules)}$$

$$\frac{T_g}{T_m} = \frac{2}{3} \text{ (asymmetrical molecules)}$$

### *The glass transition temperature of blends and copolymers*

The glass transition temperature of a polymer blend is highly dependent on the morphology. The most common case is that the polymer components are immiscible, forming a two-phase system. Some polymer blends exhibit partial miscibility. They have a mutual, limited solubility indicated by a shift in the two  $T_g$ 's accompanying a change in the phase composition of the blend. Several equations relating  $T_g$  and composition in this case have been proposed. One of them is the Fox equation:

$$\frac{1}{T_g} = \frac{w_1}{T_{g1}} + \frac{w_2}{T_{g2}} \quad (2-58)$$

where  $T_g$  is the glass transition temperature of the binary blend,  $T_{g1}$  and  $T_{g2}$  are the glass transition temperatures of polymers 1 and 2, and  $w_1$  and  $w_2$  are the mass fractions of polymers 1 and 2.

Amorphous polymers always show a glass transition process ( $\alpha$ ) and also one or more so-called subglass processes, referred to as  $\beta$ ,  $\gamma$ ,  $\delta$ . The existence of the subglass processes proves that the glassy polymer does have some limited segmental mobility. The relaxation processes can be categorized as side-chain or main-chain. Subglass processes appear both in polymers with pendant groups such as poly(methyl methacrylate) and in linear polymers such as polyethylene or poly(ethylene terephthalate). In the latter case, the subglass process must involve motions in the backbone chain.

The  $\alpha$  process is clearly the glass transition and it obeys the William-Landel-Ferry temperature dependence. It is present in all polymethacrylates. The high-temperature subglass process  $\beta$  is present in all polymethacrylates and it assigned to rotation of the side group.

The low-temperature subglass process  $\gamma$  is not present in poly(methyl methacrylate), it appears in poly(n-propyl methacrylate) and longer alkyl homologues. It is assigned to motions in the flexible methylene sequence.

Polystyrene exhibits relatively complex relaxation behavior. Apart from the glass transition ( $\alpha$ ), polystyrene exhibits four subglass relaxation processes, referred to as  $\beta$ ,  $\gamma$ ,  $\delta$  in order of decreasing temperature. The cryogenic  $\delta$  process (55K in PS at 10kHz) is due to the

oscillatory motions of the phenyl groups or from defects associated with the configuration of the polymer. The  $\gamma$  process appearing in PS at 180K at 10kHz has also been attributed to phenyl group oscillation or rotation. The high-temperature process denoted  $\beta$  occurs in PS between  $T_g - 100K$  and  $T_g$  and is believed to be due to a rotation of the phenyl group with a main-chain cooperation.

### 2.2.3.5 The Time-Temperature Superposition Principle and its Application to Linear Viscoelasticity

It is important to know how a material will behave (creep or stress relaxation) at a fixed temperature, but over a long period that may not be realistically accessible. Long-time behavior can be evaluated by measuring stress-relaxation or creep data over a shorter period of time but at several different temperatures. Information from each of these different temperature curves may then be combined to yield a master curve at a single temperature by horizontally shifting each curve along the log time scale. This technique is called *time-temperature superposition* and is a result of linear viscoelasticity theory. In this procedure the master curve is plotted as stress-relaxation modulus or creep compliance versus reduced time,  $t/a_T$ . The *shift factor* is defined as the ratio of real time to reach a particular value of modulus at some temperature to the reference-scale time coordinate,  $t_r$ , corresponding to the same value of modulus in the master curve at the reference temperature,  $T_r$ ,

$$a_T = \frac{t}{t_r} \quad (2-59)$$

The time-temperature superposition says that

$$E(T, t) = E(T_r, t_r) \quad (2-60)$$

The dependence of the shift factor  $a_T$  on temperature is given by the *Williams-Landel-Ferry (WLF) relationship*:

$$\log a_T = \frac{-C_1(T - T_r)}{C_2 + (T - T_r)} \quad (2-61)$$

where  $C_1$  and  $C_2$  are constants for a given polymer and  $T_r$  is the reference temperature. When  $T_r$  is taken to be the polymer glass transition  $T_g$ , as it often is,  $C_1$  and  $C_2$  may be approximated by the "universal" values of 17.44 and 51.6K, respectively. However,

significant deviations from these values may exist for some polymers, as shown by values given for some common polymers in Table 2-2.

Polymer	$T_g$ (K)	$C_1$	$C_2, K$
Natural rubber	200	16.7	53.6
Polyisobutylene	202	16.6	104
Polyurethane	238	15.6	32.6
Poly(vinyl acetate)	304	17.4	43.4
Poly(ethyl methacrylate)	335	17.6	65.5
Poly(ethylene terephthalate), amorphous	343	17.1	31.7
Poly(ethylene terephthalate), crystalline	353	30.4	106.6
Poly(vinyl chloride)	353	16.2	49.7
Polystyrene	373	13.7	50

**Table 2-2.** WLF parameters of some common polymers.

If  $C_1$  and  $C_2$  are not known, each curve may be horizontally shifted to the reference temperature curve until a value of modulus on the shifted curve coincides with one on the reference curve. The shift factor may then be calculated by use of the defining relationship for  $a_T$  given by eq 2-59. The WLF parameters,  $C_1$  and  $C_2$ , may then be determined by plotting  $(T - T_r)/\log a_T$  versus  $(T - T_r)$  where rearrangement of eq 2-61 gives

$$\frac{T - T_r}{\log a_T} = -\frac{1}{C_1}(T - T_r) - \frac{C_2}{C_1} \quad (2-62)$$

Following this procedure,  $C_1$  is obtained directly from the inverse of the slope, and  $C_2$  can then be calculated from the intercept ( $C_2/C_1$ ).

The fact that time and temperature can be superimposed means that the change in modulus of the material with increasing time at constant temperature is equivalent to the change in modulus when measured at identical times but at increasing temperature.

Gibbs and DiMarzio have suggested that a true second-order transition should occur at a temperature ( $T_2$ ) where the conformational entropy is zero. Therefore, the WLF relation can be used to determine the relationship between the thermodynamic transition-temperature and the kinetic  $T_g$  by noting that shifting from a finite to an infinite time-scale requires that the

shift factor approach infinity or that the denominator from eq 2-61 goes to zero ( $C_2 + T - T_r = 0$ ), where  $T_r = T_g$  and  $T = T_2$ . This means that

$$T_2 = T_g - C_2 \approx T_g - 52 \quad (2-63)$$

using the universal value for  $C_2$ . The true second-order transition temperature should lie approximately 52°C *below* the experimentally measured  $T_g$ .

#### 2.2.4 Rheo-optic Method Combined with LAOS. Definition of Alignment Regime

The measurement of the interaction of light with a material while it is subject to flow is termed *optical rheometry*. Optical rheometry provides additional information on the flow-induced alignment of block copolymers.<sup>67,70</sup> In Figure 2-7 are shown three families of alignment trajectories observed for a symmetric SI diblock copolymer. To explain the observed frequency-dependent alignment behavior, two characteristic frequencies have been proposed: the frequency  $\omega_C$ , above which the distortion of chain conformation dominates the viscoelastic response, and the frequency  $\omega_d$ , below which the relaxation of domains becomes important. Although different methods for obtaining these frequencies have been proposed, the most reliable values are obtained from the master curve.<sup>70</sup> According to the critical frequencies  $\omega_C$ ,  $\omega_d$ , a detailed classification of the alignment regimes is made as the following: i)  $\omega_d < \omega < \omega_C$ , perpendicular alignment (Regime I); ii)  $\omega > \omega_C$  results in a parallel orientation through two different routes: at frequencies slightly above  $\omega_C$ , parallel orientation results through a transient orientation consisting of parallel and perpendicular orientations as well as a range of orientation between them (Regime II). In contrast, for  $\omega \gg \omega_C$ , the parallel alignment results from a bimodal distribution rich in parallel and transverse orientations (Regime III). For low frequencies  $\omega < \omega_d$ , the parallel orientation is obtained (Regime IV). Due to the computer simulations made by Pakula<sup>133</sup> it was shown that there are additional parameters in controlling the lamellar orientations as follows: the affinity of the blocks to the surface and the layer thickness.

Some of the important features of the rheo-optical approach are as follows:

1. the measured quantity is a direct effect of molecular orientation and shape while the sample is subjected to a flow; in contrast a mechanical experiment senses the dissipation and/or storage of energy

2. an optical experiment can detect the behavior of one selected component in a multicomponent fluid. For example, molecules can be labeled by refractive index, polarizability anisotropy, isotopic substitution, or chromophore attachment. This kind of specificity is impossible to achieve in a mechanical experiment.
3. optical experiments are very sensitive due to the availability of lasers emitting  $\sim 10^{20}$  photons/s, it is possible to make measurements of very weak signals

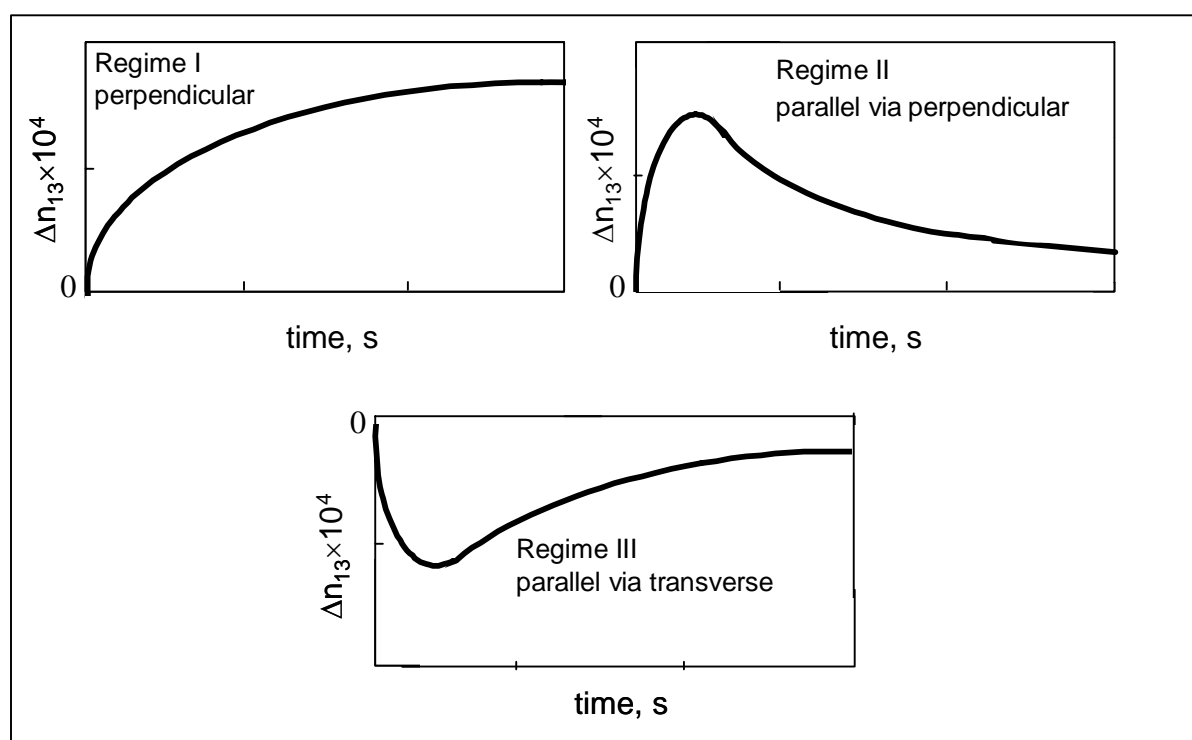


**Figure 2-7.** Three alignment trajectories observed for a symmetric SI diblock copolymer. (a) Regime I showing the route to perpendicular, (b) Regime II and route to parallel, (c) Regime III and route to parallel.<sup>70</sup>

Some restrictions of the rheo-optical approach are:

- i). the sample must have suitable optical properties in terms of transparency and must not be contaminated by large particles (dust)
- ii). additional characterization is often required; although the direct measurement of a modulus or a viscosity is often of immediate utility, in the optical case some additional measurements may be required to establish the relationship between the optical and mechanical properties. For example, the shear stress and first normal stress difference may be

obtained from birefringence measurements, only after a quantity called the stress-optic coefficient is determined.

When incident electromagnetic radiation interacts with matter, three classes of phenomena are of interest. The energy can be *absorbed*, with the possible subsequent emission, the energy can be *scattered* (change direction) with either no change in energy (elastic scattering) or a measurable change in energy (inelastic scattering). The light can *propagate* through the material with no change in direction or energy, but with a change in its state of polarization, statement which is the basis for birefringence technique.

A light wave propagates through a nonabsorbing medium with a speed  $v$ , which is reduced from the speed in vacuum  $c$ . The ratio  $c/v$  defines the refractive index of the material,  $n$ . The wavelength of the radiation is also changed from  $\lambda_0$  in vacuum to  $\lambda$  in the medium, with  $\lambda = \lambda_0 / n$  but the frequency (and thus the energy) remains constant. The change in speed results in a change in propagation direction at an interface between two materials of different  $n$ , as given by Snell's law:

$$n_1 \sin \psi_1 = n_2 \sin \psi_2 \quad (2-64)$$

this phenomenon is called *refraction*. The actual value of  $n$ , which is always greater than or equal to one, reflects the polarizability of the constituent molecules  $\alpha$ , the ability of the electric field of the light wave to distort the electron distribution of the molecules. In general, the more polarizable the molecules, the larger  $n$  will be. Typical values for  $n$  for transparent liquids and glasses are in the range 1.3–1.7. Most molecules actually possess an anisotropic polarizability, which can be represented as a tensor quantity. Thus, nitrobenzene, chloroform, and biphenyl are *anisotropic*, whereas carbon tetrachloride and methane are *isotropic*. Due to the chain structure, almost all polymers exhibit some degree of optical anisotropy. If anisotropic molecules in a material are oriented preferentially in one direction, the value of  $n$  will depend of the relative orientation of the electric field of the light to the molecular axes. This is the origin of *birefringence* or double refraction. The birefringence,  $\Delta n$  can be defined as  $\Delta n = n_1 - n_2$ , where  $n_1$  and  $n_2$  are the refractive indices of the material along two appropriately orthogonal axes. The OAM apparatus built on an ARES instrument (Figure 2-8) measures the retardation, which is the phase shift between two orthogonal electric field waves experiencing the refractive indices  $n_1$  and  $n_2$ , respectively. From this phase shift the refractive index difference (birefringence,  $\Delta n$ ) along axis 1, and 3 respectively, is calculated as well as its sign and its magnitude. A red helium-neon (He-Ne) laser at a wavelength of 633 nm was used. Shear flow coordinates within the parallel plates geometry were defined as follows: 1-

flow direction ( $v$ ), 2-velocity gradient direction ( $\nabla v$ ), 3-vorticity direction ( $\nabla v \times v$ ). Besides birefringence with the same set up illustrated in Figure 2-8 it is possible to monitor as well the dichroism. The phenomenon of linear dichroism occurs when the absorbance of linearly polarized light depends on the direction of polarization. For linear dichroic measurements a removing of circular polarizer 5 (Figure 2-8) before the light pass through the detector 6 is required.

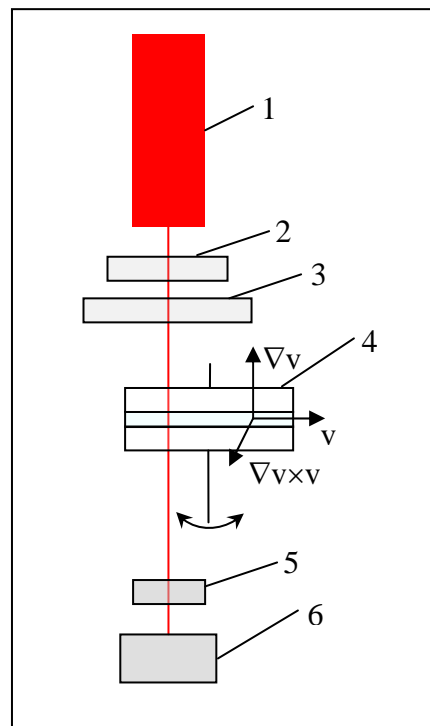


**Figure 2-8.** Schematic setup (OAM) for simultaneous measurements of dynamic stress and birefringence. 1-laser He-Ne,  $\lambda=633$  nm; 2-linear polarizer; 3-rotating half-wave plate; 4-parallel glass plates within the sample; 5-circular polarizer; 6-detector; ( $v$ )-flow direction (axis 1); ( $\nabla v$ )-velocity gradient (axis 2); ( $\nabla v \times v$ )-vorticity (axis 3).

### 2.2.5 Setup ( Optical Analysis Module)

A block diagram of the *optical train* components is provided in Figure 2-9. The components comprising the light path of the OAM are referred to as the optical train. Collimated laser light is emitted from the *laser diode* and is polarized by the *polarizer cube*. The linearly polarized light is converted to circularly polarized light by the *rotating half wave plate*. Next, the light passes through the beam splitter which splits it into two orthogonal

beams (a reference beam and a data beam). The circularly polarized reference beam is sent through a linear polarizer to extract only one component for the *modulation detector* to examine. The modulation detector provides a phase reference for the lock-in amplifier in the control electronics. The circularly polarized data beam goes directly to the sample. After interacting with the sample, the data beam travels through a circular polarizer (which is removed for dichroism tests). The resultant beam is picked up by the *detector*, which sends information to the control electronics.

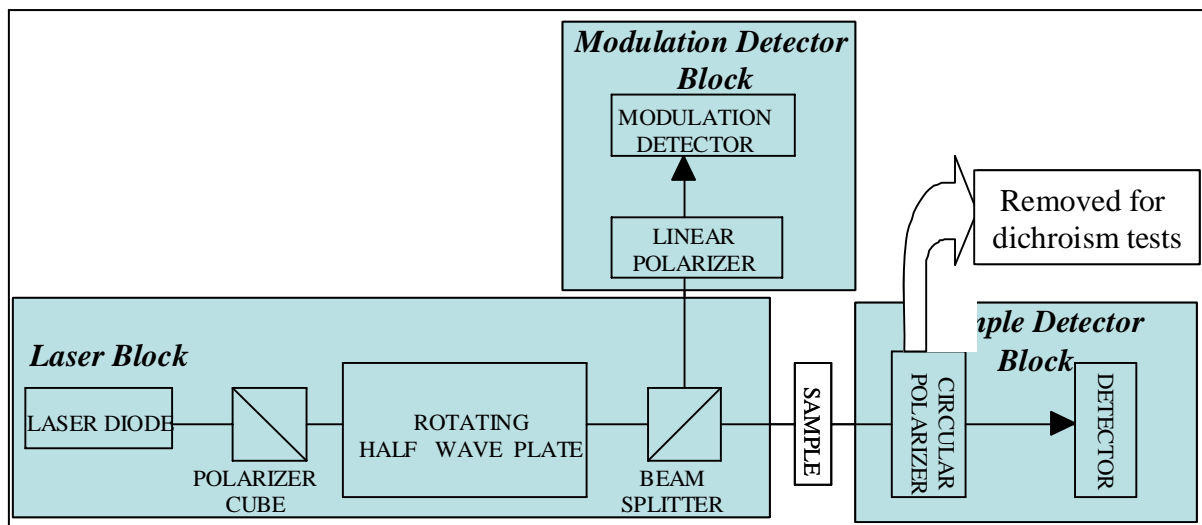


**Figure 2-9.** Optical train block diagram.

### ***Laser Block***

*Laser diode* provide the light for the experiment and is built to emit light at wavelength of 632.8 nm, which is red visible. The generated laser light is polarized with a ratio of 100 to 1.

*Polarizer cube* is a linear polarizer with an extinction ratio of 1000:1. The light passes through a polarizer cube, providing another order of magnitude of polarization.

*Half wave plate* rotates the polarization of the electric vector of light that is transmitted through it. The spinner motor provides rotation for the half wave plate. The transmitted light from the rotating half wave plate will be circularly polarized. The OAM utilizes a half wave plate that rotates at speed of 400 Hz.

*Beam splitter*. This crystal prism will split the beam into two parts of equal intensity. Half of the light will be sent to the sample and the other half will be used as a reference beam for phase information.

*Prism*. There are two additional prisms held down at the exit to the laser block. These prisms divert the light down through the sample at 90° from the initial path of the beam.

***Modulation detector block***

*Linear polarizer* transmits only one component of the circularly polarized light to the modulation detector.

*Modulation detector* sends phase information to the lock-in amplifier located in the control electronics.

***Sample detector block***

*Circular polarizer* will convert circularly polarized light into plane polarized light. The mechanism is basically the reverse of the plane-to-circular polarization process. When the OAM is used for the birefringence testing, the light exiting the sample will still be circularly polarized, and needs to be converted to plane polarization in order for the detected light to have relevance in subsequent signal processing. This is not the case for the dichroic tests. Therefore, the circular polarizer is only used for birefringence tests, and must be removed for dichroism testing.

*Detector.* The detector collects the light that has passed through the sample. The information is passed on to the control electronics for analysis.

## 2.2.6 Polarization

The light is considered as an electromagnetic wave, and only electric component is important for understanding the measurements using the OAM. When using the OAM, the primary interaction of materials with light is with its electric component. If the light is propagating along the  $z$  direction, the electric field is written as:

$$E = E_0 \cos\left(\frac{2\pi n}{\lambda} z - \omega t\right) \quad (2-65)$$

where  $n$  is the refractive index of the material,  $\lambda$  the wavelength of the light,  $\omega$  the frequency of the light,  $E_0$  the vector amplitude of the electric field.

Polarization is used to describe the vector character of the electric field. Since the electric field is contained within the plane perpendicular to the propagation direction of the light, it is sufficient to describe it by the following two component vector:

$$E = \begin{bmatrix} E_x \\ E_y \end{bmatrix} \quad (2-66)$$

If light propagates through a birefringent material of thickness  $d$  in a manner that has the  $E_x$  component sensing the refractive index  $n_1'$  and the  $E_y$  component sensing  $n_2'$ , then the electric field will have the form

$$E = \begin{bmatrix} E_{0x} \cos\left(\frac{2\pi n_1' d}{\lambda} + \frac{2\pi n}{\lambda} z - \omega t\right) \\ E_{0y} \cos\left(\frac{2\pi n_2' d}{\lambda} + \frac{2\pi n}{\lambda} z - \omega t\right) \end{bmatrix} \quad (2-67)$$

If the birefringence is zero and  $n_1' = n_2'$ , the phase of both components will be equal. This type of polarization is called *linearly polarized* light, which is mapped out as a straight line in the (x,y) plane (Figure 2-10, a). If the birefringence is finite and of a magnitude such that the retardation (eq 2-68)

$$\delta' = \frac{2\pi\Delta n' d}{\lambda} = \frac{\pi}{2} \quad (2-68)$$

the electric field will be

$$E = \begin{bmatrix} E_{0x} \cos\left(\frac{2\pi n_1' d}{\lambda} + \frac{2\pi n}{\lambda} z - \omega t\right) \\ E_{0y} \cos\left(\frac{2\pi n_2' d}{\lambda} + \frac{2\pi n}{\lambda} z - \omega t - \frac{\pi}{2}\right) \end{bmatrix} \quad (2-69)$$

which is mapped out as a circle in (x,y) plane if  $E_{0x} = E_{0y}$  (Figure 2-10,b). The most general form of perfectly polarized light is elliptical polarization, depicted in Figure 2-10,c).

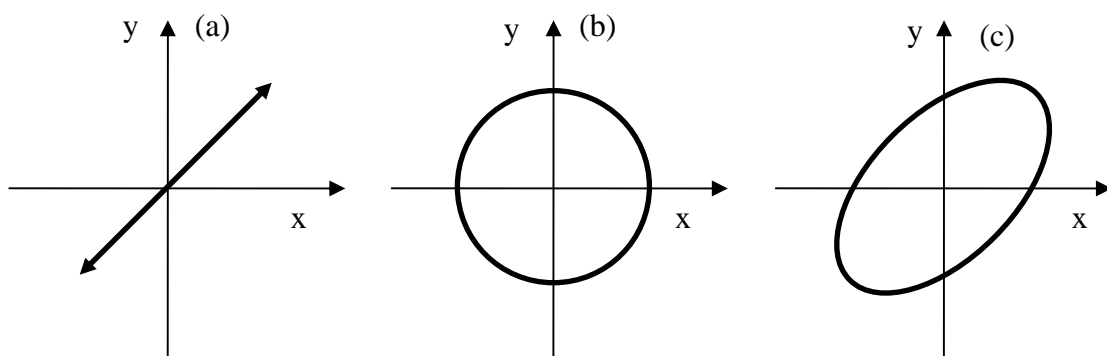


**Figure 2-10.** Polarized light: (a) linear (b) circular (c) elliptical.

### 2.2.7 Refractive index, anisotropy, birefringence

Normally, the refractive index of a material is considered as a single value, scalar property. To understand the output of the OAM, it is important to consider two general properties: 1) the refractive index is a complex number; 2) the refractive index is a tensor. According to the first feature, the refractive index as a number complex can be written as:

$$n = n' + in'' \quad (2-70)$$

The real part,  $n'$ , is the value that is commonly used when refractive indices of materials are employed. However, when the full form of the refractive index is used, eq 2-65 is rewritten as:

$$E = E_0 \cos\left(\frac{2\pi n'}{\lambda} - \omega t\right) e^{-\frac{2\pi n''}{\lambda} z} \quad (2-71)$$

It should be mentioned that the real part of the refractive index belongs within cosine term and affects the phase of the electric wave vector, while the imaginary part is inside of a decreasing exponential term and causes attenuation (absorption and scattering). The reason that is considered only the real part of the refractive index when discussing a material is that some materials do not absorb visible light and the imaginary part can be neglected. The imaginary part of the refractive index depends strongly on the wavelength of the light that is used.

The second important feature of the refractive index is that it is not always a scalar property. In general it can have different values along different directions, which allow to refer to it as a *tensor*.

If one considers a transparent material free of stress and the polymer chains are random in their configuration, the refractive index will be *isotropic* and characterized by a single value. Upon deformation of the chains, the intrinsic anisotropy of the oriented segments of the chain will lead to a net *anisotropy* as illustrated in Figure 2-11. This anisotropy is the source of birefringence and dichroism.

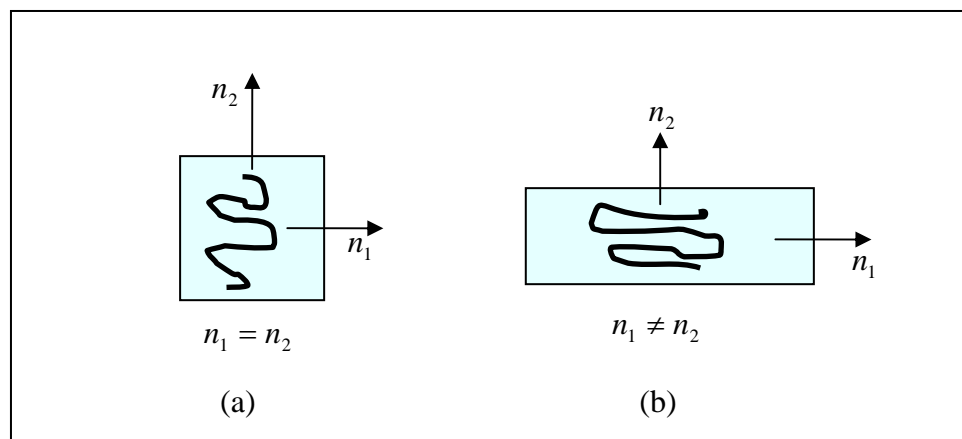


**Figure 2-11.** Refractive index of polymer samples: (a) isotropic polymer sample; (b) anisotropic polymer sample.

For a refractive index containing both the real and imaginary parts, these properties are defined as following:

$$\text{Birefringence: } \Delta n' = n_1' - n_2' \quad (2-72)$$

$$\text{Dichroism: } \Delta n'' = n_1'' - n_2'' \quad (2-73)$$

An additional property measured by OAM is *angle of orientation* of the principle axes of alignment of the sample relative to the laboratory frame (flow direction). In general the average orientation will not be in the flow direction, but in direction with the angle  $\theta$ .

The OAM is capable to measure the retardation  $\delta'$ , the extinction  $\delta''$  and the orientation angle,  $\theta$ . From the first two quantities the birefringence,  $\Delta n'$ , and the dichroism,  $\Delta n''$  can be calculated, respectively.

### 2.2.8 Intrinsic and form birefringence

Measurements of birefringence and dichroism reveal information on the microstructure of complex liquids subjected to flow. The origins of birefringence or dichroism will depend on the particular system being studied. Both anisotropies (birefringence and dichroism) arise from two sources: *intrinsic contributions* and *form or scattering effects*.

#### ***Systems in which form birefringence is significant.***

Form birefringence arises from a spatially anisotropic arrangement of domains with different mean refractive indices<sup>134,135</sup>. It can occur in polymer solution, block copolymer melts, polymer blends but not in homopolymer melts. As a result multiple scattering from the

various domains modify the polarization state of the transmitted beam. Even a suspension of perfect spheres can give rise to form birefringence if the spheres are arranged in an anisotropic manner. **The form birefringence** is generally very difficult to treat rigorously, but its contribution to the measured signal **is always positive in sign** and can be minimized by matching the refractive indices of the components. Form birefringence increases with molecular weight. There are two situations in which the form birefringence effect is major: a) in phase separated dilute polymer solutions<sup>136</sup> and suspensions and b) in microphase separated block copolymer liquids. For polystyrene solutions<sup>136</sup> in steady shear at low shear rates the overall birefringence signal is positive due to the form effect, while at high shear rates the birefringence response is negative according to the high contribution from the intrinsic birefringence. Because polystyrene has a negative stress optical coefficient,  $C$ , the intrinsic birefringence (due to the molecular polarizability anisotropy) is negative. For block copolymers, the microdomains formed by microphase separation can give rise to substantial form effects.<sup>137</sup>

### 2.2.9 Stress Optical Rule (SOR)

Many polymeric liquids show a proportionality between the stress tensor and the refractive index tensor, following the expression:

$$\bar{n} = C\bar{\sigma} \quad (2-74)$$

where  $\bar{n}$  is the refractive index tensor,  $\bar{\sigma}$  is the stress tensor and  $C$  is the stress-optic coefficient.

This is the case of polymer melts, solutions and many surfactant systems. For flexible homopolymer melts (polystyrene, polyethylene), the stress-optical relation is almost universally valid. Values of  $C$  are found to be independent of shear rate (even in shear thinning regime), molecular weight, and molecular weight distribution. Furthermore,  $C$  depends of the identity of the monomer unit, slightly on temperature and optical wavelength. In solutions,  $C$  is independent of polymer concentration and applies only to the polymer contributions. Some typical values of  $C$  are given in Table 2-3 and some of  $C$  the values are negative (polystyrene), thus the birefringence can be negative.

Polymer	$C, [10^{-9} m^2 / N]$
Polybutadiene	+2.2
Polydimethylsiloxane	+0.14 to +0.26
Polyethylene	+1.2 to +2.4
Polyisobutylene	+1.5
Polyisoprene	+1.9
Polypropylene	+0.6 to +0.9
<b>Polystyrene</b>	<b>-4 to -6</b>
Poly(vinyl chloride)	-0.5

**Table 2-3.** Typical values of stress-optic coefficients<sup>138,139</sup> for homopolymer melts.

The applicability of stress-optical relation (SOR) does not rely on fundamental physical laws. The observation of a breakdown of SOR can inform about the molecular level contributions to the stress tensor and the rheo-optical measurements can be informative in regions where the SOR does not apply.

A given polymer will exhibit different values of  $C$  above and below its glass transition, which may even differ in sign. This is a consequence of the different conformational rearrangements available in the two regimes. Below the glass transition the SOR may not hold and the onset of crystallization will also cause the SOR to fail.

For solutions and block copolymers a macroscopic SOR will not be observed in general. This, it can be explained due to the different values of  $C$  upon changing shear rate or frequency, the individual components will not contribute to the total stress in constant proportions. The failure of SOR can be due to the saturation of orientation at very high shear rates or local dynamics (chain stiffness, internal viscosity).

An evaluation of stress-optic coefficient can be obtained from the simultaneously measurements of birefringence and the shear stress dependencies with the shear rate, as follows:<sup>138</sup>

$$\Delta n' = C \sqrt{4\sigma_{12}^2 + N_1^2} \quad (2-75)$$

where  $\sigma_{12}$  is shear stress,  $N_1$  is first normal stress difference. An expression relating  $C$  to the optical anisotropy of the chain molecules is borrowed from the theory of ideal rubbery<sup>140</sup> as follows:

$$C = \frac{2\pi}{45kT} \frac{(n^2 + 2)^2}{n} (\alpha_1 - \alpha_2) \quad (2-76)$$

where  $n$  is the mean refractive index,  $k$  is Boltzmann's constant,  $T$  is temperature,  $(\alpha_1 - \alpha_2)$  is anisotropic polarizability of the monomer. Because  $C$  depends on the anisotropic polarizability of the monomer is expected to be nearly independent of molecular weight and molecular architecture.

## 2.3 Experimental section

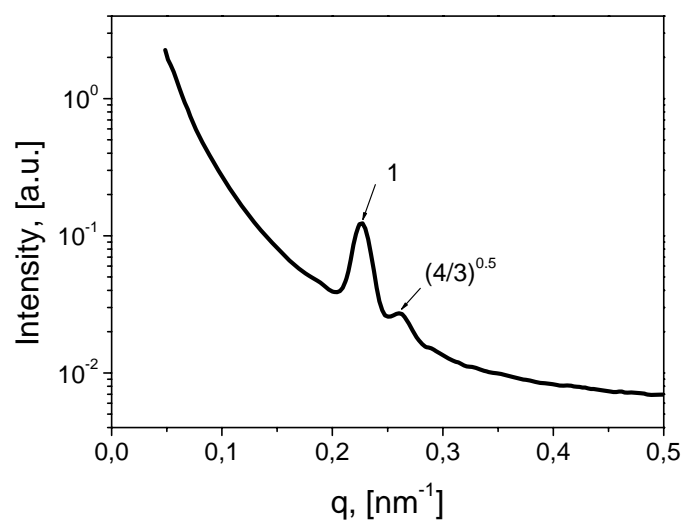
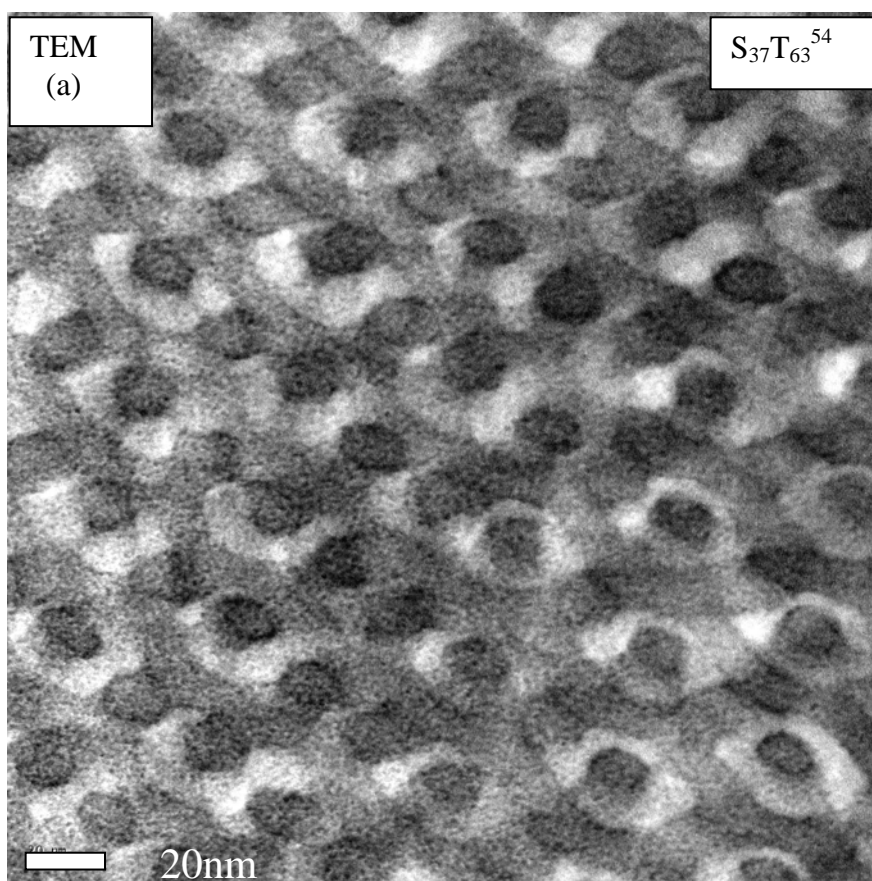
### 2.3.1 Synthesis of polystyrene-*b*-poly(*t*-butyl methacrylate)

The series of diblock copolymers polystyrene-*b*-poly(*t*-butyl methacrylate) were synthesized via sequential anionic polymerization.<sup>62,141</sup> Styrene is polymerized at  $-70^\circ\text{C}$  in tetrahydrofuran (THF) for 1 hour using *sec*-butyl lithium as initiator. 1,1-diphenylethylene (DPE) is added to reduce the reactivity of the anionic end groups before adding *t*-butyl methacrylate, otherwise there will be significant termination by attack to the carbonyl groups of *t*-butyl methacrylate. After warmed to  $-60^\circ\text{C}$ , the second block was slowly added and colourless solution is polymerized for 1 hour at  $-40^\circ\text{C}$ . The diblock copolymer was terminated and precipitated in methanol. The molecular weights of the block copolymers synthesized were determined from the molecular weight of polystyrene precursor obtained by gel permeation chromatography (GPC) and calculation of the composition of each block have been made by using proton nuclear magnetic resonance ( $^1\text{H-NMR}$ ). The molecular characteristics of all samples are given in Table 2-4.

Polymer <sup>1)</sup>	$M_n$ , kg/mol	$M_w/M_n$ <sup>2)</sup>	$w_{\text{PS}}$ <sup>3)</sup>	$f_{\text{PS}}$ <sup>4)</sup>	Morphology (TEM <sup>a)</sup> and SAXS <sup>b)</sup> )
S <sub>51</sub> T <sub>49</sub> <sup>34</sup>	34	1.04	0.51	0.54	<sup>a),b)</sup> lamellar
S <sub>48</sub> T <sub>52</sub> <sup>72</sup>	72	1.01	0.48	0.51	<sup>a)</sup> lamellar
*S <sub>50</sub> T <sub>50</sub> <sup>100</sup>	100	1.03	0.50	0.53	<sup>a)</sup> lamellar
S <sub>55</sub> T <sub>45</sub> <sup>117</sup>	117	1.02	0.55	0.58	<sup>a)</sup> lamellar
S <sub>37</sub> T <sub>63</sub> <sup>54</sup>	54	1.03	0.37	0.40	<sup>a),b)</sup> gyroid
S <sub>75</sub> T <sub>25</sub> <sup>50</sup>	50	1.03	0.75	0.77	<sup>a)</sup> cylindrical

<sup>1)</sup> Subscript: weight fraction in %; superscript:  $M_n$  in kg/mol calculated from  $M_n(\text{PS})$  and  $^1\text{H-NMR}$ . <sup>2)</sup> GPC (THF) (PS-calibration). <sup>3)</sup>  $^1\text{H-NMR}$ . <sup>4)</sup> volume fraction. <sup>a),b)</sup> cast films from  $\text{CHCl}_3$ . \*synthesized by Thorsten Goldacker.

**Table 2-4.** Molecular characteristics of the polystyrene-*b*-poly(*t*-butyl methacrylate) with different morphologies.



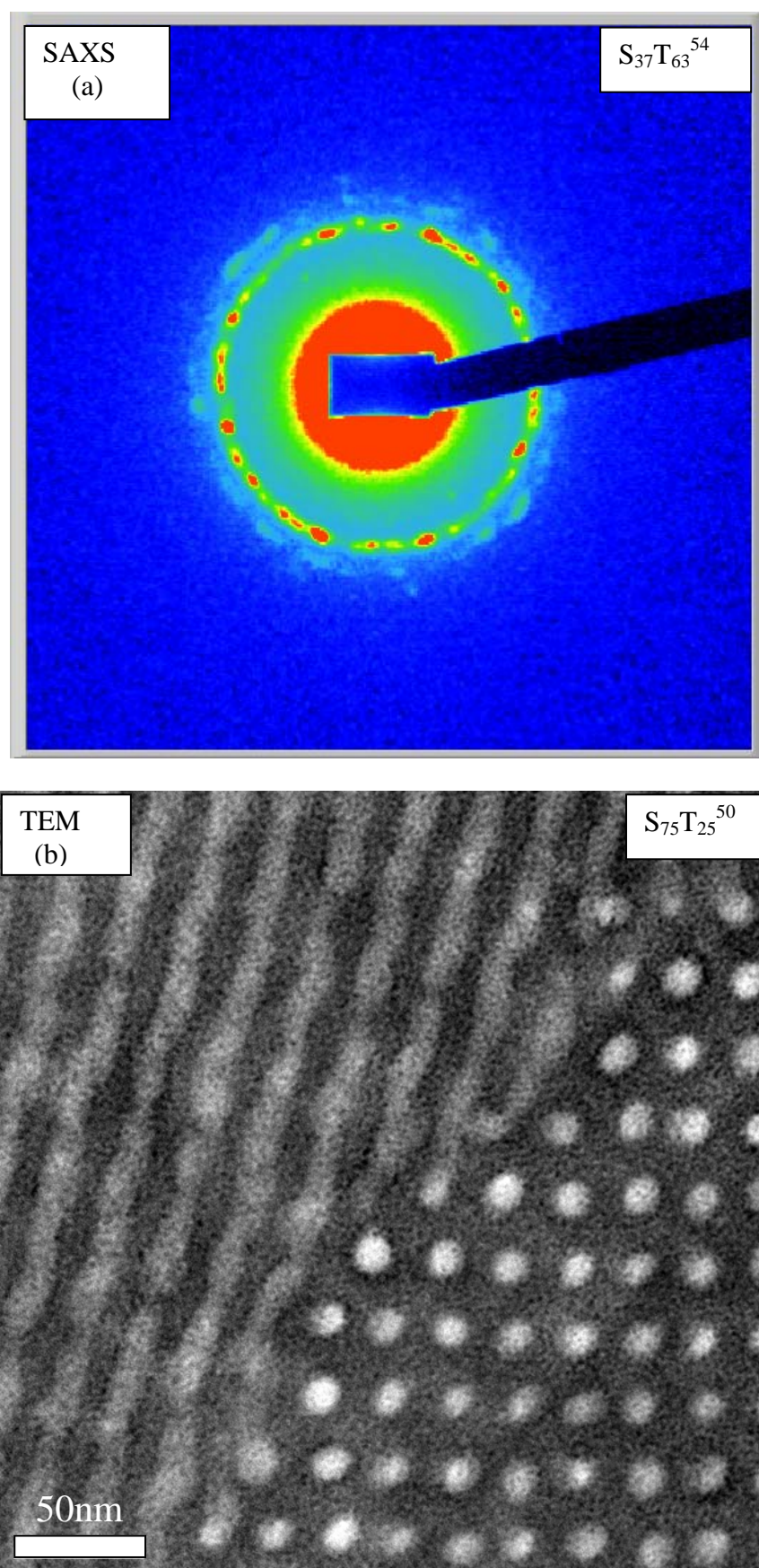


**Figure 2-12.** (a) Transmission electron micrograph, scattering profile (Intensity versus  $q$ ) and 2D-pattern for the  $S_{37}T_{63}^{54}$  gyroid morphology, from cast film in  $CHCl_3$ ; (b) Transmission

electron micrograph for  $S_{75}T_{25}$ <sup>50</sup> cylindrical morphology, from cast film in  $CHCl_3$ . The TEM micrographs were stained with  $RuO_4$ , whereas polystyrene appears dark and poly(*t*-butyl methacrylate) appears white.

The TEM micrographs of gyroid (a) and cylindrical (b) morphologies are presented in Figure 2-12 whereas the dark domains represent the polystyrene block while the poly(*t*-butyl methacrylate) block is represented by the white domains. The SAXS profile such as intensity versus scattering vector,  $q$ , presented in Figure 2-12 has proved as well the gyroid morphology through the correlation peaks of  $1 : (4/3)^{0.5}$ , and allowed a calculation of the long period for the gyroid morphology of  $L \sim 27.7\text{nm}$ .

### 2.3.2 Synthesis of polystyrene-*b*-polybutadiene-*b*-poly(methyl methacrylate)/poly(*t*-butyl methacrylate)

A detailed characterization regarding the synthesis of triblock terpolymers such as polystyrene-*b*-polybutadiene-*b*-poly(*t*-butyl methacrylate) (SBM) has been made previously by Stadler et al.<sup>142</sup> Furthermore, the morphology and thermodynamics<sup>34</sup> of the triblock terpolymers SBM and their hydrogenated analogues polystyrene-*b*-poly(ethylene-*co*-butylene)-*b*-poly(methyl methacrylate) (SEBM) were investigated earlier as well.

The synthesis of SBM series was accomplished by sequential anionic polymerization of styrene, butadiene and methyl methacrylate in THF in the presence of lithium alkoxides using *sec*-butyl lithium as initiator. The same protocol has been used to synthesize the triblock terpolymer  $S_{33}B_{33}T_{34}$ <sup>160</sup> whereas the *t*-butyl methacrylate is treated as methyl methacrylate except for the polymerization temperature which is increased over 2h from  $-60^\circ\text{C}$  to  $-40^\circ\text{C}$ . In the Table 2-5 are presented some of the synthesized triblock terpolymers which have been used in the further alignment investigations. The expected morphology was checked by TEM and SAXS experiments on cast films of the specimens from  $CHCl_3$ .

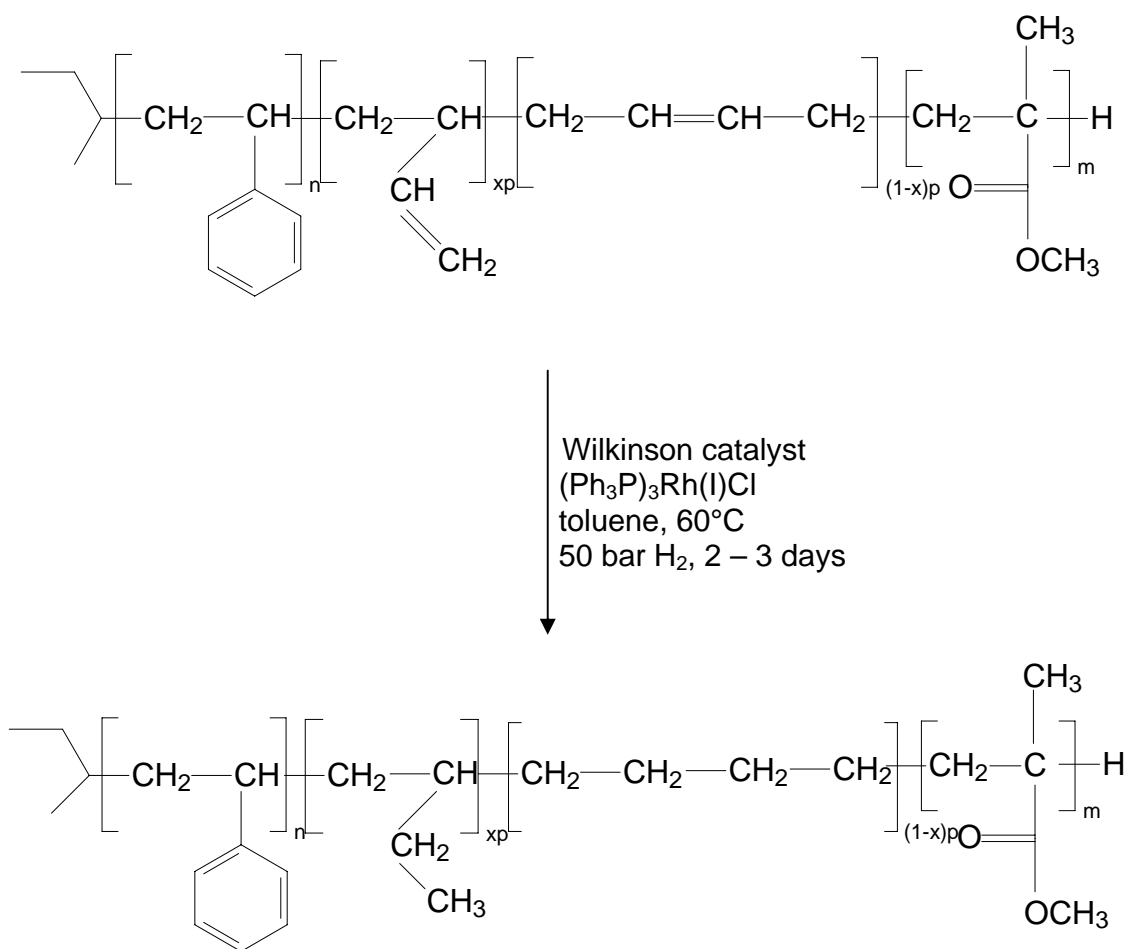
Polymer <sup>1)</sup>	M <sub>n</sub> , kg/mol	M <sub>w</sub> /M <sub>n</sub> <sup>2)</sup>	w <sub>PS</sub> <sup>3)</sup>	f <sub>PS</sub> <sup>4)</sup>	f <sub>1,2-PB</sub>	f <sub>PMMA</sub>	Morphology (TEM <sup>a)</sup> and SAXS <sup>b)</sup> )
S <sub>37</sub> B <sub>14</sub> M <sub>49</sub> <sup>37</sup>	37	1.03	0.37	0.38	0.15	0.46	<sup>b)</sup> cylindrical
S <sub>34</sub> B <sub>19</sub> M <sub>47</sub> <sup>65</sup>	65	1.03	0.34	0.35	0.21	0.44	<sup>a),b)</sup> cylindrical+gyroid
S <sub>37</sub> EB <sub>14</sub> M <sub>49</sub> <sup>37</sup>	38	1.05	0.37	0.38	0.15	0.46	<sup>b)</sup> lamellar
S <sub>34</sub> EB <sub>19</sub> M <sub>47</sub> <sup>65</sup>	66	1.05	0.34	0.35	0.21	0.44	<sup>a),b)</sup> knitting pattern
** S <sub>33</sub> B <sub>33</sub> T <sub>34</sub> <sup>160</sup>	160	1.04	0.33	0.34	0.34	0.31	<sup>a),b)</sup> lamellar

<sup>1)</sup> Subscript: weight fraction in %; superscript: M<sub>n</sub> in kg/mol calculated from M<sub>n</sub>(PS) and <sup>1</sup>H-NMR. <sup>2)</sup> GPC (THF) (PS-calibration). <sup>3)</sup> <sup>1</sup>H-NMR. <sup>4)</sup> volume fraction; <sup>a),b)</sup> cast films from CHCl<sub>3</sub>. \*\*synthesized by Thorsten Goldacker.

**Table 2-5.** Characteristics of triblock terpolymers.

### 2.3.3 Hydrogenation of S<sub>37</sub>B<sub>14</sub>M<sub>49</sub><sup>37</sup> and S<sub>34</sub>B<sub>19</sub>M<sub>47</sub><sup>65</sup>

Homogeneous catalytic hydrogenation of SBM triblock terpolymers with different compositions and molecular weights (S<sub>37</sub>B<sub>14</sub>M<sub>49</sub><sup>37</sup>, S<sub>34</sub>B<sub>19</sub>M<sub>47</sub><sup>65</sup>) was performed using the Wilkinson catalyst<sup>143</sup> ((Ph<sub>3</sub>P)<sub>3</sub>Rh(I)Cl) to yield the corresponding polystyrene-*b*-poly(ethylene-*co*-1-butene)-*b*-poly(methyl methacrylate). As an example, the hydrogenation of PS-PB-PMMA triblock copolymers is depicted in Scheme 2-5. In a typical procedure 10 - 15 g of the triblock terpolymer along with a small amount of stabilizer (2,6-di-*t*-butyl-4-methylphenol) were dissolved in dry toluene (p.a., Merck) and degassed for at least 30 min with dry nitrogen. Subsequently, Wilkinson catalyst (1 mol-% with respect to the number of double bonds) was added to the solution in a slight stream of nitrogen. This solution was transferred into a steel autoclave, which was previously rinsed with nitrogen for several times followed by hydrogen in order to remove traces of oxygen. The hydrogenation was carried out at 60°C and 50 bar hydrogen pressure for 2 – 3 days. After complete hydrogenation of PB block, the triblock terpolymers were isolated from the solution by precipitation in methanol. In order to remove residual catalyst completely a further purification is necessary, by refluxing a solution of the polymer in toluene with a small amount of concentrated HCl for a short time followed by precipitation in methanol. The success of the purification can be followed by the disappearance of the brown color, which arises from residual catalyst.



**Scheme 2-5.** Preparation of PS-PEB-PMMA triblock terpolymers by homogeneous catalytic hydrogenation of PS-PB-PMMA triblock terpolymers using Wilkinson catalyst. (x-fraction)

Alternatively, PS-PB-PMMA triblock terpolymers can be hydrogenated with diimide, generated in situ by thermolysis of *p*-toluenesulfonyl hydrazide.<sup>144</sup>

As a result, the PB blocks get completely hydrogenated by using Wilkinson catalyst method, the resulting PS-PEB-PMMA triblock copolymers preserved the narrow molecular weight distribution, shown by the GPC traces of the hydrogenated triblock copolymers in comparison with the unsaturated triblock copolymers and  $^1\text{H-NMR}$  spectra (Figures 2-13, 2-14). According to a quantitative hydrogenation, the absorptions between 4.8 and 5.4 ppm completely disappeared.

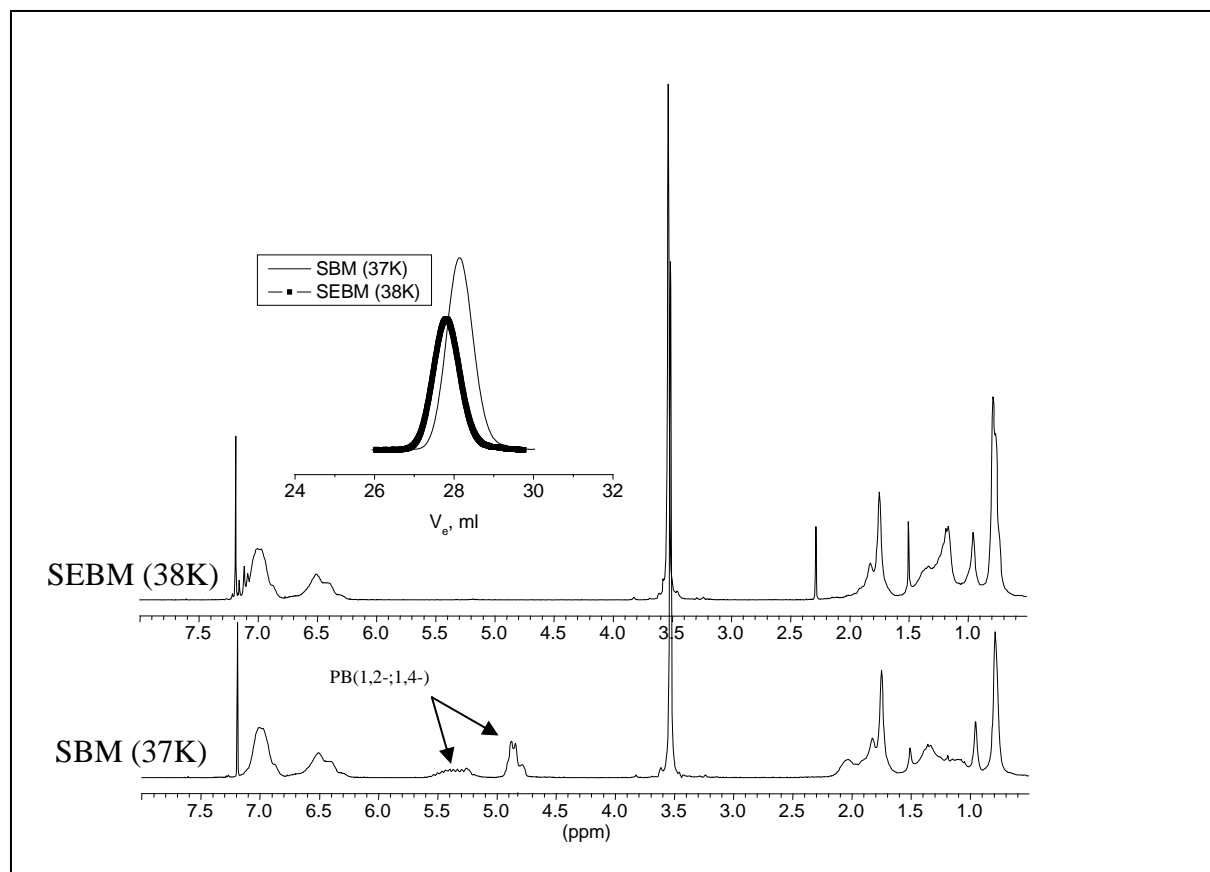


**Figure 2-13.**  $^1\text{H-NMR}$  analysis of the PS-b-PB-b-PMMA (37K) and its hydrogenated analogous PS-b-PEB-b-PMMA (38K) with Wilkinson catalyst. Inset: GPC (RI signal) analysis of the unsaturated (SBM) and the hydrogenated (SEBM) triblock terpolymers.

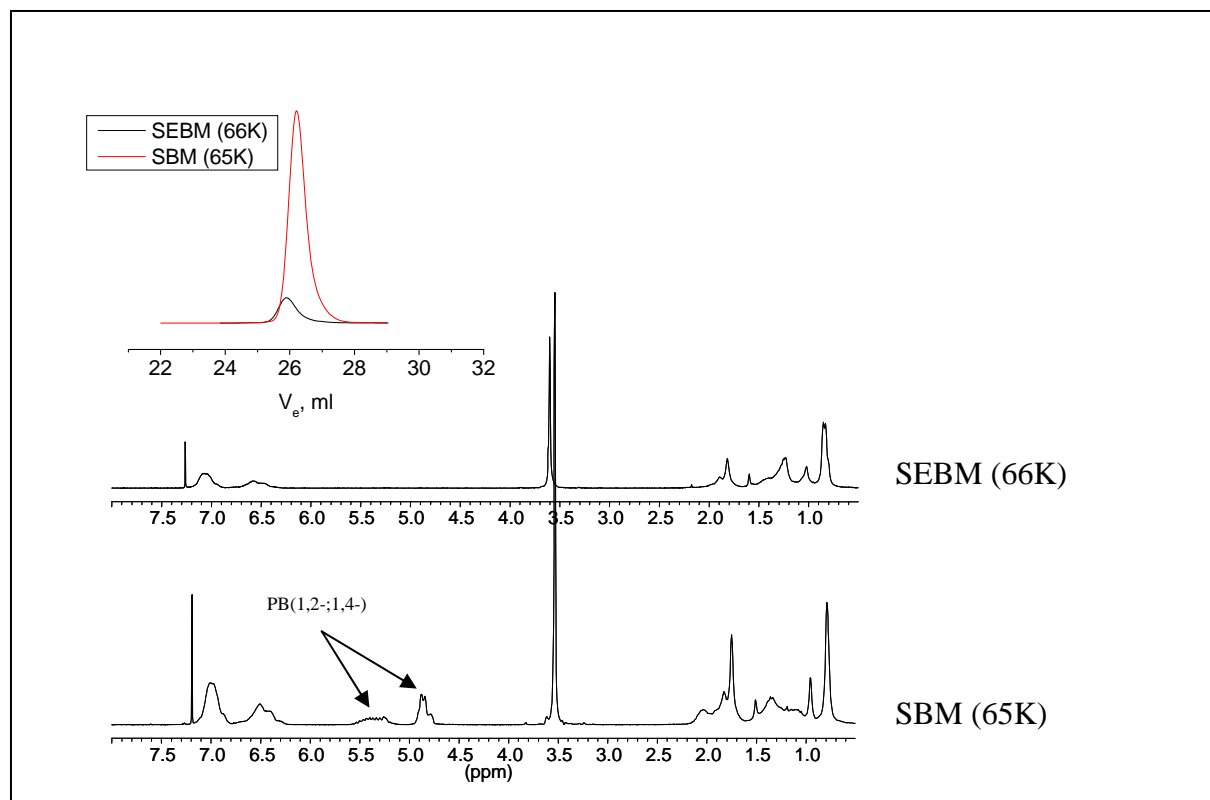


**Figure 2-14.**  $^1\text{H-NMR}$  analysis of the PS-b-PB-b-PMMA (65K) and its hydrogenated analogous PS-b-PEB-b-PMMA (66K) with Wilkinson catalyst. Insert: GPC (RI signal) analysis of the unsaturated (SBM) and the hydrogenated (SEBM) triblock terpolymers.

### 3. Morphological transitions in block copolymer solutions with a selective solvent

#### 3.1 Introduction

Many research groups in the past have investigated the order-disorder transition (also referred to as the microphase-separation transition, MST) behavior of block copolymers, both theoretically and experimentally. The order-disorder transition temperature ( $T_{ODT}$ ) of a block copolymer is defined by the temperature at which the microdomain structure in a block copolymer disappears completely as the temperature is raised or by the threshold temperature at which the microdomain structure begins to appear when the temperature of a block copolymer in the homogeneous state is lowered. The order-disorder transition temperature of a block copolymer can be predicted using the theories of Helfand-Wasserman<sup>24,145</sup>, and Leibler.<sup>12</sup> Due to the Helfand-Wasserman theory,  $T_{ODT}$  can be calculated from the temperature at which the difference of the free-energy density of the microphase separated block copolymer and the homogeneous phase becomes zero. It should be mentioned that the Helfand-Wasserman theory describes the strong segregation limit, in which microphases are separated by sharp interfaces. Leibler's theory describes the weak segregation limit, at the onset conditions of domain formation or for the final step of the domain dissolution. By including composition fluctuations<sup>26</sup> which are important for chains of finite molecular weight a good agreement between Leibler theory and Helfand-Wasserman theory is achieved. From Leibler's theory it follows a correlation hole peak in scattering experiments on block copolymers in the homogeneous state due to the connectivity of the blocks and in his seminal paper the use of especially small-angle neutron scattering (SANS) was suggested to probe for this prediction. Using small-angle X-ray scattering (SAXS)<sup>146</sup> or (SANS)<sup>147</sup> this correlation hole was found and the temperature dependence of the maximum could be used to determine the ODTs of block copolymers. Spinodal decomposition temperature ( $T_s$ ) for microphase separation, as well as the  $T_{ODT}$  were mainly the parameters resulting from Leibler's theory and it was shown for diblock copolymers that the microdomain structure (lamellar, cylindrical, or spherical) of the ordered phase, influences the value of  $T_{ODT}$ .

Rheological investigations from some groups<sup>148,149</sup> established different interpretations for  $T_{ODT}$  as the temperature at which the dynamic storage modulus  $G'(\omega)$  drops abruptly or by observing the temperature at which the Newtonian viscosity is observed when the temperature of a block copolymer with microdomain structure is increased. Han and co-workers<sup>54</sup> have proposed to use the logarithmic plots of the dynamic storage modulus  $G'(\omega)$  versus the

dynamic loss modulus  $G''(\omega)$  to determine the  $T_{ODT}$  of block copolymers; specifically, the  $T_{ODT}$  of a block copolymer can be determined by the temperature at which  $\log G'$  versus  $\log G''$  plots cease to vary with temperature as the temperature is increased.

It was well established by transmission electron microscopy (TEM) that microphase separated diblock copolymers can adopt spherical, cylindrical, lamellar and the inverse cylindrical and spherical microdomain structures for varying volume fraction,  $f$  and the experimental observations were in good agreement with theoretical predictions.<sup>150</sup> In addition, between the cylindrical and lamellar region there is the gyroid phase, which was found later and cannot be satisfactorily described by the weak and strong segregation approaches of Leibler and Helfand-Wasserman. Its description is possible using the self-consistent field theory (SCFT) approach developed by Matsen.<sup>28</sup>

In order to understand the order-disorder transition temperature and the microphase separation transition of block copolymer solutions we have synthesized via anionic polymerization lamellar diblock copolymers of polystyrene-*b*-poly(*t*-butyl methacrylate) with high molecular weights. An attempt was made to determine  $T_{ODT}$  for entangled systems with high molecular weight and to compare ODTs determined by using different treatments of data obtained by dynamic mechanical spectroscopy (DMS). An expression for the interaction parameter,  $\chi$ , has been developed based on the rheological results and by applying Leibler's dilution approximation theory.<sup>151</sup>

### 3.1.1 Sample preparation

Dioctyl phthalate (DOP) is known to be a nonselective solvent for polystyrene-*b*-polyisoprene (SI) block copolymers with different morphologies.<sup>151,152</sup> It thus was also used as a solvent for the ST block copolymers, due to the similarity of the solubility parameters of poly(*t*-butyl methacrylate) ( $\sim 18 \text{ MPa}^{1/2}$ )<sup>153</sup> and polyisoprene ( $\sim 16.8 \text{ MPa}^{1/2}$ ).<sup>153</sup> The investigated solutions were prepared at different concentrations by first dissolving the polymer into methylene chloride (p.a). After adding dioctyl phthalate, the solution was stirred for several hours. The cosolvent was removed initially in open air at room temperature and then by placing the solution under vacuum until the solution reached the constant weight expected for the block copolymer and DOP.

### 3.2 Measurement of dynamic mechanical properties

Rheological measurements were performed on an ARES instrument (Rheometric Scientific), using parallel plates of 25 mm diameter and gap widths of 0.5÷1mm. Care was taken to ensure that strain amplitudes were sufficiently small to remain within the linear viscoelastic regime. All experiments were conducted under a nitrogen atmosphere to avoid oxidative degradation of the samples.

#### 3.2.1 Determination of order-disorder transition temperature ( $T_{ODT}$ ) from *temperature sweep tests*

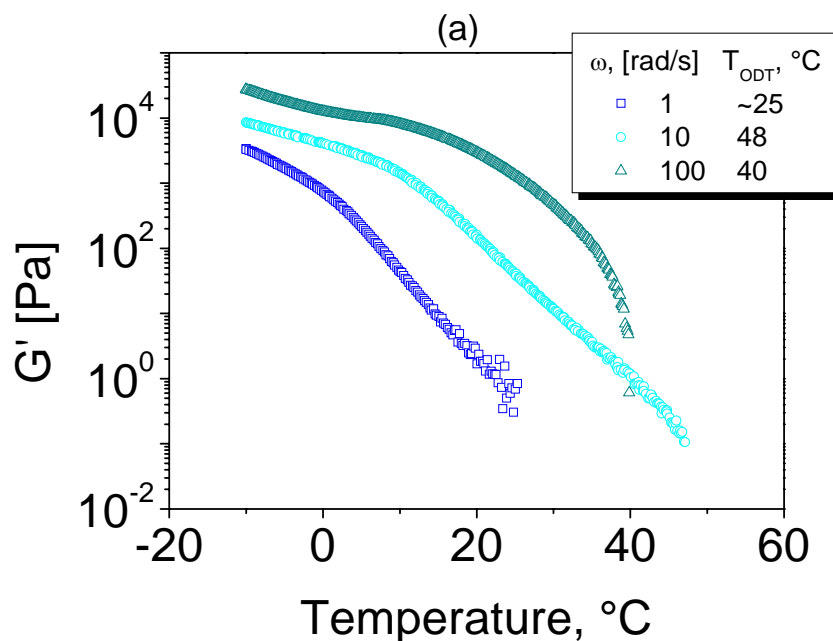
Many studies have been carried out on diblock copolymers with low molecular weights in the melt<sup>3,149,154</sup>, others were done with diblock copolymers with intermediate molecular weights in solution.<sup>151,155</sup> Rheology or its combination with flow birefringence have been applied to study  $T_{ODT}$ . As can be seen in the Table 3-1 we are interested in block copolymers with high molecular weight ( $S_{55}T_{45}^{117}$ ,  $S_{48}T_{52}^{72}$ ) and for such systems, in the melt state the  $T_{ODT}$  value is too high for experimental analysis. In order to shift  $T_{ODT}$  to an accessible range, we have used these systems as solutions in dioctyl phthalate (DOP).

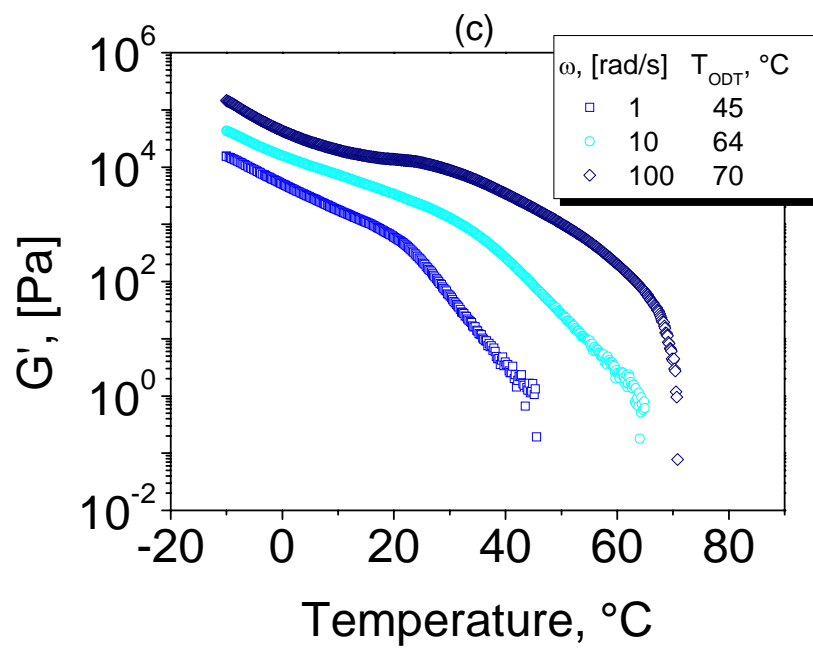
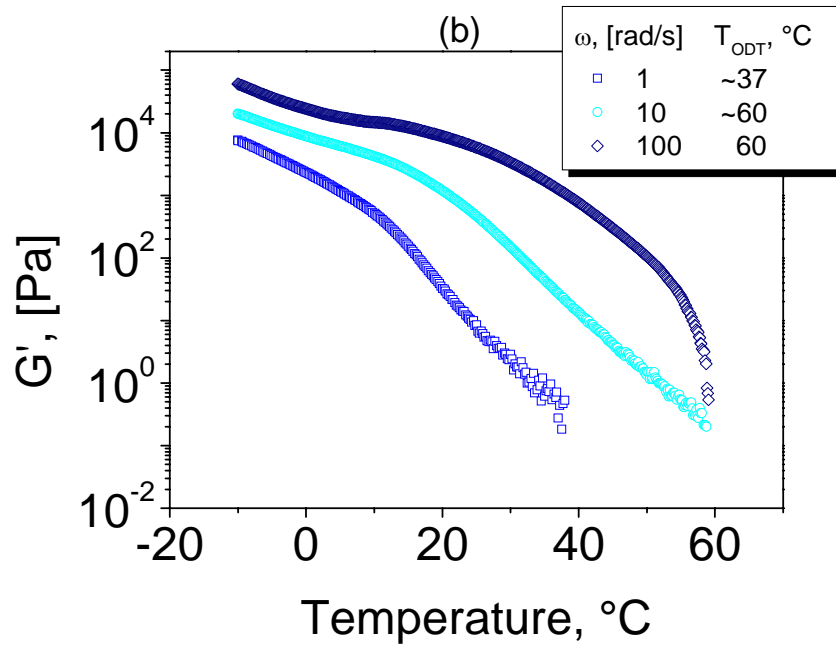
Sample	Weight concentration of ST diblock in DOP, %wt	Volume fraction of diblock in DOP, $\phi$
ST72_S1	23.5	0.2136
ST72_S2	26.5	0.2417
ST72_S3	30	0.2748
ST72_S4	35	0.3225
ST117_C1	25	0.2291
ST117_C2	26	0.2385
ST117_C3	27	0.2480
ST117_C4	28	0.2497
ST117_C5	33	0.3052

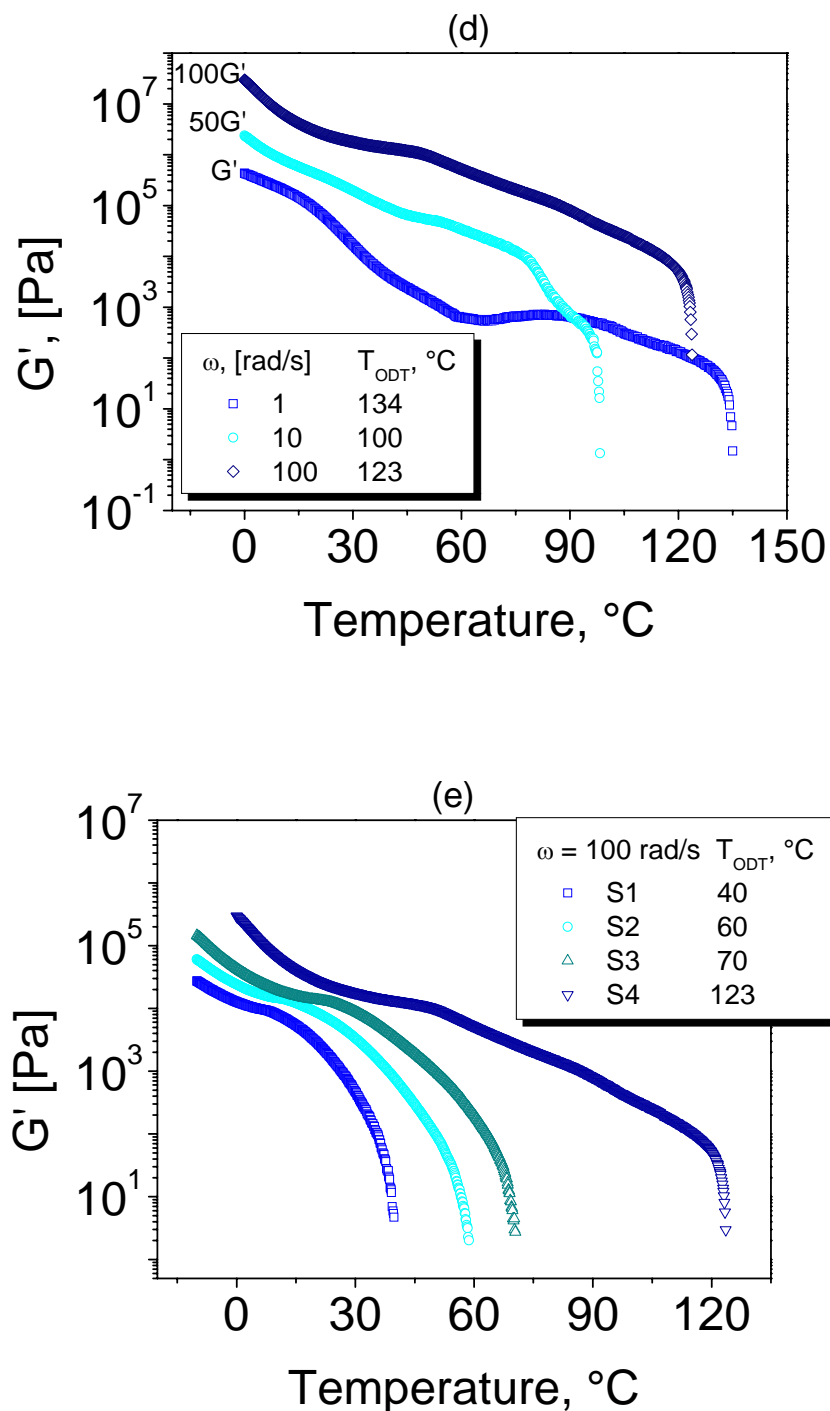
**Table 3-1.** Solutions of the ST diblock copolymers.

In Table 3-1 are presented the following sets of solutions, with different concentrations which have been used in this study.

Using an ARES instrument and parallel plates geometry, we carried out temperature sweep experiments at various angular frequencies,  $\omega = 1, 10$  and  $100$  rad/s within heating rate  $1^\circ\text{C}/\text{min}$ . All the experimental results reported in this section were obtained during heating. Figure 3-1 gives overlay plots of storage modulus  $G'$  versus temperature for the solution of ST72 at different concentrations S1, S2, S3, S4 in DOP, at  $\omega = 1, 10, 100$  rad/s, respectively. From the plots given in the Figures 3-1a, b, c, at  $\omega = 1$  rad/s it is not easy to determine a certain temperature at which the value of  $G'$  for the block copolymer solution drops obviously, which would indicate a phase transition. At higher frequencies like  $\omega = 10$  or  $100$  rad/s the moduli drop off at a certain temperature, which depends strongly on the system's concentration. As already observed in the plots from Figures 3-1a,b at a certain concentration  $T_{\text{ODT}}$  is smaller at  $\omega = 100$  rad/s than the one obtained at  $\omega = 10$  rad/s. This behavior might be a consequence of the induced high shear stress leading the system toward a separation into layers with different viscosity. Moreover, the shear heating<sup>86</sup> process appearing for the highest frequency has a higher contribution in the sense of a gradient of temperature occurring along the gradient of velocity axis (thickness of the sample) which induces a non-isothermal flow. Thus, a sudden decrease of the torque within a drop of moduli shifted  $T_{\text{ODT}}$  to lower temperatures.



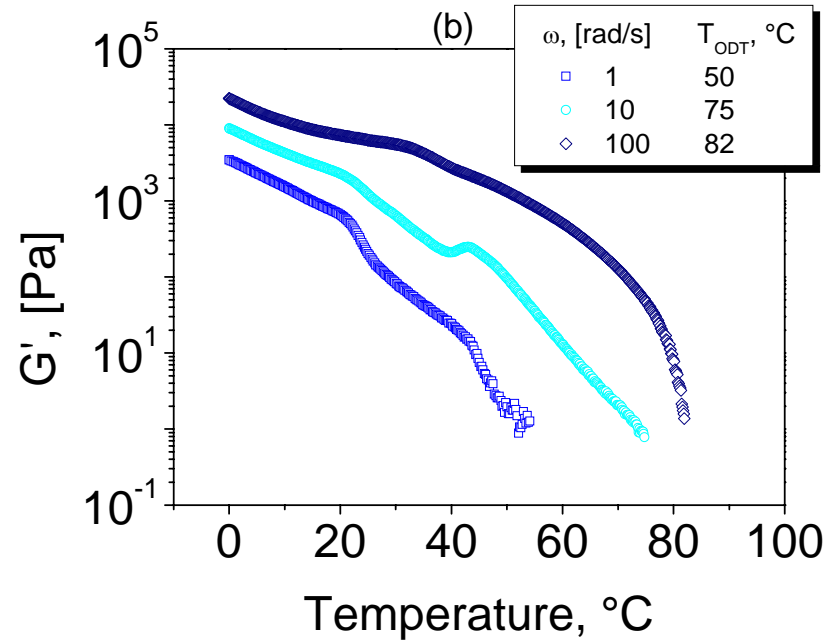
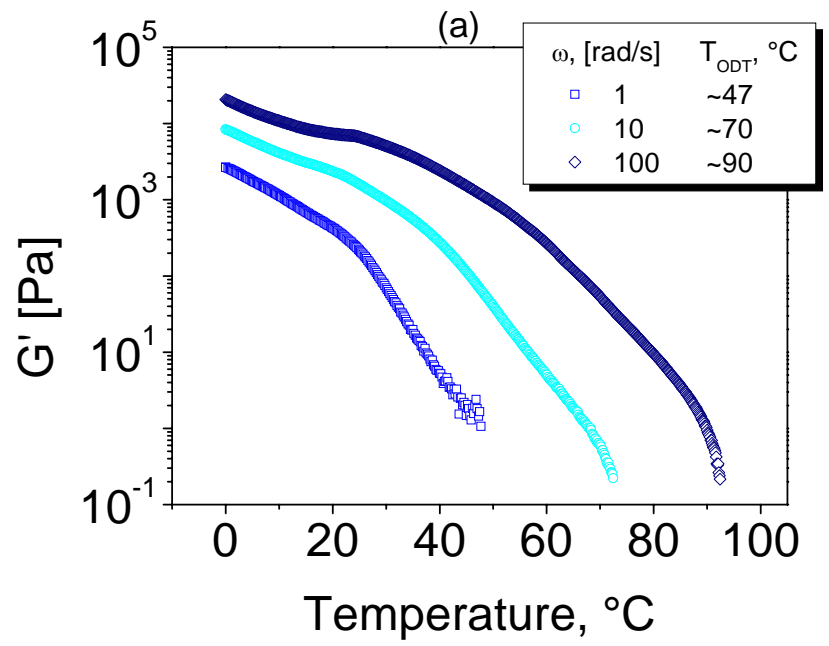


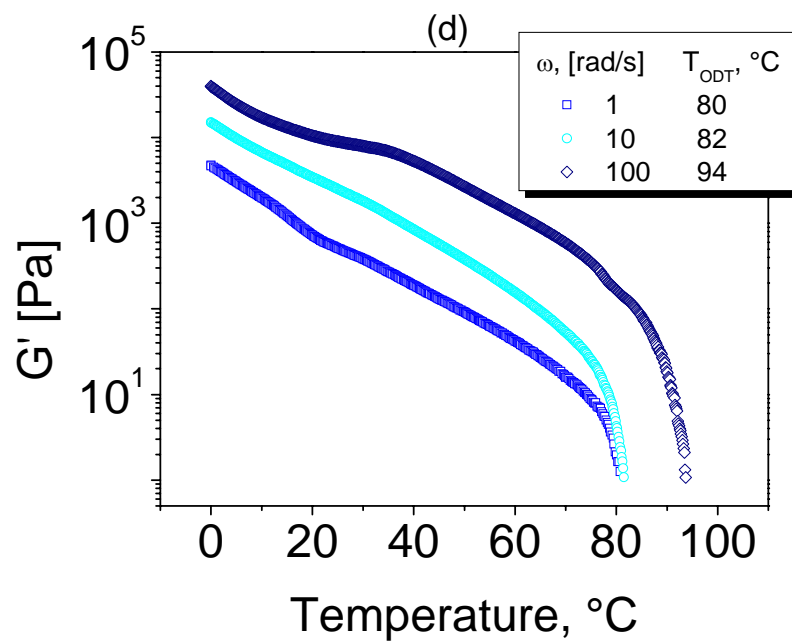
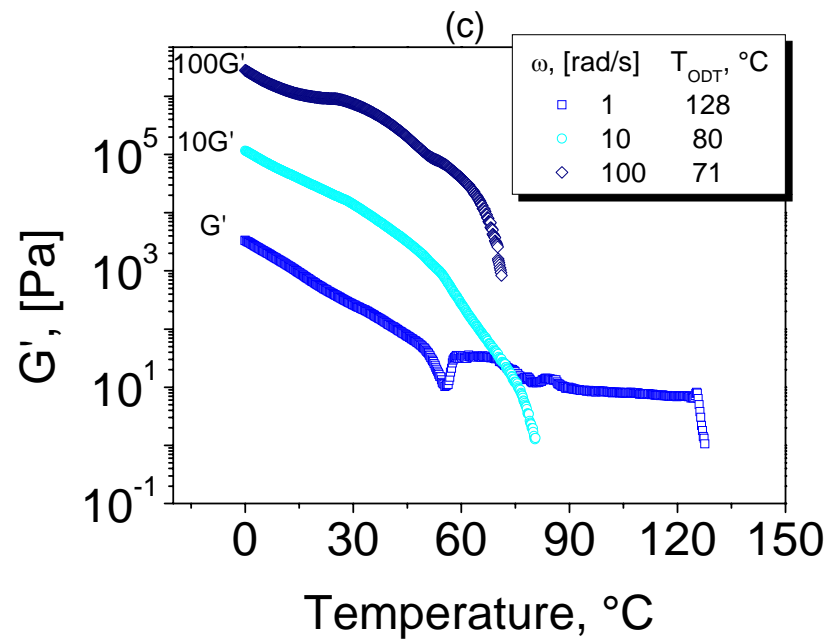


**Figure 3-1 a, b, c, d, e.** Variation of  $G'$  with increasing temperature obtained at  $\omega = 1, 10, 100$  rad/s for solutions of ST72 in DOP at different concentrations S1(a), S2(b), S3(c), S4(d) within the linear viscoelastic regime. A drop in  $G'$  is discernible at higher frequencies (a, b, c, d at  $\omega = 100$  rad/s) and higher concentration (d) for the overall range of frequencies at the order-disorder transition temperature. A comparison of  $T_{ODT}$  at different concentrations (S1, S2, S3, S4) and frequency  $\omega = 100$  rad/s is presented in Figure 3-1e.

As mentioned previously by Hashimoto et al.<sup>55</sup>, highly asymmetric diblock and triblock copolymer melts undergo morphological transitions before crossing the order-disorder temperature, as evidenced by a minimum of the storage modulus as a function of temperature. Such behavior has been encountered for the solution ST72\_S4 at the low angular frequency  $\omega = 1$  rad/s, as shown in Figure 3-1d whereas the other curves do not show a minimum in storage modulus. For a clear comparison they were shifted above ( $100G'$  at  $\omega = 100$  rad/s and  $50G'$  at  $\omega = 10$  rad/s) than the reference curve ( $G'$  at  $\omega = 1$  rad/s). Over the entire range of  $0\div 140^\circ\text{C}$  under isochronal conditions of  $\omega = 1$  rad/s,  $G'$  goes through a broad minimum at ca.  $65^\circ\text{C}$  (Figure 3-1d at  $\omega = 1$  rad/s) followed by a rapid increase toward a maximum at ca.  $84^\circ\text{C}$  and then begins to drop significantly at ca.  $134^\circ\text{C}$ . It is clear that the minimum in  $G'$  appears due to morphological change of the sample. This is a possible consequence of the selectivity of DOP for one of the blocks of ST72, which is therefore asymmetrically swollen. Whether the sample is lamellar or cylindrical under these conditions, is unknown. However, the sample first undergoes an order-order transition before finally disordering. This morphological rearrangement is an endothermic process accompanied by a softness during transformation to the new structure which means low modulus values followed by developing the new structure as reflected by an increased modulus. On the other hand in Figure 3-1d it is observed that the applied values of frequencies  $\omega$  have a profound influence on the qualitative temperature dependence of  $G'$ . For the higher frequencies 10 and 100 rad/s no minimum is found. At  $\omega = 10$  rad/s in Figure 3-1d, a slight decrease in  $G'$  value in the range of temperature  $27\div 53^\circ\text{C}$  might be due to the presence of morphological changes shifted close to ODT, which are as well illustrated by a "step" decreasing of moduli within a sudden change of the slope (range  $80\div 87^\circ\text{C}$ ) corresponding to a maximum in  $\tan \delta$  (not shown) before ODT. However, the evidence of morphological changes are not as strong as for  $\omega = 1$  rad/s. At  $\omega = 100$  rad/s the minimum in  $G'$  is more developed in the range  $0\div 48^\circ\text{C}$ . Thus morphological transitions are more pronounced than in the case of  $\omega = 10$  rad/s but less than for  $\omega = 1$  rad/s which may explain the higher value of ODT at  $\omega = 100$  rad/s than at  $\omega = 10$  rad/s. These findings suggest that lower angular frequencies may be more sensitive for the detection of morphological transitions, as already mentioned by Hashimoto and co-workers<sup>55</sup> and lead us to conclude that the ST72 system has an asymmetric structure at a certain concentration (S4) and a certain frequency ( $\omega = 1$  rad/s). A lack of overlapping of the ODT's values as shown in Figure 3-1d, for different frequencies ( $T_{\text{ODT}} = 134^\circ\text{C}$  at  $\omega = 1$  rad/s,  $T_{\text{ODT}} = 100^\circ\text{C}$  at  $\omega = 10$  rad/s and  $T_{\text{ODT}} = 123^\circ\text{C}$  at  $\omega = 100$  rad/s) implies a high contribution from the "shear heating" errors

already mentioned by Macosko<sup>156</sup> for the parallel plates geometry combined as well with the different levels of viscosity induced along the gradient of velocity axis by high angular frequencies. Figure 3-1e illustrates a comparison of the  $T_{ODT}$  values which are shifted to higher temperatures by increasing concentration at the fixed frequency of  $\omega = 100$  rad/s. In Figure 3-2 the set of storage modulus data for the solutions of ST117 is presented over a wide range of temperature and different frequencies. A remarkable fluctuation effect takes place at low frequency (1 rad/s) within a spreading of data around the order-disorder temperature without clear evidence of a certain  $T_{ODT}$ , similar like for the system ST72 at low concentrations and low angular frequency. The lowest concentration (ST117\_C1) showed a typical liquid-like behaviour illustrated by a straightforward line over a gradient of temperature  $\Delta T \sim 15^\circ\text{C}$  with a continuous decrease of moduli over almost 2 orders of magnitude. One important feature encountered for these systems is the enlargement of the terminal flow region in a temperature range of  $\Delta T \sim 58 \div 78^\circ\text{C}$  over all frequencies (Figure 3-2d). As well, the presence of a rubbery plateau has been encountered by increasing the concentration of a diblock copolymer solution like ST117\_C4 and the highest enlargement of the rubbery plateau has been achieved in the case of the system ST117\_C5. A much lower decrease of modulus as a function of temperature is seen at high concentrations (Figure 3-2d) while at low concentrations (Figure 3-2a) a stronger drop indicates that the flow process is not as much hindered as for the high concentration and thus entanglements effects have been diminished. A qualitative comparison of  $T_{ODT}$  with concentration is given in Figure 3-2e, which allowed to identify the systems in which morphological transitions could be detected (C2, C3). The  $T_{ODT}$ s at high frequency (100 rad/s) were shifted to lower temperatures as a consequence of the "shear heating" effect, and above a critical concentration (C4)  $T_{ODT}$  is increased due to the lower contribution from "shear heating" effect for high concentrations.





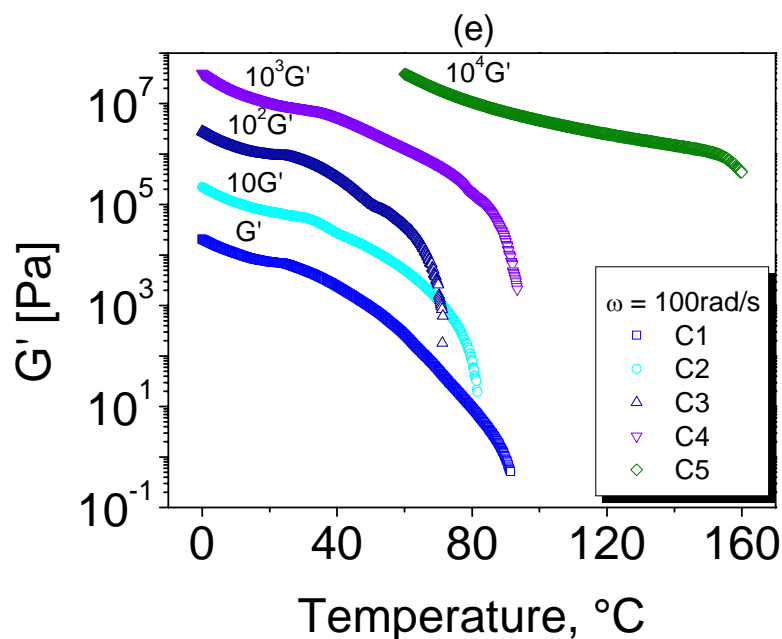


**Figure 3-2 a, b, c, d, e.** Variation of  $G'$  with temperature at  $\omega = 1, 10, 100$  rad/s for solution of ST117 at different concentrations in DOP like C1(a), C2(b), C3(c), C4(d). A comparison of  $T_{ODT}$  values at different concentrations (C1, C2, C3, C4, C5) and at fixed frequency  $\omega = 100$  rad/s, is given in Figure 3-2e.

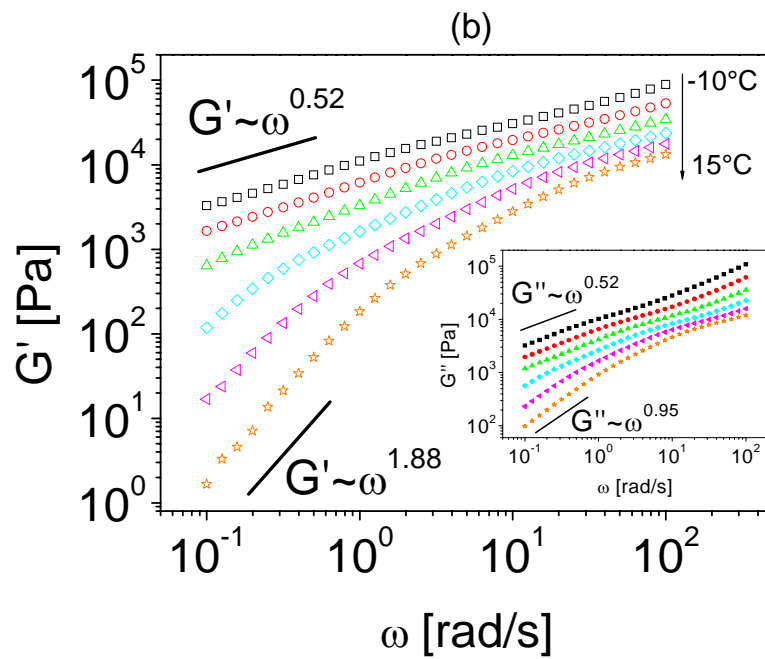
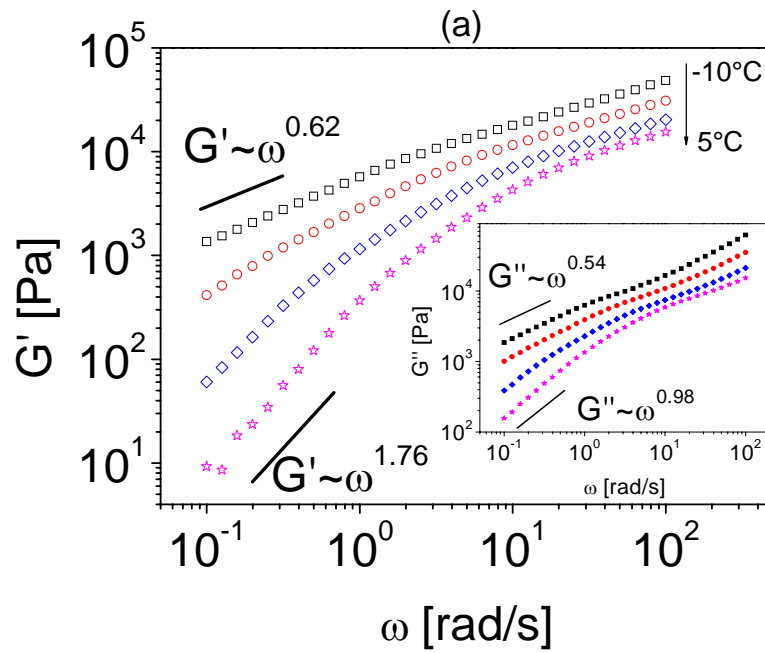
Temperature sweep experiments in oscillatory shear flow mode were not effective to determine the  $T_{ODT}$  for some of the systems (lower concentration) presented in Table 3-1 in the case of using low angular frequency. Morphological transitions have been encountered as well for the high molecular weight system ST117 within a certain range of concentrations and angular frequencies as illustrated in Figures 3-2b,c through a minimum: (i) at  $\omega = 10$  rad/s the solution ST117\_C2 undergoes a minimum in  $G'$  at ca. 40°C followed by an enhancement of modulus and the  $T_{ODT}$  is reached at 80°C; (ii) at  $\omega = 1$  rad/s the solution ST117\_C3 shows a sharp minimum around 55°C followed by two other close minima at 76°C and 80°C, respectively. According to the phase diagram for diblock copolymer melts developed by Matsen and Bates<sup>28</sup> we may assign the multiple minima in  $G'$  (Figure 3-2c) as follows: (i) the first sharp minimum (55°C) is attributed to the transition from cylindrical toward body-centered cubic (bcc) accompanied by an almost constant modulus over a temperature range of  $\Delta T \sim 10^\circ\text{C}$  (onset temperature at 59°C), as a signature of a thermodynamically stable state; (ii) gradual decreasing of moduli until reaching the slight minimum at 76°C as evidence for a transition to centered packed spheres; (iii) the next minimum more pronounced at 80°C is due

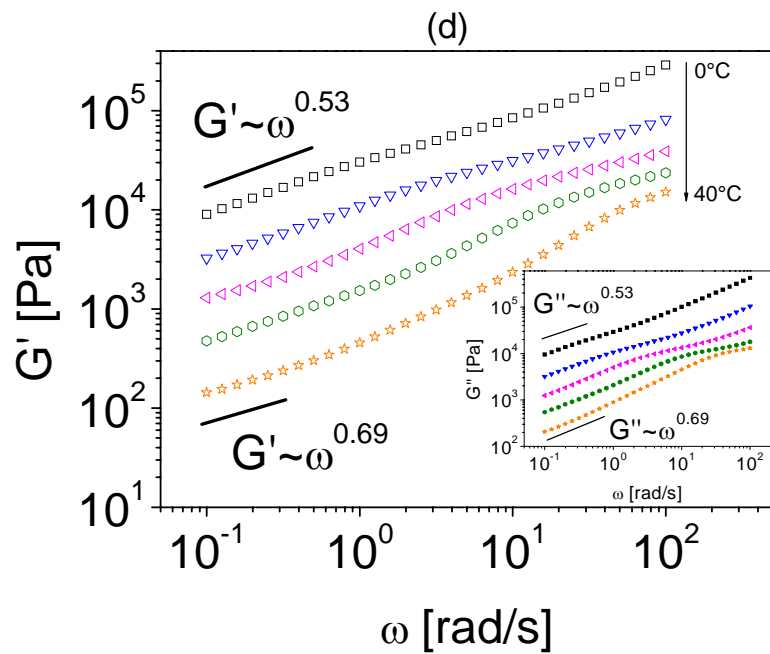
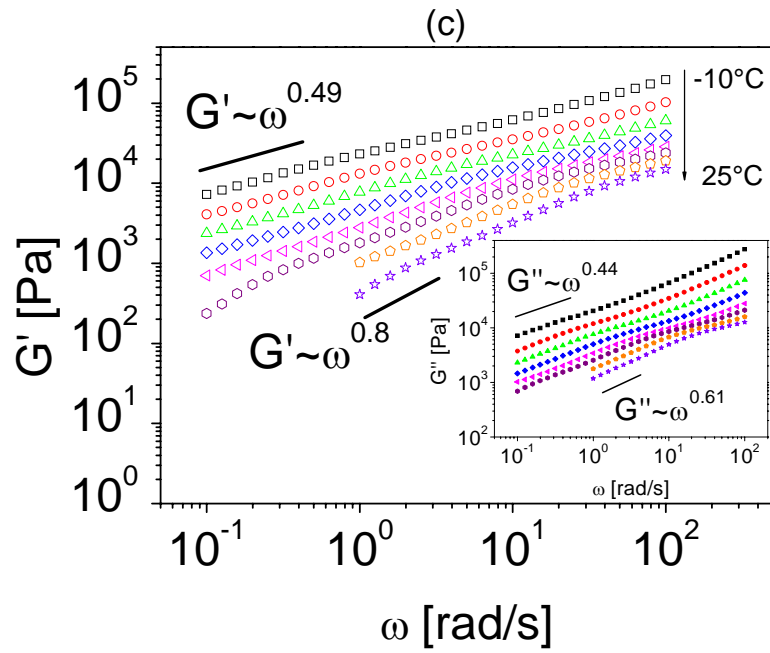
to the coexistence of both bcc and centered packed spheres. It might be that "metastable states" like OBDD (ordered bicontinuous double diamond) or HPL (hexagonal perforated layer) would be also accounted for the minima at 76°C and 80°C due to the fact that those minima are not well defined indicating thermodynamically less stable states, if the initial structure is a lamellar one. As a consequence of multiple morphological transitions (Figure 3-2c, at  $\omega = 1$  rad/s) the "apparent"  $T_{ODT}$  has been shifted to a higher temperature within a delay over a temperature range of  $\Delta T = 50\div 60^\circ\text{C}$  than the  $T_{ODT}$  at higher frequencies (10 and 100 rad/s). We may claim that the system ST117\_C3 which showed a rich behavior over the investigated temperature range at a fixed frequency  $\omega = 1$  rad/s is designed as a critical concentration, because lower and higher concentrations manifested a quite simple behavior (Figures 3-2a, d) without any significant changes in moduli.

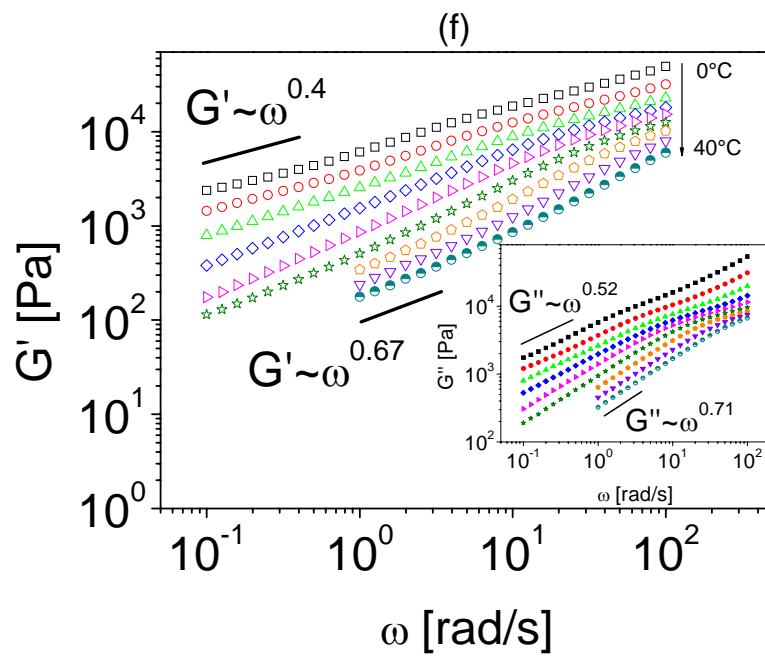
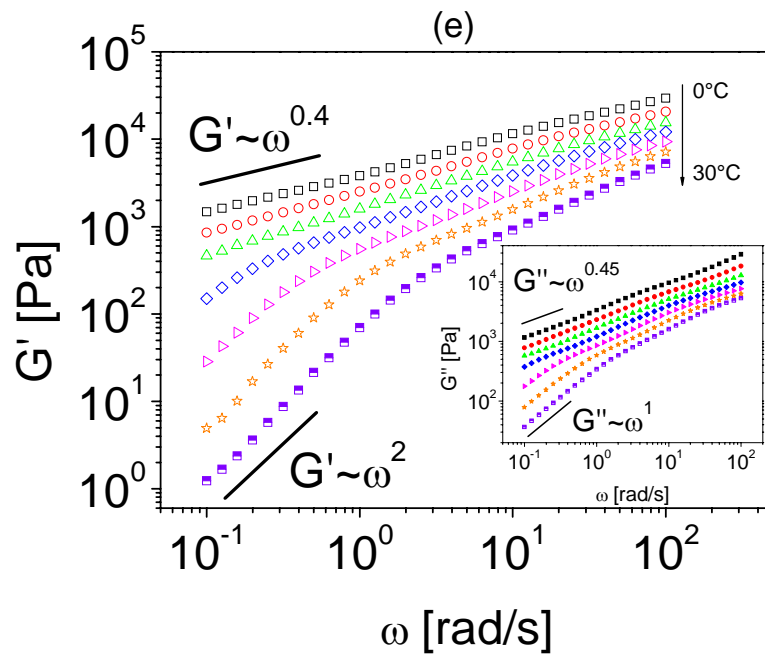
In Figure 3-2a, for the frequency  $\omega = 100$  rad/s the applied stress did not induce a stratification of levels within different viscosities along the thickness of the sample disk and no significant effect attributable to "shear heating" errors has been encountered. Thus  $T_{ODT}$  was shifted to higher temperatures with increasing frequency. Similarly, Figure 3-2d which corresponds to the higher concentration (ST117\_C4) showed the same behavior like the low concentrated system (ST117\_C1) leading to the conclusion that above and below the critical concentration (ST117\_C3) the typical behavior of a homogeneous system is manifested. The highest concentration investigated, ST117\_C5 did not show a clear  $T_{ODT}$  at  $\omega = 100$  rad/s due to the limitations of temperature with respect to thermal degradation of the specimen, giving only the indication that  $T_{ODT}$  is higher than 160°C.

### 3.2.2 Determination of order-disorder transition temperature ( $T_{ODT}$ ) from frequency sweep tests

The solutions of the two specimens of diblock copolymers ST72 and ST117 at different concentrations presented in Table 3-1 were used as well in frequency dependent shear flow measurements at various temperatures in order to determine  $T_{ODT}$ . Figures 3-3 (a), (b), (c), (d) give plots of  $\log G'$  and  $\log G''$  versus  $\log \omega$  for ST72\_S1, S2, S3 and S4 at different temperatures. In the terminal flow region at low temperatures the slope of the plots  $\log G'$  and  $\log G''$  versus  $\log \omega$  is about 0.5.







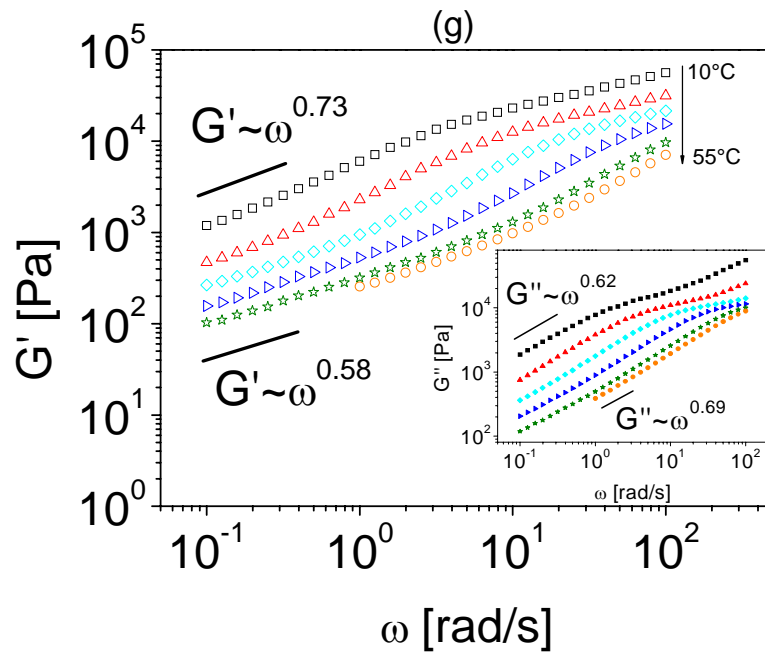


**Figure 3-3.**(a), (b), (c), (d) Plots of  $\log G'$  and  $\log G''$  versus  $\log \omega$  for ST72 at different weight concentrations in DOP S1(a), S2(b), S3(c), S4(d) by heating, at various temperatures as illustrated in the plot by the vertically arrow: (a) ( $\square$ )  $-10^\circ\text{C}$  to ( $\star$ )  $5^\circ\text{C}$  with  $\Delta T=5^\circ\text{C}$ ; (b) ( $\square$ )  $-10^\circ\text{C}$  to ( $\star$ )  $15^\circ\text{C}$  with  $\Delta T=5^\circ\text{C}$ ; (c) ( $\square$ )  $-10^\circ\text{C}$  to ( $\star$ )  $25^\circ\text{C}$  with  $\Delta T=5^\circ\text{C}$ ; (d) ( $\square$ )  $0^\circ\text{C}$  to ( $\star$ )  $40^\circ\text{C}$  with  $\Delta T=10^\circ\text{C}$ . (e), (f), (g) Plots of  $\log G'$  and  $\log G''$  versus  $\log \omega$  for ST117 at the different concentrations in DOP C1(e),C2(f),C3(g), by heating, at various temperatures: (e) ( $\square$ )  $0^\circ\text{C}$  to ( $\square$ )  $30^\circ\text{C}$  with  $\Delta T=5^\circ\text{C}$ ; (f) ( $\square$ )  $0^\circ\text{C}$  to ( $\bullet$ )  $40^\circ\text{C}$  with  $\Delta T=5^\circ\text{C}$ ; (g) ( $\square$ )  $10^\circ\text{C}$ ; to ( $\circ$ )  $55^\circ\text{C}$  with  $\Delta T=10^\circ\text{C}$ .

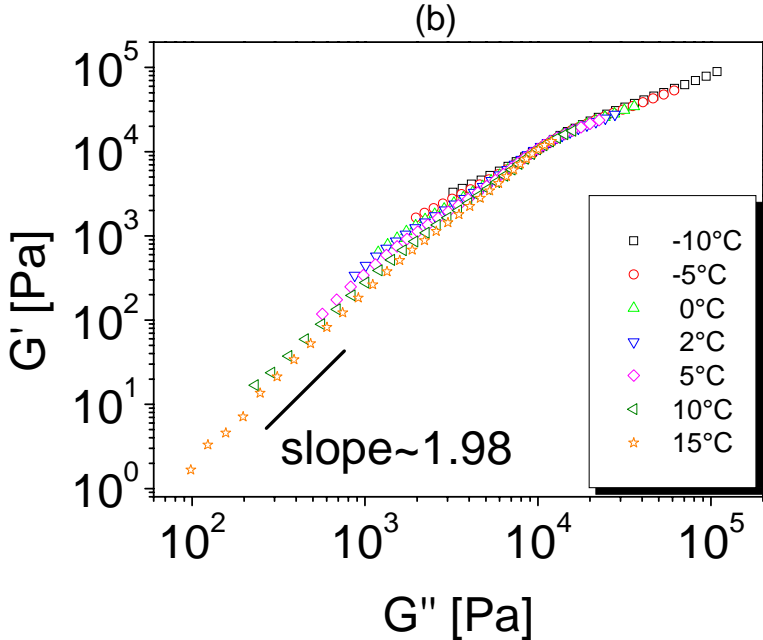
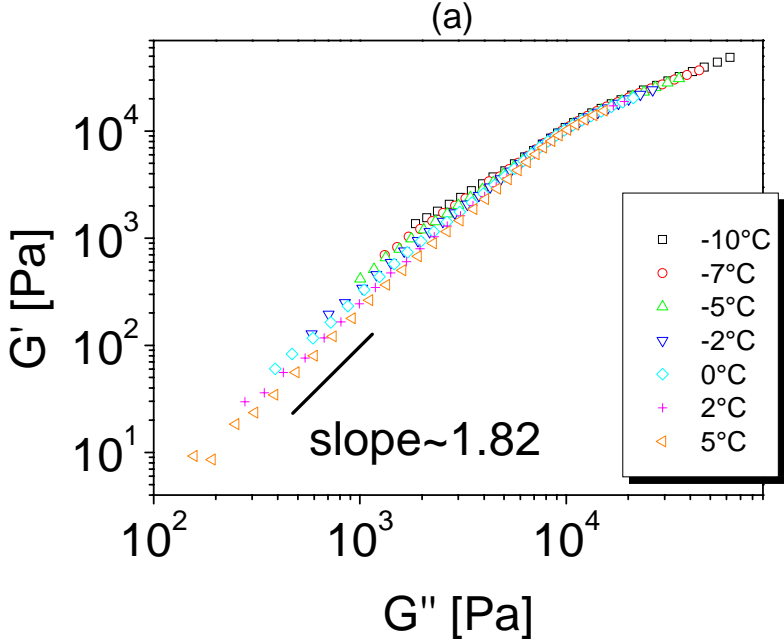
At high temperatures in the terminal flow region the slope of the plots of  $\log G'$  and  $\log G''$  versus  $\log \omega$  is about 2 and 1, typically observed for flexible homopolymers or random copolymers. In the plot of  $\log G'$  versus  $\log \omega$  a sudden displacement is observed at  $5^\circ\text{C}$  (Figure 3-3a),  $15^\circ\text{C}$  (Figure 3-3b),  $30^\circ\text{C}$  (Figure 3-3e) but no sudden displacement is observed in the plots of  $\log G''$  versus  $\log \omega$ . This observation indicates that  $G'$ , which describes the elastic property, is much more sensitive to a change in phase morphology at a certain temperature than  $G''$ , which describes the viscous property.<sup>8</sup> The temperature  $5^\circ\text{C}$  from the plot  $\log G'$  versus  $\log \omega$  for the system ST72\_S1 (Figure 3-3a) at which a sudden displacement occurred within the slope of about 1.76 is in disagreement with the value ( $\sim 40^\circ\text{C}$  at 100 rad/s) at which there is a drop in the storage modulus from the plot  $\log G'$  versus

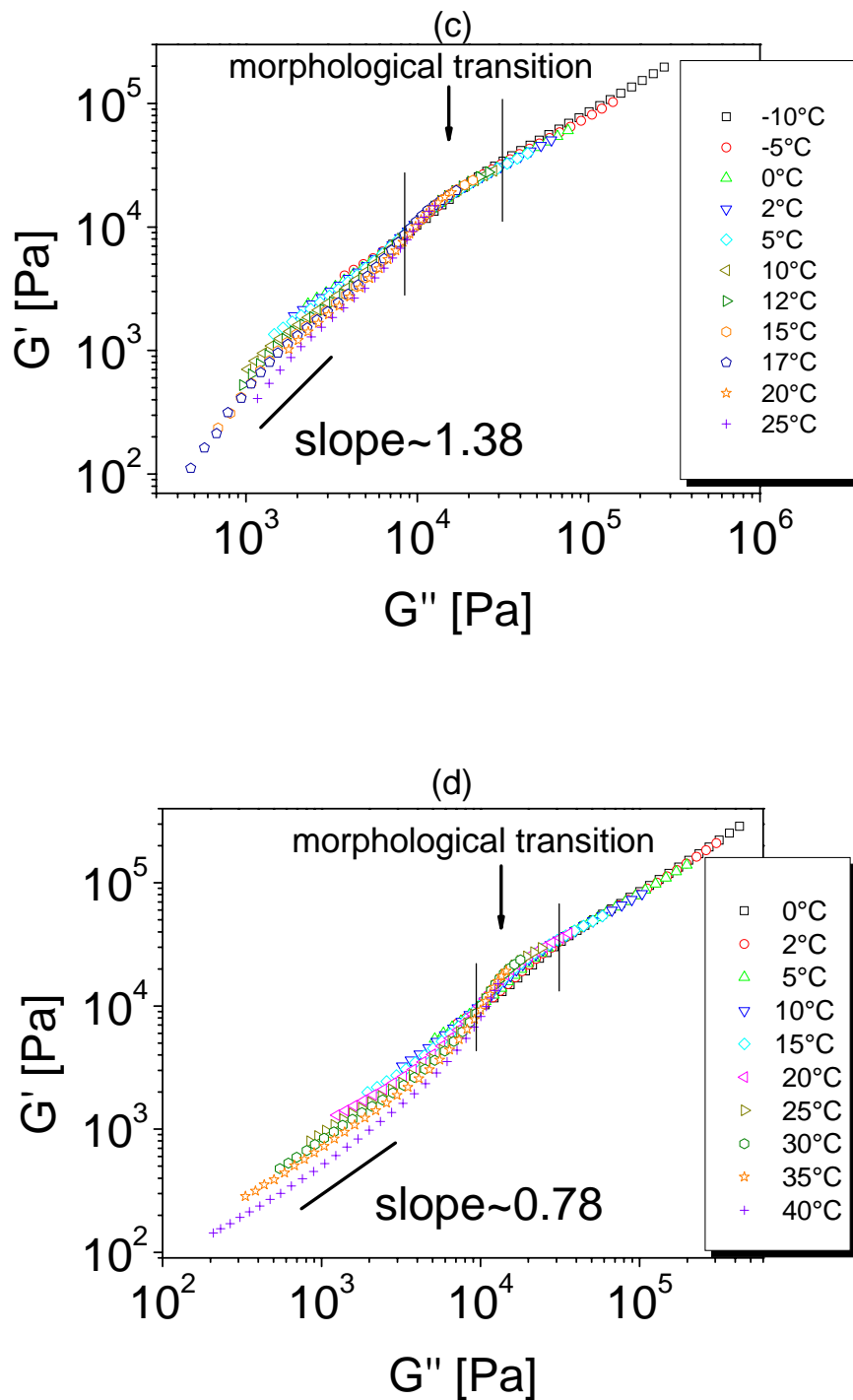
temperature (Figure 3-1a). While for the low concentrated solutions like the systems ST72\_S1, ST72\_S2 (Figure 3-3a, b) the frequency sweep tests showed a continuous increase in the slope from 0.5 at low temperatures toward the values closer to 2 at high temperatures, this was not the case for the systems ST72\_S3, ST72\_S4 (Figure 3-3c, d) for which the values of slope were slightly changed remaining within a power law dependence  $G' \sim \omega^{0.5 \div 0.8}$  and  $G'' \sim \omega^{0.5 \div 0.7}$ , respectively. A remarkable change in the slope by increasing temperature from 5°C to 10°C has been observed in the case of ST72\_S2 (Figure 3-3b) as a proof of increasing solubility of the polystyrene block in DOP, which is a  $\Theta$  solvent for polystyrene with the  $\Theta$  temperature,  $T_{\Theta} \sim 7^{\circ}\text{C}$ .<sup>157</sup> As for the systems ST72\_S3, ST72\_S4 where no significant changes in the slope have been encountered, similar behavior was found for ST117\_C2 over a gradient of temperature  $\Delta T = 40^{\circ}\text{C}$  within a power law dependence  $G' \sim \omega^{0.4 \div 0.67}$ . Moreover, an unusual decrease in the slope from 0.73 to 0.57 by raising the temperature from 10°C to 25°C followed by a slow increase was encountered for the system ST117\_C3 (Figure 3-3g) which might indicate the existence of a morphological transition induced by raising the temperature within a certain concentration. Because the frequency sweep tests were performed at temperatures above  $\Theta$  temperature of polystyrene in DOP, in the case of ST117\_C3, the adopted morphology of ST117 in DOP is changing with temperature before attaining the disordered state. Our assumption of a cylindrical morphology is illustrated (Figure 3-3g) by the decrease of slope in two steps: (1) from slope  $\sim 0.78$  at 20°C to slope  $\sim 0.57$  at 25°C, (2) from slope  $\sim 0.63$  at 45°C to slope  $\sim 0.58$  at 55°C.

### 3.2.3 Determination of order-disorder transition temperature ( $T_{\text{ODT}}$ ) using plots of $\log G'$ versus $\log G''$

Using the same rheological data as in Figure 3-3, in Figures 3-4a,b,c,d the plots of  $\log G'$  versus  $\log G''$  for ST72\_S1, S2, S3, S4 are presented. It can be seen from such plots that  $\log G'$  versus  $\log G''$  becomes independent of temperature at  $\geq 5^{\circ}\text{C}$  for ST72\_S1 and at  $\geq 15^{\circ}\text{C}$  for ST72\_S2. By raising the temperature (Figure 3-4a, b) a large displacement is seen in the plot  $\log G'$  versus  $\log G''$ , while at 5°C and 15°C, respectively the slope is close to the value 2, which is typical for homopolymers in the bulk state in the terminal flow region. Following the plot  $\log G'$  versus  $\log G''$ , we can conclude that  $T_{\text{ODT}}$  is about 15°C in the case of ST72\_S2, a value which is in agreement with the one determined from the plot  $\log G'$  versus  $\omega$ . In the temperature sweep experiments the abrupt change in the slope of the plot  $\log G'$  versus temperature (Figure 3-1a) is about  $0 \div 5^{\circ}\text{C}$  for the lower concentrated system ST72\_S1

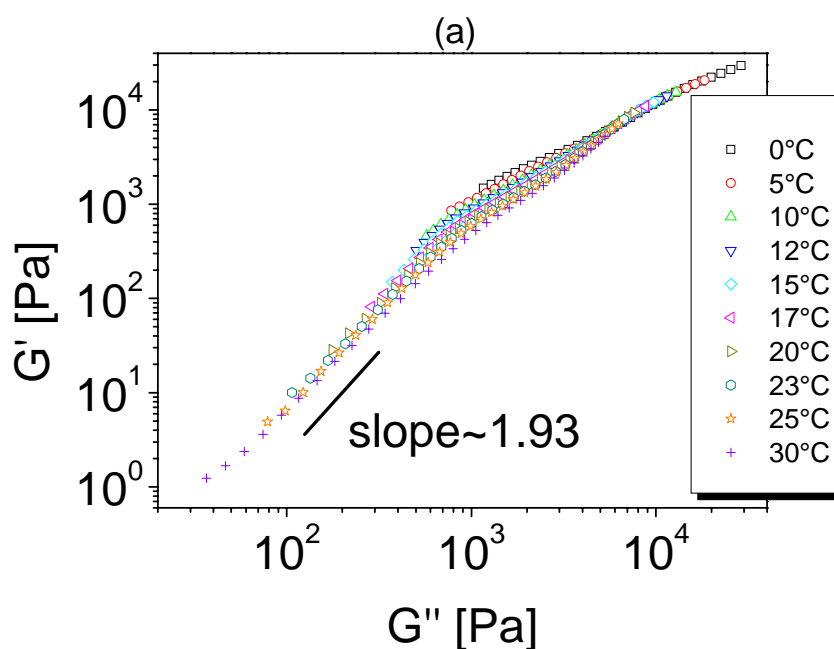
followed by a gradually decreasing of moduli at  $T > 5^\circ\text{C}$ , instead from the plot  $\log G'$  versus  $\log G''$  a slope of 1.82 (close to 2) at  $5^\circ\text{C}$  indicates a disordered state around  $5^\circ\text{C}$ . This is a large difference and this cannot be explained by limitations in experimental accuracy. Within increasing concentration in the series ST72\_S3, S4 from the plot  $\log G'$  versus  $\log G''$  the slope in the terminal flow region decreases from 1.38 (ST72\_S3) to 0.78 (ST72\_S4) which is a clear indication of ordered systems. The curves starting with  $-2^\circ\text{C}$  (Figure 3-4a) and  $2^\circ\text{C}$  (Figure 3-4b) are displaced upward from the other curves at higher temperatures ( $5^\circ\text{C}$ ,  $15^\circ\text{C}$ ) and lie together. Previously, similar observations were noted by Bates and coworkers<sup>149</sup> who investigated  $T_{\text{ODT}}$  of 1,2-polybutadiene-*b*-1,4-polybutadiene (1,2PB-*b*-1,4PB) copolymers and by Rosedale<sup>41</sup> who investigated the  $T_{\text{ODT}}$  of poly(ethylenepropylene)-*b*-poly(ethylethylene) (PEP-*b*-PEE) copolymers. This behavior may be due to the composition fluctuations starting at those temperatures. A prominent upward displacement of the overlapped curves (Figures 3-4c, d) illustrated by a "moduli loop" (Figure 3-4d) is correlated with the morphological transitions. From Figure 3-4d we might conclude that the upward displacement of the curve starting with  $15^\circ\text{C}$  suggests a lattice disordering/ordering transition (LDOT) before attaining the disordered state ( $T_{\text{ODT}}$ ) within the corresponding slope of 0.53 at  $15^\circ\text{C}$  from frequency sweep test followed by a 0.47 slope at  $25^\circ\text{C}$ . Such a LDOT could indicate that the swollen system ST72\_S4 has changed the initial morphology from lamellae ( $S_{48}T_{52}$ <sup>72</sup> bulk) to a cylindrical phase (in swollen state) and then toward a spherical morphology due to the selectivity of DOP for the poly(*t*-butyl methacrylate) block. The typical behavior of the plot  $\log G'$  vs  $\log G''$  as reported by Hashimoto<sup>55</sup> for symmetric SI diblock and SIS triblock copolymers without large displacements upward of the curves at different temperatures, is not found for our systems, ST72 and ST117 swollen in DOP as a consequence of asymmetry due to the selective swelling of the blocks. Previous work<sup>158,159</sup> on polystyrene solutions in dioctyl phthalate suggested demixing of such polymer solutions in flow fields and separation into two phases of different concentration. Helfand and Fredrickson<sup>160</sup> described solution turbidity as a result of stress-enhanced fluctuations of concentration. The "butterfly" light scattering patterns predicted by theories were observed by Wu et al.<sup>161</sup> which have been interpreted as evidence for phase separation. The "two-fluid" theory applied to experimental results<sup>162</sup> on the rheology and turbidity measurements on solutions of polystyrene in DOP indicates the occurrence of phase separation. So far, by accounting the previous mentioned aspects within our rheological data on swollen ST diblock copolymers (ST72, ST117) we might conclude that the polystyrene block adopts a cylindrical morphology in a matrix of poly(*t*-butyl methacrylate).

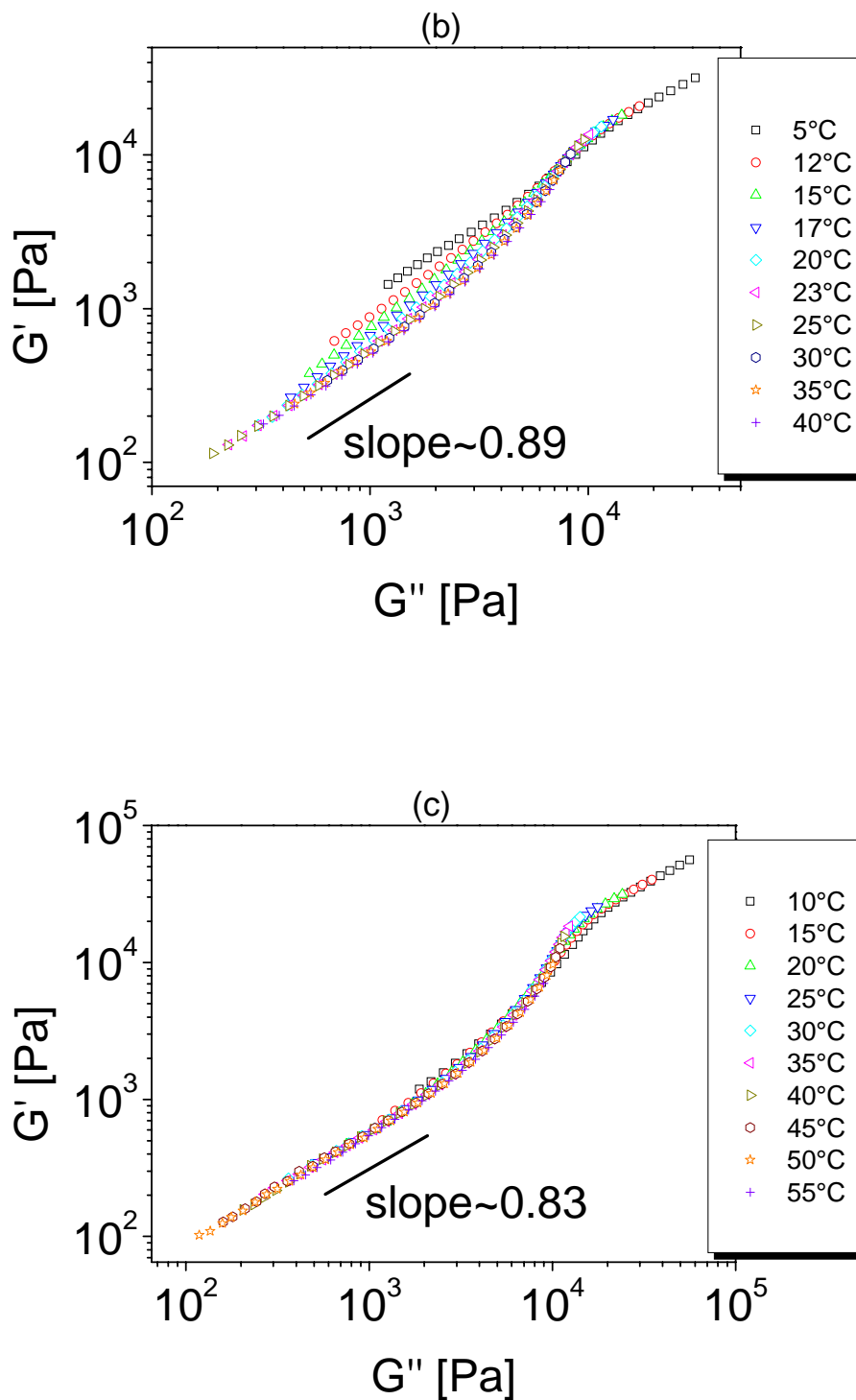




**Figure 3-4a,b,c,d.** Plots of  $\log G'$  versus  $\log G''$  by heating for ST72\_S1(a), S2(b), S3(c), S4(d) wt-% in DOP, at various temperatures: (a) ( $\square$ ) -10°C; ( $\circ$ ) -7°C; ( $\triangle$ ) -5°C; ( $\nabla$ ) -2°C; ( $\diamond$ ) 0°C; ( $+$ ) 2°C; ( $\triangleleft$ ) 5°C; (b) ( $\square$ ) -10°C; ( $\circ$ ) -5°C; ( $\triangle$ ) 0°C; ( $\nabla$ ) 2°C; ( $\diamond$ ) 5°C; ( $\triangleleft$ ) 10°C; ( $\star$ ) 15°C; (c) ( $\square$ ) -10°C; ( $\circ$ ) -5°C; ( $\triangle$ ) 0°C; ( $\nabla$ ) 2°C; ( $\diamond$ ) 5°C; ( $\triangleleft$ ) 10°C; ( $\triangleright$ ) 12°C; ( $\circ$ ) 15°C; ( $\square$ ) 17°C; ( $\star$ ) 20°C; ( $+$ ) 25°C; (d) ( $\square$ ) 0°C; ( $\circ$ ) 2°C; ( $\triangle$ ) 5°C; ( $\nabla$ ) 10°C; ( $\diamond$ ) 15°C; ( $\triangleleft$ ) 20°C; ( $\triangleright$ ) 25°C; ( $\circ$ ) 30°C; ( $\star$ ) 35°C; ( $+$ ) 40°C.

The plots of  $\log G'$  vs  $\log G''$  for the higher molecular weight block copolymer ST117 at different concentrations are presented in Figure 3-5. A slope of 1.93 for the system ST117\_C1 (Figure 3-5a), determined in the terminal flow region suggested a disordered state at 30°C, while solutions with higher concentration like ST117\_C2 (Figure 3-5b) showed a slope of 0.98 at 40°C as an evidence of an ordered state. Morphological transitions (upward displacement of the overlapped curves) are clearly present in the case of ST117\_C3 (Figure 3-5c) and take place within the temperature range of 20÷45°C as it is also evidenced through the slope values from the frequency sweep tests, reaching a slope value of 0.83 at higher temperatures (Figure 3-5c) without attaining the disordered state.

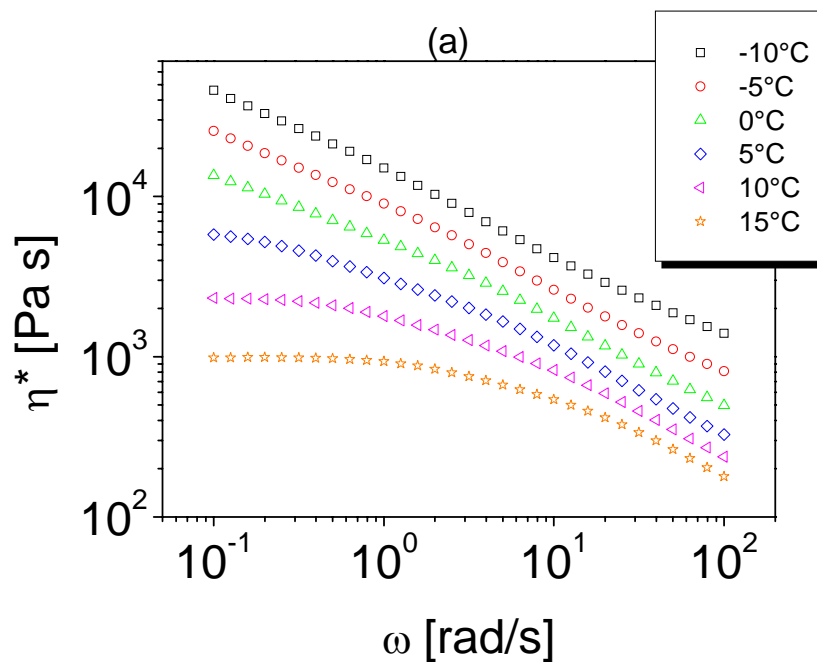




**Figure 3-5a,b,c.** Plots of  $\log G'$  versus  $\log G''$  by heating for ST117\_C1 (a), C2 (b), C3 (c) wt-% in DOP, at various temperatures: (a) ( $\square$ ) 0°C; ( $\circ$ ) 5°C; ( $\triangle$ ) 10°C; ( $\nabla$ ) 12°C; ( $\diamond$ ) 15°C; ( $\triangleleft$ ) 17°C; ( $\triangleright$ ) 20°C; ( $\odot$ ) 23°C; ( $\star$ ) 25°C; ( $+$ ) 30°C; (b) ( $\square$ ) 5°C; ( $\circ$ ) 12°C; ( $\triangle$ ) 15°C; ( $\nabla$ ) 17°C; ( $\diamond$ ) 20°C; ( $\triangleleft$ ) 23°C; ( $\triangleright$ ) 25°C; ( $\odot$ ) 30°C; ( $\star$ ) 35°C; ( $+$ ) 40°C; (c) ( $\square$ ) 10°C; ( $\circ$ ) 15°C; ( $\triangle$ ) 20°C; ( $\nabla$ ) 25°C; ( $\diamond$ ) 30°C; ( $\triangleleft$ ) 35°C; ( $\triangleright$ ) 40°C; ( $\odot$ ) 45°C; ( $\star$ ) 50°C; ( $+$ ) 55°C.

### 3.2.4 Determination of order-disorder transition temperature ( $T_{ODT}$ ) using $\log|\eta^*|$ versus $\log\omega$

The values of  $|\eta^*|$  were calculated using the equation  $|\eta^*| = \left[ (G'/\omega)^2 + (G''/\omega)^2 \right]^{1/2}$ , and some plots are given in Figure 3-6. In such plots it is seen that at low values of  $\omega$  and temperature below a certain critical value a yield behavior is exhibited, which is observed as well in concentrated suspensions and molten polymers. By increasing the temperature above a critical value a Newtonian behavior occurs, which indicates a phase transition from an ordered state to the disordered state. From the plot  $\log|\eta^*|$  versus  $\log\omega$  this transition to the disordered state can be distinguished, which begins at a temperature of about  $10^\circ\text{C}$  (Figure 3-6a).  $T_{ODT}$  determined from the plot  $\log|\eta^*|$  versus  $\log\omega$  is in good agreement with the one determined from the plots  $\log G'$  versus  $\log G''$ , and  $\log G'$  versus  $\log\omega$  within experimental uncertainties. By raising the concentration of the system (ST72\_S3) it was not possible to determine  $T_{ODT}$  by using this plot (Figure 3-6b).



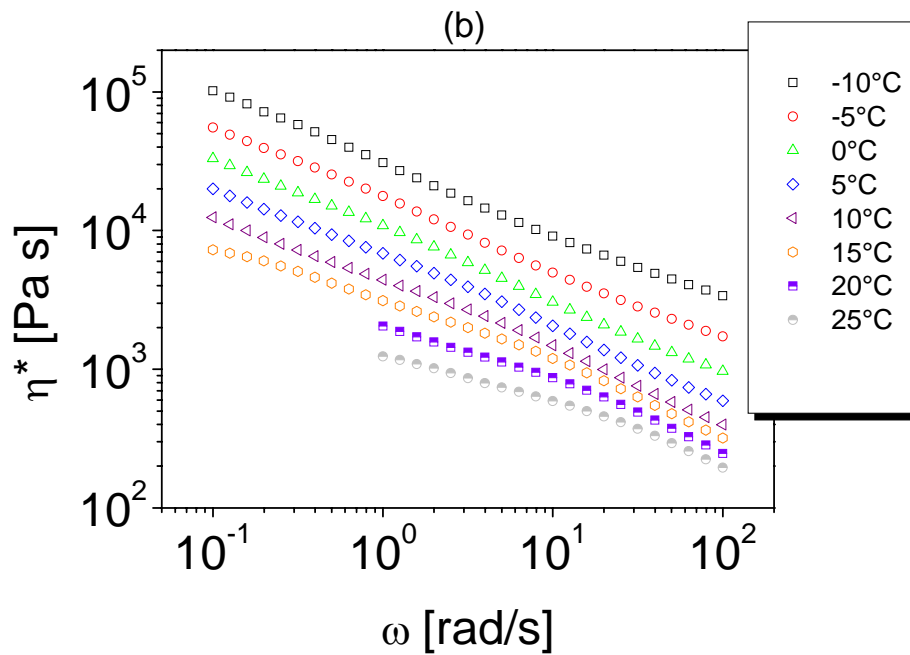


**Figure 3-6.** Plots of  $\log |\eta^*|$  versus  $\log \omega$  for (a) ST72\_S2 wt-% in DOP and (b) ST72\_S3 wt-% in DOP, by heating, at various temperatures: (a): ( $\square$ )  $-10^\circ\text{C}$ ; ( $\circ$ )  $-5^\circ\text{C}$ ; ( $\triangle$ )  $0^\circ\text{C}$ ; ( $\diamond$ )  $5^\circ\text{C}$ ; ( $\nabla$ )  $10^\circ\text{C}$ ; ( $\star$ )  $15^\circ\text{C}$ ; (b): ( $\square$ )  $-10^\circ\text{C}$ ; ( $\circ$ )  $-5^\circ\text{C}$ ; ( $\triangle$ )  $0^\circ\text{C}$ ; ( $\diamond$ )  $5^\circ\text{C}$ ; ( $\nabla$ )  $10^\circ\text{C}$ ; ( $\circ$ )  $15^\circ\text{C}$ ; ( $\square$ )  $20^\circ\text{C}$ ; ( $\circ$ )  $25^\circ\text{C}$ .

### 3.2.5 Time-temperature superposition principle applied to block copolymer solutions

Many investigators<sup>41,53,148,149,163-165</sup> have applied the time-temperature superposition (TTS) principle<sup>166</sup> to block copolymers. From a rheological point of view, microphase-separated block copolymers should be regarded as being a different material at different temperatures. By increasing temperature the compatibility between the two blocks in a given diblock copolymer is increased before reaching  $T_{\text{ODT}}$ . The frequency-dependent viscoelastic properties for our solutions are illustrated in Figure 3-7. These reduced frequency plots were obtained using the time-temperature superposition principle by 2D-shifting with different reference temperatures. Time-temperature superposition worked well as illustrated in Figures 3-7a, 3-8c within the range of temperatures employed while for the other cases the critical frequencies  $\omega_C'$ ,  $\omega_C''$ ,  $\omega_d$  and the corresponding ordered-disordered states were defined as

well. Due to the instrumental limitations (Torque  $\sim 0.2\div 200$  g cm ) of the ARES instrument, the measurements were performed in a very low temperature range within the linear viscoelastic regime and thus the obtained master curves were shifted in the range of low frequency ( $\sim 10^{-5}$  rad/s). As reference temperatures for each of the master curves the lowest temperature corresponding to the set of data were taken for which a measurable torque was obtained. A Newtonian region ( $\eta^*$  vs  $a_T\omega$ ) has been found for ST72\_S1 in the low range of frequency as illustrated by the master curve in Figure 3-7a and a good agreement within time-temperature superposition principle was achieved. Typical terminal flow behavior of  $G' \sim \omega^2$  and  $G'' \sim \omega$  found for homopolymers, is almost also encountered in the master curve (Figure 3-7a) for ST72\_S1, in the range of low reduced frequency, with  $G' \sim \omega^{1.73}$  and  $G'' \sim \omega^{0.92}$ .

The dynamic mechanical properties of ST117\_C3 can be well described by TTS as well, which lead us to treat these systems similar like flexible homopolymers. We thus calculated a plateau modulus,  $G_N^0$ , for the above mentioned systems and compared these values with the literature<sup>166,167</sup> data corresponding to pure homopolymers (polystyrene, poly(alkyl methacrylates)) and copolymers (Table 3-2). The presence of entanglements seems to be an essential requirement for a polymeric system to exhibit a plateau modulus and the inverse relationship between plateau modulus and molecular weight between entanglements,  $M_e$ , is :  $G_N^0 = c\rho RT / M_e$  where  $\rho$  is the polymer density under test conditions,  $R$  is the universal gas constant,  $T$  is the temperature,  $c$  is the polymer concentration. When the viscosity of a pure polymer measured in the molten state is plotted against the molecular weight,  $M$ , in log-log scale a break in the curve is observed at the point where the molecular weight dependence of the viscosity changes over a narrow range from dependence of  $\eta \propto M^1$  to a dependence of  $\eta \propto M^{3.4}$ . The molecular weight at which the break in the curve occurs is the characteristic molecular weight for entanglement,  $M_C$ , which has been observed as well in solutions. The results obtained in solution and in the melt indicate that  $(cM)_C = M_C$ , where  $c$  is the concentration<sup>168</sup>. It was found<sup>169</sup> that the ratio  $M_C / M_e$  is about 2, therefore an approximate value of  $G_N^0$  can be calculated from the known  $M_C$ . Upon these considerations, for ST72\_S1 were determined the following values:  $\log(cM)_C \sim 4.26$  and  $G_N^0 \sim 5.58 \times 10^4$  Pa .

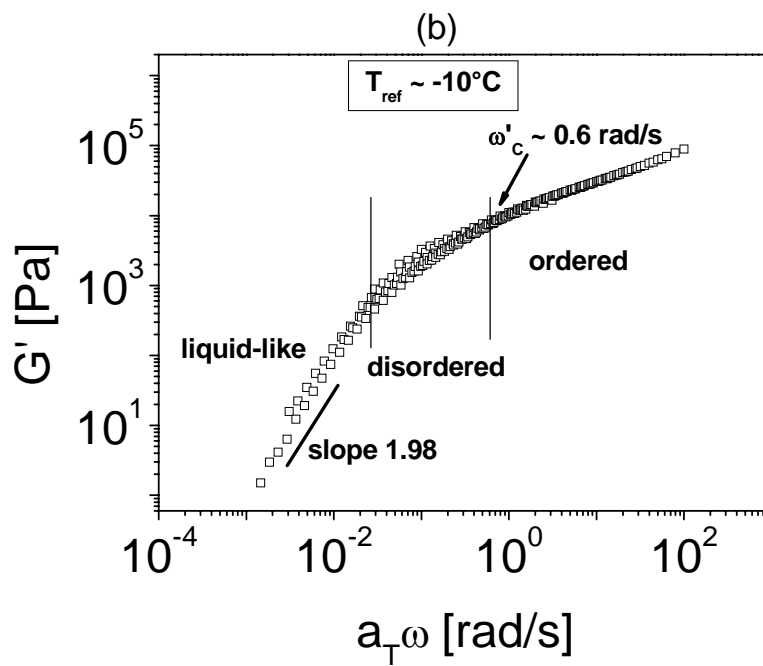
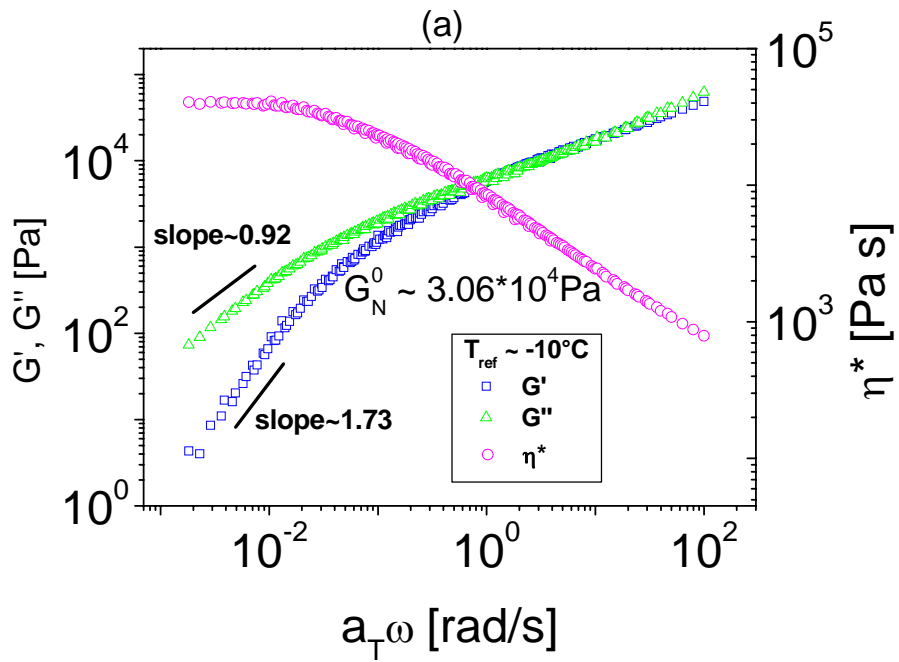
Sample	$G_N^{experimental, 0}, Pa$
ST72_S1 ( $M_c \sim 18197$ )	$3.06 \times 10^4$ (calculated $\sim 5.58 \times 10^4$ )
ST117_C3	$9.32 \times 10^4$
*Polystyrene ( $M_c \sim 35000$ )	$20 \times 10^4$
*Poly(methyl methacrylate) ( $M_c \sim 31530$ )	$62 \times 10^4$
*Poly( <i>n</i> -butyl methacrylate) ( $M_c \sim 60435$ )	$22 \times 10^4$
**Styrene-butadiene(random copolymer) at 25°C ( $M_e \sim 3000$ )	$10 \times 10^{4.89}$

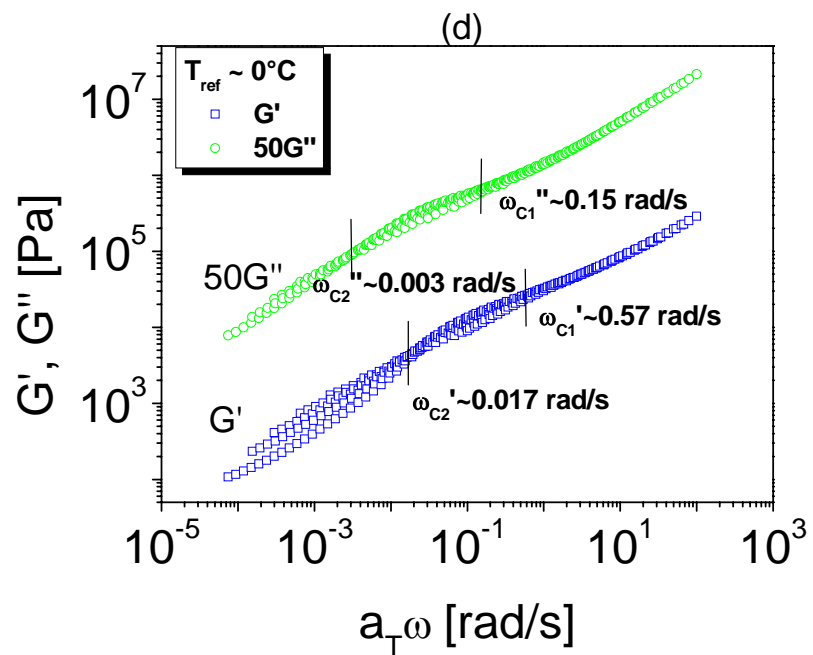
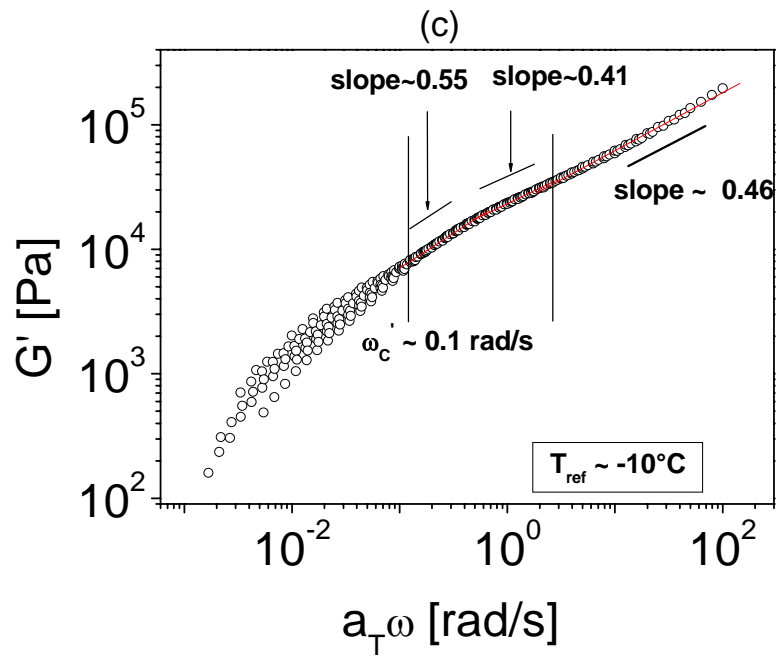
\* Values from literature<sup>167</sup> data corresponding to the melt state. For the ST72\_S1 a theoretical estimation of the plateau modulus has been made as illustrated by the value between brackets, within a good agreement with the experimental value determined from the master curve.

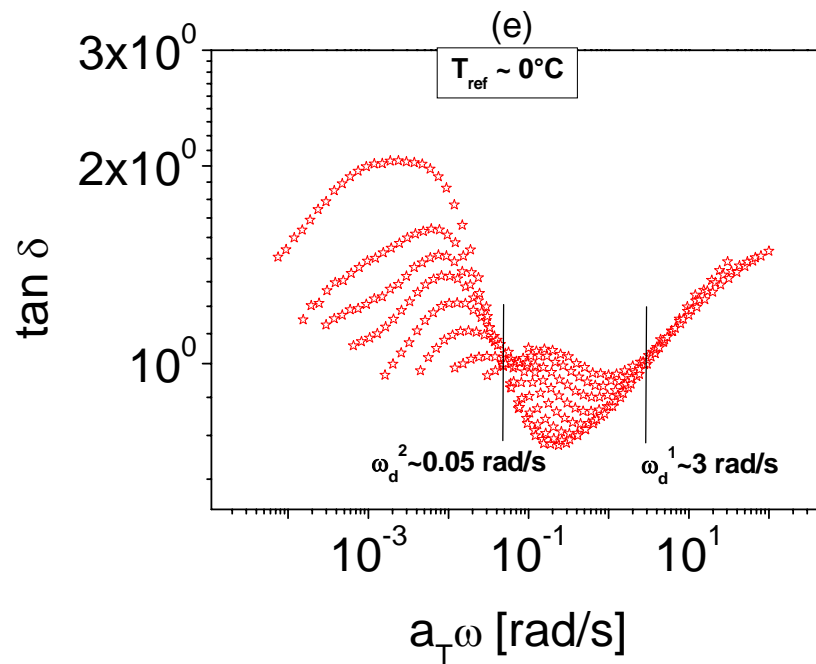
\*\* ref.<sup>166</sup>

**Table 3-2.** Comparison of plateau modulus of block copolymer solutions with the plateau modulus of homopolymers and copolymers melts.

For the ST72\_S2wt-% in DOP the master curve of the storage modulus (Figure 3-7b) indicates an approximately reduced critical frequency,  $\omega_c' \sim 0.6 \text{ rad/s}$ , above this value it shows clearly the ordered state and below the disordered state toward liquid-like behavior with a slope of 1.98. At higher concentrations like ST72\_S3, S4, an unusual behavior of the master curve was found as seen in Figures 3-7c, d. Within the range of reduced frequency an enlargement of the ordered state is achieved illustrated by shifting of the critical frequency from  $\omega_c' \sim 0.6 \text{ rad/s}$  corresponding to lower concentration (ST72\_S2) to  $\omega_c' \sim 0.1 \text{ rad/s}$  (ST72\_S3) and a decrease in the slope from 0.46 to 0.41, followed by a slight increase to 0.55 (Figure 3-7c) is observed, which is an evidence for a morphological transition.

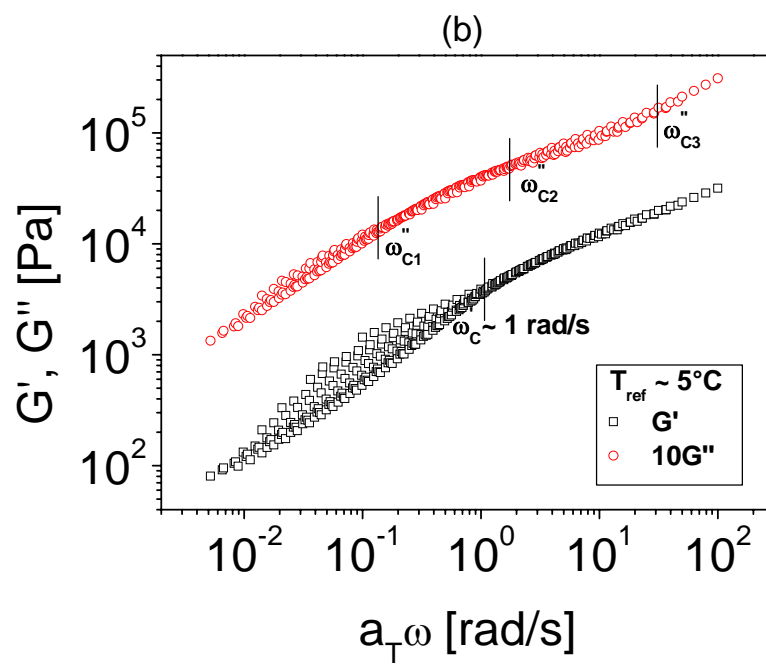
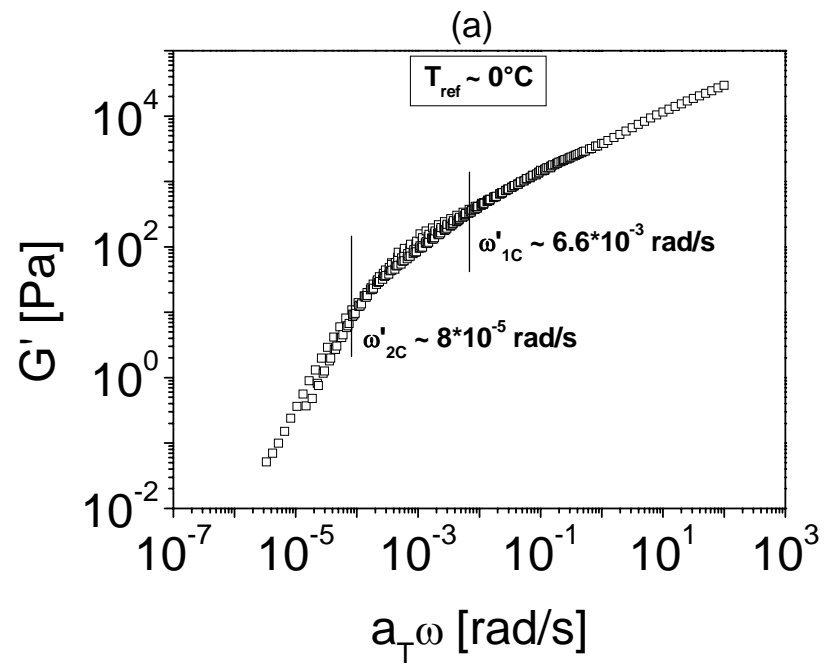






**Figure 3-7a,b,c,d,e.** Master curves for solutions of diblock copolymer ST72\_S1(a), S2(b), S3(c), S4(d, e), wt-% in DOP. (a): ( $\square$ ) $G'$ , ( $\triangle$ ) $G''$ , ( $\circ$ ) $\eta^*$  at  $T_{\text{ref}} \sim -10^\circ\text{C}$ ; (b) ( $\square$ ) $G'$  at  $T_{\text{ref}} \sim -10^\circ\text{C}$ ; (c) ( $\circ$ )  $G'$  at  $T_{\text{ref}} \sim -10^\circ\text{C}$ ; (d) ( $\square$ ) $G'$ , ( $\circ$ ) $50G''$  at  $T_{\text{ref}} \sim 0^\circ\text{C}$ ; (e) ( $\star$ ) $\tan \delta$  at  $T_{\text{ref}} \sim 0^\circ\text{C}$ .

Moreover, the evidence of an ordered state enclosed by a range of critical frequencies,  $\omega_c'(G') \sim 0.017 \div 0.57 \text{ rad/s}$ ,  $\omega_c''(G'') \sim 0.003 \div 0.15 \text{ rad/s}$ ,  $\omega_d(\tan \delta) \sim 0.05 \div 3 \text{ rad/s}$  within a region of decreasing slope upon raising temperature is illustrated in Figures 3-7d,e for ST72\_S4. A so called "moduli-loop" evidenced the morphological transition from cylindrical to spheres morphology before attaining disordered state.



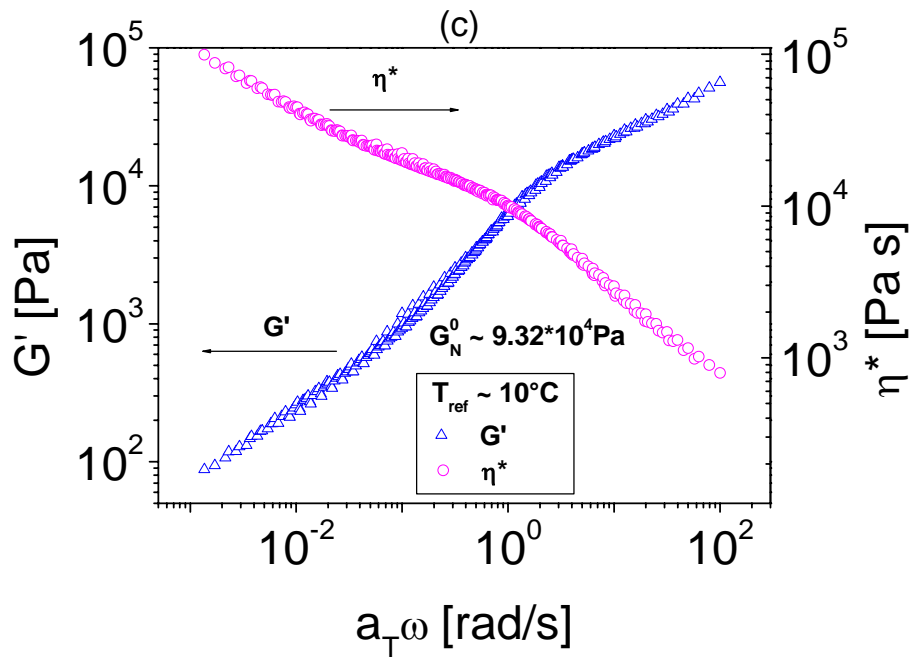


**Figure 3-8a,b,c.** Master curves for the solutions of diblock copolymer ST117\_C1(a), C2(b), C3(c). (a) ( $\square$ ) $G'$  at  $T_{\text{ref}} \sim 0^\circ\text{C}$ ; (b) ( $\square$ ) $G'$ , ( $\circ$ ) $10G''$  at  $T_{\text{ref}} \sim 5^\circ\text{C}$ ; (c) ( $\triangle$ ) $G'$ , ( $\circ$ ) $\eta^*$  at  $T_{\text{ref}} \sim 10^\circ\text{C}$ .

Further investigations were made as well on the system ST117 at different concentrations, and the corresponding master curves are presented in Figures 3-8a,b,c. The ordered state is encountered until a minimum critical frequency,  $\omega_{1c}'(G') \sim 6.6 \times 10^{-3} \text{ rad/s}$ , followed by the disordered state until  $\omega_{2c}'(G') \sim 8 \times 10^{-5} \text{ rad/s}$  toward liquid-like behavior with a slope  $\sim 2$  (Figure 3-8a). The evidence of multiple crossovers of the loss moduli (Figure 3-8b) by increasing the temperature while the slope varies within the range  $0.52 \div 0.7$  over a gradient of temperature  $\Delta T \sim 40^\circ\text{C}$ , clearly indicates the transition from one ordered state (cylindrical) to another ordered state (spherical) without any indication of a disordering state ( $G' \sim 10^2 \text{ Pa}$ , torque  $\sim 0.2 \text{ g cm}$  at  $\omega \sim 0.1 \text{ rad/s}$  and  $T \sim 40^\circ\text{C}$ ). Instead, at higher concentration (ST117\_C3) a good agreement within time-temperature superposition principle has been obtained (Figure 3-8c) illustrating a typical homopolymer behavior. The features of the master curves presented in Figures 3-7, 3-8 within a different concentration regime together with the results presented in Figures 3-1, 3-2 lead us to conclude that morphological transitions take place at a certain concentration, defined for the two systems as follows: S4  $\sim 35\text{wt-\%ST72}$  ( $G'$  versus temperature and  $G'$  versus  $a_T\omega$ , respectively) and C2  $\sim 26\%$ , C3  $\sim 27\%$  ( $G'$  versus temperature), C2  $\sim 26\text{wt-\%ST117}$  ( $G'$  versus  $a_T\omega$ ).

The time-temperature superposition as it is classically applied to simple fluids assumes that the changes in temperature affect all relaxation times in the same way. For ordered systems such as microphase-separated block copolymers, this may not be the case. As it was already shown by Fesko and Tschoegl<sup>170</sup> for SBS triblock copolymer, master curves were valid only above and below the  $T_g$ 's of both blocks. Although the use of time-temperature superposition on rheologically complex materials such as block copolymers is not rigorously correct, this method is useful in comparing the qualitative changes that occur at low frequencies near the microphase separation transition.

### 3.2.6 Comparison of experimental $T_{ODT}$ with theoretical predictions

The location of the microphase separation transition (MST) is predicted to depend on the composition,  $f$ , the Flory-Huggins interaction parameter,  $\chi$ , and the degree of polymerization,  $N$ .<sup>145,24,12</sup> For a lamellar, symmetric system it is given as

$$(\chi N)_{MST} = 10.495 + 43.16\bar{N}^{-1/3} \quad (3-1)$$

with

$$\bar{N} = (a^6 / v^2)N \quad (3-2)$$

where  $a$  and  $v$  are the statistical segment length and volume, respectively. The constant term from eq 3-1 corresponds to Leibler's theory while the term  $\bar{N}^{-1/3}$  is the fluctuation correction necessary for finite chain lengths.<sup>26</sup> In general, the segment-segment interaction parameter<sup>41</sup> is linear with inverse temperature, as illustrated in the eq 3-3 and

$$\chi = AT^{-1} + B \quad (3-3)$$

our attempt is to determine the coefficients  $A$ ,  $B$  for the nearly symmetric diblock copolymer  $S_{48}T_{52}$ <sup>72</sup> in solution, respectively. Firstly, calculations to determine theoretically  $T_{ODT}$  are made for the bulk diblock copolymer using eq 3-4 (as a rough estimation due to the close solubility parameters between polyisoprene and poly(*t*-butyl methacrylate)), which was used for the polystyrene-*b*-polyisoprene.<sup>56</sup>

$$\chi_{MST} = -0.0419 + \frac{39}{T_{ODT}} \quad (3-4)$$

For the diblock copolymer  $S_{48}T_{52}$ <sup>72</sup>, the numbers of PS and PtBMA monomers per chain are  $N_{PS} \sim 388$ ,  $N_{PtBMA} \sim 318$  and by using eq 3-1 the value  $(\chi N)_{MST} \sim 15.44$  is obtained. It follows  $\chi_{MST} \sim 0.0218$ . Including this value of  $\chi_{MST}$  into eq 3-4 it follows a calculated

$T_{ODT} \sim 612K(339^\circ C)$ . Since the calculated  $T_{ODT}$  is much higher than the degradation temperature of the sample, this value was not checked experimentally. From preliminary rheological investigations on bulk  $S_{48}T_{52}$ <sup>72</sup> (not shown) we have checked that  $T_{ODT}$  occurs at high temperatures ( $> 200^\circ C$ ). Thus the system's  $\chi$ -parameter had to be reduced which could be achieved by introducing a neutral solvent (assumption), in order to investigate  $T_{ODT}$  of this entangled system by rheological methods. Furthermore, direct extension of Leibler's theory to concentrated solutions of AB diblock copolymers in a neutral solvent<sup>171</sup> suggests that  $T_{ODT}$  occurs when the product  $\chi(N_A + N_B)\phi$  reaches a critical value,  $c$ , which depends on the composition of the block copolymer. By using the usual assumption that  $\chi = \alpha/T + \beta$ , where  $\alpha$  and  $\beta$  are system-dependent constants,  $1/T_{ODT}$  should scale linearly with  $1/\phi$ , where  $\phi$  is the polymer volume fraction, and  $N_A$  and  $N_B$  are the number of A and B monomers in a chain.<sup>93</sup>

$$\frac{1}{T_{ODT}} = \frac{c}{\alpha(N_A + N_B)} \left( \frac{1}{\phi} \right) - \frac{\beta}{\alpha} \quad (3-5)$$

The validity of eq 3-5 in the case of our nearly symmetric  $S_{48}T_{52}$ <sup>72</sup> dissolved in DOP at different concentrations was checked by plotting the experimentally determined  $1/T_{ODT}$  as a function of  $1/\phi$ . (Table 3-3, Figure 3-9).

Sample	$\phi$ , volume fraction	$1/\phi$	<sup>a)</sup> $T_{ODT}, ^\circ C$	$(1/T_{ODT}) \times 10^3, K^{-1}$
ST72_S1	0.215±0.005	4.65±0.11	40± 0.5	3.19±0.01
ST72_S2	0.24±0.012	4.17±0.21	60±1.3	3.00±0.01
ST72_S3	0.275±0.01	3.63±0.14	70±1	2.91±0.01
ST72_S4	0.32±0.007	3.12±0.07	123±1.5	2.52±0.01

<sup>a)</sup>Temperature sweep tests with heating rate  $1^\circ C/min$  at  $\omega = 100$  rad/s (Figure 3-1e) where a discernible drop in moduli has been encountered for overall concentrations.

**Table 3-3.** ODT temperatures determined by temperature sweep measurements for  $S_{48}T_{52}$ <sup>72</sup> at different concentrations (S1, S2, S3, S4) in DOP.

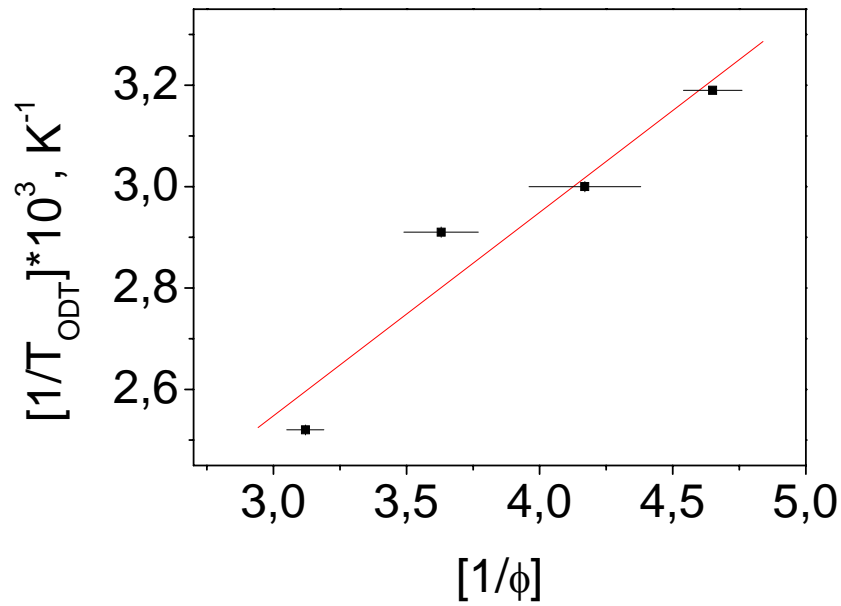


**Figure 3-9.** Plot  $1/T_{ODT}$  versus  $1/\phi$  for the ST72\_S1, S2, S3, S4, block copolymer solutions.

The solid line represents the best linear fit through the data from which we estimate  $\alpha$ ,  $\beta$  and  $c$  from eq 3-5. The intercept  $A$  and slope  $B$  taken from the plot  $1/T_{ODT}$  versus  $1/\phi$  are given in Table 3-4. As seen in Figure 3-9, within experimental errors a slight nonlinearity was encountered. This may be a consequence of morphological transitions and due to the fact that eq 3-5 has been used under the assumption that DOP is a neutral solvent. An attempt to apply eq 3-5 for the system ST117 (S<sub>55</sub>T<sub>45</sub><sup>117</sup>) has been made and probably due to the asymmetric structure induced by DOP the linearity between  $1/T_{ODT}$  and  $1/\phi$  has not been found.

$N_{PS}$	$N_{PiBMA}$	$N = N_{PS} + N_{PiBMA}$	<sup>1)</sup> $A$	<sup>1)</sup> $B$
388	318	706	1.3117	0.4102

<sup>1)</sup>where the coefficients  $A$ ,  $B$  represent:  $A = -\frac{\beta}{\alpha}$ ,  $B = \frac{c}{\alpha(N_A + N_B)}$

**Table 3-4.** The intercept  $A$  and slope  $B$  used to estimate the system-dependent constants  $\alpha$ ,  $\beta$  and  $c$  from eq 3-5.

Theories for Flory-Huggins interaction parameter,  $\chi_{eff}$ , in solutions of polymer mixtures have been extended to block copolymer solutions by Fredrickson and Leibler<sup>171</sup> and by Olvera de

la Cruz.<sup>172</sup> In semidilute solutions the scaling  $\chi_{eff} = \phi^{1.6}\chi$  is anticipated. For the system polystyrene-*b*-poly(*t*-butyl methacrylate), the interaction parameter between *i*, *j* components is calculated using eq 3-6:

$$\chi_{ij} = \frac{V}{RT}(\delta_i - \delta_j)^2 \quad (3-6)$$

where: *V* - molar segmental volume, cm<sup>3</sup>/mol; *R* - gas constant, J K<sup>-1</sup>mol<sup>-1</sup>; *T* - temperature, K;  $\delta_{i,j}$  - solubility parameter at room temperature for the components *i*, *j*. Applying eq 3-6 to the diblock copolymer S<sub>48</sub>T<sub>52</sub><sup>72</sup> and assuming the styrene unit as a reference component ( $V \sim 10^{-4} m^3 / mol$ ), the resulting value for the interaction parameter between styrene and *t*-butyl methacrylate units is  $\chi_{ST} \sim 0.010095$ , which is in a good agreement with the positive values of  $\chi_{ij}$  (for the monomers pair *i*, *j*) resulting from experiments<sup>173</sup> ( $\chi_{ij} \sim 10^{-3} \div 10^{-1}$ ). Further calculations resulted with  $\alpha = \chi/V$  in  $\alpha \sim 0.00010095 mol / cm^3$ ,  $A = 1.3117$  and with  $A = -\frac{\beta}{\alpha}$ ,  $\beta = -1.3241 \times 10^{-4}$ . Thus the dependence of the effective interaction parameter on temperature follows the relation:  $\chi_{eff} = 100.95/T - 1.3241 \times 10^{-4}$ . A similar dependence of  $\chi$  versus *T* was found by Rosedale and Bates for a series of diblock copolymers poly(ethylene-*alt*-propylene)-poly(ethylethylene)<sup>41</sup> and by Cochran and Bates for symmetric diblock copolymer systems in the melt state, containing poly(cyclohexylethylene) as one block and polyethylene, polyethylethylene or poly(ethylene-*alt*-propylene) as a second block.<sup>174</sup>

Furthermore, the expression for the coefficient *B* allowed us to gain the critical concentration of block copolymer in the solution, *c*, below which no microphase separation occurs for S<sub>48</sub>T<sub>52</sub><sup>72</sup> in DOP:  $c = B\alpha(N_{PS} + N_{PBMA})$ ,  $c = 0.0292$  (2.92%). In comparison,  $c = 15\%$  was found for concentrated solutions of polystyrene-*b*-polyisoprene ( $M_n \sim 31K$ ).<sup>93</sup>

### 3.3 Conclusions

The dynamic mechanical spectroscopy was applied to the analysis of diblock copolymer systems, particularly to high molecular weight S<sub>48</sub>T<sub>52</sub><sup>72</sup> and S<sub>55</sub>T<sub>45</sub><sup>117</sup> in DOP. As it was shown in previous work done on asymmetric triblock copolymer melts of polystyrene-*b*-polyisoprene-*b*-polystyrene triblock copolymer (SIS, Vector 4111) with a high molecular weight ( $1.4 \times 10^5$ )<sup>50</sup>, the rheological measurements do not always give rise to the same value

of  $T_{ODT}$ , especially for highly asymmetric block copolymers. By using classical rheology (temperature sweep tests), the order-disorder transition temperature  $T_{ODT}$  was not clearly found at low angular frequency for such high molecular weight systems, due to the high contribution of fluctuations effect present in the diluted systems. Furthermore, it turned out that the microdomain structure is asymmetrically swollen, which resulted from the selectivity of the solvent (DOP) for the poly(*t*-butyl methacrylate) block, in the sense of being a good solvent for poly(*t*-butyl methacrylate) and a  $\Theta$  solvent for polystyrene as already reported by other groups. Upon dynamic mechanical investigations on high molecular weight ST diblock copolymer solutions in DOP we have shown that: (1) the dynamic temperature sweep experiments under isochronal conditions (1, 10, 100 rad/s) during heating were effective to determine order-order transitions followed by the order-disorder transitions at a certain critical concentration and at a certain frequency; (2) plots of frequency sweep tests in isothermal conditions, by heating were not effective to investigate ODT for high concentrated systems (Figures 5-3c, d, f, g); (3) the shape of plots of  $\log G'$  vs  $\log G''$  indicated a selectivity of the solvent (DOP) for one of the blocks, as well the upward shift of the curves (Figures 3-4d, 3-5b,c) at a certain temperature within a decreasing slope by increasing temperature clearly indicates a morphological transition; (4) an unusual behavior of master curves through the appearance of the so-called "moduli loop" as shown in Figures 3-7d,e and 3-8b have evidenced the morphological transition. This transition could be an OOT, which is due to the initially perhaps cylindrical structure toward a spherical one before attaining ODT. Thus, the dynamic temperature sweep experiment under isochronal conditions appears to depend very much on the block copolymer composition.<sup>154</sup>

So far in our investigation Leibler's dilution approximation theory was used as a tool and the following expression for the interaction parameter of this system has been developed:  $\chi_{eff} = 100.95/T - 1.3241 \times 10^{-4}$ . While for the ST72 system in the swollen state Leibler's dilution approximation theory has been found to fit, this was not true for the system ST117 where the morphological transitions have been detected as well. Due to the different volume fractions of polystyrene in each of both systems ( $f_{ps} \sim 0.58$  (ST117) and  $f_{ps} \sim 0.51$  (ST72), (Table 3-1)) the higher asymmetry in case of ST117 than in ST72 may be the reason for the failure of eq 3-5, which is based on a symmetrically swollen block copolymer. This disagreement with Leibler's dilution approximation theory may serve as one more evidence that DOP is a selective solvent for ST block copolymers.

## 4. *In Situ* Monitoring of Domain Orientation in Block Copolymers Solutions by Large Amplitude Oscillatory Shear (LAOS)

### 4.1 Introduction

Rheology is a very sensitive tool for the detection of i) the order-disorder transition, ii) the different ordered phase, iii) the phase transformation kinetics between the disordered and ordered phases of block copolymers.

In addition, **rheology serves to orient ordered phase on a macroscopic scale** using external mechanical fields. The multigrain structure is characteristic of unoriented block copolymers, the size of the grains being determined by the temperature and the type of morphology. Application of a large amplitude oscillatory shear (LAOS) field (well in the nonlinear viscoelastic regime) results in the macroscopic orientation of grains through the elimination of interfaces perpendicular to the shear direction and reorientation of the domains along the shear direction. During LAOS the magnitude of the complex shear modulus ( $G^*$ ) is a decreasing function of time, and the magnitude of this decrease depends on temperature, frequency, strain amplitude, and distance from the order-disorder transition. The shape of the complex modulus versus time ( $G^*(t)$ ) reflects the kinetics of the morphological reorientation and on complex relationships between the morphology and the mechanical properties of the system. The resulting ordered material due to an applied external field, will exhibit anisotropic properties, such as optical, transport, and electrical properties.

The direction of alignment can be switched between different orientations, which may be useful for designing switchable material properties. Flow is not the only way to induce macroscopic order; electric fields<sup>95,97</sup> can also serve this purpose, but flow in its different forms (oscillatory and steady, extrusion, roll-casting, extensional flow) provide efficient means of obtaining macroscopic alignment. The effects of mechanical fields on block copolymers was pioneered by the work of Keller et al.<sup>175</sup> using an extrusion flow field. Since then the process of flow alignment in block copolymers has attracted interest.<sup>176,177,75,76,6,178,7,73,179,67,70</sup>

When subjecting a lamellae-forming block copolymer to reciprocating shear, the lamellae orient with their lamellar normal parallel to the shear gradient direction (parallel orientation) (Scheme 1-2, chapter 1). It was shown in two block copolymer systems<sup>75,73,179</sup> that another orientation is also possible, namely the perpendicular orientation. Zhang et al.<sup>73</sup> showed for the polystyrene-*b*-polyisoprene ( $M_n \sim 18.4K$ ) that parallel orientation is obtained at low and high frequencies, but at intermediate frequencies the perpendicular orientation is produced.

These experiments demonstrated that the orientation of the lamellar microstructure of the SI block copolymers under large amplitude oscillatory shear in the vicinity of the order-disorder transition temperature depends strongly on frequency. Wiesner<sup>180</sup> has shown that annealing effects are important for the observation of parallel orientation at low frequencies.

## 4.2 Results and Discussion

### 4.2.1. Rheological and SAXS investigations of $S_{50}T_{50}^{100}$ and $S_{33}B_{33}T_{34}^{160}$ solutions

***Rheological behavior of unaligned ordered sample 30wt-%  $S_{50}T_{50}^{100}$  in DOP. Order-Disorder Transition Temperature ( $T_{ODT}$ ).*** As mentioned previously, it is necessary to have an indication about viscoelasticity in the terminal flow regime which is a good indicator of the order-disorder transition temperature ( $T_{ODT}$ ) in block copolymers. Since the order-disorder transition temperature is known, clearly the information about enhancing the ordered state in a certain range of temperatures is obtained. In Figure 4-1a the order-disorder transition temperature over a broad range of frequencies  $\omega=1\div 100$  rad/s has been investigated and the following values were obtained: (1)  $T_{ODT} \sim 60^{\circ}\text{C}$  at  $\omega=1$ rad/s; (2)  $T_{ODT} = 79^{\circ}\text{C}$  at  $\omega=10$ rad/s; (3)  $T_{ODT} = 85^{\circ}\text{C}$  at  $\omega=100$ rad/s and a detailed explanation of the ODT values' frequency dependence has been given in Chapter 3. The plots of storage and loss moduli as functions of reduced frequency ( $a_T\omega$ ) are presented for 30wt-% ST in DOP, providing the information about the existence of ordered and disordered states within a certain range of temperatures. The time-temperature superposition principle has been applied and a 2D shifting has been used to construct master curves as presented in Figure 4-1b. In the whole frequency range the curves at different temperatures superimposed well with each other. In the low frequency range the dependence  $G' \propto \omega^2$  and  $G'' \propto \omega$  indicated that the disordered state shows a typical homopolymer-like terminal flow behavior. In general, the main features resulting from the master curves of block copolymer systems are the critical frequencies  $\omega_c'$ ,  $\omega_c''$ , and  $\omega_d$ . Below these critical frequencies the relaxation dynamics are dominated by relaxation of the microdomain structure. Due to the fact that time-temperature superposition principle worked well for the solution of 30wt-% ST in DOP (Figure 4-1b) within the employed temperature range, the critical frequencies  $\omega_c'$ ,  $\omega_c''$ , and  $\omega_d$  could not be detected, in order to allow the definition of the type of alignment within a certain range of frequency as previously mentioned by Kornfield et al.<sup>70</sup>

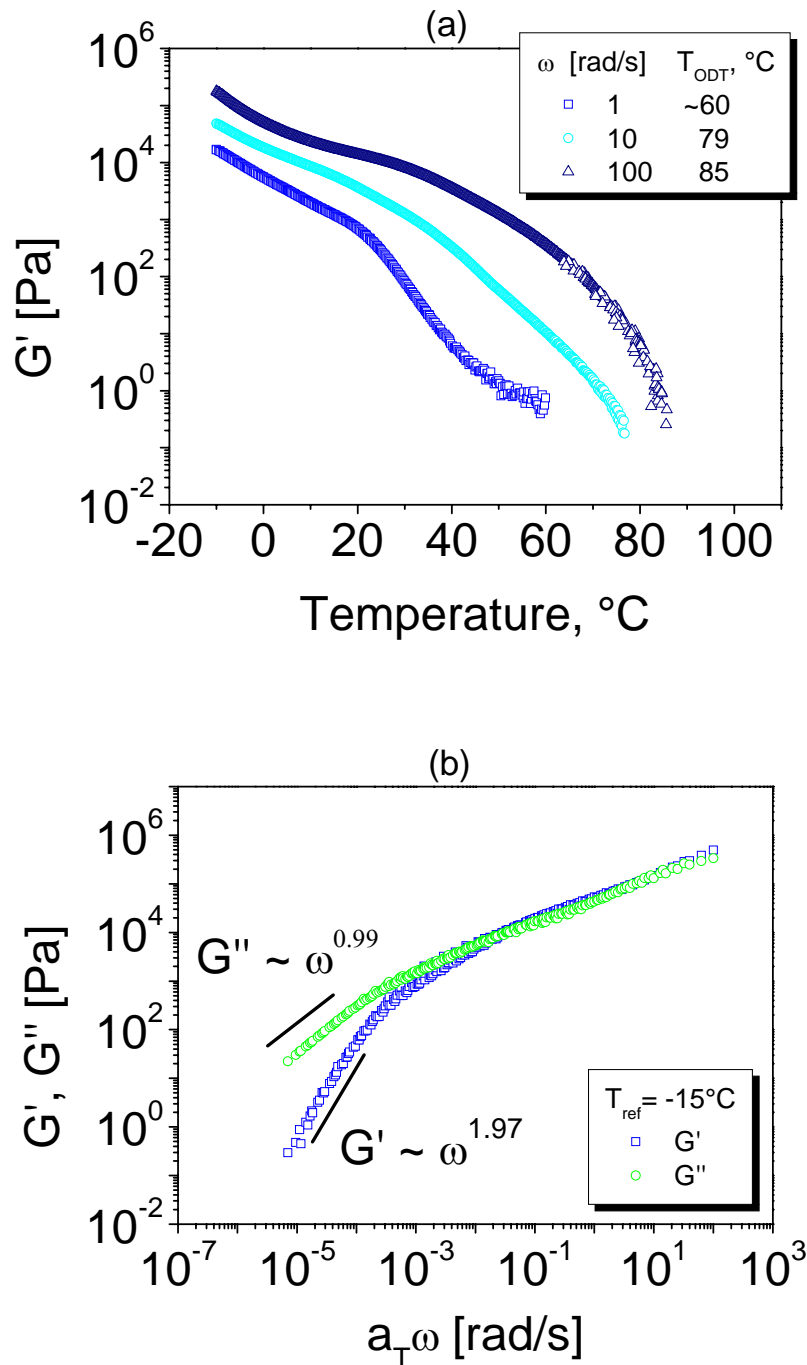
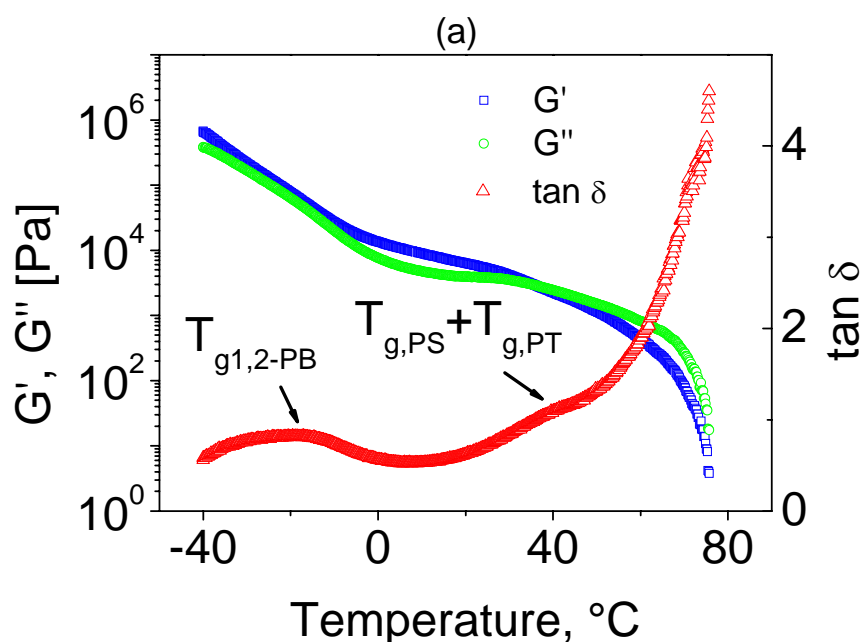


**Figure 4-1.** (a) Variation of  $G'$  with increasing temperature obtained at  $\omega = 1, 10, 100$  rad/s for solution of 30wt-%  $S_{50}T_{50}^{100}$  in DOP within the linear viscoelastic regime. A drop in  $G'$  is discernible at higher frequencies at the order-disorder transition temperature. (b) The storage ( $G'$ ) and loss ( $G''$ ) moduli versus a shifted frequency scale,  $a_T \omega$ , at a reference temperature  $T_{ref} = -15^\circ\text{C}$ , for the solution of 30wt-%  $S_{50}T_{50}^{100}$  in DOP. The investigated range of temperatures was from  $T = 55^\circ\text{C}$  to  $T = -15^\circ\text{C}$  and the material's constants within the William-Landel-Ferry equation have been obtained:  $C1 = 30.59$ ;  $C2 = 365.46\text{K}$ .

### Linear Dynamic Mechanical Properties of 20wt-% $S_{33}B_{33}T_{34}^{160}$ in DOP.

Beside the investigations made on  $S_{50}T_{50}^{100}$  in DOP, furthermore our attention was focused on the triblock terpolymer  $S_{33}B_{33}T_{34}^{160}$  to study the main changes induced by the introduction of the elastomeric block, polybutadiene (PB) between the two harder blocks polystyrene (PS) and poly(*t*-butyl methacrylate) (PT). As a consequence of the high molecular weight of this specimen, as illustrated already in Table 2-5, we used a solution of 20 wt%  $S_{33}B_{33}T_{34}^{160}$  in DOP in order to shift the ODT to the accesible range of temperatures.

A preliminary rheological investigation (Figure 4-2a) by DMA of a solution 20wt-%  $S_{33}B_{33}T_{34}^{160}$  triblock terpolymer in DOP gave evidence of just two individual glass transition temperatures. One of them is assigned to the 1,2-polybutadiene block, and the other is a combined signal for the polystyrene and poly(*t*-butyl methacrylate) blocks (Figure 4-2a). A sudden drop in moduli as an indication of  $T_{ODT}$  has been encountered as well. It should be reminded that individual glass transition temperatures were shifted to lower temperatures than the corresponding  $T_g$ 's of the bulk homopolymers due to the presence of DOP. As an evaluation of  $T_g$  for each block it is reliable to take the maximum of the loss tangent ( $\tan\delta$ ), being more sensitive within the changes in temperature than the loss modulus ( $G''$ ).



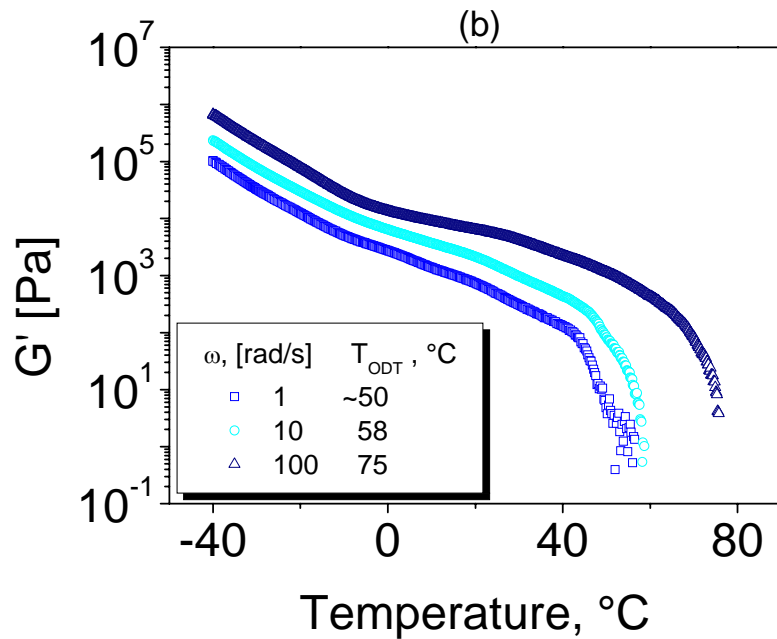


**Figure 4-2.** (a) Characterization of the individually glass transition temperatures and order-disorder transition. Temperature sweep by heating (1°C/min,  $\omega=100$  rad/s) of a solution 20 wt-%  $S_{33}B_{33}T_{34}^{160}$  terpolymer in DOP within the following estimated parameters:  $T_{g1,2-PB} \sim -20^\circ\text{C}$ ,  $(T_{gPS} + T_{gPT}) \sim 40^\circ\text{C}$ ,  $T_{ODT} \sim 75^\circ\text{C}$ . (b) The order-disorder transition temperatures by heating (1°C/min) at different frequencies as following: i)  $\omega=1$  rad/s,  $T_{ODT} \sim 50^\circ\text{C}$ ; ii)  $\omega=10$  rad/s,  $T_{ODT} = 58^\circ\text{C}$ ; iii)  $\omega=100$  rad/s,  $T_{ODT} = 75^\circ\text{C}$ .

Before attempting to obtain an aligned state for the solution of 20wt-%  $S_{33}B_{33}T_{34}^{160}$  in DOP, the viscoelastic behavior of the specimen as a function of reduced frequency is required, as given in Figure 4-3. Frequency sweep experiments at 10°C, 15°C, 20°C, 25°C, and 30°C reveal the relationship between the moduli and frequency as:  $G', G'' \sim \omega^{0.3 \pm 0.5}$ . This gives a clear evidence for a microphase separated system. A straight line in the master curve of the storage modulus (Figure 4-3) corresponding to the high reduced frequency range at the chosen two reference temperatures,  $T_{ref} \sim 10^\circ\text{C}$  and  $T_{ref} \sim 15^\circ\text{C}$  indicates the existence of an ordered system above the critical frequency  $\omega_c' \sim 5$  rad/s.

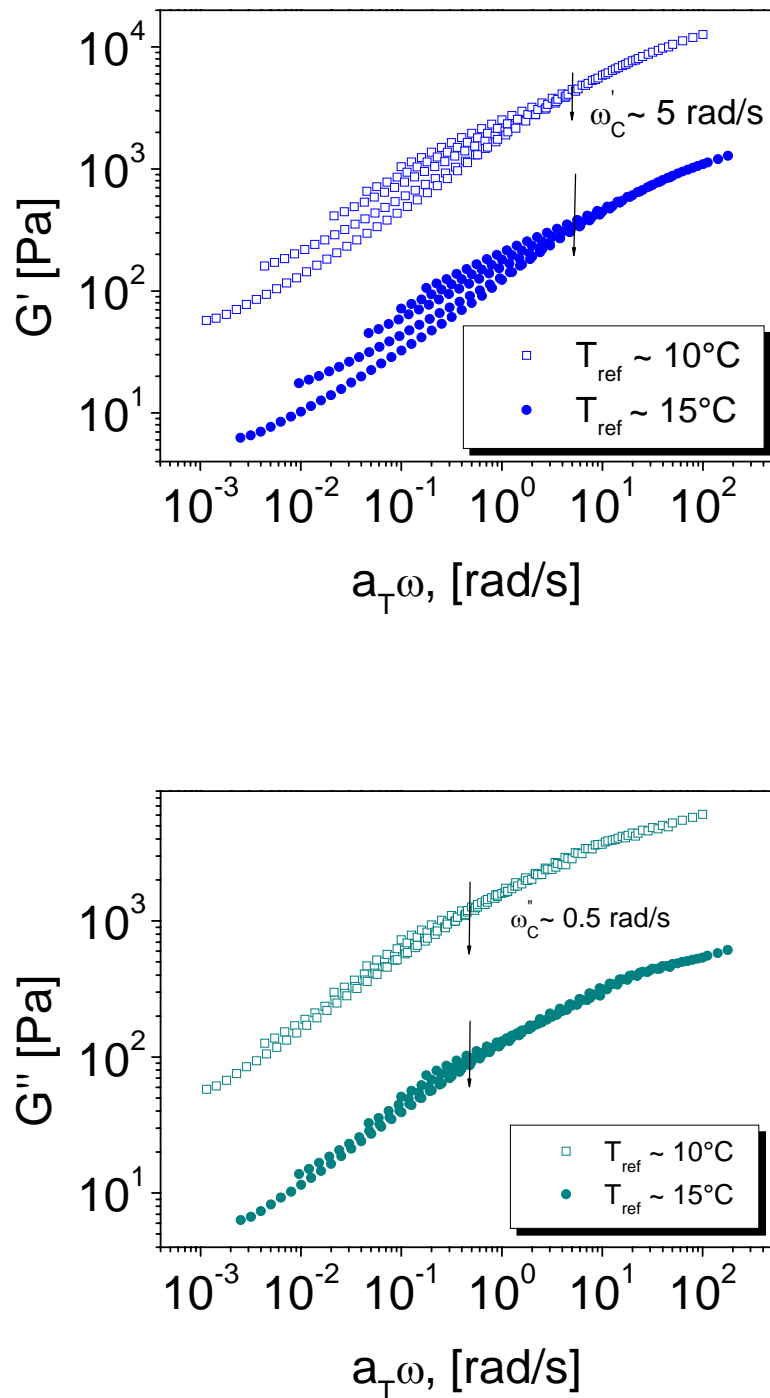


**Figure 4-3.** Master curves of storage ( $G'$ ) and loss moduli ( $G''$ ) by 2D-shifting at reference temperature  $T_{ref} \sim 10^\circ\text{C}$  and  $T_{ref} \sim 15^\circ\text{C}$  of a solution 20 wt%  $S_{33}B_{33}T_{34}^{160}$  terpolymer in DOP and the corresponding critical frequencies:  $\omega_C' \sim 5$  rad/s,  $\omega_C'' \sim 0.5$  rad/s.

Similarly, the critical frequency  $\omega_C'' \sim 0.5$  rad/s has been defined in the master curve of the loss modulus (Figure 4-3), above which the system is ordered and an attempt of

macroscopical shear alignment process could be reliable above the critical frequencies  $\omega_c'$  and  $\omega_c''$ .

### SAXS profiles of $S_{33}B_{33}T_{34}^{160}$

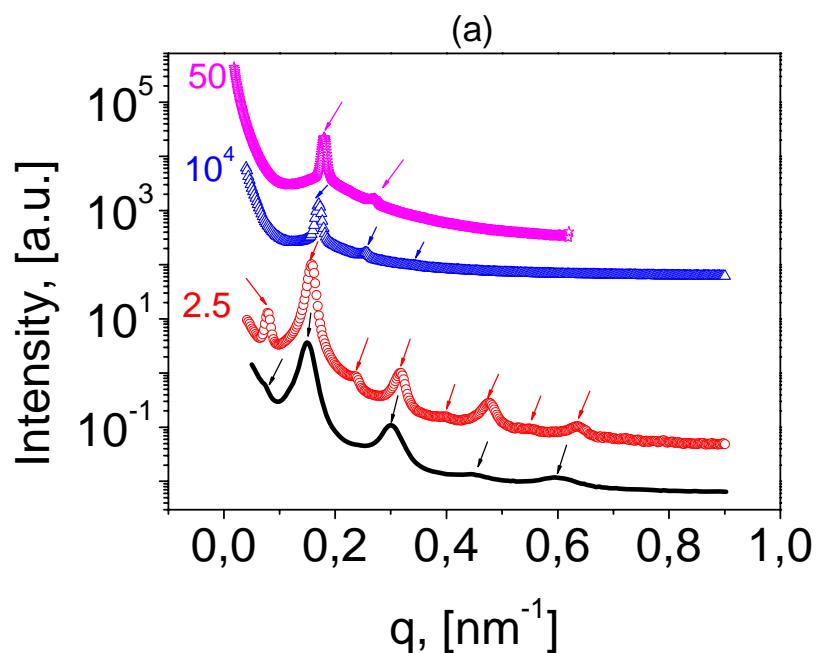
The phase state of the system was also monitored by SAXS at room temperature. It turned out that the temperature sweep findings like the existence of a microphase separated structure at room temperature (Figure 4-2a,  $G' > G''$  at 25°C) are in agreement with the scattering profiles at different concentrations in Figure 4-4a, which indicate lamellar structures for all concentrations. The reason of appearance of correlation peaks with the ratio 1:1.5 and not as we may expect for the lamellar morphology 1:2, respectively is related with the different miscibility behavior of each block. As seen in the overlay plot in Figure 4-4a or more clearly in Figure 4-4b with an expanded scale at very low  $q$ -range, the long period of lamellar  $S_{33}B_{33}T_{34}^{160}$  cast film from chloroform is 86 nm, while by dilution with DOP a smaller long period occurs due to swelling of the blocks (and thus decreasing their repulsive interactions) as illustrated in Table 4-1.

Sample	$q_{hkl} / q_{100}$								L, nm	Morphology
	1	2.06	4.1	6.1	8.19	-	-	-		
$S_{33}B_{33}T_{34}^{160}$ cast film <sup>1)</sup>	1	2.06	4.1	6.1	8.19	-	-	-	~86	lamellar
70wt-% $S_{33}B_{33}T_{34}^{160}$ in DOP	1	1.97	2.98	3.98	5	6	7	8	80.3	lamellar
25wt-% $S_{33}B_{33}T_{34}^{160}$ in DOP	1	1.5	2	-	-	-	-	-	36.8	lamellar
20wt-% $S_{33}B_{33}T_{34}^{160}$ in DOP	1	1.5	-	-	-	-	-	-	34.7	lamellar

<sup>1)</sup>thermal annealing: 1h at 50°C, 1h at 80°C, 4h at 150°C; L-long period calculated from the first order reflexion peak as following,  $L = 2\pi / q_{100}$ .

**Table 4-1.** The scattering correlation peaks for the  $S_{33}B_{33}T_{34}^{160}$  as cast film from  $CHCl_3$  and for the swollen state at different concentrations 70wt-%, 25wt-%, 20wt-%  $S_{33}B_{33}T_{34}^{160}$  in DOP.

However, an investigation of scattering profiles for higher concentrations like 70wt-%  $S_{33}B_{33}T_{34}^{160}$  proved really the existence of a first order peak which appeared quite weak in the scattering profile from the cast film and further vanished at high degree of dilution. Indeed, at 25wt-%  $S_{33}B_{33}T_{34}^{160}$  in DOP the first order peak is shifted at high  $q$  range and three correlation peaks are present at this concentration while for 20wt-%  $S_{33}B_{33}T_{34}^{160}$  in DOP only two correlation peaks are seen due to the shifting toward high  $q$  range. A summary of the ratio of correlation peaks within the corresponding morphologies at different concentrations is given in Table 4-1. From the detailed analysis of the scattering profiles (Table 4-1) in respect with the correlation peaks ratio it may be concluded that the  $S_{33}B_{33}T_{34}^{160}$  system in diluted state preserved the same lamellar morphology as evidenced through the weight fractions analysis (Table 2-5) and not preferential swelling of the microdomains was found. From the viscoelastic behavior and SAXS profiles we might conclude as potential parameters of alignment a temperature of 15°C with a frequency of 10 rad/s.



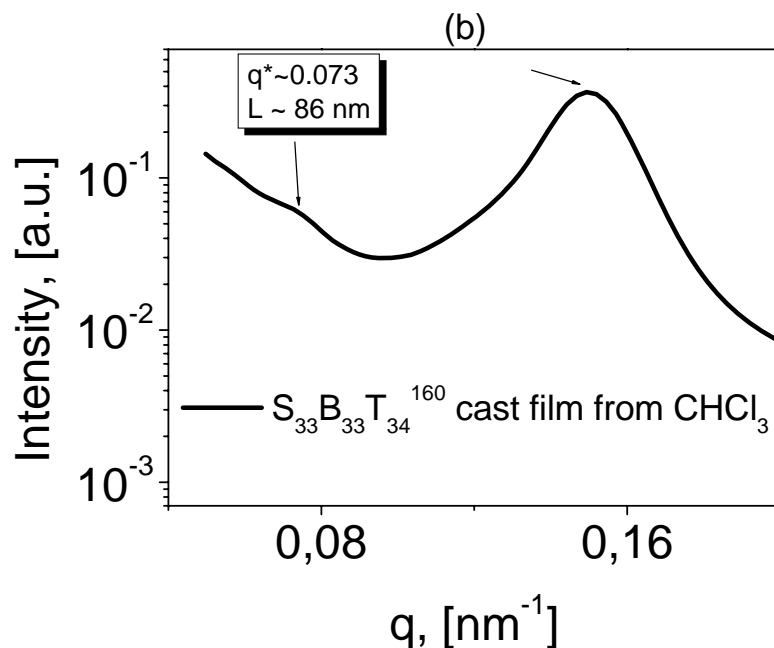


**Figure 4-4.** (a) The comparison of the scattering profiles at room temperature for  $S_{33}B_{33}T_{34}^{160}$  (—) as cast film from  $CHCl_3$  and as swollen state at different concentrations 70wt-% (—○—), 25wt-% (—△—) and 20wt-% (—☆—)  $S_{33}B_{33}T_{34}^{160}$  terpolymer in DOP in a 1 mm thick sample (25wt-%, 20wt-%  $S_{33}B_{33}T_{34}^{160}$  in DOP) sealed between 10  $\mu m$  thick mica windows with beamline settings  $6 \times 10^{12}$  photon/s/100mA. For better visibility of scattering peaks the curves were shifted vertically. The arrows indicate the position of the correlation peaks. (b) First order peak from the cast film of  $S_{33}B_{33}T_{34}^{160}$  in  $CHCl_3$ .

#### 4.2.2. Alignment of High Molecular Weight Polystyrene-b-Poly(*t*-butyl methacrylate) $S_{50}T_{50}^{100}$ solution

##### *In situ Monitoring of Birefringence and Dynamic Moduli at various frequencies for 30wt-% $S_{50}T_{50}^{100}$ diblock in DOP.*

Over a wide range of frequencies (0.1÷10 rad/s) flow alignment experiments at a fixed temperature and different strain amplitudes have been carried out. The flow alignment process has been achieved by performing a timesweep test in dynamic mode, resulting in a plot of dynamic moduli ( $G'$ ,  $G''$  or  $G^*$ ) versus time and simultaneously by using the OAM set up, a plot of birefringence versus time was calculated.

Alignment kinetics at low frequency,  $\omega=0.1$  rad/s and  $T=10^\circ\text{C}$ .

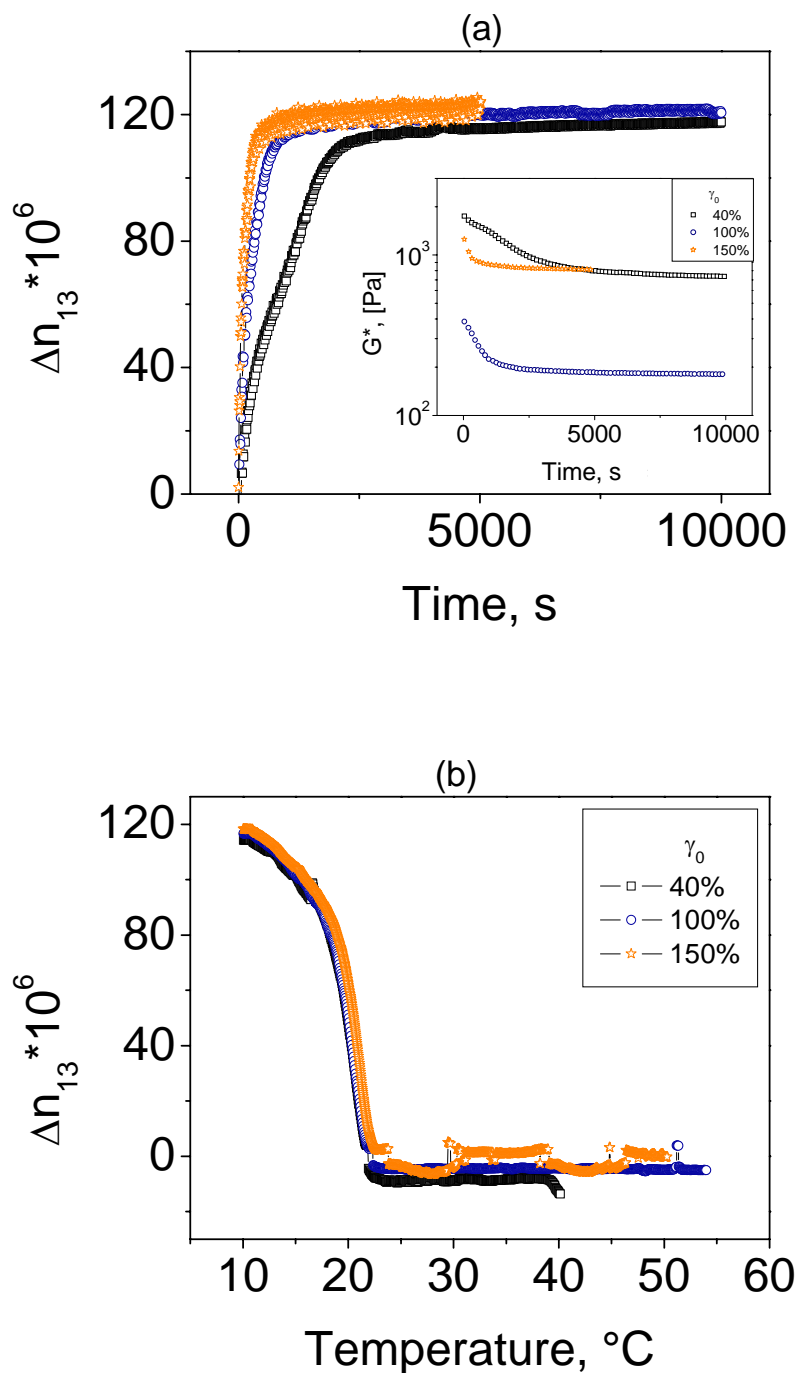


**Figure 4-5.** (a) Evolution of 1,3 birefringence ( $\Delta n_{13}$ ) during large amplitude oscillatory shear at  $T = 10^\circ\text{C}$  and  $\omega = 0.1$  rad/s at different strain amplitudes  $\gamma_0$ : ( $\square$ )40%, ( $\circ$ )100%, ( $\star$ )150%. The inset shows the evolution of complex modulus ( $G^*$ ) during the large amplitude oscillatory shear alignment; (b) Changes in birefringence upon cessation of shear and heating with  $0.3^\circ\text{C}/\text{min}$ .

The plot shown in Figure 4-5a illustrates a perpendicular alignment ( $\Delta n_{13} > 0$ ) induced by large amplitude oscillatory shear in the solution of 30 wt-% S<sub>50</sub>T<sub>50</sub><sup>100</sup> in DOP. A saturated and positive value of birefringence  $\Delta n_{13} \sim 1.2 \times 10^{-4}$  (Figure 4-5a) is reached after a long time, approximately 10000 sec. The complex moduli (inset of Figure 4-5a) showed an initial fast decrease, followed by a gradual decrease to a constant value. At the smallest strain amplitude  $\gamma_0 = 40\%$ , the modulus decreases much slower in two steps than for higher strain amplitudes implying a faster and slower relaxation of the chains where the latter might occur due to the entanglement effects. Thus the need of higher flow time is achieved by an increase of applied strain amplitude. A higher strain amplitude of  $\gamma_0 = 150\%$  revealed a slight decrease in complex modulus and moreover a higher value of modulus has been induced which may lead to assign it as a critical strain amplitude,  $\gamma_C$  above which the elastic behavior of the system is dominant and the maximum rate of alignment has been reached. It may be seen that higher strain amplitudes are related with fast decrease of moduli and fast increase in birefringence. An influence of strain amplitude over shear moduli is given in the plot of complex modulus ( $G^*$ ) versus time (inset Figure 4-5a). Unusual behavior was encountered in decreasing of moduli values within increased strain amplitude ( $\gamma_0$ ), thus at intermediate strain amplitude ( $\gamma_0 = 100\%$ ) the moduli reached the lowest value and at the highest strain amplitude ( $\gamma_0 = 150\%$ ) the value of moduli is intermediate and does not show the lowest value as it may be expected. This unusual behavior of moduli with strain amplitude does not affect the birefringence value and its sign but is given an insight over the relaxation dynamics of the chain. The highest strain amplitude and its relationship with moduli is a proof of the "entanglements", the experimental time scale is smaller than the reptation time and thus the chain flow is hindered illustrating an intermediate value of moduli.

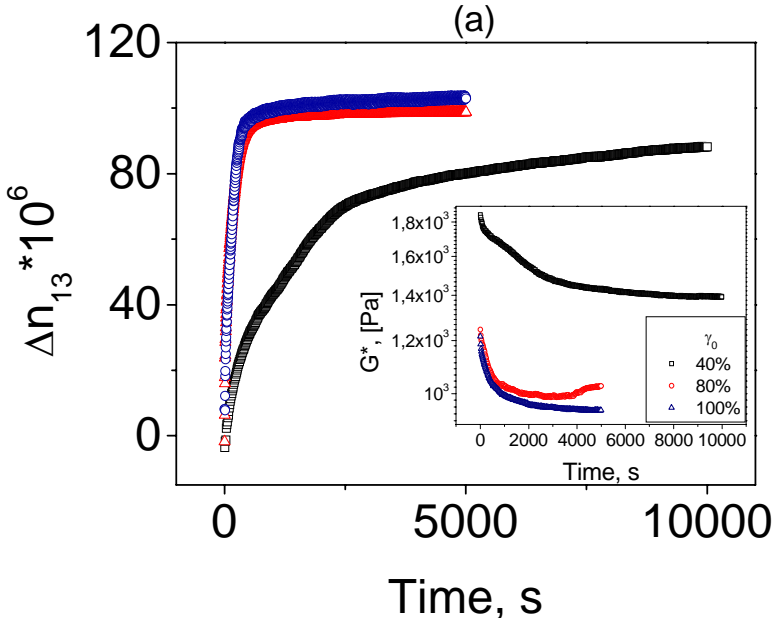
The value of birefringence of the perpendicular state, as an order of magnitude higher at the end of alignment process, is in good agreement with those values encountered for lamellae PS-PI diblock copolymer with a molecular weight of 20K in the melt state, which did not exceed  $\Delta n_{13\max} \sim 10 \times 10^{-4}$ .<sup>1</sup> While our system is well segregated in the bulk state, its solution in DOP affects the sharpness of the block interface, the interfacial tension between blocks decreases proportionally with the increasing amount of solvent and at the end results in a weakly segregated system.

The stable value of the finally achieved birefringence in Figure 4-5a indicates a stable aligned structure. A further proof of such stable structure was checked by heating up the sample with a rate of 0.3°C/min after cessation shear, as indicated in Figure 4-5b. A sharp decrease of the birefringence value down to zero value indicated the order-disorder transition temperature,

$T_{ODT} \sim 22^{\circ}\text{C}$ . The scatter of data around zero in Figure 4-5b is due to the sensitivity of the instrument.

**Alignment kinetics at intermediate frequency,  $\omega=1 \text{ rad/s}$  and  $T=10^{\circ}\text{C}$ .**

Shearing at  $\omega=1 \text{ rad/s}$  and  $T=10^{\circ}\text{C}$  produces a predominantly perpendicular alignment as well as the lower frequency. The system showed at higher frequency (1 rad/s) a lower but still positive values of birefringence for similar strain amplitudes than at 0.1 rad/s as shown in Figure 4-6. The aligned structure toward perpendicular alignment is developed faster at high shear amplitude ( $\gamma_0=80\%$  and  $100\%$ ) within a short time scale (450sec) while at low shear amplitude ( $\gamma_0=40\%$ ) a monotonic increase in birefringence is observed during the whole experiment. In the inset of Figure 4-6a nearly the same values of dynamic complex moduli ( $G^*$ ) corresponding to high shear amplitudes are illustrated within a sharp downward displacement of the modulus. This behavior may happen as a consequence of frequency influence on dynamics and relaxation chain, thus the experimental time scale is high enough to induce the occurrence of reptation phenomenon, subsequently the induced chain flow is favored and the low value of moduli are encountered. Figure 4-6b shows the determination of the order-disorder transition temperature in subsequent heating steps, as discussed before, and the  $T_{ODT} \sim 22^{\circ}\text{C}$  found here corresponds well to the value obtained at 0.1 rad/s.



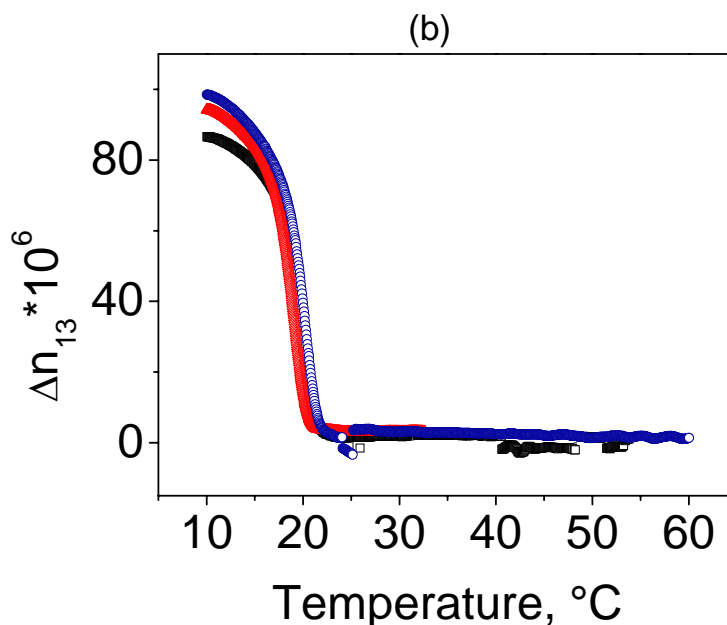


**Figure 4-6.** (a) Evolution of 1,3 birefringence ( $\Delta n_{13}$ ) during large amplitude oscillatory shear at  $T = 10^\circ\text{C}$  and  $\omega=1$  rad/s at different strain amplitudes  $\gamma_0$  : ( $\square$ )40%, ( $\triangle$ )80%, ( $\circ$ )100%. The corresponding inset shows the evolution of dynamic complex moduli ( $G^*$ ) within increasing strain amplitude. (b) Changes in birefringence upon cessation of shear and heating rate of  $0.3^\circ\text{C}/\text{min}$ . The order-disorder transition temperature is  $T_{\text{ODT}} \sim 22^\circ\text{C}$ .

***Alignment kinetics at high frequency,  $\omega=10$  rad/s and  $T=14^\circ\text{C}$ .***

An increased frequency at  $\omega=10$  rad/s required an increase in temperature due to the high torque developed during the alignment process. Since the initial parameters were adjusted ( $\omega$ ,  $T$ ) the performed shear alignment underwent the same perpendicular alignment as well as for low and intermediate frequencies, as shown in Figure 4-7. A careful analysis of the plot illustrated in Figure 4-7a allowed us to point out the "two steps" alignment process at low strain amplitude,  $\gamma_0=40\%$  as a strong evidence of entanglements effect at low strain amplitude. We can distinguish two stages of the fast process, namely the "first fast process" arised at the very early stage of the shearing process and the occurrence of the "second fast process" at the later stage of the shearing process which is different from the first one by a monotonic increase of birefringence toward the plateau value. In the inset from Figure 4-7a, a strong dependence of complex moduli upon increasing the strain amplitude is evidenced through a sharp decay at the first stages of the shear process and also a decreasing initial value of modulus with increasing strain amplitude has been evidenced.

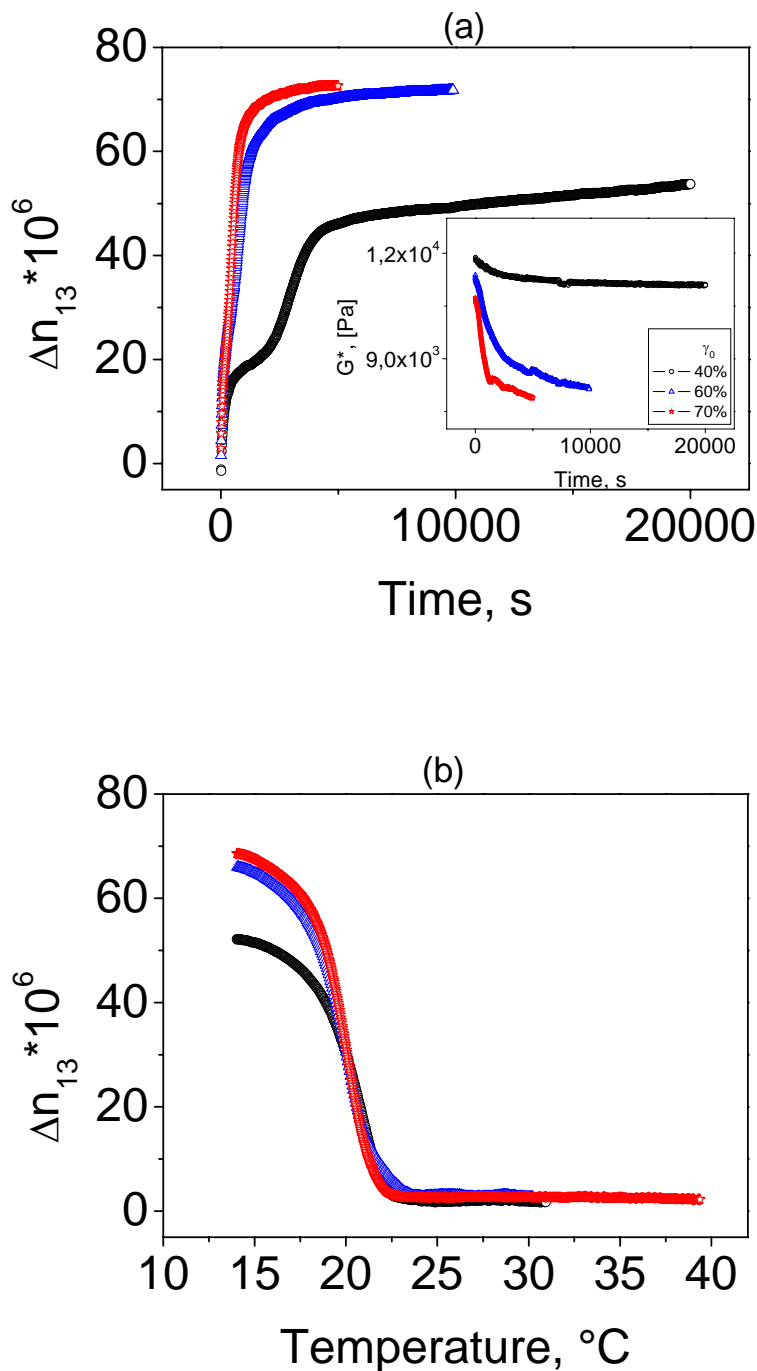


**Figure 4-7.** (a) Evolution of 1,3 birefringence ( $\Delta n_{13}$ ) during large amplitude oscillatory shear at  $T = 14^{\circ}\text{C}$  and  $\omega = 10 \text{ rad/s}$  at different strain amplitudes  $\gamma_0$ : (○) 40%, (△) 60%, (☆) 70%. The inset ( $G^*$  vs time) illustrates the evolution of complex modulus during alignment process. (b) Changes in birefringence upon cessation of shear and heating with  $0.3^{\circ}\text{C/min}$ . The resulting order-disorder transition temperature from the aligned state is  $T_{\text{ODT}} \sim 22^{\circ}\text{C}$  for

$\Delta n_{13} \sim 0$ .

Such behavior may be due to the alignment temperature ( $T=14^{\circ}\text{C}$ ) in close proximity to  $T_{\text{ODT}}$ , which favours the induced flow toward alignment and as a consequence the involved viscoelastic contrast is diminished. Moreover, the fast process (Figure 4-7a, strain 40%) takes place at longer time scale than the previous alignment at  $T=10^{\circ}\text{C}$  illustrated in Figures 4-5a, 4-6a (strain 40%), while the final birefringence value at  $T=14^{\circ}\text{C}$  is lower than the one achieved at  $T=10^{\circ}\text{C}$ . The kinetic parameters which characterize the alignment process for the solution 30wt-%  $S_{50}T_{50}^{100}$  in DOP are summarized in Table 4-2. As already pointed out in Table 4-2 for the strain amplitude  $\gamma_0=40\%$  the required time for the fast process at temperature  $T=14^{\circ}\text{C}$  is two times higher than the required time at  $T=10^{\circ}\text{C}$  as a consequence of the less ordered system at  $T=14^{\circ}\text{C}$ . The complex moduli at  $T=10^{\circ}\text{C}$  and  $\omega=0.1$  and 1 rad/s are rather comparable as absolute values, while at higher frequency and slightly higher temperature  $T=14^{\circ}\text{C}$  they increase by almost one order of magnitude. The main feature of the aligned solution 30 wt-%  $S_{50}T_{50}^{100}$  in DOP, illustrated in Figures 4-5a, 4-6a, 4-7a over a wide range of frequencies ( $\omega=0.1, 1, 10$  rad/s) is that it shows only one type of alignment (perpendicular) which does not agree with previous findings for lamellar PS-PI ( $\sim 80\text{K}$ ) in DOP.<sup>69</sup> However, we should be aware doing such comparison due to the different chemical nature of the linked blocks which may induce different viscoelastic behavior during the alignment process and topological constraints as a consequence of high molecular weight system. Taking into account the viscoelastic behavior of an unaligned sample, an attempt of comparison between order-disorder transition temperature  $T_{\text{ODT}}$  determined using different methods (temperature sweep and birefringence methods) is given in Figure 4-8.

30wt-% ST in DOP	$\omega$ , [rad/s]								
	0.1 T=10°C			1 T=10°C			10 T=14°C		
	$\gamma_0$ , [%]								
	40	100	150	40	80	100	40	60	70
<sup>1)</sup> time, s	2000	800	350	2400	450	250	4100	1500	1000
$G^* \times 10^{-3}$ , [Pa] at t = 0s	1.7	0.3	1.2	1.8	1.2	1.2	11.8	11.3	10.7

<sup>1)</sup> the required time for occurrence of the fast process.

**Table 4-2.** The kinetic parameters of the alignment process from the solution 30wt-%  $S_{50}T_{50}^{100}$  diblock in DOP.

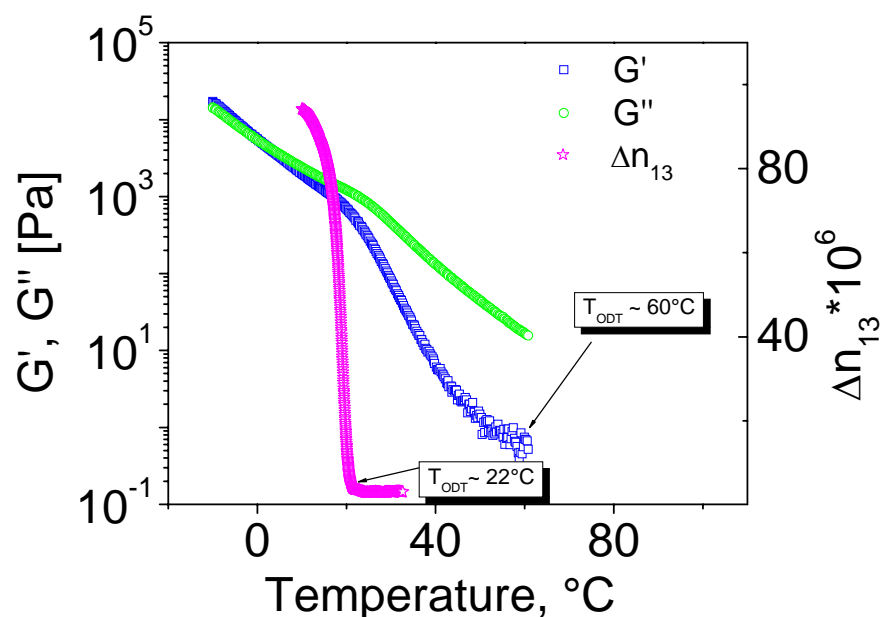


**Figure 4-8.** Temperature dependence of the diblock copolymer solution 30 wt-%  $S_{50}T_{50}^{100}$  in DOP in dynamic mechanical analysis (DMA) with an unaligned sample by comparison with rheo-optic method for a sample which was previously perpendicularly oriented. Monitoring of the dependence moduli-temperature by cooling rate of  $1^{\circ}\text{C}/\text{min}$ , at  $\omega=1$  rad/s within linear viscoelastic regime. After shear induced alignment at frequency  $\omega=1$  rad/s and strain amplitude  $\gamma_0=80\%$  by cessation of shear it follows monitoring continuous decrease of birefringence to zero by heating within a rate  $0.3^{\circ}\text{C}/\text{min}$ .

From DMA the resulting order-disorder transition temperature at  $\omega=1$  rad/s is  $T_{\text{ODT}} \sim 60^{\circ}\text{C}$  and the rheo-optical method indicates a value of  $T_{\text{ODT}} \sim 22^{\circ}\text{C}$ . This lack of agreement between the  $T_{\text{ODT}}$  values determined using different methods has been reported as well for a diblock copolymer concentrated solution of 70 wt-% polyisoprene-*b*-polystyrene (IS) in DOP, but low molecular weight (20K)<sup>181</sup> using the same protocol as described in Figure 4-8. As a conclusion the birefringence method is a much more sensitive tool for the detection of  $T_{\text{ODT}}$  than DMA. Basically the  $T_{\text{ODT}}$  obtained from DMA experiments is an "apparent ODT" due to the fluctuation effects which play an important role in the terminal flow region, as already mentioned by Olvera de la Cruz.<sup>172</sup>

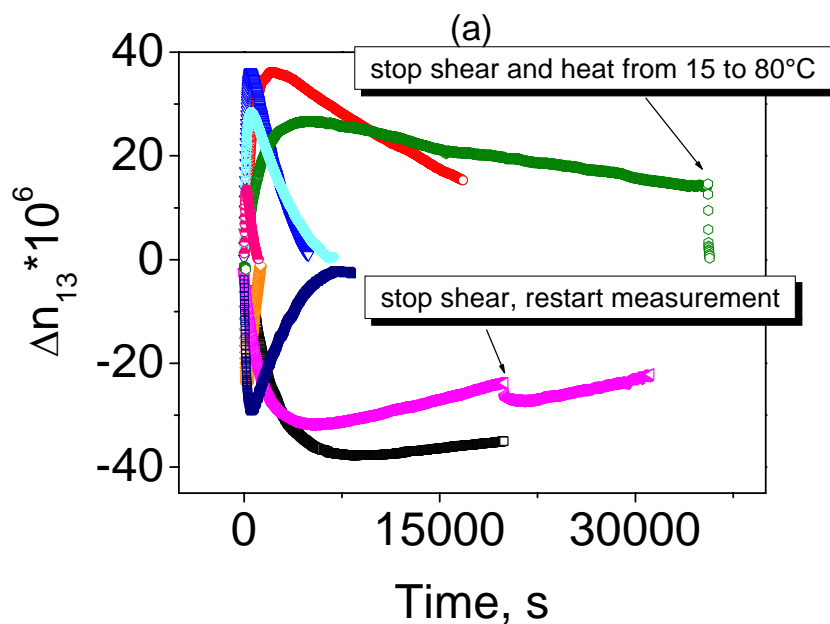
***Relationship between shear flow and  $T_{ODT}$ .***

The Figures 4-5b, 4-6b, 4-7b show a rheoptical determination of the ODT upon heating in oscillatory shear flow within a range of frequencies (0.1, 1, 10 rad/s). While the magnitude of the induced birefringence varies, there is no change in the transition temperature over the investigated range of frequencies, remaining always approximately at  $T_{ODT} \sim 22^\circ\text{C}$ . On the other hand, oscillatory flow experiments in which the strain amplitude was varied in a similar way, showed no effect on the ODT. For PS-PI (~80K) in DOP the change from a perpendicular alignment at low frequency toward a parallel alignment at higher frequency has been proven by Zryd et al.<sup>69</sup>. This behavior agrees with that of diblock copolymer melts. It thus appears that our solution exhibits only *perpendicular alignment* over a broad range of frequencies and strain amplitudes and does not flip from perpendicular to parallel alignment by increasing the strain amplitude. If there would occur such a transition at higher values for frequency and/or strain amplitudes, cannot be checked due to experimental limitations. In the accessible range of frequencies and shear amplitudes the main factor influencing the flip from perpendicular to parallel orientation is the viscoelastic contrast between blocks. Due to the absence of this viscoelastic contrast,  $S_{50}T_{50}^{100}$  in DOP shows only one type of alignment.

**4.2.3 Alignment of high molecular weight  $S_{33}B_{33}T_{34}^{160}$  triblock terpolymer solution*****Alignment kinetics of terpolymer 20wt-%SBT solution in DOP at  $\omega=10$  rad/s and  $T=15^\circ\text{C}$ .***

In this section we report on the sensitivity to shear of a  $S_{33}B_{33}T_{34}^{160}$  solution in the initially ordered state, under predetermined alignment conditions obtained from the previous rheological and SAXS investigations. In agreement with Kornfield's definition of the alignment regimes, the chosen frequency of 10 rad/s for the alignment process would be expected to generate a parallel alignment of lamellae. The following protocol is that the sample before loading is heated up above the order-disorder transition, to erase the thermal history, afterwards it follows a cooling down at a certain temperature to assure growing and segregation into randomly oriented grains. By applying large amplitude oscillatory shear always parallel alignment is induced by different intermediate pathways as shown in Figure 4-9a. The evolution of birefringence during alignment is dramatically different while as a final state always a parallel alignment is reached at low strain amplitudes  $\gamma_0=40\%$  and  $60\%$  after long time scale higher than 20000s. At the first stages of the alignment process, the birefringence value,  $\Delta n_{13}$  rapidly becomes large with alternating positive and negative values

even in the case of the repeated experiments at the same strain amplitudes. These initial fast processes ( $t \sim 5000$ s) are followed by a much slower decrease of birefringence to a value close to zero, which is not seen in Figure 4-9a for the case of low strain amplitude  $\gamma_0=40\%$  due to the required long time ( $t > 40000$ s). A positive birefringence  $\Delta n_{13}$  implies as intermediate route the perpendicular alignment of lamellae and negative birefringence  $\Delta n_{13}$  implies transverse alignment as intermediate route. The coexistence of a mixed perpendicular and transverse intermediate aligned state is obvious through the same maximum absolute value of birefringence reached at the same strain amplitude but different signs, as already shown in Figure 4-9a and summarized in Table 4-3. A slight difference between absolute value of birefringence has been encountered for the same experimental conditions due to the impossibility to achieve a zero birefringence as a starting value before applying shear. The same sample has been used for all experiments presented in Figure 4-9a and the history of the sample has influenced the maximum absolute value of birefringence. Therefore shear experiments were repeated few times for the same shear strain amplitude and the different sign of the birefringence value evidenced coexistence of a mixture of perpendicular and transverse transient states. Although, the final parallel aligned state has been induced due to the applied shear, a route to check the validity of induced macroscopic alignment has been achieved through a cessation of shear and increasing the temperature from  $15^\circ\text{C}$  to  $80^\circ\text{C}$  (Figure 4-9a,  $\gamma_0=40\%$ ) lead to zero birefringence. Thus, the macroscopic alignment was erased by heating up close to ODT and the system became homogeneous.



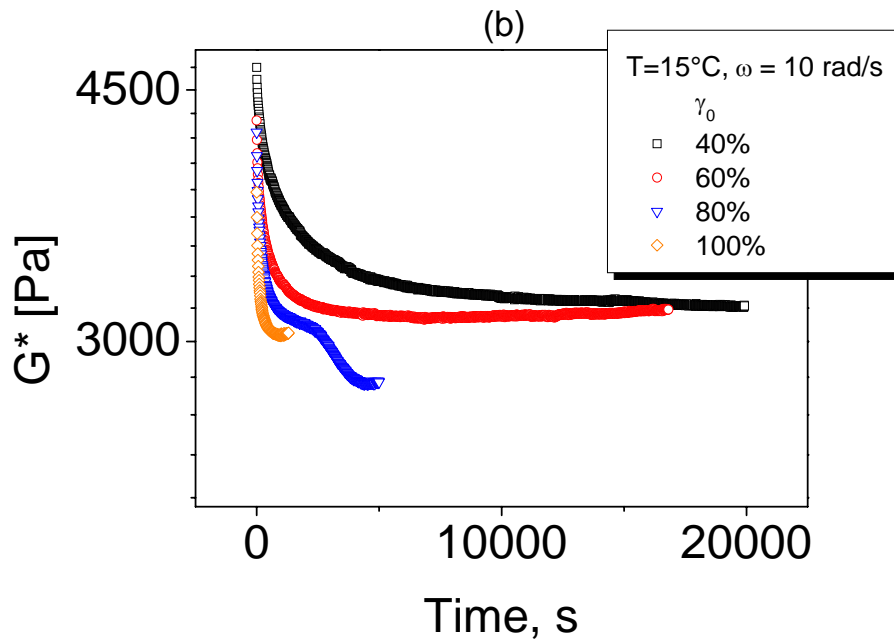


**Figure 4-9.** (a) Evolution of 1,3-birefringence ( $\Delta n_{13}$ ) during large amplitude oscillatory shear alignment at  $T=15^\circ\text{C}$ ,  $\omega=10$  rad/s within different strain amplitudes  $\gamma_0$ : ( $\square$ )40%; ( $\circ$ )60%; ( $\nabla$ )80%; ( $\diamond$ )100% to a final parallel aligned state. Some of the measurements at different strain amplitudes  $\gamma_0$ : ( $\blacktriangleleft$ )40%; ( $\odot$ )40%; ( $\boxplus$ )80%; ( $\oplus$ )80%; ( $\ominus$ )100% were repeated in order to elucidate the transient state leading toward a final parallel aligned state. (b) Evolution of complex moduli versus time during large amplitude oscillatory shear at the following strain amplitudes: ( $\square$ )40%; ( $\circ$ )60%; ( $\nabla$ )80%; ( $\diamond$ )100%. For clarity there have been not plotted the repeated experiments since they showed the same dependence with time scale.

Strain amplitude, $\gamma_0$ [%]	$\Delta n_{13}^{\text{max.}} \times 10^6$	Time, s
40	(-)38	6900
60	(+)36	2000
80	(+)36	380
100	(-)24	230
40 repeat	(-)31	4300
40 repeat	(+)26	4700
80 repeat	(-)29	380

80 repeat	(+)29	380
100 repeat	(+)13	230

**Table 4-3.** The sign and absolute values of birefringence,  $\Delta n_{13}$ , versus strain amplitudes within the required time to achieve a maximum value of birefringence, shown previously in Figure 4-9a.

The complex dynamic moduli during shear show initially a sharp drop followed by a gradual flattening as illustrated in Figure 4-9b. At small strain amplitudes ( $\gamma_0 = 40\%$  and  $60\%$ ) the moduli behavior is like for usual bulk systems, first decreasing and then followed by an asymptotically constant value. Higher strain amplitudes ( $\gamma_0 = 80\%$  and  $100\%$ ) have induced a two steps process in decreasing of moduli, which may be related to the existence of entanglements. Relaxation dynamics of the chain are quite important for the high strain amplitudes ( $\gamma_0 = 80\%$  and  $100\%$ ) which cause a minimum of moduli due to the lack of equilibrium in the long period of lamellae, followed by an enhancing of the moduli value and finally a gradual decreasing of moduli is achieved ( $\gamma_0 = 80\%$ ). This unusual behavior of moduli when a *priori* transverse alignment occurred reveals an insight into the dynamics of the chain without inducing changes in the sign and absolute value of birefringence. These dynamic moduli measurements together with the values of birefringence approaching zero, allow us to infer that the final alignment is along parallel direction.

According to Figure 4-3, the master curves revealed critical values of frequencies,  $\omega_c' \sim 5$  rad/s and  $\omega_c'' \sim 0.5$  rad/s and confirm the Kornfield's classification for  $\omega > \omega_c'$  where a parallel alignment was encountered for the bulk systems. In our experiments, the chosen frequency  $\omega = 10$  rad/s was above the highest critical frequency which arised from different chosen reference temperature, namely  $\omega_c' = 5$  rad/s and the alignment process toward a parallel aligned state, as expected, has been achieved.

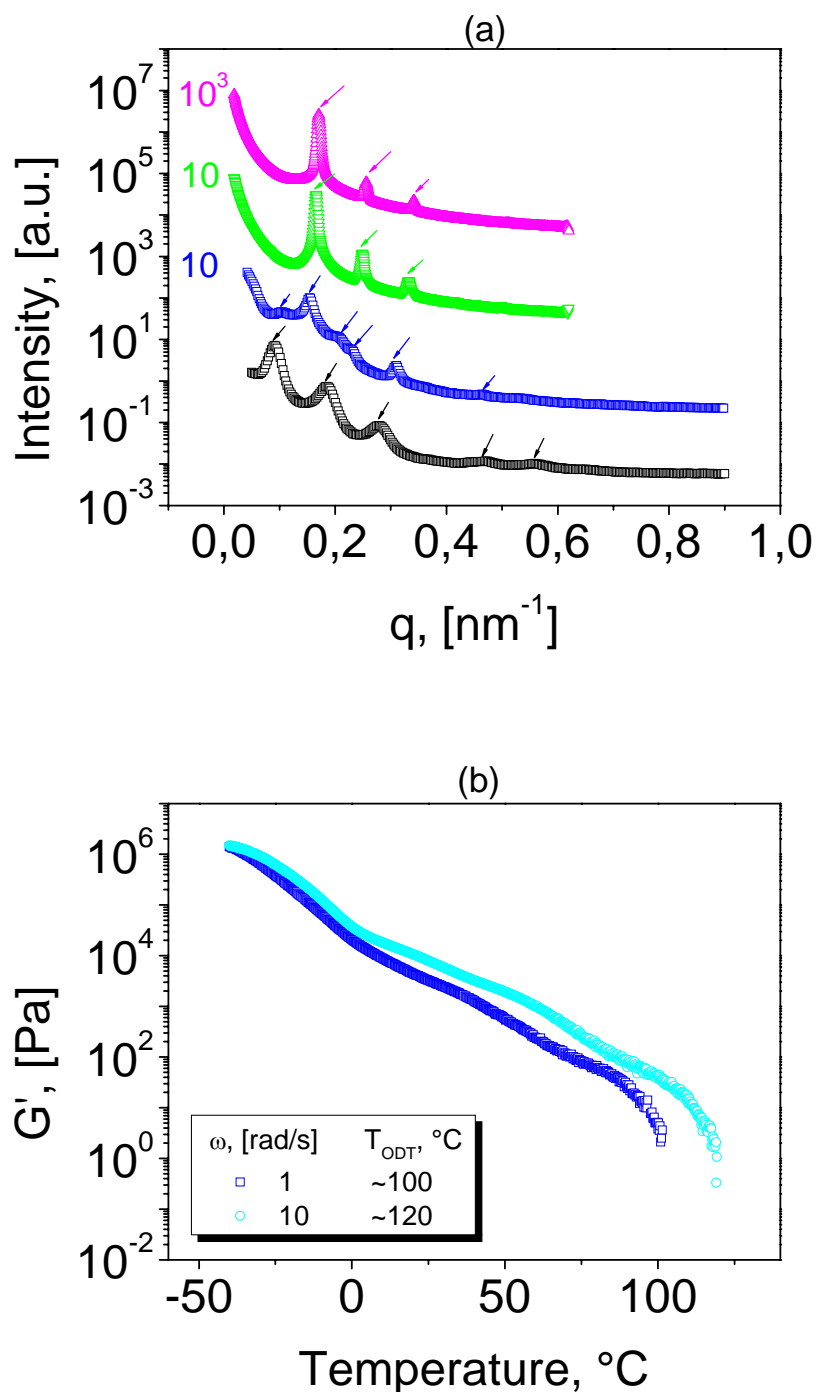
#### 4.2.4 Alignment of non-centrosymmetric blend $S_{33}B_{33}T_{34}^{160}:S_{50}T_{50}^{100}=60:40$ in solution

##### ***Rheological behavior, SAXS profiles and alignment kinetics for a non-centrosymmetric blend SBT:ST=60:40 as solution 30 wt-% in DOP***

*A priori* investigation whether the system is microphase separated has been accomplished by using small angle X-ray scattering and rheological methods as illustrated in Figure 4-10. Scattering profiles from the cast film from  $CHCl_3$  show the correlation peaks corresponding to the lamellar morphology within ratio 1 : 2 : 3 : 5 : 6 while from a solution of 40wt-% blend in DOP the first order reflexion is diminished and it follows the correlation peaks 1 : ( $2^{0.5}$ ) : ( $4^{0.5}$ ) : ( $5^{0.5}$ ) : ( $9^{0.5}$ ) : 4.43 which may be assigned to an induced bcc morphology. Due to the low content of polybutadiene block in the blend it may happen that swollen polybutadiene forms spheres embedded in a matrix of polystyrene and poly(*t*-butyl methacrylate) giving rise to the induced bcc morphology. Furthermore, for a 30wt-% blend in DOP three well defined peaks are developed corresponding to the ratio 1 : 1.48 : 2 at  $T=27^\circ C$  and a slight shift of the peaks toward higher  $q$  values with the same preserved ratio 1 : 1.49 : 2 at  $T=50^\circ C$  is encountered. Over the range of investigated concentrations the long period has been decreased within the increasing dilution ratio from  $L\sim 70nm$  in the cast film toward  $L\sim 60nm$  for 40wt-% blend in DOP and furthermore to  $L\sim 38nm$  for 30wt-% blend in DOP. Thus, increasing the temperature at  $T=50^\circ C$  in the case of 30wt-% blend in DOP is accompanied through a shifting of peaks at higher scattering vectors as a consequence of transitions of the ordered morphology to less ordered and further to disordered state at higher temperature than  $50^\circ C$ .

Additionally, the order-disorder transition temperature,  $T_{ODT}$  has been investigated through a scanning of moduli with increasing temperature for the solution 30wt-% blend in DOP, as illustrated in Figure 4-10b. At  $\omega=1$  rad/s has been obtained the order-disorder transition temperature of  $T_{ODT} \sim 100^\circ C$  while at higher frequency  $\omega=10$  rad/s the ODT has been shifted at higher values  $T_{ODT} \sim 120^\circ C$  without an indication of intermediate order-order transition temperature at 30wt-% blend in DOP. Instead, at 40wt-% blend in DOP the SAXS profile indicated a bcc morphology which allows us to claim the selectivity of DOP for this blend. According to the above mentioned investigations we are aware about the lamellar morphology at the concentration of 30 wt-% blend in DOP and about the existence of a microphase separated system at room temperature. Thus, for the microphase separated 30wt-% blend in DOP the most reliable parameters for the alignment process could be the temperatures of

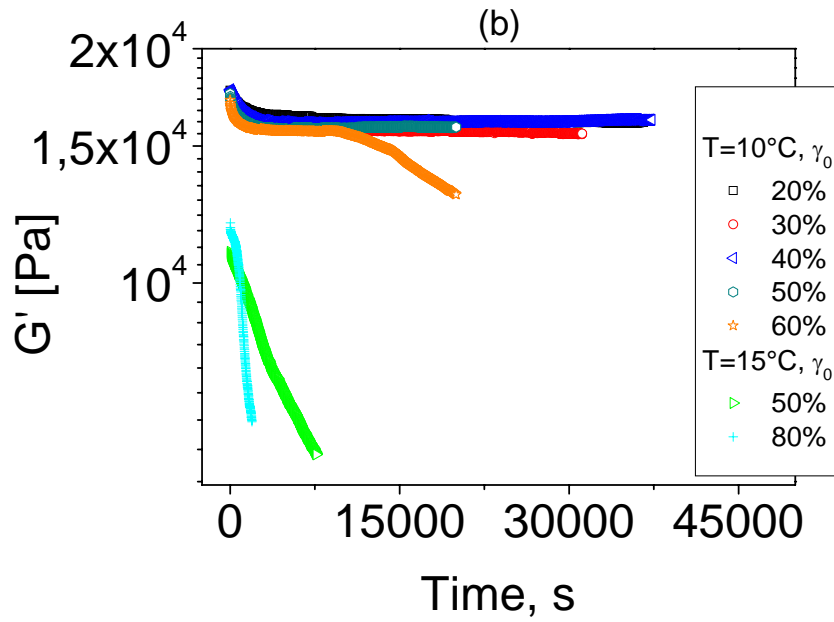
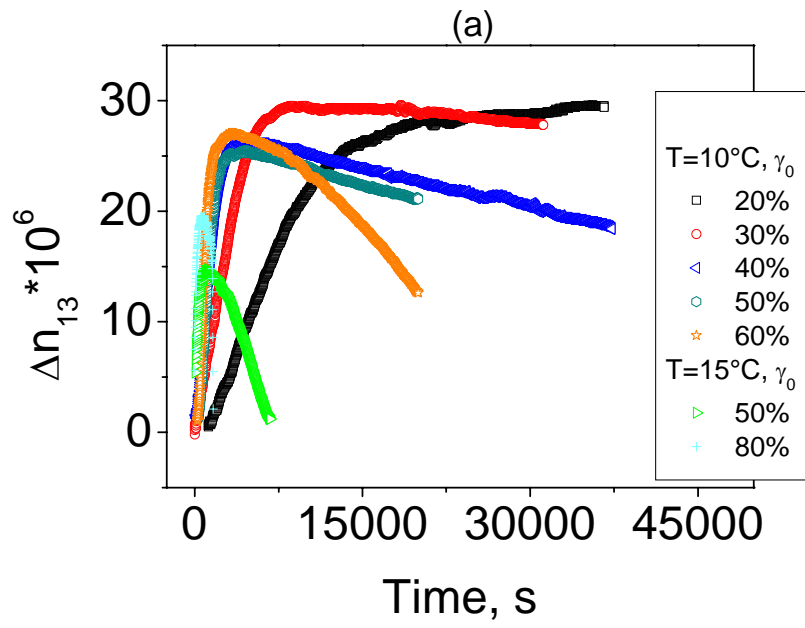
$T=10^{\circ}\text{C}$  or  $T=15^{\circ}\text{C}$ , respectively with a frequency of  $\omega=10$  rad/s (Figure 4-10b) or  $T=25^{\circ}\text{C}$  (Figure 4-10a).



**Figure 4-10.** (a) Comparison of the scattering profiles at  $T=25^{\circ}\text{C}$  for a non-centrosymmetric blend SBT:ST=60:40 as cast film from  $\text{CHCl}_3$  and different concentrations in DOP as following: (—□—) cast film; (—□—) 40wt-% blend in DOP; (—▽—) 30wt-% blend in DOP at  $T=27^{\circ}\text{C}$ ; (—△—) 30wt-% in DOP at  $T=50^{\circ}\text{C}$ . The arrows from the plots indicate the position of correlation peaks. (b) The dependence of moduli with temperature for 30wt-%

blend in DOP at the frequencies  $\omega=1$ , and 10 rad/s within heating rate 1°C/min. A strain amplitude of 0.15% has been employed in the isochronal test, to remain within the linear viscoelastic regime.

The established conditions for the alignment process during an applied shear have been summarized in the plot  $\Delta n_{13}$  versus time, in Figure 4-11a. The encountered birefringence has positive values over the whole range of strain amplitudes at both temperatures, the only difference is related to the fast process which has been developed at the very early stages for the highest strain amplitudes. An enhancement in the fast process was achieved at large strain amplitudes. For example at strain amplitude of  $\gamma_0=50\%$  and alignment temperature of  $T=10^\circ\text{C}$  the fast process occurs within  $t=3500\text{s}$  instead at  $\gamma_0=50\%$  and  $T=15^\circ\text{C}$  the development of the fast process was faster than  $t=1000\text{s}$ . This might be explained by the increased mobility of the chain with increasing temperature and the sliding of lamellae toward the energetically favored state is accomplished. As it might be seen in the Figures 4-11b,c an overlapping of moduli at low strain amplitudes ranging from  $\gamma_0=20\%$  to  $\gamma_0=50\%$  was reached, instead a yield behavior in the corresponding 1,3 birefringence plot was encountered. Upon a critical strain amplitude  $\gamma_0=60\%$  and  $T=10^\circ\text{C}$  a large drop in moduli (Figures 4-11b,c) has been observed. Furthermore, due to the increased temperature at  $T=15^\circ\text{C}$  at high strain amplitudes  $\gamma_0=50\%$  and  $\gamma_0=80\%$  a dramatic drop in moduli accompanied through a rich behavior in birefringence was monitored. For these particular conditions ( $T=15^\circ\text{C}$ ,  $\gamma_0=50\%$  and  $\gamma_0=80\%$ ) is obvious the parallel alignment as a final state (Figure 4-11a), while for the low strain amplitude  $\gamma_0=20\%$  over the investigated time scale is assumed the occurrence of a perpendicular alignment which flips toward parallel at a critical strain amplitude,  $\gamma_C > 30\%$ .



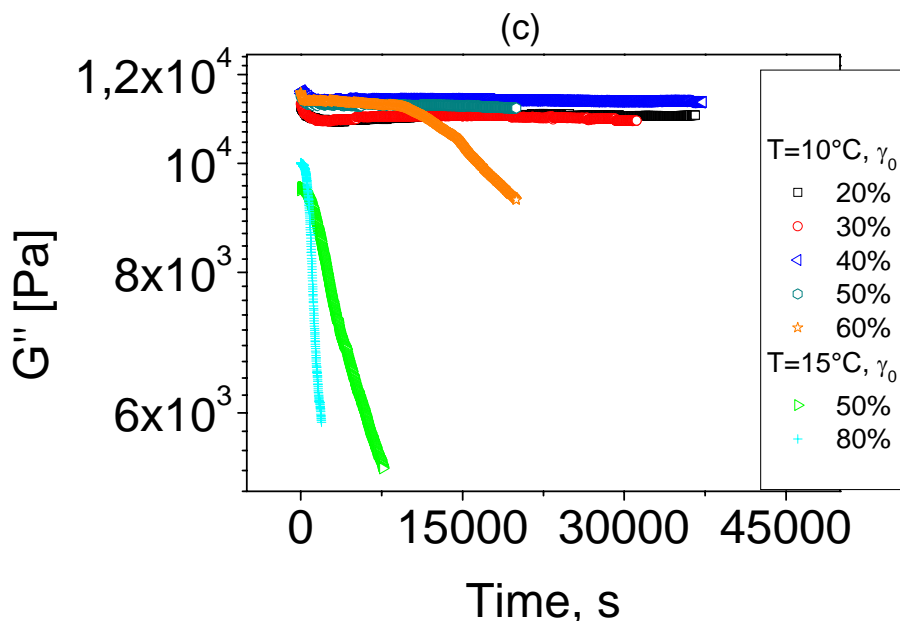


**Figure 4-11.** (a) Evolution of 1,3 birefringence toward a final parallel aligned state for the non-centrosymmetric blend 30wt-% in DOP by applying shear at two temperatures and different strain amplitudes: i)  $T=10^{\circ}\text{C}$  and ( $\square$ )20%, ( $\circ$ )30%, ( $\triangleleft$ )40%, ( $\diamond$ )50%, ( $\star$ )60%; ii)  $T=15^{\circ}\text{C}$  and ( $\triangleright$ )50%, ( $+$ )80%; (b), (c) The evolution of storage and loss moduli during alignment process from part (a).

As a conclusion the lamellar blend as solution of 30wt-% SBT:ST=60:40 in DOP undergoes only parallel alignment which is obvious above a critical strain amplitude of  $\gamma_c > 30\%$ .

A quantitative approach of aligned system illustrated in Figure 4-11a has been summarized in Table 4-4. The investigated non-centrosymmetric blend SBT:ST=60:40 develops toward parallel alignment via perpendicular as transient state for which the polybutadiene block has been responsible.

Strain amplitude, $\gamma_0$ %		$\Delta n_{13}^{\text{max.}} \times 10^6$	<sup>1)</sup> Time, s
30 wt-% SBT:ST=60:40 in DOP, $\omega=10$ rad/s			
T=10°C	20	(+)30	>35000
	30	(+)30	8000
	40	(+)26	4500
	50	(+)25	4400
	60	(+)26	3200
T=15°C	50	(+)14	1000

	80	(+)19	650
--	----	-------	-----

<sup>1)</sup>the required time for occurrence of the fast process with a maximum in birefringence value.

**Table 4-4.** Comparison of the sign and absolute values of birefringence,  $\Delta n_{13}$ , within strain amplitudes,  $\gamma_0$  and the required time for attaining a maximum value of birefringence shown previously in Figure 4-11a.

At very low strain amplitudes,  $\gamma_0=20\%$  the effect of strain on the slow process is also profound, it seems that below a critical strain the fast process is missing and the alignment is never perfected (Figures 4-11a).

#### 4.2.5 Theoretical estimation of birefringence in diluted diblock copolymer

##### $S_{50}T_{50}^{100}$ in DOP

The first reports about static birefringence measurements on well-ordered lamellar and cylindrical block copolymers have been developed by Folkes and Keller<sup>182,183</sup> and later other groups examined birefringence for symmetric polystyrene-b-poly(methyl methacrylate) low molecular weight (37K, 31K) near the order-disorder transition in the melt state.<sup>184</sup> Previously, it has been assumed that the form birefringence of a block copolymer morphology would completely dominate the intrinsic contribution. Moreover, the numerical estimation of intrinsic birefringence shows that, in general, this is not the case for a “single-crystal”. For example, in the case of polystyrene-polydiene<sup>72,183</sup> the form contribution is relatively large due to the difference in the refractive index between the two blocks, whereas the intrinsic contribution is reduced because the polarizability anisotropies differ in sign. Therefore, using the concept of strongly-stretched chains as a function of distance from the grafting surface, so called “tethered chains”, the birefringence of polymer brushes and strongly segregated block copolymer has been computed.

In this section our attempt is directed on evaluation of form and intrinsic birefringence contributions for the solution of 30wt-%  $S_{50}T_{50}^{100}$  in DOP. A classification of this system whether it is in the strong or weak segregation limit has been achieved by making use of the correlation between layer thickness ( $L$ ) and degree of polymerization ( $N$ ). For a block copolymer in the strong segregation limit (SSL), due to the Helfand-Wasserman theory<sup>24</sup>, the relationship is valid  $L \sim N^{0.67}$ . Taking into account this power law relationship with *a priori* determination of long period from transmission electron micrograph (cast film from

chloroform), for the ST bulk system it was found:  $L(TEM) \propto 43nm$  and an exponent of 0.55, which may corresponds to an intermediate regime of segregation, where  $N(ST) \sim 832$ . Assuming that the system ST is in intermediate regime of segregation (ISL), an attempt of theoretical estimation of birefringence has been made by using an expression valuable for a lamellar melt diblock in strong segregation limit. The form birefringence for diblock copolymer melt has been estimated using the expression:<sup>185</sup>

$$\Delta n_f = (n_A n_B) / [\phi_A n_B^2 + \phi_B n_A^2]^{0.5} - ([\phi_A n_A^2 + \phi_B n_B^2]^{0.5}) \quad (4-1)$$

where  $n_A = n_{PS}$ ,  $n_B = n_{PT}$ .

Using the values of refractive indices<sup>186</sup> for polystyrene (PS) and poly(*t*-butyl methacrylate) (PT)  $n_{PS} = 1.59$ ;  $n_{PT} = 1.492$  within the corresponding volume fractions,  $\phi_{PS} = 0.53$ ;  $\phi_{PT} = 0.46$  (Table 2-4) should be taken into account that a contribution part (namely 70%) from each refractive indices is due to the solvent, DOP ( $n_{DOP} = 1.48$ ) and the rest (30%) is due to the pure chains. According to this assumption has been involved the concept of “swollen chain”, and the most likely expressions for the refractive indices are written:  $n_{PSswollen} = 0.3n_{PS} + 0.7n_{DOP}$  and  $n_{PTswollen} = 0.3n_{PT} + 0.7n_{DOP}$ , respectively. These expressions for the refractive indices of the swollen chains have been used in the relation (4-1) and the form birefringence has been calculated  $\Delta n_f(ST) = 0.01467$ . In addition, the intrinsic birefringence contribution can be calculated with the expression:

$$\Delta n_i = (\pi^3 / 90) N_A [(M_A / \rho_A) + (M_B / \rho_B)]^{-1} \left\{ (n_A^2 + 2)^2 / n_A (\alpha_1 - \alpha_2)_A (L_A^2 / \langle h_{A,0}^2 \rangle) + [(n_B^2 + 2)^2 / n_B] (\alpha_1 - \alpha_2)_B (L_B^2 / \langle h_{B,0}^2 \rangle) \right\} \quad (4-2)$$

where A and B denote the polystyrene (PS) and poly(*t*-butyl methacrylate) (PT),  $\rho_{A,B}$ -mass density of the blocks PS and PT,  $M_{A,B}$ -molecular weight for PS and PT, g/mol,  $L_{A,B}$ -thickness of PS and PT, respectively, nm;  $\langle h_{A,B,0}^2 \rangle$  is the mean-square end-to-end distance of the unperturbed chain; for the refractive indices  $n_{A,B}$  from eq. 4-2 there have been used the expressions of refractive indices for the swollen chains. The polarizability anisotropy,  $(\alpha_1 - \alpha_2)_{A,B}$ , may be estimated as  $-1.5 \times 10^{-23} cm^3$  for PS<sup>185</sup> and  $1.37 \times 10^{-23}$  for PT.<sup>222</sup> The ratio  $L_{A,B}^2 / \langle h_{A,B,0}^2 \rangle$  represents the degree of stretching for each chain under the assumption that the lamellar interface between blocks plays the role of a fixed surface and the chains are stretching away accordingly from this interface. Due to the nearly symmetric diblock copolymer in ISL, the relative stretching of the two blocks should be comparable,

which may be written as:  $(L_{PS}^2 / \langle h_{PS}^2 \rangle_0) \approx (L_{PT}^2 / \langle h_{PT}^2 \rangle_0)$ . A rough estimation of the degree of stretching of PS has been made:  $\langle h_{PS}^2 \rangle_0 \propto 6R_g^2 \propto 6(0.00087M) \propto 261nm^2$  and  $L_{PS}(TEM) \propto 11nm$ , resulting  $(L_{PS}^2 / \langle h_{PS}^2 \rangle_0) \propto 0.46$ . Assuming the same degree of stretching for the chains, the intrinsic birefringence calculated with eq 4-2 is:  $\Delta n_i = -0.2041 \times 10^{-4}$ . The experimental birefringence measured by generating “single-crystal” induced by shear, has been found in the range:  $\Delta n_{exp} = (0.5 \div 1.2) \times 10^{-4}$  quite in a good agreement with the calculated intrinsic birefringence. Table 4-5 summarizes some literature data in comparison to our system. We should mention regarding the literature data that the birefringence values were obtained from the melt state of a lamellar and cylindrical SBS triblock copolymer without any influence from solvent, which is different from our system.

Sample	<sup>a)</sup> $\Delta n_{form}$	<sup>b)</sup> $\Delta n_{intrin}$	<sup>c)</sup> $\Delta n_{exp}$
<sup>1)</sup> 30wt-% ST in DOP	$14.67 \times 10^{-3}$	$-0.2041 \times 10^{-4}$	$(0.5 \div 1.2) \times 10^{-4}$
<sup>2)</sup> SBS lamellar	$-1.54 \times 10^{-3}$	$-0.7 \times 10^{-3}$	$(-2.7 \pm 0.2) \times 10^{-3}$
<sup>2)</sup> SBS cylindrical	$5.2 \times 10^{-4}$	$8.7 \times 10^{-4}$	$4.9 \times 10^{-4}$

<sup>a)</sup>calculated using eq 4-1; <sup>b)</sup>calculated using eq 4-2; <sup>c)</sup>determined experimental from the Figures 4-5a, 4-6a, 4-7a.; <sup>1)</sup>our investigated diluted system; <sup>2)</sup>literature data such as polystyrene-b-poly(1,2-butadiene)-b-polystyrene (SBS) with the corresponding molecular weights for each block and different morphologies: i) lamellar,  $M_{PS} \sim 14K$ ,  $M_{PB} \sim 30K$ ; ii) cylindrical,  $M_{PS} \sim 10K$ ,  $M_{PB} \sim 55K$ .

**Table 4-5.** Comparison of the experimentally and theoretically birefringence of the 30wt-%  $S_{50}T_{50}^{100}$  diblock copolymer in DOP with the lamellar and cylindrical triblock copolymer SBS melt. <sup>185</sup>

For the diluted system  $S_{50}T_{50}^{100}$  a high discrepancy between the form birefringence and the experimental values has been encountered, while a quite good agreement seems to exist between the calculated intrinsic birefringence and the experimental one, on an absolute scale. An induced morphology slightly different from the lamellar one may be possible due to the fact that DOP is a  $\Theta$ -solvent for PS<sup>157</sup> ( $T_{\Theta} = 7^{\circ}C$ ) and the selectivity of DOP for poly(*t*-butyl methacrylate) should be involved. The alignment protocol for 30wt-% $S_{50}T_{50}^{100}$  in DOP was performed at  $T=10^{\circ}C$  and  $T=14^{\circ}C$  quite close to  $T_{\Theta}$  for PS and different contributions in terms of form and intrinsic birefringence from each block should be involved and accounted

to the overall birefringence value. Moreover, the experimental birefringence for diluted  $S_{50}T_{50}^{100}$  has been monitored under an applied shear, while the equations 4-1 and 4-2 were developed for static quantities, in the sense that no external field was applied. Furthermore, we have made the assumption for the bulk system to be in ISL, but we have not taken into account that for a swollen system the degree of segregation is decreased. Thus, we may claim that the monitored experimental birefringence is due to the chain stretching, therefore a lack of equilibrium was found between form and intrinsic contributions for the diluted ST system. The following values of polarizability anisotropy of the involved monomers and solvent are obtained:  $(\alpha_1 - \alpha_2)_{PS} = -1.5 \times 10^{-23} \text{ cm}^3$ ;  $(\alpha_1 - \alpha_2)_{PT} = 1.37 \times 10^{-23} \text{ cm}^3$ ;  $(\alpha_1 - \alpha_2)_{DOP} = 4.53 \times 10^{-23} \text{ cm}^3$ . The difference in sign between the polarizability anisotropy of each monomer and solvent and between the monomers appears, so it may explain for the negative and slightly lower calculated value of intrinsic birefringence than the experimental value.

### 4.3 Conclusion

The main goal of this part was to demonstrate that by choosing an appropriate chemical sequence of blocks a selective type of macroscopic alignment by LAOS can be achieved. A concentrated solution of entangled ST diblock copolymer in DOP showed only perpendicular alignment with respect to the shear direction and no parallel orientation was found even at higher shear frequencies. This is attributed to the absence of a large viscoelastic contrast in this system, as compared to lamellar polystyrene-b-polyisoprene diblock copolymers with a large viscosity contrast.

The theoretical intrinsic birefringence in close proximity to the experimental birefringence, allowed us to point out the high intrinsic birefringence contribution for the solution of ST diblock copolymer. The evidence of only a preferred perpendicular alignment of lamellae is obvious through the alignment processes illustrated in Figures 4-5a, 4-6a, 4-7a.

The introduction of the third elastomeric block as a middle block between the thermoplastic outer blocks, namely SBT triblock terpolymer in the diluted state, lead to significant changes in the sense of tunable intermediate (perpendicular and transverse) aligned states by applying shear toward stable and energetically favorable final parallel oriented states.

Finally, the investigation of non-centrosymmetric blend SBT:ST=60:40 allowed preferential type of alignment (parallel) above a critical strain amplitude,  $\gamma_c$  as following: i)  $\gamma$

$< \gamma_C$  only perpendicular alignment is achieved which was not perfected toward a saturated value within the time scale used in our experiments; ii)  $\gamma \cong \gamma_C$  a tendency toward a final parallel alignment via perpendicular was found; iii)  $\gamma > \gamma_C$  and together with an increased temperature from 10°C to 15°C showed an obvious parallel alignment through an intermediate perpendicular state.

It is worth to point out the opportunity to create designed aligned structures by carefully choosing the block sequences of the block copolymer.

For the overall alignment processes of the block copolymer solutions investigated here, it may be pointed out the extended behavior of block copolymer melts of low molecular weight to block copolymer solutions of high molecular weight, diblock and triblock terpolymer, for which the alignment protocol in the bulk state would be impossible due to the required high temperatures for the alignment and the high viscosity involved which would be a disadvantage at macroscale processing.

## 5. Weak Segregated Systems (Lamellae-Cylinder Morphology) in LAOS and Steady Mode

### 5.1 Introduction

In the past decade, beside usual block copolymers containing unsaturated bonds along the main chain, many investigators have utilized fully saturated polymers<sup>41,187</sup>, to study various topics in polymer science including rheology, chain dimensions, and block copolymers thermodynamics.

Two hydrogenation techniques, heterogeneous and homogeneous, have been shown to be effective methods for attaining saturated polymers. In a study comparing these techniques the homogeneous method led to the incorporation of metal fragments into the polymer chain.<sup>188</sup> Homogeneous hydrogenation yields high conversions, sometimes causes chain scission and often leads to metal contamination due to catalyst extraction difficulties. The hydrogenated systems possess greater stability toward oxidative and thermal degradation and offer a higher use temperature associated with the increased  $T_g$ . The most interesting parameter accomplished from the hydrogenated block copolymers is the segment-segment interaction parameter,  $\chi$  which becomes larger than the one for unsaturated block copolymers. Due to the increased value of the interaction parameter,  $\chi$ , the hydrogenation method is one of the tools to achieve an improvement in the degree of segregation.

The process of flow-induced alignment in lamellae-cylinder triblock copolymer SBM is investigated using simultaneous measurements of shear stress and birefringence. Rheo-optical measurements were used as in-situ methods to characterize the form and orientation of these nanostructures under shear. The simplicity of birefringence measurements was recognized earlier by Pakula.<sup>189</sup> It has been already pointed out that birefringence technique can be applied to any microstructured block copolymer, even for samples which exhibit little or no form birefringence, with a measurable intrinsic birefringence. Moreover, it has been shown that in certain cases<sup>190</sup> rheo-optical investigations are ten times more sensitive than the mechanical methods giving information about dynamic behavior of local and global structures, intermolecular and intramolecular interactions and detect changes in the solution structure. Kornfield<sup>70</sup> has already shown the possible alignment kinetics of lamellar block copolymers, mostly for diblock copolymers<sup>1,191</sup>, by using the rheo-optical method. Shearing at different frequencies but at the same temperature and strain amplitudes<sup>192,75</sup> can produce alignment either with layer normals along the shear gradient direction (parallel) or with layer

normals along the vorticity direction (perpendicular). Much of the experimental work was focused on two classes of systems: (1) polystyrene-polydiene<sup>79,80,193,83</sup> and (2) well entangled polyolefin diblocks wherein the components have similar glass transition temperatures and flow alignment is performed at temperatures much higher than either component's glass transition temperature. For some of the investigated lamellar polystyrene-polydiene, induced alignment in the parallel direction<sup>194</sup> was found and other experiments on polyolefin diblocks showed perpendicular alignment.<sup>75</sup>

Koppi and coworkers<sup>75</sup> found perpendicular alignment for lamellar poly(ethylene-alt-propylene)-b-poly(ethyl ethylene) at temperatures near  $T_{ODT}$  while parallel alignment was produced at low shear frequency. Using small-angle neutron scattering (SANS), transmission electron microscopy (TEM), and small-angle X-ray scattering (SAXS), such characterization does not provide any information on the microstructural dynamic response during flow alignment. Thus, in-situ studies are essential to understand the mechanism of flow alignment. Flow birefringence is sensitive to chain orientation, and the birefringence has proven to be a much more sensitive indicator of a final well-aligned state than mechanical properties. Many questions regarding flow-induced alignment in triblock copolymer lamellae-cylinder morphology are raised. For example, when cylinders are present at the interfaces between lamellae in ABC triblock copolymer, does it alter the alignment behavior of the lamellar superstructure? Do the cylinders orient along the flow direction? Are there parallel and perpendicular regimes for the layers? Using birefringence measurements on  $S_{37}B_{14}M_{49}$ <sup>37</sup> and  $S_{34}B_{19}M_{47}$ <sup>65</sup> a systematic study of the effects of shear frequency, strain amplitude, and temperature on the rate, the route and the final direction of alignment was performed.

## 5.2 Results and Discussion

### 5.2.1 Alignment of $S_{37}B_{14}M_{49}$ <sup>37</sup> and $S_{34}B_{19}M_{47}$ <sup>65</sup>

Block copolymers composed of at least two different blocks, undergo a microphase separation, when the different blocks become incompatible with each other. The most characteristic feature of a block copolymer is the strong repulsion between sequences even when the repulsion between monomers is relatively weak. When microphase separation occurs, the microdomains are not located at random but they may form a regular arrangement giving rise to a periodic structure. The influence of the incompatibility, as well as the influence of the composition and degree of polymerization, on the formation of the morphology is quite well understood.<sup>12</sup> Auschra et al. observed cylindrical microdomains of

the minority center block (polybutadiene (PB)) along the polystyrene/poly(methyl methacrylate) (PS/PMMA) lamellar interface in a polystyrene-*block*-polybutadiene-*block*-poly(methyl methacrylate) (SBM) triblock terpolymer.<sup>195</sup> This microdomain geometry has also been confirmed by the theoretical calculations of Zheng and Wang.<sup>196</sup> The materials we are using are triblock terpolymers ( $S_{37}B_{14}M_{49}$ <sup>37</sup>,  $S_{34}B_{19}M_{47}$ <sup>65</sup>) and their hydrogenated analogous ( $S_{37}EB_{14}M_{49}$ <sup>37</sup>,  $S_{34}EB_{19}M_{47}$ <sup>65</sup>), with the characteristics given in the Table 2-5.

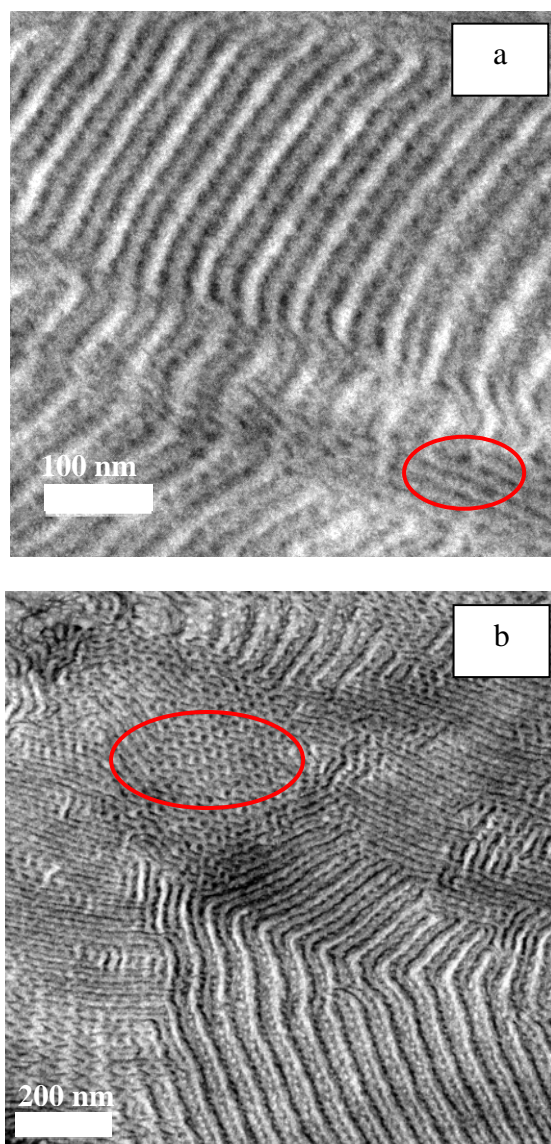


**Figure 5-1.** Morphology of the triblock terpolymer  $S_{34}B_{19}M_{47}$ <sup>65</sup> cast from  $CHCl_3$  and stained with  $OsO_4$  (PS, PMMA lamellae, bright; PB cylinders, dark) at different magnifications. The enclosed arrays represent the gyroid morphology.

Microphase-separated morphologies on the example of polystyrene-*block*-polybutadiene-*block*-poly(methyl methacrylate) (SBM) triblock copolymers were reported earlier.<sup>66</sup> Some of the morphologies of SBM triblock copolymers are presented in a ternary phase diagram at

room temperature (Figure 1-7, Chapter 1). In agreement with the ternary phase diagram the systems under investigation having weight fractions of the midblock more than 10 and less than 17 wt% (E)B showed lamellae-cylinder morphology, as proven by transmission electron microscopy (TEM). However, a weight fraction of PB about 19wt% in  $S_{34}B_{19}M_{47}^{65}$  would involve a morphology at the boundary between cylindrical and gyroid. Figure 5-1 shows micrographs at 100nm (a) and 200nm (b) for the same  $S_{34}B_{19}M_{47}^{65}$  triblock terpolymer where it can be seen that the midblock (polybutadiene) forms cylinders between two lamellae PS and PMMA (PS/PMMA~1:1) and also a gyroid morphology is present as well evidenced within enclosed arrays on TEM micrographs.

However, the lamellar surfaces are not flat, the surface modulation is the result of the formation of cylinders of (E)B at the PS/PMMA phase boundary.

In order to obtain more information about the degree of segregation and the comparison between the unsaturated system SBM and saturated SEBM, respectively, an attempt was to check the validity of the relation

$$L \sim N^x \quad (5-1)$$

for cylindrical block terpolymers and their hydrogenated analogues. Depending on the absolute value of the exponent  $x$  might be possible a classification in weak ( $x \sim 0.5$ ) or strong ( $x \sim 0.66$ ) segregated systems. An evaluation of the long period has been made either by using TEM micrographs or from the scattering profile depending on the electron density contrast of the specimen.

System	N	<sup>a)</sup> L, nm (TEM or SAXS)	<sup>b)</sup> $x$
$S_{37}B_{14}M_{49}^{37}$ (Ic)	410	25.83 (SAXS)	0.54
$S_{34}B_{19}M_{47}^{65}$ (Ic)	755	38.57 (TEM)/41.39(SAXS)	0.55-0.56
$S_{37}EB_{14}M_{49}^{37}$ (II)	410	28.18 (SAXS)	0.55
$S_{34}EB_{19}M_{47}^{65}$ (kp)	755	49.51 (SAXS)	0.58

<sup>a)</sup> Determined from TEM micrograph and/or Synchrotron-SAXS; <sup>b)</sup> using relation:  $L \sim N^x$

**Table 5-1.** Comparison of long period values (L) for the lamellae-cylinder morphology and their homologous hydrogenated.

According to the  $x$  values from the Table 5-1 we conclude that the systems are approximately in the intermediate segregation limit. The long periods determined by using two different methods (TEM and SAXS) are quite different due to the electron density contrast relatively similar in the case of polystyrene and poly(methyl methacrylate) blocks. Thus, for the

lamellae-cylinder morphology SAXS distinguishes the butadiene block from the other two components and the long period measured by X-ray scattering is the distance between two next-neighbour B cylinders following the sequence BMMBSSB. The possible shrinkage of S and even more pronounced M blocks in the TEM micrograph due to the beam damage may explain the different values found for the long period from SAXS and TEM. As seen in Table 5-1 for the hydrogenated specimens the exponent  $x$  is slightly increased as a consequence of increased degree of segregation due to the hydrogenation, as expected.

On the other hand, in the most successful theories of block copolymers in the strong segregation limit of Helfand,<sup>24,25,32</sup> the contribution of the interface free energy is balanced by the requirement of retaining homogeneous segment density. The long spacing,  $L$  is mainly determined by the overall molecular weight, while different compositions differ in the interface free energies calculated for the different morphologies. The interface free energies in the case of S(E)BM systems, take into account three interaction parameters  $\chi_{SB}, \chi_{SM}, \chi_{BM}$ , and the corresponding for hydrogenated system,  $\chi_{SEB}, \chi_{EBM}, \chi_{SM}$ , respectively. According to the Helfand theory<sup>32</sup> for the block copolymers (AB or ABA) with cylindrical microdomains, the interfacial tension,  $\gamma$  in the strong segregation limit is related to the interaction parameter,  $\chi$  according to the relation:

$$\gamma = k_B T \alpha^{1/2} \left[ \frac{\beta_A + \beta_B}{2} + \frac{1}{6} \frac{(\beta_A - \beta_B)^2}{\beta_A + \beta_B} \right] \quad (5-2)$$

where  $\beta_K^2 = \rho_{0K} b_K^2 / 6$  with  $K = A, B$  in the case of diblock copolymer, AB;  $\rho_{0K}$  - monomer density of pure polymer  $K$ ,  $b_K$  - Kuhn statistical length of a monomer unit,  $k_B$  - Boltzmann's constant,  $T$  - temperature,  $\alpha$  - degree of repulsion between  $A$  and  $B$ ,  $\alpha = \chi \rho_0$  with  $\chi$  - Flory-Huggins parameter. By replacing the  $\alpha$  value, relation (5-2) can be written as:

$$\gamma = k_B T \rho_0^{1/2} \left[ \frac{\beta_A + \beta_B}{2} + \frac{1}{6} \frac{(\beta_A - \beta_B)^2}{\beta_A + \beta_B} \right] \chi^{1/2},$$

where the term in brackets could be written as a constant  $C$  taking different values depending on the monomer pair.

$k_B T \rho_0^{1/2} \left[ \frac{\beta_A + \beta_B}{2} + \frac{1}{6} \frac{(\beta_A - \beta_B)^2}{\beta_A + \beta_B} \right] \propto C$  is calculated for each pair of monomers and has values of  $\sim 10^{-33} \text{ N mol m}^{-1}$ . As a consequence of small values of the constant term  $C$ , a rough approximation of the interfacial tension with the interaction parameter was made:

$$\gamma_{xy} \sim (\chi_{xy})^{1/2} \quad (5-3)$$

where  $\chi_{xy}$  are the three combinations S/(EB)B, (EB)B/MMA, and S/MMA. Strong incompatibility (large positive  $\chi$ ) leads to high interfacial tensions. Table 5-2 gives a comparison of the interfacial tensions between the components of the triblock terpolymers SBM, SEBM and literature data (first row in the Table 5-2).

	Components		
	PS/PMMA	PS/B(EB)	B(EB)/PMMA
* $\gamma(150^\circ\text{C})$ [dyn/cm]	1.5	3(5)	(9.5)
<sup>a)</sup> $\chi_{xy}(150^\circ\text{C})$	0.007112	0.034422(0.034422)	0.07282(0.07282)
<sup>b)</sup> $\gamma(150^\circ\text{C})$	0.0843	0.1855	0.2698

\*literature data<sup>197</sup>; <sup>a)</sup>value obtained using relation:  $\chi_{xy} = \frac{V}{RT}(\delta_x - \delta_y)^2$ , where x,y correspond to PS, PB, PMMA; <sup>b)</sup>calculated using relation (5-3).

**Table 5-2.** Interfacial tensions<sup>197</sup> between the components in PS-*b*-P(EB)B-*b*-PMMA and the calculated segment-segment interaction parameter  $\chi_{xy}$  and interfacial tension corresponding to each pair of monomers from triblock terpolymer.

It should be mentioned that the relation (5-2) from the Helfand-Wassermann theory is valid for the systems in the strong segregation limit and we have used it for our systems in order to check whether the systems are in SSL or ISL. According to data from the Table 5-2, the calculated values for interfacial tensions  $\gamma$ , due to the relation (5-3) are much smaller than the interfacial tension values given in the literature, which give us the indication of intermediate or weak segregated system. The interfacial tension between B(EB)/PMMA and B(EB)/PS is much larger than between the less immiscible PS/PMMA pair. Thus the system will tend to minimize its overall interface free energy by reducing the surface of the (B)EB domains. These unfavorable intramolecular repulsive interactions between B(EB)/PMMA, B(EB)/PS are replaced by less unfavorable PS/PMMA interfacial contacts, a behavior encountered as well for homopolymer/copolymer blends.<sup>198,199,200</sup>

While in diblock copolymers the segregation strength may be described by a single dimensionless parameter  $\chi N$ , an analogous parameter in triblock copolymers ABA is described using self-consistent field theory.<sup>33</sup> While the order-disorder transition in symmetric diblock copolymers (AB) occurs at  $\chi N \approx 10.495$ , in multiblock copolymers it is shifted to higher values. For asymmetric ABA triblock copolymers in the WSL a critical value of  $\chi N \approx 18$  was determined<sup>201</sup> and this result was confirmed by works dealing with ABA

triblock copolymers having arbitrary ratio between the two end blocks.<sup>202</sup> Subsequently, Matsen<sup>33</sup> developed the phase diagrams for asymmetric ABA triblock copolymer melts using SCFT spanning the range from WSL to SSL and found the same value of  $\chi N_{ODT} \approx 18$  for ABA triblock copolymers. As an approximation, taking into account these findings from previously work, for the critical value for the parameter  $\chi N$  corresponding to ABA triblock copolymer, our trying in evaluation of  $\chi N$  for lamellae-cylinder triblock terpolymer is summarized in the Table 5-3.

Sample	$N_{PS}$	$N_{PB}$	$N_{PMMA}$	$N$	$^1)f_{PS}$	$^2)\chi N$
$S_{37}B_{14}M_{49}^{37}$	129.8	97.6	182.5	$\sim 410$	0.38	23.5
$S_{34}B_{19}M_{47}^{65}$	213	$\sim 232$	310	$\sim 755$	0.35	22.5

<sup>1)</sup>volume fraction of polystyrene;<sup>2)</sup>using similar approximation like for diblock copolymers,  $\chi N = 18 + \frac{41.022}{N^{1/3}}$ , approach made due to the critical value of  $\chi N \approx 18$  from the phase diagram<sup>33</sup> for ABA triblock copolymer.

**Table 5-3.** Calculated  $\chi N$  values for lamellae-cylinder triblock terpolymers SBM.

For the two SBM specimens presented in Table 5-3 with the calculated values of the product,  $\chi N$  an evaluation of the expected morphology could be reached according to the phase diagram<sup>33</sup> for asymmetric ABA triblock copolymers. Thus, for  $S_{37}B_{14}M_{49}^{37}$  with the volume fraction of polystyrene block,  $f_{PS} \approx 0.38$  and the product  $\chi N \approx 23.5$  it follows the cylindrical morphology, while for the system  $S_{34}B_{19}M_{47}^{65}$  with  $f_{PS} \approx 0.35$  and  $\chi N \approx 22.5$  the corresponding morphology is at the boundary between cylindrical and gyroid morphology. We should mention that all these findings related with the calculated  $\chi N$  making use of the phase diagram<sup>33</sup> developed for ABA triblock copolymers were under the assumption that polystyrene and poly(methyl methacrylate) blocks manifest similar behavior in terms of interfacial tensions with the middle block (Table 5-2) and we may treat these blocks as chemically similar.

So far, our attempt is to align the structures of lamellae-cylinder morphology  $S_{37}B_{14}M_{49}^{37}$ ,  $S_{34}B_{19}M_{47}^{65}$  triblock terpolymers and their homologous hydrogenated  $S_{37}EB_{14}M_{49}^{37}$ ,  $S_{34}EB_{19}M_{47}^{65}$  triblock terpolymers, into a mesoscopic monodomain under influence of mechanical field (LAOS). Using the phase diagram valid for asymmetric ABA triblock copolymers we have shown that the polymers  $S_{37}B_{14}M_{49}^{37}$ ,  $S_{34}B_{19}M_{47}^{65}$ ,  $S_{37}EB_{14}M_{49}^{37}$  and

$S_{34}EB_{19}M_{47}^{65}$  are intermediate segregated systems according to the calculated values of  $\chi N$ . It is useful to have access to the weak and intermediate segregation regimes just below the order-disorder transition temperature ( $T_{ODT}$ ) where temperature-dependent morphological transitions and ordered phases are known to exist. Additionally the study of morphology alignment under shear has proven to be most interesting near or even slightly above the  $T_{ODT}$ .<sup>177,1,203</sup>

Before attempting to obtain aligned systems by applying LAOS, and for a qualitative evaluation of the degree of alignment, these systems were investigated as well by rheological means. More information about limits of processing such systems like order-disorder transition temperature, decomposition temperature, was accomplished by performing tests at constant temperature and variable frequency or monitoring the modulus in a large range of temperature at constant stress (deformation).

The order-disorder transition temperatures ( $T_{ODT}$ ) of the two triblock terpolymers  $S_{37}B_{14}M_{49}^{37}$ ,  $S_{34}B_{19}M_{47}^{65}$  were determined by using measurements of dynamic viscoelastic properties.  $T_{ODT}$  is purely a function of the degree of polymerization ( $N$ ) and volume fraction ( $f$ ). To attain an experimentally accessible  $T_{ODT}$ , the triblock terpolymers specimens were used as solutions in dioctyl phthalate (DOP) at different concentrations. Dynamic mechanical measurements were conducted with a Rheometrics Scientific ARES strain-controlled rheometer fitted with 25 or 50 mm parallel plates. Frequency sweep experiments within linear viscoelastic regime were performed at several temperatures as can be seen in Figure 5-2. At temperatures in the range 10÷26°C a gradually increase in the slope was observed and with increasing temperature is observed an abruptly change in the slope giving raise at a maximum value of approximately 2, ordered materials usually has  $G'(\omega) \propto \omega^{0.5}$  and the disordered materials  $G'(\omega) \propto \omega^2$ . In the inset from Figure 5-2 as well can be seen the scaling factor of loss modulus  $G''$  in the terminal flow region follows the dependence  $G''(\omega) \propto \omega^1$ . This behavior in terminal flow region found for the system 30wt-%  $S_{37}B_{14}M_{49}^{37}$  in DOP, is similar to the behavior of block copolymers melts investigated earlier by other groups.<sup>41,2,204</sup>

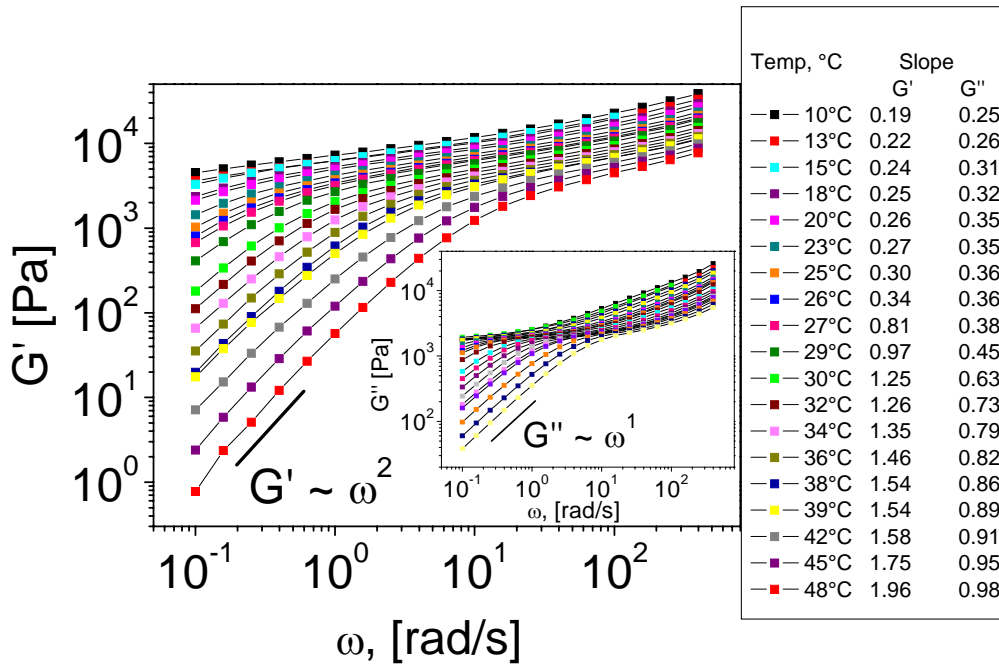


Figure 5-2. Plot log  $G'$  versus log  $\omega$  for a solution 30wt-%  $S_{37}B_{14}M_{49}^{37}$  in DOP,  $T_{ODT} \sim 48^\circ\text{C}$ .

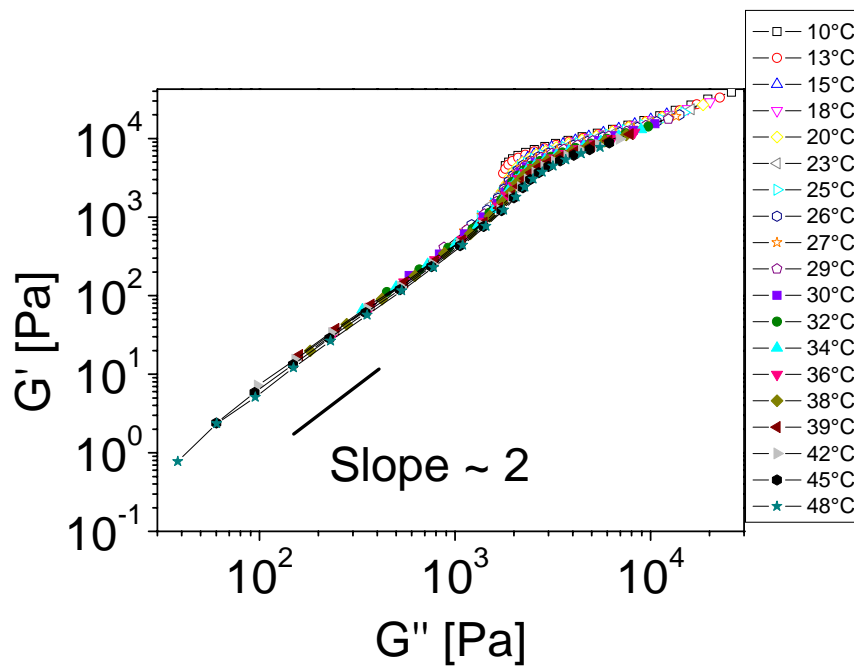
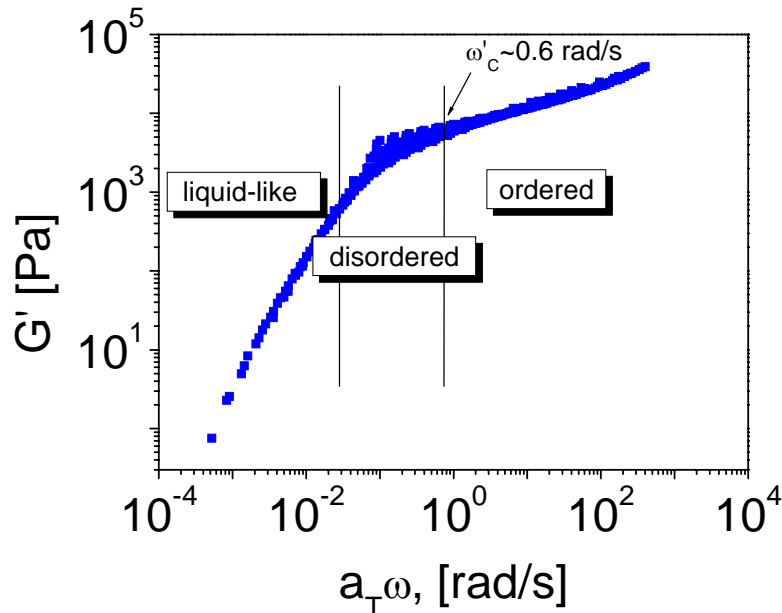


Figure 5-3. Cole-Cole plot of 30wt-%  $S_{37}B_{14}M_{49}^{37}$  in DOP, during heating at various temperatures,  $T_{ODT} \sim 48^\circ\text{C}$

In Figure 5-3 the storage modulus is shown as a function of the loss modulus, such as  $\log G'$  vs  $\log G''$  plot at various temperatures ranging from 10°C to 48°C, so-called Cole-Cole plot. At storage modulus larger than  $10^4$  Pa, the system is vitrifying, between  $10^4 - 10^3$  Pa the system is in the rubbery plateau and below that a linear relationship between  $G'$  and  $G''$  is observed with a slope of 2 (above 45°C) which indicates neighborhood to the order-disorder transition (ODT). To determine the  $T_{\text{ODT}}$  of 30wt-% $S_{37}B_{14}M_{49}$ <sup>37</sup> in DOP as accurately as possible, the dynamic frequency sweep measurements were taken at a temperature increment varied from 1°C to 2°C over a range of temperature from 10 to 48°C. An unusual shape of the  $\log G'$  vs  $\log G''$  plot is seen in Figure 5-3 which differs from the known behavior found for symmetric or nearly symmetric block copolymers. The distinct differences in the temperature dependence of  $\log G'$  vs  $\log G''$  plot for the 30wt-%  $S_{37}B_{14}M_{49}$ <sup>37</sup> in DOP is the downward displacement of the curves with increasing temperature (above 25°C) giving rise to a slope close to 2 in the terminal flow region and makes a downward displacement parallel shift until reaching a critical temperature at which it begins to show temperature independence. It has been reported for the symmetric and nearly symmetric diblock and triblock copolymers melts<sup>55</sup> the  $\log G'$  vs  $\log G''$  plot did not exhibit a parallel shift with increasing temperature. Obviously, according to the phase diagram of ABA triblock copolymers<sup>33</sup> with the degree of asymmetry specific to ABA systems, by increasing temperature the asymmetric structures first transform into intermediate structures before reaching the homogeneous state whereas the symmetric structures transform directly into the homogeneous phase. Specifically, the lamellae-cylinder morphology  $S_{37}B_{14}M_{49}$ <sup>37</sup> under the assumption of keeping the same morphology in the swollen state, with increasing temperature undergoes morphological transitions before reaching the order-disorder transition temperature. Evidence for morphological transitions is given by the upward displacement of the curves upon raising the temperature. From Figure 5-3, we conclude that 30wt-%  $S_{37}B_{14}M_{49}$ <sup>37</sup> in DOP is in the homogeneous state at approximately 48°C, when the  $\log G'$  vs  $\log G''$  no longer varies with temperature. Thus, we conclude that 30wt-%  $S_{37}B_{14}M_{49}$ <sup>37</sup> in DOP undergoes a lattice disordering/ordering transition (LDOT) before attaining order-disorder transition (ODT), a feature especially characterizing highly asymmetric triblock copolymer melts<sup>55</sup>.

Time-temperature superposition at a reference temperature,  $T_{\text{ref}}=10^\circ\text{C}$  was used to construct storage modulus,  $G'$ , namely the master curve given in Figure 5-4. In the ordered phase, storage modulus  $G'$  roughly follows a power law scaling with frequency, which can be approximated as  $G' \propto \omega^{0.3}$ . The disordered state,  $G'$  shows almost typical homopolymer-like terminal behavior with  $G' \propto \omega^{1.7}$ . Furthermore is defined a critical frequency ( $\omega_c'$ ) below

which the relaxation dynamics are dominant due to the relaxation of the microdomain microstructure. The critical value  $\omega_c'$  is estimated at reference temperature ( $T_{\text{ref}}=10^\circ\text{C}$ ) about  $\omega_c' \sim 0.6$  rad/s and is taken as a frequency below which the storage moduli of ordered and disordered states follow different curves.



**Figure 5-4.** Storage modulus on a shifted frequency scale ( $T_{\text{ref}}=10^\circ\text{C}$ ) for ordered ( $T < 30^\circ\text{C}$ ) 30wt-%  $S_{37}B_{14}M_{49}$ <sup>37</sup> in DOP but macroscopically unaligned state and the disordered state ( $T > 39^\circ\text{C}$ ).

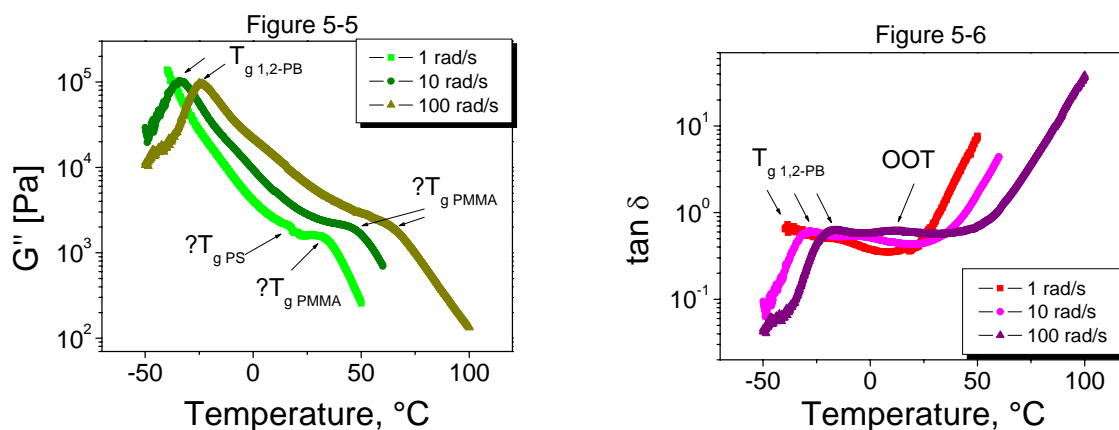
Figures 5-5 and 5-6 show the temperature dependence of the loss modulus and loss tangent of 30wt-%  $S_{37}B_{14}M_{49}$ <sup>37</sup> in DOP. The loss modulus,  $G''$  versus temperature shows the transition from the glassy into the rubbery plateau and also the transition to the terminal flow region.

A careful analysis of the loss modulus from the isochronal dynamic temperature sweep experiment at  $\omega = 1$  rad/s (Figure 5-5) has shown that the values of  $G''$  pass through a minimum at ca.  $20^\circ\text{C}$  followed by a slight increase and then finally start to decrease rapidly at  $35^\circ\text{C}$ . The appearance of a minimum in  $G''$  represents the onset of OOT, due to the morphological transition from lamellae-cylinder phase to bcc-sphere phase before transforming into the disordered state. To determine whether this is the case, there were not possible TEM investigations for such sample (solution in DOP).

The plot  $\tan \delta$  versus temperature (Figure 5-6) at different frequencies, shows a maximum which is related to the dynamic glass transition of the elastomeric block (1,2-PB) and for all

the frequencies  $\tan \delta$  increases monotonically versus higher temperature indicating flow. This behavior is similar to amorphous entangled homopolymers.<sup>205</sup>

Similarly as discussed already above, the same minimum at 20°C is encountered in the loss tangent from the isochronal dynamic temperature sweep experiment at  $\omega = 1$  rad/s (Figure 5-6) as a clear evidence for morphological transitions taking place at low angular frequency (1 rad/s).



**Figures 5-5 and 5-6.** Loss modulus ( $G''$ ) and loss tangent ( $\tan \delta$ ) as a function of temperature for a solution 30wt-%  $S_{37}B_{14}M_{49}$ <sup>37</sup> in DOP, at different frequencies.

From these dynamic mechanical properties we conclude that in the case of  $S_{37}B_{14}M_{49}$ <sup>37</sup> solution (30% in DOP) all the blocks mix together above the highest  $T_g$  of hard blocks.  $T_g$  of PS and PMMA are somehow hidden in the rubbery plateau of the elastomeric block, which may be the reason for the slight spread of the data in the rubbery region of the Cole-Cole plot (for a perfectly homogeneous material one master-curve would be expected for all temperatures). The solution of  $S_{37}B_{14}M_{49}$ <sup>37</sup> (30% in DOP) behaves like diblock copolymer consisting of a mixed polystyrene / poly(methyl methacrylate) from poly(1,2-butadiene); thus the system is not really strongly segregated between PS and PMMA (with a sharp interface) proved as well by calculated interfacial tensions between components and comparison with the data reported in the literature (Table 5-2). As a summary of the rheological investigations on the system  $S_{37}B_{14}M_{49}$ <sup>37</sup> (30% in DOP), order-disorder transition temperature ( $T_{ODT}$ ) is not clearly evidenced like an abruptly drop in modulus when the temperature of a block copolymer is increased, instead the existence of homogeneous state at a certain temperature is achieved.

Significant composition fluctuations near to the transition temperature of a block copolymer may occur when the segment molecular weights exceed entanglement molecular

weights ( $M_e$ ) of the constituent components. As a comparison of  $S_{37}B_{14}M_{49}^{37}$ , and  $S_{34}B_{19}M_{47}^{65}$ , we would expect higher composition fluctuations for the latter system due to the two segment molecular weights higher than the corresponding  $M_e$  ( $M_{PS} \sim 22K > M_{e, PS} \sim 19K$  and  $M_{PMMA} \sim 31K > M_{e, PMMA} \sim 7K$ ) while in the case of first system only one segment exceeds the entanglement molecular weight ( $M_{PMMA} \sim 18K > M_{e, PMMA} \sim 7K$ ).

Therefore, we can conclude that composition fluctuations for sample  $S_{37}B_{14}M_{49}^{37}$  30% in DOP near  $T_{ODT}$  are negligibly small.

The mechanical and optical properties of these triblock terpolymers,  $S_{37}B_{14}M_{49}^{37}$  and  $S_{34}B_{19}M_{47}^{65}$  were characterized using a rheo-optical apparatus suited for simultaneous measurements of dynamic stress and birefringence over a wide range of frequency (0.01-100 rad/s) and a maximum temperature about  $100^\circ\text{C}$  due to the instrumental limitations of OAM device. All experiments were performed under an inert nitrogen atmosphere using the "shear-sandwich" geometry, with light propagation along the velocity gradient direction ( $\nabla v$ ). A He-Ne laser at a wavelength of 633 nm was used.

Alignment of the system 40wt-%  $S_{37}B_{14}M_{49}^{37}$  in DOP at frequencies 1rad/s, 10 rad/s, temperatures  $10^\circ\text{C}$  and  $15^\circ\text{C}$ , and different strain amplitudes ( $\gamma_0$ ) was accomplished as illustrated in Figure 5-7.

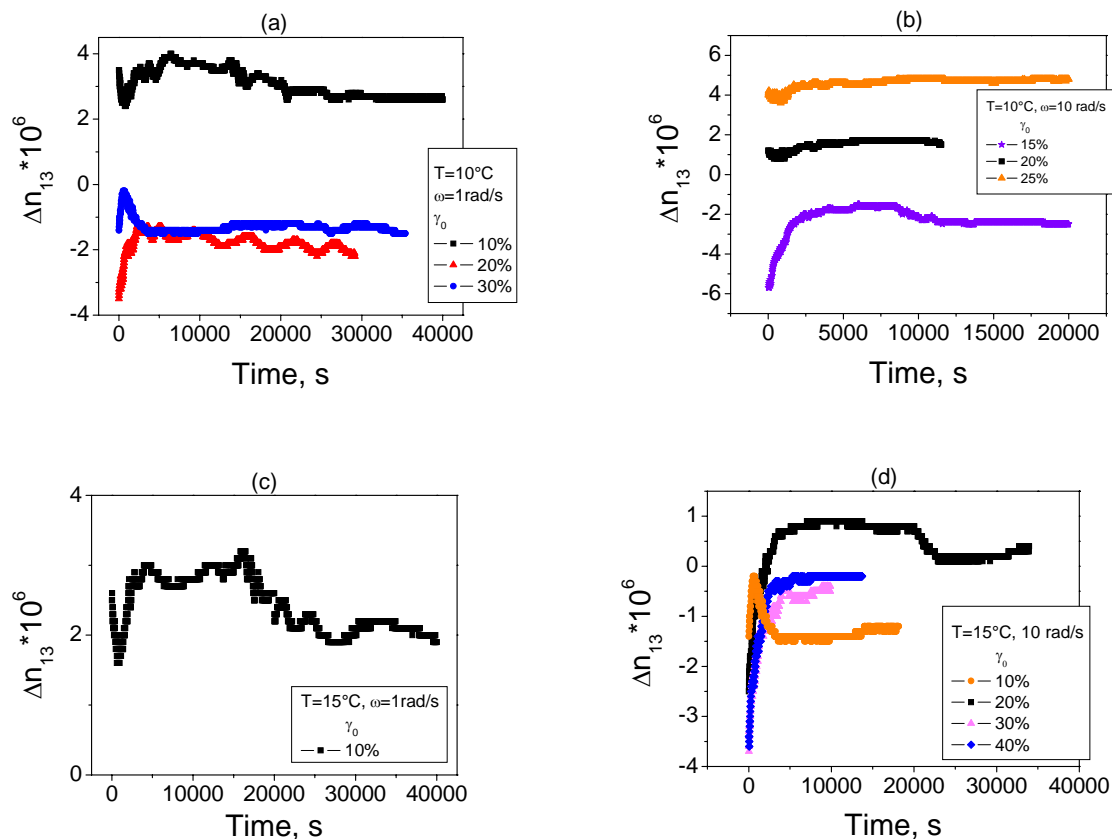


**Figure 5-7.** Evolution of birefringence ( $\Delta n_{13}$ ) during applying LAOS for 40wt-%  $S_{37}B_{14}M_{49}$ <sup>37</sup> in DOP at different conditions: (a)  $T=10^{\circ}C$ ,  $\omega=1rad/s$ ,  $\gamma_0=10\%$ , 20%, 30%; (b)  $T=10^{\circ}C$ ,  $\omega=10rad/s$ ,  $\gamma_0=15\%$ , 20%, 25%; (c)  $T=15^{\circ}C$ ,  $\omega=1rad/s$ ,  $\gamma_0=10\%$ ; (d)  $T=15^{\circ}C$ ,  $\omega=10rad/s$ ,  $\gamma_0=10\%$ , 20%, 30%, 40%.

The alignment conditions illustrated in Figure 5-7 were determined prior from the storage modulus,  $G'$  master curve and the existence of an ordered structure through the monitored birefringence during shearing was shown at  $10^{\circ}C$  and  $15^{\circ}C$ . The frequency used in the alignment experiments was chosen above the critical frequency ( $\omega_c' = 0.6 \text{ rad/s}$ ) where there is an ordered but unaligned structure (Figure 5-4). Since the critical frequency of  $\omega_c' = 0.6 \text{ rad/s}$  was determined in the case of 30wt-%  $S_{37}B_{14}M_{49}$ <sup>37</sup> in DOP, an increase of the system's concentration toward 40% would enlarge the ordered region in the reduced frequency scale by shifting the ordered region to the lower range of reduced frequency. Thus, using of  $\omega_c' = 0.6 \text{ rad/s}$  as a reference for searching the proper frequency for alignment of 40wt-%  $S_{37}B_{14}M_{49}$ <sup>37</sup> in DOP is justified.

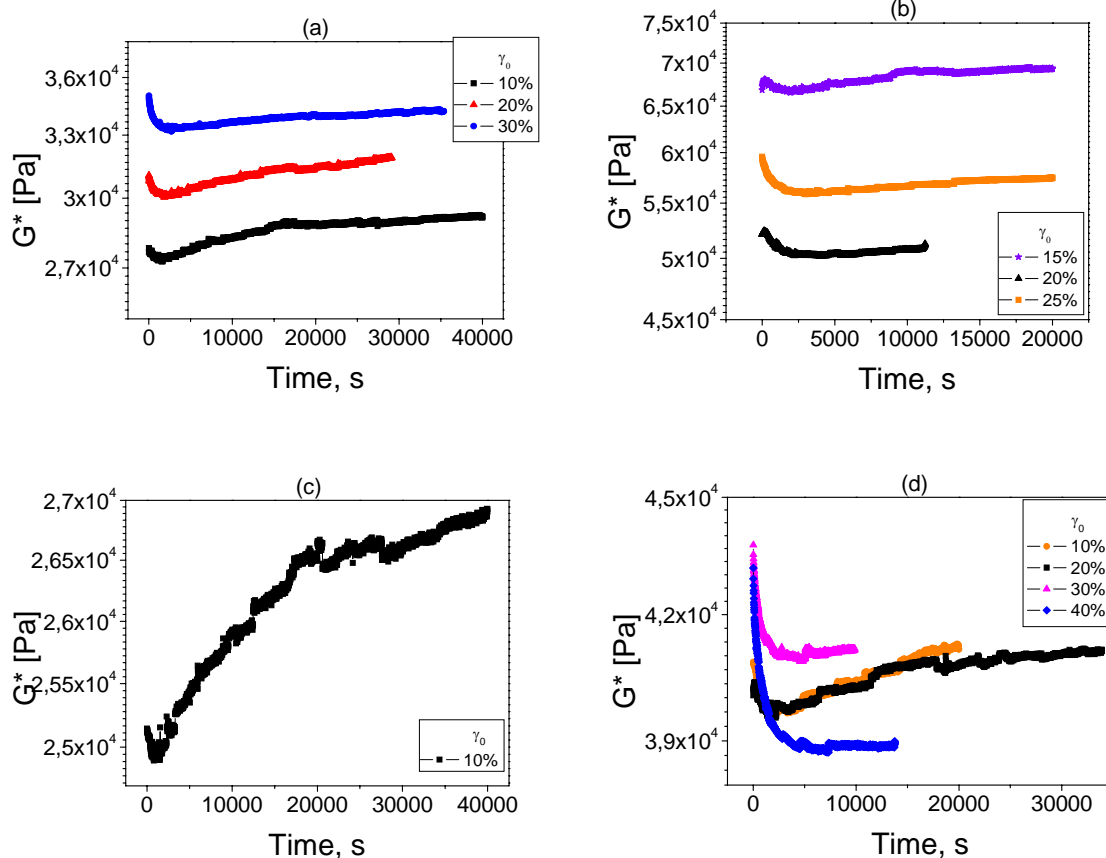


**Figure 5-8.** Evolution of complex moduli during the large amplitude oscillatory shear described in Figure 5-7. (a)  $T=10^{\circ}\text{C}$ ,  $\omega=1\text{rad/s}$ ,  $\gamma_0=10\%$ , 20%, 30%; (b)  $T=10^{\circ}\text{C}$ ,  $\omega=10\text{rad/s}$ ,  $\gamma_0=15\%$ , 20%, 25%; (c)  $T=15^{\circ}\text{C}$ ,  $\omega=1\text{rad/s}$ ,  $\gamma_0=10\%$ ; (d)  $T=15^{\circ}\text{C}$ ,  $\omega=10\text{rad/s}$ ,  $\gamma_0=10\%$ , 20%, 30%, 40%.

The final state of alignment was characterized by the relatively constant values of birefringence ( $\Delta n_{13}$ ) and simultaneously the monitored strain moduli (complex modulus  $G^*$ ), which are given in Figure 5-8.

The initial condition of each experiment is obtained by annealing the sample at a temperature above the microphase transition temperature ( $T_{\text{ODT}}$ ) and then cooling to a certain temperature in the ordered state. By this route the resulting sample morphology is expected to consist of randomly oriented grains.

Shearing at  $\omega=1\text{rad/s}$ , and strain amplitudes of  $\gamma_0=10\%$ , 20%, 30% (Figure 5-7a) produced a rapid raise in the birefringence value ( $\Delta n$ ) followed by a slow saturation. The encountered absolute value of birefringence were smaller than the reported value in the literature.<sup>1</sup> For example, lamellar styrene-diene<sup>185</sup> block copolymers in the strong segregation limit suggest a value of  $\Delta n \sim 16 \times 10^{-4}$  for a perfectly aligned sample. The investigated system  $S_{37}B_{14}M_{49}$ <sup>37</sup> (40% in DOP) is in intermediate segregation limit, furthermore the solvent (DOP) is used, resulting in smaller birefringence than a strongly segregated PS-PI. As it is shown in Figure 5-7 (a), (b), (c), (d), in the experiments using different strain amplitudes and frequencies, the observed final value of birefringence never exceeds  $\Delta n \sim 0.03 \times 10^{-4}$ .

The complex dynamic modulus ( $G^*$ ) during shear alignment, showed an initial rapid drop, followed by a gradual decrease and then toward a slightly increasing until yield a constant value (Figure 5-8, (a), (b), (d)). Comparison of the complex moduli from Figure 5-8a and b indicates a strong dependence of frequency, where at lower frequencies a lower value of moduli is obtained. Similarly, a comparison between Figure 5-8c and d indicates that higher frequencies are required when the alignment temperature is closer to  $T_{\text{ODT}}$  as illustrated by a continuous increase in the complex modulus over a large time scale (Figure 5-8c) without yielding a plateau of modulus as encountered at 10 rad/s (Figure 5-8d). Moreover, as seen in Figure 5-8d because the alignment temperature is closer to  $T_{\text{ODT}}$ , beside higher frequencies also higher strain amplitudes are required, and the evidence of "improved" alignment is illustrated through the constant values in complex modulus at  $\gamma_0=30\%$  and 40% and small time scales ( $\sim 10000\text{s}$ ). Due to the very low value of birefringence, we cannot assign a well defined aligned state like parallel or perpendicular state. The *form* and *intrinsic* contributions

to the birefringence, undergo lack of balance in weak segregated system. Upon variation of strain amplitude and temperature, in shearing experiments both negative and positive value of birefringence are obtained. The evolution of birefringence from negative values, through zero to positive values with increasing strain amplitude is illustrated in Figure 5-7b. Since, the ordered state is reached at 10°C upon cooling, the *intrinsic* birefringence is not too high by applying shear and the degree of stretching of the chains is not well developed. Due to the weak segregation between PS and PMMA in the diluted state the application of shear may induce a mixing of these two blocks and the system behaves like an ABA triblock copolymer with a low birefringence in terms of the *form* component. Nevertheless, when increasing the temperature to T=15°C and applying a frequency of  $\omega=10$  rad/s at different strain amplitudes (Figure 5-7d) a sharp increase in birefringence is achieved at small time scale, through a relaxation process (as indicated by a slight decrease of birefringence value) and constant value as final state. As shown in Figure 5-7d, the absolute value of birefringence is smaller than in the case (b), at higher temperature *form* birefringence contributions diminish and the *intrinsic* contributions become dominant. Since, the intrinsic contribution is a few orders of magnitude smaller than the form birefringence<sup>185</sup>, the overall birefringence in the aligned state in Figure 5-7b is higher than in the experiment at T=15°C, Figure 5-7d. In Figure 5-8d, the complex moduli during shear show a large initial drop followed by a gradual flattening. This drop is rather larger than that in Figure 5-8 (a), (b), (c) and the small values of the moduli are an indication of "slightly parallel alignment", since the birefringence value is raising from negative values toward zero.

Rheological investigation of high molecular weight system  $S_{34}B_{19}M_{47}^{65}$  as solution in DOP exhibit order-disorder transition temperature at low concentration of triblock terpolymer (20%) as illustrated in Figure 5-9b, whereas at high concentration the appearance of individually glass transition temperature of each block is illustrated without any indication of  $T_{ODT}$  (Figure 5-9d). A drop in moduli at temperature 100°C and frequency 10rad/s for the 20wt-%  $S_{34}B_{19}M_{47}^{65}$  in DOP corresponds to the order-disorder transition. At higher concentration the system (Figure 5-9d) shows an improving in the degree of segregation within detectable individually glass transition temperature for each block ( $T_{g, 1,2-PB} \sim 10^\circ\text{C}$ ,  $T_{g, PS} \sim 80^\circ\text{C}$ ,  $T_{g, PMMA} \sim 120^\circ\text{C}$ ) but the order-disorder transition was shifted in the higher range of temperature ( $T_{ODT} > 160^\circ\text{C}$ ). At  $\omega=1$  rad/s and 100 rad/s the temperature dependence of moduli (Figure 5-9 a, c) did not illustrate a clear evidence of  $T_{ODT}$  only a monotonically decrease of moduli with a change in the slope as indication of flow.

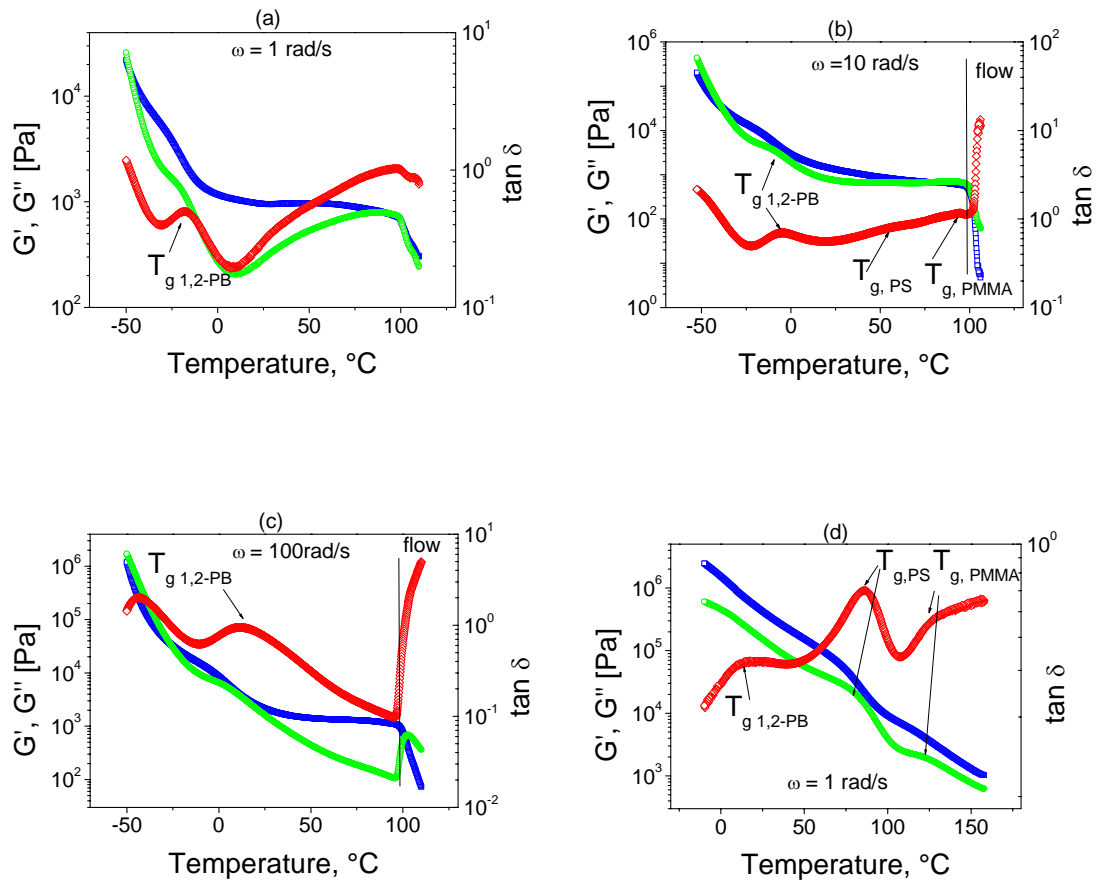


**Figure 5-9.** Detection of order-disorder transition temperature by temperature sweep test at different concentrations: i) 20wt-%  $S_{34}B_{19}M_{47}^{65}$  in DOP (a)  $\omega=1\text{rad/s}$ , (b)  $\omega=10\text{rad/s}$ , (c)  $\omega=100\text{rad/s}$ ,  $T_{ODT}\sim 100^{\circ}C$ ; ii) 40wt-%  $S_{34}B_{19}M_{47}^{65}$  in DOP (d)  $\omega=1\text{rad/s}$ ,  $T_{ODT} > 160^{\circ}C$ , ( $\square$ )  $G'$ , ( $\circ$ )  $G''$ , ( $\diamond$ )  $\tan \delta$ .

An intermediate concentration of 30wt-%  $S_{34}B_{19}M_{47}^{65}$  in DOP has been chosen and the temperature dependence of storage modulus is presented in Figure 5-10.

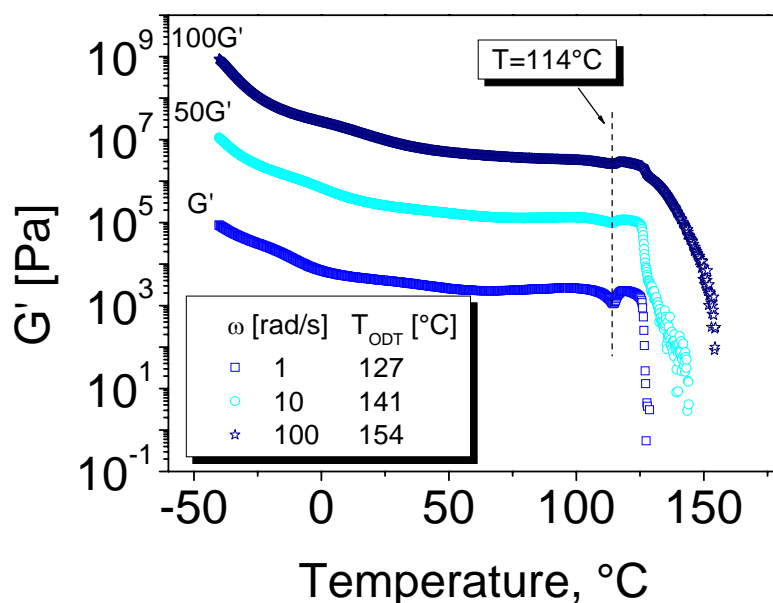


**Figure 5-10.** Variation of  $G'$  with temperature by heating ( $1^\circ\text{C}/\text{min}$ ) obtained at  $\omega = 1, 10, 100$  rad/s for solution 30wt-%  $S_{34}B_{19}M_{47}$ <sup>65</sup> in DOP within the linear viscoelastic regime ( $\gamma < 1\%$ ). The curves at  $\omega = 10$  and 100 rad/s, respectively were shifted up in order to avoid overlapping and for a qualitative evidence of morphological transition (vertically dashed line).

According to the asymmetrically microstructure it may be expected some morphological transition like order-to-order transition before order-disorder transition in agreement with theoretical phase diagram developed for ABA asymmetrically triblock copolymer melts.<sup>33</sup> An unusual behavior of moduli within increasing temperature evidenced through a minimum before attaining  $T_{ODT}$  is related with morphological transition. Previously similar behavior has been reported by Hashimoto and co-workers<sup>50,55</sup> in the case of highly asymmetric diblock and triblock copolymer melts. They attributed the minimum in the storage modulus for the cylindrical triblock copolymer polystyrene-*b*-polyisoprene-*b*-polystyrene (vector 4111, polystyrene-cylinders) due to the softening of the hexagonally packed PS cylinders and may be due to the transformation from hexagonally-packed cylinders to the cubic sphere phase. The minimum in moduli is followed by an increasing in moduli as a evidence of the new developed structure. As illustrated in Figure 5-10 the sharpest minimum in moduli is strongly frequency dependent, such as the low angular frequency (1 rad/s) favors the most clear evidence of morphological transition. The new microstructure arises due to the minimum in moduli (Figure 5-10) which is assumed to be a spherical one according to the phase diagram

developed by Matsen<sup>33</sup>, its evidence has not been checked experimentally due to technical problems encountered in sample preparation for the TEM investigations.

A summary of the  $T_{ODT}$ 's determined from the temperature sweep tests under isochronal conditions for the cylindrical morphologies with different molecular weights  $M \sim 37K$  ( $S_{37}B_{14}M_{49}$ <sup>37</sup>) and  $M \sim 65K$  ( $S_{34}B_{19}M_{47}$ <sup>65</sup>) respectively is presented in Table 5-4.

Sample	% weight triblock in DOP		$T_{ODT}$ , °C	Obs
$S_{37}B_{14}M_{49}$ <sup>37</sup>	30		~48	$T_{ODT}$ values obtained from different plots $G'$ vs $\omega$ and $G'$ vs $G''$ , respectively
$S_{34}B_{19}M_{47}$ <sup>65</sup>	20	1 rad/s	>100	change in moduli slope
		10 rad/s	~105	drop in moduli
		100 rad/s	>110°C	continuously change in moduli slope
	30	1 rad/s	127	drop in moduli
		10 rad/s	141	drop in moduli
		100 rad/s	154	drop in moduli
	40		>160	$G'$ vs temperature

**Table 5-4.** Summary of  $T_{ODT}$ 's values for the triblock terpolymer.

Using similar set up as already mentioned, shear alignment measurements at the same concentration, and different temperatures and frequencies were performed as can be seen in Figure 5-11. In Figures 5-11a, b the same temperature alignment has been used instead the frequency and strain amplitudes have been varied. Thus, the sign and absolute value of the monitored birefringence are changed within the strain amplitude. As can be seen in Figure 5-11a at low angular frequency a quite constant value of birefringence is achieved after 10000s, whereas at high frequency after 10000s the alignment process is not well defined. The common feature present in Figures 5-11a, b, c, e is the occurrence of the "fast process" in the first stages illustrated through a sudden decrease or increase in birefringence followed by a plateau in birefringence at sufficiently large time scale. At lower temperature,  $T=15^\circ\text{C}$  as seen in Figure 5-11c, the value of birefringence on the first stages of the alignment process has positive value and higher as absolute value compared with other alignment process presented in Figures 5-11a, b, e. It could be explained that by lowering the temperature the degree of segregation is increased and the contribution of form birefringence is higher than in the other alignment process at higher temperatures. From the moduli temperature dependence at  $\omega=10$  rad/s (Figure 5-9b) follows a roughly estimation of glass transition temperature of polybutadiene block,  $T_{g, 1,2-PB} \sim -5^\circ\text{C}$  and not clear indication of  $T_{gs}$  for PS and PMMA blocks. Thus, it could be an evidence that at this concentration (20%  $S_{34}B_{19}M_{47}$ <sup>65</sup> in DOP) those blocks are not well segregated and our attempt to treat the system like a diblock (PB cylinders

in a matrix of mixed PS and PMMA) is justified. Taking into account this assumption, the decay in birefringence is due to diminished contribution of form birefringence within shearing and grow up the contribution from intrinsic birefringence according to the stretched chains of polybutadiene. In Figure 5-11e, an increasing of temperature at  $T=10^\circ\text{C}$  imply an increased of chain mobility and degree of segregation is decreased. Thus the degree of stretching of polybutadiene chains is lowered and shearing at  $\omega=100\text{ rad/s}$  induces stretching followed by a chain relaxation.

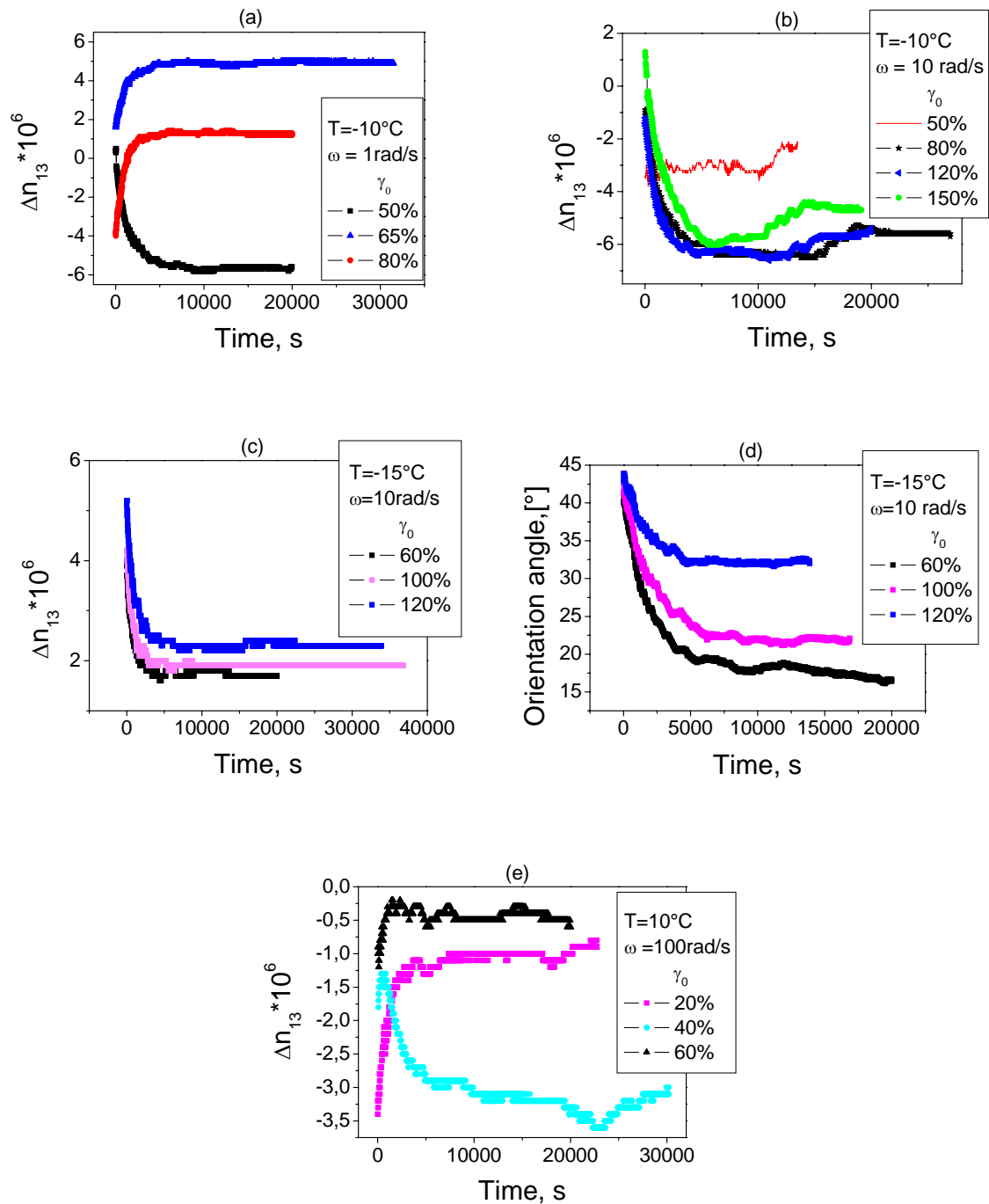


**Figure 5-11.** Evolution of birefringence ( $\Delta n_{13}$ ) during applying LAOS for 20wt-%  $S_{34}B_{19}M_{47}^{65}$  in DOP at different conditions: (a)  $T = -10^\circ\text{C}$ ,  $\omega = 1\text{rad/s}$ ,  $\gamma_0 = 50\%$ , 65%, 80%; (b)  $T = -10^\circ\text{C}$ ,  $\omega = 10\text{rad/s}$ ,  $\gamma_0 = 50\%$ , 80%, 120%, 150%; birefringence (c), and orientation angle (d) at  $T = -15^\circ\text{C}$ ,  $\omega = 10\text{rad/s}$ ,  $\gamma_0 = 60\%$ , 100%, 120%; (e)  $T = 10^\circ\text{C}$ ,  $\omega = 100\text{rad/s}$ ,  $\gamma_0 = 20\%$ , 40%, 60%.

The orientation angle versus time presented in Figure 5-11d which arises from the same data as presented in Figure 5-11c, an approaching of values close to  $0^\circ$  at low strain amplitudes may indicate the evidence of alignment. From Figure 5-11 may be concluded that for the low concentration system the alignment is favored for low temperatures such as below  $T_g$ 's PB, low angular frequency and low strain amplitude favors high degree of alignment.

Since, the lower concentration such as 20wt-%  $S_{34}B_{19}M_{47}^{65}$  in DOP required low alignment temperatures, an attempt was made toward increasing system's concentration at 30wt-%  $S_{34}B_{19}M_{47}^{65}$  in DOP under the assumption of improving degree of segregation and shifting at higher alignment temperatures. Therefore, the alignment of 30wt-%  $S_{34}B_{19}M_{47}^{65}$  in DOP is presented in Figure 5-12. The monitored birefringence showed only positive values at the alignment conditions illustrated in Figure 5-12a and at high strain amplitude ( $\gamma_0 = 40\%$ ) the plot ( $\Delta n_{13}$ ) versus time shows typical behavior of "Regime I" as described previously by Kornfield et al.<sup>70</sup>

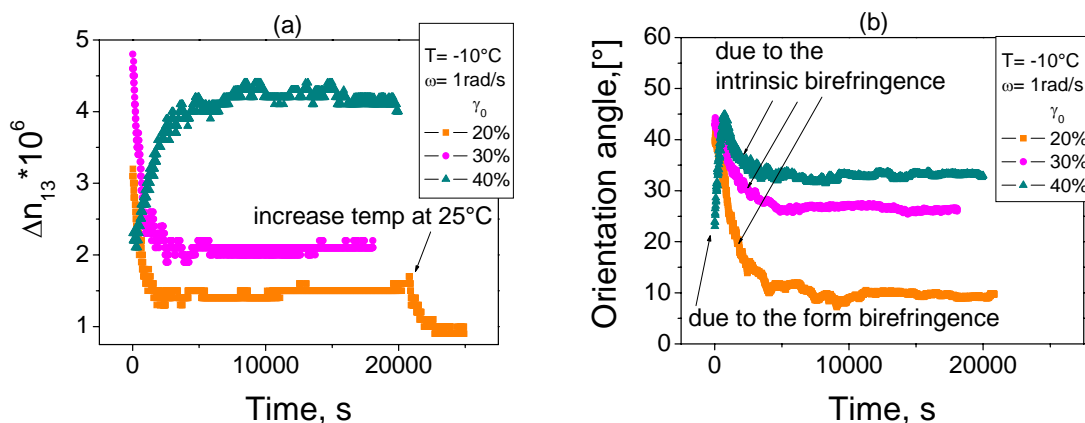


**Figure 5-12.** Evolution of birefringence ( $\Delta n_{13}$ ) (a) and orientation angle (b) during applying LAOS for 30wt-%  $S_{34}B_{19}M_{47}^{65}$  in DOP at different conditions:  $T = -10^\circ\text{C}$ ,  $\omega = 1\text{rad/s}$ ,  $\gamma_0 = 20\%$ , 30%, 40%.

Specifically, for the lamellar diblock copolymer system "Regime I" is analogous to the type of "perpendicular alignment" of lamellae with lamellae's normal perpendicular to the plane

( $v$ ,  $\nabla v$ ). One possible explanation responsible for such behavior (Figure 5-12a,  $\gamma_0=40\%$ ) would be that *form* birefringence has higher contribution due to the shifting of overall birefringence value ( $\Delta n_{13}$ ) toward positive and high values. For all the experiments presented in Figure 5-12a at overall strain amplitudes the initial birefringence value before applying shear were different which may be related with the duration of annealing process before starting shear. More insight into the alignment process has been approached through an evaluation of the orientation angle versus time presented in Figure 5-12b, orientation which has been monitored simultaneously during the alignment process. An orientation angle of  $45^\circ$  means a completely random distribution of the microdomains in the shear direction, while an orientation angle of  $0^\circ$  indicates complete orientation in the shear direction. A plateau in the birefringence values from the plot  $\Delta n_{13}$  versus time at overall strain amplitudes corresponds to a similar plateau in the orientation angle plot, both plateaus encountered after  $\sim 5000$ s which could be interpreted as an aligned state. The orientation angle plot qualitatively gives an indication about aligned state reached after a certain time but quantitatively never reached the complete orientation corresponding to a  $0^\circ$  in orientation angle. As it is seen in Figure 5-12b a strongly dependence of orientation angle within strain amplitude is encountered, low strain amplitude leads to high degree of orientation. At high strain amplitude,  $\gamma_0=40\%$  a low value in orientation angle ( $\sim 20^\circ$ ) in the beginning of the alignment process is equivalent with a "slightly oriented microdomains" due to the anisotropic composition pattern, contribution diminished due to the high strain amplitude combined with large time scale which lead to a mixing of the PS and PMMA blocks. The maximum in orientation angle involves randomly distribution of microdomains in the shear direction as a consequence that the microdomains are not well defined (intermediate segregation limit) and an orientation without mixing blocks is not possible. A decrease in orientation angle is due to the stretching of the PB chains, which are anchored at the surface matrix formed from PS and PMMA mixed blocks, analogous to a purely contribution from *intrinsic* birefringence. At low strain amplitude  $\gamma_0=20\%$  corresponds a value of orientation angle of  $10^\circ$  instead at  $\gamma_0=30\%$  corresponds an orientation angle  $25^\circ$  which means that low strain amplitudes allowed slightly *form* birefringence contributions leading the overall orientation at smaller value close to complete orientation. A way to distinguish between *form* and *intrinsic* birefringence contributions is to apply high shear strain amplitudes while the low strain amplitudes show the purely *intrinsic* contribution of birefringence.

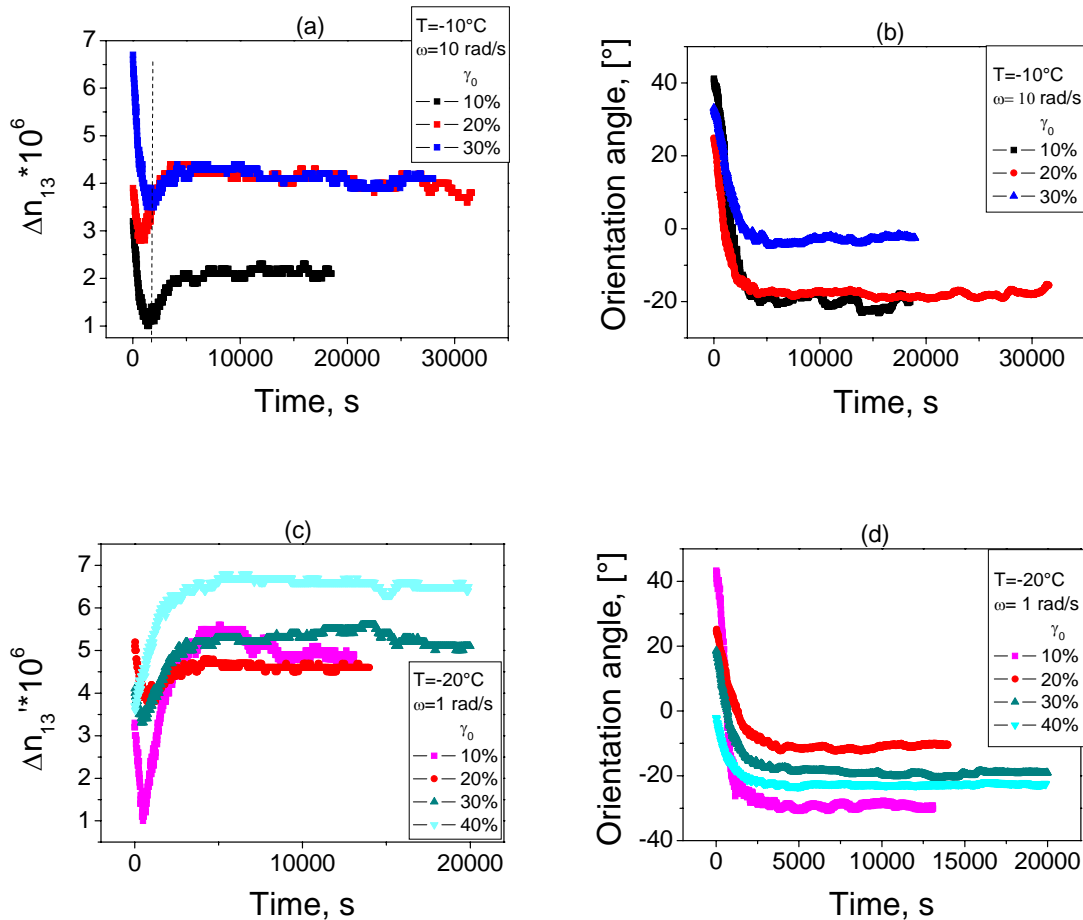


**Figure 5-13.** Evolution of birefringence and the corresponding orientation angle during applying LAOS for 30wt-%  $S_{34}B_{19}M_{47}^{65}$  in DOP at different conditions: ( $\Delta n_{13}$ ) (a) and orientation angle (b) at:  $T = -10^\circ\text{C}$ ,  $\omega = 10 \text{ rad/s}$ ,  $\gamma_0 = 10\%$ ,  $20\%$ ,  $30\%$ ; and ( $\Delta n_{13}$ ) (c) and orientation angle (d) at:  $T = -20^\circ\text{C}$ ,  $\omega = 1 \text{ rad/s}$ ,  $\gamma_0 = 10\%$ ,  $20\%$ ,  $30\%$ ,  $40\%$ . The vertically dashed line from (a) indicates the boundary between "fast" and "slow" process.

Different alignment conditions such as higher frequency  $\omega = 10 \text{ rad/s}$  and lower alignment temperature  $T = -20^\circ\text{C}$  were used in the alignment process as presented in Figure 5-13.

A sudden decrease in birefringence values at overall strain amplitudes is encountered after 1700s of shearing at  $T = -10^\circ\text{C}$  and  $\omega = 10 \text{ rad/s}$  as it may be seen in Figure 5-13a. It thus means the *form* birefringence contribution is diminished and an increasing from *intrinsic* birefringence contribution is developed within time scale, the final birefringence underwent to a saturation value at approximately 20000s. Similarly, the orientation angle decrease toward reaching a plateau value after 5000s as in Figure 5-13b. The orientation angle during shearing goes through zero value toward a negative value since the alignment process is a dynamic one. The lowest negative values monitored in Figures 5-13b,d show the efficiency of alignment process at low strain amplitudes were beside *intrinsic* birefringence contribution a slightly *form* birefringence

contribution is still present. The contribution from the *form* birefringence is obviously seen in Figure 5-13c at  $\gamma_0=10\%$  where the overall birefringence in the beginning of the shearing process is decreasing to a minimum and then increasing until a saturation value is achieved. As a common feature from the plots presented in Figures 5-12 and 5-13 is that the low strain amplitudes give rise to a minimum in orientation angle, meaning of aligned state and low alignment temperatures favor high absolute value for the final birefringence (  $T= -20^\circ\text{C}$ ,  $\Delta n_{13}=5$  ( $\gamma_0=10\%$ ), Figure 5-13c and  $T= -10^\circ\text{C}$ ,  $\Delta n_{13}=1.5$  ( $\gamma_0=20\%$ ), Figure 5-12a)

A summarizing of the absolute birefringence values within frequency, shear amplitude and temperature is given in Table 5-5.

$S_{34}B_{19}M_{47}^{65}$ 20% in DOP													
	15°C			-10°C							10°C		
	10 rad/s			1 rad/s			10 rad/s				100 rad/s		
$\gamma_0, \%$	60	100	120	50	65	80	50	80	120	150	20	40	60
$\Delta n_{13}^*$ $10^6$	1.7	1.8	2.5	-6	5	1	-2	-5.5	-5	-4.5	-0.7	-3	-
[°]	30	20	15	20	-40	-25	-10	17	12	16	-35	3	30
$S_{34}B_{19}M_{47}^{65}$ 30% in DOP													
	-20°C				-10°C								
	1 rad/s				1 rad/s			10 rad/s					
$\gamma_0, \%$	10	20	30	40	20	30	40	10	20	30			
$\Delta n_{13}^*$ $10^6$	4.5	4.5	5	6.5	1.5	2	4	2	3.5	4			
[°]	-30	-10	-19	-23	9	26	33	-22	-18	-2.7			

**Table 5-5.** The monitored birefringence values within orientation angles during applying LAOS for 20wt-%  $S_{34}B_{19}M_{47}^{65}$  in DOP and 30wt-%  $S_{34}B_{19}M_{47}^{65}$  in DOP, respectively at different alignment conditions.

The negative values in orientation angle corresponding to the most of the alignment conditions to the analogous negative values in birefringence are seen in Table 5-5 which may arise from the applied oscillatory shearing mode. In steady shear mode reported by other groups the orientation angle values found for the homopolymers of hydroxypropylmethyl cellulose<sup>206</sup> and barley(1→3)(1→4)- $\beta$ -glucan<sup>207</sup> were decreased within increasing shear rate and not negative values shown due to the unidirectional applied shear. Similarly, in oscillatory shear the orientation angle decreases from  $45^\circ$  and  $-45^\circ$  toward lower values approaching  $0^\circ$ , which were favored just for the low strain amplitudes. At high strain amplitudes (Figure 5-13d), the SBM system reach homogeneous state and a slightly decrease from  $45^\circ$  or  $-45^\circ$  toward values close to  $0^\circ$  is found.

5.2.2 Alignment of  $S_{37}EB_{14}M_{49}^{37}$  and  $S_{34}EB_{19}M_{47}^{65}$ 

The narrow molecular weight is retained in the hydrogenated PS-PEB-PMMA triblock terpolymers, as is shown by the GPC traces (Figures 2-13, 2-14) and polydispersities value from Table 2-5. Due to the enhanced thermal stability, the block terpolymers can be annealed at high temperatures without cross-linking of the elastomeric center block.

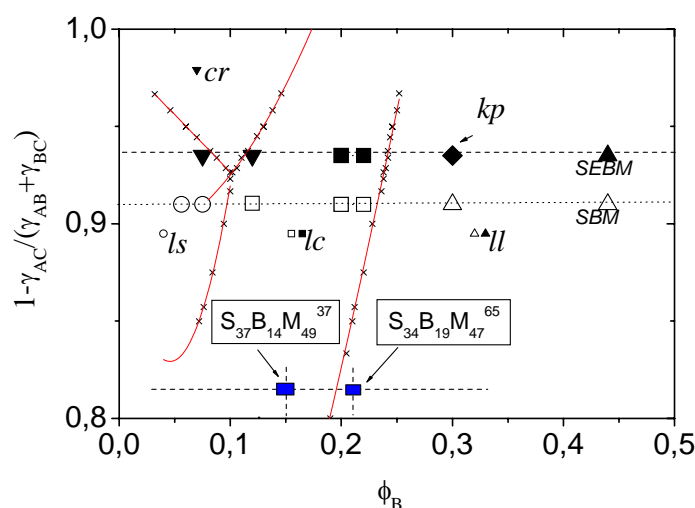
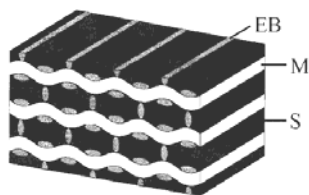


**Figure 5-14.** Phase diagram<sup>34</sup> of symmetric ABC triblock terpolymers with  $\phi_A = \phi_C$ . cr: cylinder-ring-morphology, kp: knitting pattern morphology, ls: lamellae-sphere-morphology, lc: lamellae-cylinder-morphology, ll: lamellae-morphology. The assumption  $\gamma_{AB}=\gamma_{BC}$  which has been used in the calculation of interfacial tension is not strictly valid for SBM and SEBM triblock terpolymers. The  $S_{37}B_{14}M_{49}^{37}$  and  $S_{34}B_{19}M_{47}^{65}$  are figured by the blue squares and  $1 - \gamma_{AC} / (\gamma_{AB} + \gamma_{BC}) = f$

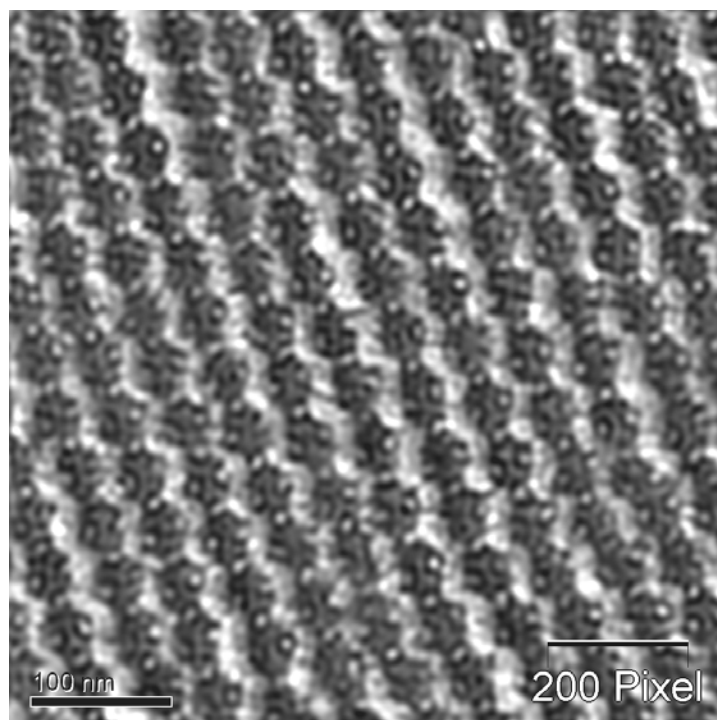
According to the phase diagram from Figure 5-14 for each of our systems has been calculated the following values:  $\phi_B=0.15$  and  $f=0.8148$  for  $S_{37}B_{14}M_{49}^{37}$  and  $\phi_B=0.21$  and  $f=0.8148$  for  $S_{34}B_{19}M_{47}^{65}$  thus it was possible to place them into the phase diagram. The  $S_{37}B_{14}M_{49}^{37}$  exhibits the cylinders at the lamellar interface while the  $S_{34}B_{19}M_{47}^{65}$  is close to the boundary transition between lamellae-cylinder (lc) and lamellae-lamellae (ll). As already mentioned by Stadler et al.<sup>39</sup> at the borderline between ll and lc morphologies within a range of  $\phi_B=0.2\div 0.24$  the kp morphology has been found. Hydrogenation of  $S_{37}B_{14}M_{49}^{37}$  would lead to cr (B rings around S cylinders in a matrix of MMA) morphology which has not been obvious from TEM micrograph, while the hydrogenation of  $S_{34}B_{19}M_{47}^{65}$  clearly led to the knitting pattern, as illustrated in Figure 5-16. The morphological transition upon hydrogenation of the middle

block is attributed due to the incompatibility between the middle block and the two end blocks. Beside hydrogenation of the SBM triblock terpolymer, the "knitting pattern" has been obtained as well via blending of two SBM triblock terpolymers.<sup>208</sup> Such as, the theoretical knitting pattern morphology illustrated by Figure 5-15, represents interest to study as solution in DOP, because is unknown the type of morphology adopted in DOP solvent. Due to the fact that the solution of 30wt-%  $S_{34}EB_{19}M_{47}$ <sup>65</sup> in DOP has not been optically transparent it was not possible to study by using rheo-optical technique. Further investigations on  $S_{34}EB_{19}M_{47}$ <sup>65</sup> system as solution in DOP will be presented in Chapter 8 by using in situ rheo-SAXS technique to monitor the structural changes during applying shear. Therefore, here will be presented only alignment kinetics on 30wt-%  $S_{37}EB_{14}M_{49}$ <sup>37</sup> in DOP as shown in Figure 5-17.

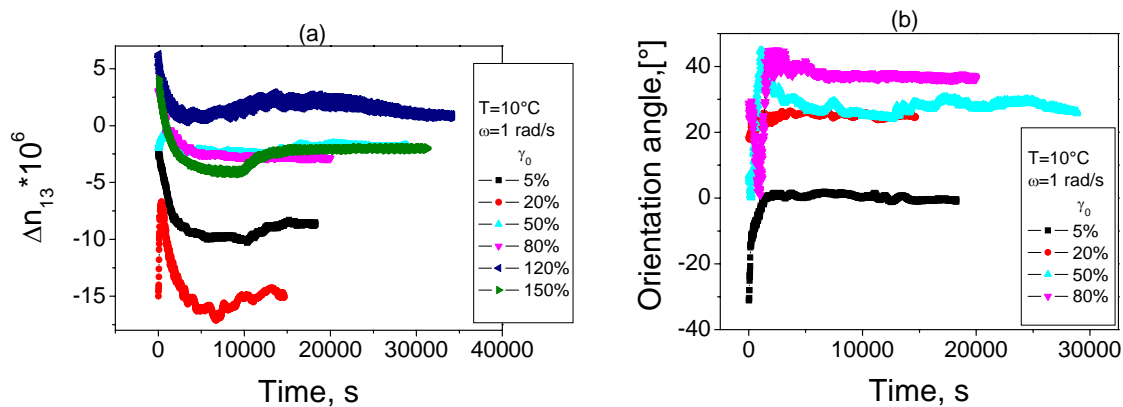
Since the TEM micrograph of  $S_{37}B_{14}M_{49}$ <sup>37</sup> as cast film from  $CHCl_3$  did not show a clear morphological transition due to the hydrogenation, from the previous work<sup>209</sup> on SBM systems with different weight fractions between blocks for example:  $\phi_B=0.11$ ,  $\phi_S=0.45$ , and  $\phi_{MMA}=0.44$  by hydrogenation the lc-morphology has been converted at cr-morphology, whereas the B becomes rings around MMA cylinders in a matrix of S. Our assumption is that  $S_{37}EB_{14}M_{49}$ <sup>37</sup> undergoes cr-morphology with EB-rings surrounding the S cylinders in a matrix of MMA. At  $\gamma_0=5\%$  (Figure 5-17a) a decay in birefringence from  $\Delta n_{13} \sim -2.5 \cdot 10^{-6}$  to  $\Delta n_{13} \sim -10 \cdot 10^{-6}$  followed by a slightly increase to  $\Delta n \sim -8 \cdot 10^{-6}$  while the corresponding orientation angle is increasing from  $-45^\circ$  to  $0^\circ$  as evidence of an achieved alignment. By increasing the strain amplitude  $\gamma_0=120\%$ ,  $150\%$  the final birefringence has a value close to zero and the final orientation angle value (not shown) was oscillating around  $45^\circ$ . It could mean that the system cr-morphology, at high strain amplitudes underwent toward a homogeneous state and the orientation angle values still high ( $\sim 45^\circ$ ) within a small decreased after long time scale are related with the intrinsic birefringence due to the stretching of the "long" chains (from cylinder and matrix).



**Figure 5-15.** The theoretical "knitting pattern" morphology.



**Figure 5-16.** TEM micrograph for  $S_{34}EB_{19}M_{47}^{65}$  as cast film from  $CHCl_3$ , stained with  $RuO_4$  (PS-dark, PEB-ellipsoidal grey domains, PMMA-sinusoidal white lamellae). Scale bar corresponds to 100 nm.



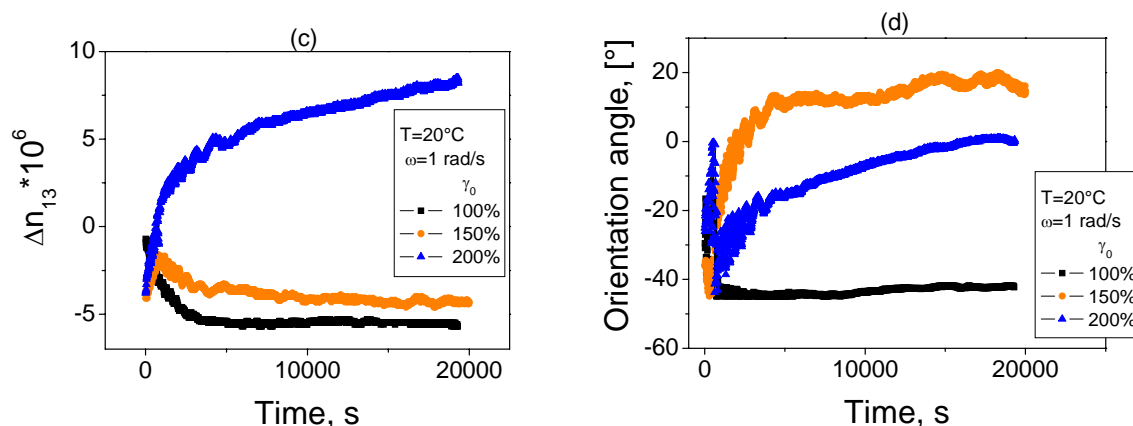


**Figure 5-17.** The birefringence (a,c) and orientation angle (b,d) for 30wt-%  $S_{37}EB_{14}M_{49}^{37}$  in DOP at different alignment conditions: (a, b)  $T=10^{\circ}C$ ,  $\omega=1$  rad/s and  $\gamma_0=5\%$ , 20%, 50%, 80%, 120%, 150%; (c,d)  $T=20^{\circ}C$ ,  $\omega=1$  rad/s and  $\gamma_0=100\%$ , 150%, 200%.

Higher alignment temperature such as  $T=20^{\circ}C$ , and  $\omega=1$  rad/s (Figures 5-17c,d) has induced higher degree of alignment illustrated through the absolute birefringence value of  $\Delta n \sim 8 \cdot 10^{-6}$  at  $\gamma_0=200\%$  and the orientation angle undergoes value close to  $0^{\circ}$ . In the beginning of the process a negative birefringence together with negative values of orientation angles  $\sim -25^{\circ}$  are monitored which may be interpreted as a slightly existing ordered state, after short time scale  $t \sim 500s$  a sharp increase to closely  $0^{\circ}$  orientation angle and zero birefringence would mean an improvement of the existing ordered state before applying shear. At larger time scale  $t > 500s$  a sudden decrease to negative orientation angle  $\sim -40^{\circ}$  followed by gradually increasing toward values close to  $0^{\circ}$  is equivalent with an reordering of the microstructure and finally ( $t \sim 20000s$ ) a roughly approximation of  $0^{\circ}$  orientation angle with the corresponding  $\Delta n_{13} \sim 8 \cdot 10^{-6}$  proved an achieved aligned state. It is not excluded that during shear mixing of the blocks would be possible and different contributions due to the stretching of the chains lead to the final birefringence value. At lower strain amplitudes  $\gamma_0=100\%$ , 150% within simultaneously orientation angles of  $\sim -40^{\circ}$ , and  $+20^{\circ}$  respectively, the indication of lack of alignment is obvious which lead to the conclusion that the shown birefringence at  $\gamma_0=200\%$  is due to the stretching of the chains. As a conclusion pointed out from Figure 5-17 is that low strain amplitudes favor a higher contribution from the intrinsic birefringence, which seems to be apparent above a critical strain amplitude ( $\gamma_0=150\%$ ). Since the  $S_{37}EB_{14}M_{49}^{37}$  has low molecular weight ( $M_n \sim 37K$ ) the degree of segregation is quite low (as illustrated through the interfacial tensions values between monomer pairs from Table 5-2) and the expected *form*

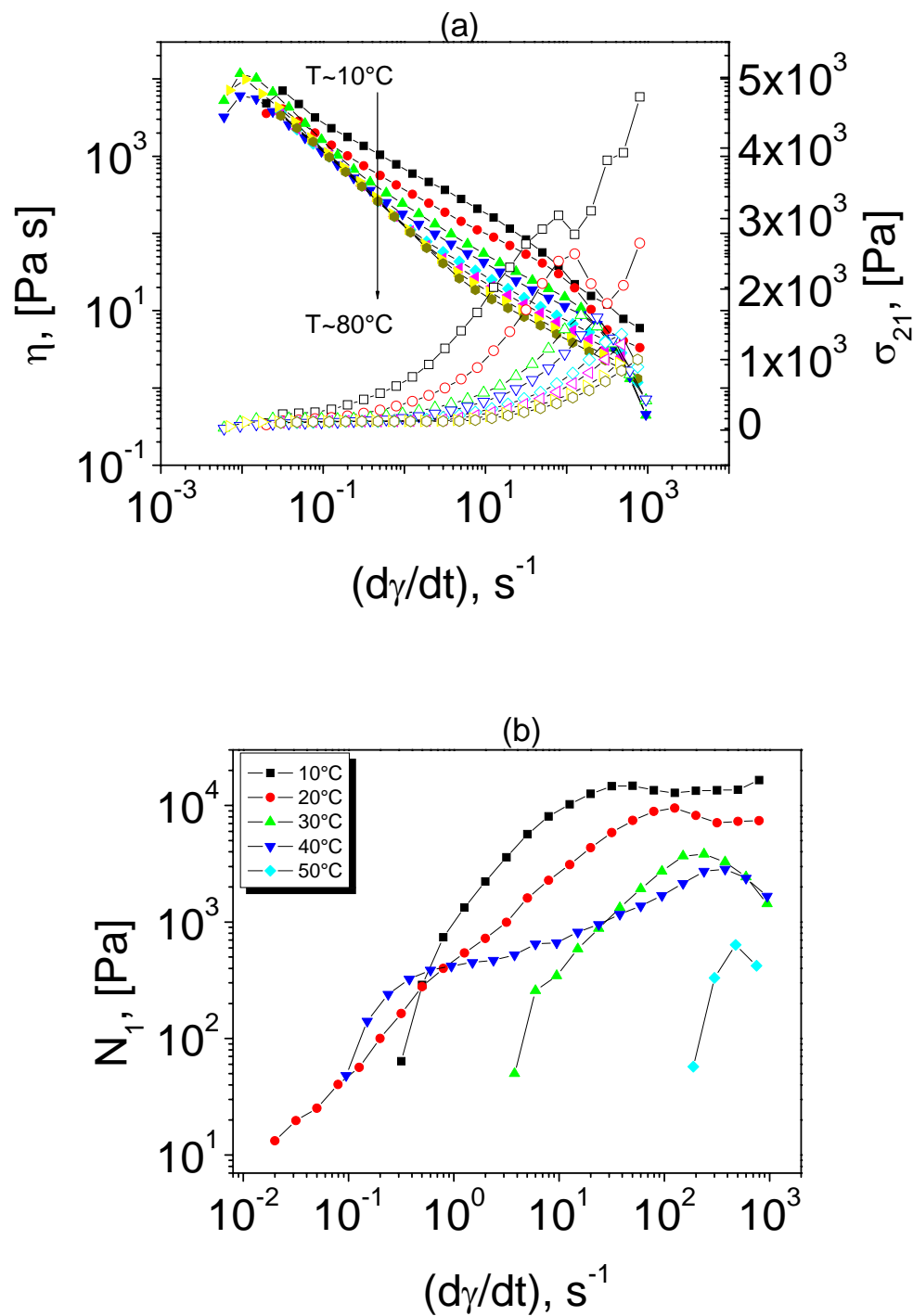
birefringence due to the anisotropic pattern is negligible. A summarizing of the alignment conditions for  $S_{37}EB_{14}M_{49}^{37}$  30% in DOP is illustrated in Table 5-6.

$S_{37}EB_{14}M_{49}^{37}$ 30% in DOP									
	T=10°C, $\omega=1$ rad/s						T=20°C, $\omega=1$ rad/s		
$\gamma_0$ , %	5	20	50	80	120	150	100	150	200
$\Delta n^* \cdot 10^6$	-8	-14	-1.5	-3	0.8	-2	-5.5	-4.3	8.4
[°]	0	25	26	36	~45	~45	-40	15	0.8

**Table 5-6.** The monitored birefringence and orientation angle for 30wt-%  $S_{37}EB_{14}M_{49}^{37}$  in DOP at different alignment temperatures.

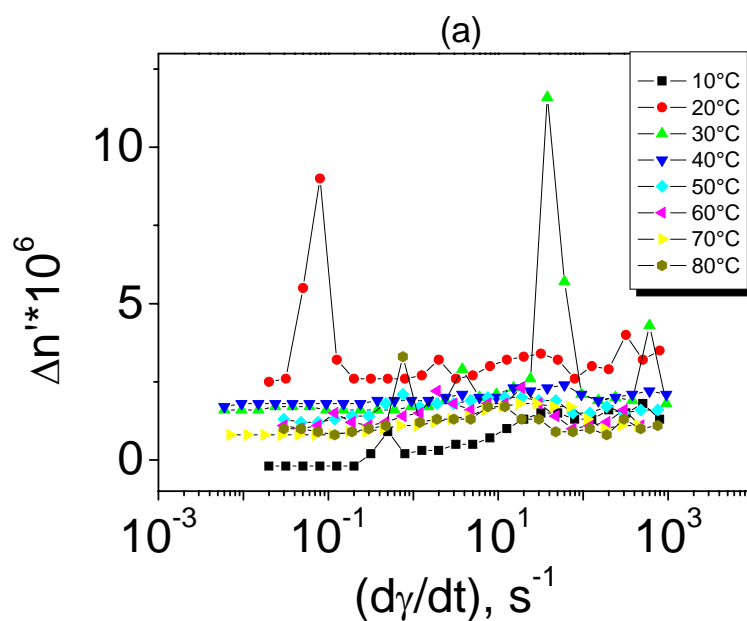
### 5.2.3 Validity of SOR for block copolymer in weak segregation limit (20 wt-% $S_{34}B_{19}M_{47}^{65}$ in DOP)

For multicomponent systems like block copolymers, a “macroscopic” SOR will not be observed in general due to the different contributions from the individually  $C$  combined with the fact that upon changing the frequency or shear rate the individual components will not contribute to the total stress in constant proportions. Ordered block copolymers can be birefringent even at rest, therefore the stress optical rule cannot be valid in general. LAOS applied on such system polystyrene-*b*-polybutadiene-*b*-poly(methyl methacrylate) as solution in DOP at different concentrations, did not show significant birefringence values within a time scale (Table 5-5) or evidence of a saturated birefringence value which allowed us to classify the system as a weakly segregated toward a shear-induced homogeneous state. However, to check whether this assumption is true, an attempt has been made to prove the validity or failure of SOR within a range of shear rate.



**Figure 5-18.**(a) Viscosity and shear stress and (b) the first normal stress difference versus shear rate of a 20 wt-%  $S_{34}B_{19}M_{47}^{65}$  triblock terpolymer in DOP at different temperatures, the filled symbols correspond to the viscosity (a) and first normal stress difference (b), the open symbols to the shear stress, respectively: (—■—)  $10^\circ C$ ; (—●—)  $20^\circ C$ ; (—▲—)  $30^\circ C$ ; (—▼—)  $40^\circ C$ ; (—◆—)  $50^\circ C$ ; (—◀—)  $60^\circ C$ ; (—▶—)  $70^\circ C$ ; (—◆—)  $80^\circ C$ . At temperatures  $T > 50^\circ C$  the first normal stress difference is negative and negligible in further calculations of  $C$ .

However, examining the particular conditions at which stress optical rule fails it provides information regarding the flow behavior of the fluid microstructure. The relative magnitude of the contributions to birefringence and stress provides a signature of the dynamics of the ordered structure. The stress optical rule requires that both the stress and birefringence be dominated by the distortion of chain configurations. We use the failure of stress optical rule to monitor the lack of balance between intrinsic and form birefringence contributions. Thus, the viscoelastic behavior performed by using a steady rate sweep test is depicted in Figure 5-18. The non-Newtonian behavior of the triblock terpolymer solution in DOP is shown at overall range of shear rate (Figure 5-18) within a continuous decrease of viscosity which becomes much more pronounced at high temperatures. Simultaneously, the shear stress rises at high shear rate and decreases with increasing temperature.



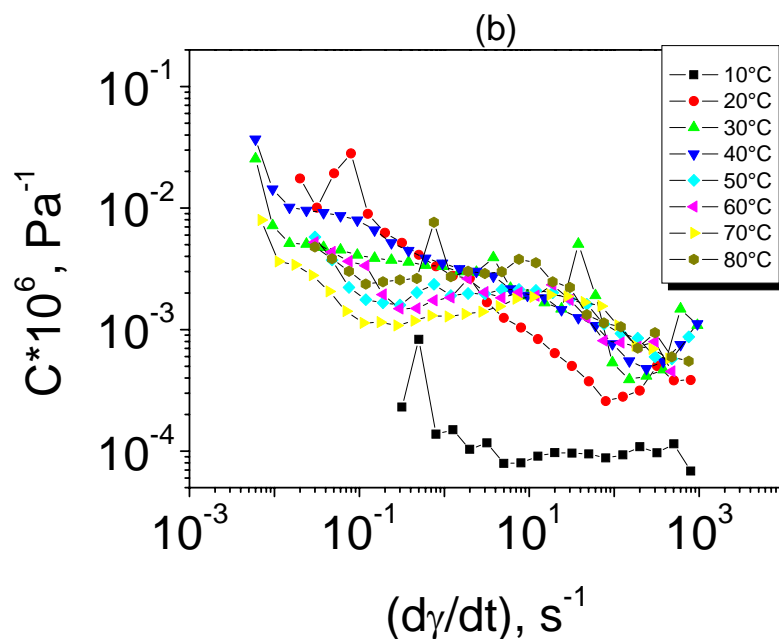


**Figure 5-19.** (a) The monitored birefringence and (b) the calculated stress optical coefficient versus shear rate for a solution of 20wt-%  $S_{34}B_{19}M_{47}^{65}$  triblock terpolymer in DOP at different temperatures.

The stress optical coefficient dependence with shear rate (Figure 5-19b) indicates a decreasing within an increased shear rate but still the plateau region is not obvious at high shear rate. This behavior at low shear rate may be interpreted as a signature of layered structure (microphase separated state) while at high shear rate a molecular contribution from the individually stretched chains corresponding to each of the blocks appear but not enough to claim a pure intrinsic birefringence contribution in this region. A quite low value of  $C$  is observed at  $T=10^{\circ}\text{C}$  (Figure 5-19b) which may be assigned due to the different individually contributions from each of the blocks at the overall value of  $C$ . The polystyrene chain in DOP shows a  $\Theta$  temperature  $T_{\Theta} \sim 7^{\circ}\text{C}^{157}$  and together with a negative stress optical coefficient corresponding to the polystyrene melt<sup>86</sup>,  $C_{PS} \approx (-4 \div -6) \times 10^{-9} \text{Pa}^{-1}$  led to higher contribution from the  $C_{PS}$  of polystyrene chain which may explain the lower value of  $C$  at  $T=10^{\circ}\text{C}$ . Further, with increasing temperature the solubility of PS chain in DOP is increased as a consequence the equal contributions from the individually  $C$  from each of the blocks are accounted thus a higher value of  $C$  is encountered. Although the results shown in Figure 5-19 did not cover a large range of shear rate due to the instrumental limitations they suggest that at higher shear rate ( $>10^3 \text{ s}^{-1}$ ) there may be encountered a plateau of stress optical coefficients.

Similarly, the validity of stress optical rule have been tried previously by Kornfield et al. for block copolymers melts like poly(ethylene-propylene)-poly(ethylethylene)( $M_w \sim 50K$ ) in oscillatory shear mode<sup>191</sup> and it was found that stress optical rule holds above a *critical frequency*.

### 5.3 Conclusions

Within this section it has been proved that the lamellae-cylinder of polystyrene-*b*-polybutadiene-*b*-poly(methyl methacrylate) triblock terpolymer with different molecular weights (37K and 65K) as solutions in DOP behaves as a weak segregated system under influence of oscillatory shear, according as well with the monitored low birefringence values. Due to a mixed of cylindrical and gyroid morphologies for the 65K specimen shown by TEM micrographs, at a certain concentration in DOP the form birefringence is much diminished and an intrinsic birefringence is dominant. Moreover, the morphological transition has been detected for the 30wt-%  $S_{34}B_{19}M_{47}$ <sup>65</sup> in DOP which may be one more reason for the low monitored birefringence values summarized in Table 5-5. The hydrogenated analogous lead to an increased of degree of segregation evidenced as well through higher monitored birefringence values.

Indeed, for different morphologies than the lamellar one the rheoptical method was not sensitive in detection of the type of induced alignment and an intrinsic birefringence has been detected.

Furthermore, the monitored birefringence in steady shear mode together with a calculated stress optical coefficient suggested a plateau for the SOC in the range of high shear rate giving an indication of pure intrinsic birefringence. The validity of SOC for the high shear rate represents as well a signature of weak segregated system.

## 6. In situ rheo-SAXS of a Block Copolymer Solution with lamellar morphology in Couette geometry

### 6.1. Introduction

Previously, an induced parallel alignment of a 20wt-%  $S_{33}B_{33}T_{34}^{160}$  solution in DOP has been achieved and monitored by a combination of LAOS with rheo-optical method. *A priori* investigation by using rheological means and small angle X-ray scattering (SAXS) experiments for the solution of 20wt-%  $S_{33}B_{33}T_{34}^{160}$  in DOP (Chapter 4) has shown the preserved lamellar morphology in diluted state. Since the intermediate pathways leading to the final parallel alignment were perpendicular and transverse states at the same experimental conditions, an in situ rheo-SAXS investigation was required to elucidate the mechanism of alignment.

According to the limitations imposed by using the SAXS method regarding the electron density contrast and temperature, an adjustment of the concentration from 20wt-% to 25wt-% was necessary to ensure the existence of microphase separated system at  $T=25^{\circ}\text{C}$ . While for the rheo-optical method the experimental setup allowed using lower temperatures ( $10^{\circ}\text{C}$ ,  $15^{\circ}\text{C}$ ), for the SAXS measurements the minimum possible temperature was  $25^{\circ}\text{C}$ .

### 6.2. The monitored alignment in block copolymer solution of 25wt-% $S_{33}B_{33}T_{34}^{160}$ triblock terpolymer in DOP

#### 6.2.1 Dynamic-mechanical characterization of the block copolymer solution with 25 wt-% $S_{33}B_{33}T_{34}^{160}$

Before attempting toward an alignment of the lamellar triblock terpolymer  $S_{33}B_{33}T_{34}^{160}$  as a solution of 25wt-% in DOP, dynamic mechanical analysis has been used to investigate the selectivity of the solvent and to determine possible morphological transitions within the experimental temperature range (order-order transition temperatures and order-disorder transition temperature). The initially (in bulk) lamellar triblock terpolymer might have another morphology in DOP due to selective swelling of the blocks.

Temperature sweeps in oscillatory shear flow over a wide range of temperatures,

$T=-40\div 100^{\circ}\text{C}$  and frequencies,  $\omega=1\div 100$  rad/s has been used as illustrated in Figure 6-1.

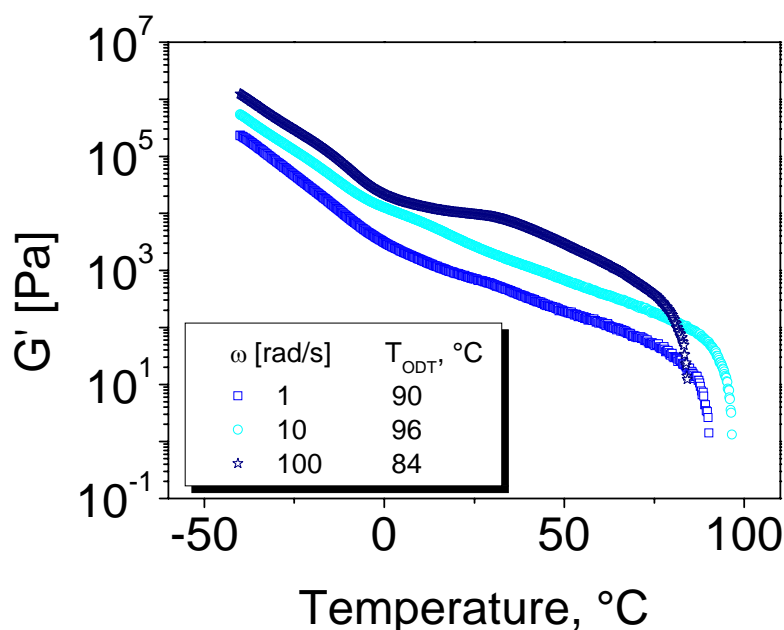


**Figure 6-1.** Variation of  $G'$  with temperature by heating ( $1^\circ\text{C}/\text{min}$ ) at  $\omega = 1, 10, 100$  rad/s for a solution 25wt-%  $S_{33}B_{33}T_{34}^{160}$  in DOP within linear viscoelastic regime ( $\gamma_0 < 1\%$ ). The following ODT's values are attributed for each frequency: i)  $\omega=1$  rad/s and  $T_{ODT}\sim 90^\circ\text{C}$ ; ii)  $\omega=10$  rad/s and  $T_{ODT}\sim 96^\circ\text{C}$ ; iii)  $\omega=100$  rad/s and  $T_{ODT}\sim 84^\circ\text{C}$ .

A continuously decreasing of moduli with increasing temperature is encountered and a plateau of moduli about  $10^4$  Pa is obvious showed at the highest frequency,  $\omega=100$  rad/s.

As already mentioned in Chapter 3, due to the high contribution from the fluctuation effects with increasing temperature an apparent order-disorder transition temperature frequency-dependence was shown. A drop of the moduli at high temperatures is attributed to the order-disorder transition temperature as follows: i)  $\omega=1$  rad/s and  $T_{ODT}\sim 90^\circ\text{C}$ ; ii)  $\omega=10$  rad/s and  $T_{ODT}\sim 96^\circ\text{C}$ ; iii)  $\omega=100$  rad/s and  $T_{ODT}\sim 84^\circ\text{C}$ .

The slight difference in ODT values with frequency is assumed due to the shear heating effect appearing at high frequency ( $\omega=100$  rad/s) leading to lower value of ODT than those at lower frequencies,  $\omega=1$  and 10 rad/s.

In agreement with the phase diagram for the ABA triblock copolymer melts developed by Matsen<sup>33</sup> in the case of the solution of 25wt-%  $S_{33}B_{33}T_{34}^{160}$  in DOP no asymmetry of the morphology has been induced by swelling as proved by the temperature sweep in Figure 6-1. Therefore it may be concluded from the rheological investigation that the bulk lamellar morphology was preserved also in solution. Moreover, the non-selectivity of DOP for

$S_{33}B_{33}T_{34}^{160}$  system has been shown also by SAXS experiments on different concentrations of  $S_{33}B_{33}T_{34}^{160}$  in DOP as already discussed in Chapter 4.

### 6.2.2 The alignment kinetics of the block copolymer solution of 25 wt-% $S_{33}B_{33}T_{34}^{160}$ in oscillatory mode

In order to characterize the structural changes and the induced alignment of the ordered morphology of the 25 wt-%  $S_{33}B_{33}T_{34}^{160}$  in DOP with lamellar morphology, in situ small angle X-ray scattering (SAXS) experiments have been used. Similarly, in situ small angle X-ray scattering studies were conducted on polystyrene-*b*-poly(ethylene-*alt*-propylene) block copolymer films with lamellar microdomains<sup>76</sup>, and with spherical microdomains<sup>210</sup> subjected to a large-amplitude oscillatory shear. A biaxial texture consisting predominantly of a “parallel” orientation which coexists with a nearly “transverse” orientation of lamellae inclined at  $\sim 80^\circ$  to the parallel orientation has been found in a bulk diblock copolymer of polystyrene-*b*-poly(ethylene-*alt*-propylene)<sup>4</sup> (110K) by shearing in oscillatory mode and afterwards investigated by SAXS from specimens taken along three principal axis specific to plate-plate geometry. A solution of 55 wt-% of polystyrene-*b*-polyisoprene (34K) in DOP has been investigated by Balsara<sup>7</sup> and coworkers and the morphological changes under a periodic shear field were determined by in situ small angle neutron scattering. They found that lamellae exhibited two orientations: one parallel to the shearing surfaces and the other perpendicular to the shearing surfaces and the perfection of the perpendicular alignment was always greater than that of the parallel alignment. The cylinder-to-gyroid transition in a polystyrene-*b*-polyisoprene<sup>211</sup> (43K) solution in di-*n*-butyl phthalate (DBP) has been studied using a combination of rheology (parallel plates geometry) and SAXS. According to the previously work, the most investigated systems were diblock copolymers in bulk and in solution with a low molecular weight.

Subsequently, there will be presented the kinetics on  $S_{33}B_{33}T_{34}^{160}$  triblock terpolymer with a lamellar morphology in the swollen state by using oscillatory shear in Couette geometry where the X-ray beam passed through in radial and tangential directions. A schematic representation of the setup (Haake rheometer equipped with aluminium Couette cell) within a defined cartesian coordinates specifically for Couette geometry are illustrated in Figure 6-2. The Couette cell consists of two concentric cylinders, an inner rotor and an outer stator with a gap between the two cylinders of 1mm. When the beam was directed through the center of the cell the setup was in the radial configuration and when the beam was directed through the

edge of the cell, the setup was in the tangential configuration. Thus, the scattering profiles were obtained in two planes. The scattering profile in the  $(\mathbf{v}, \nabla \mathbf{v} \times \mathbf{v})$  plane was obtained in the radial configuration, while that in the  $(\nabla \mathbf{v}, \nabla \mathbf{v} \times \mathbf{v})$  plane was obtained in the tangential configuration as drawn in Figure 6-2. A detailed scheme of the beamline at ESRF, Grenoble-France has been presented in Chapter 2. The SAXS intensities were corrected for background scattering and presented as a function of scattering vector,  $q$ .

***Alignment kinetics for 25 wt-%  $S_{33}B_{33}T_{34}^{160}$  in DOP,  $T=40^\circ\text{C}$ ,  $\omega=10$  rad/s,  $\gamma=10\%$ .***

The solution was placed in a Couette cell at a temperature close to ODT, such as  $T=80^\circ\text{C}$  in order to avoid inhomogeneities throughout the sample during the shearing process. The scattering profiles at  $T=80^\circ\text{C}$  showed a weak signal which confirmed the ODT determined by rheology as illustrated in Figure 6-1. The sample was then cooled to a predetermined temperature in the ordered state ( $T=40^\circ\text{C}$ ) and annealed for 15 min for equilibration. Before commence shearing the scattering profiles taken at  $T=40^\circ\text{C}$  in radial and tangential views confirmed the microphase separated state as expected from the previous dynamic mechanical test. While in the tangential view three correlation peaks were found with the ratio 1 : 1.5 : 2, in the radial view a scattering profile with only one peak was encountered which might be the reason to monitor the alignment just in the tangential view. Due to the filling protocol and surface effect from the aluminium of the Couette cell a prealignment of the morphology during the cooling process has been obtained with scattering maxima in tangential view at  $0^\circ$  and  $180^\circ$  indicating a parallel arrangement of lamellae to the wall of the cell. Shearing at a predetermined frequency  $\omega=10$  rad/s and strain amplitude  $\gamma=10\%$  after  $t=859$ s with a corresponding stress of  $\sigma=21$ Pa, has induced an almost perpendicular alignment as indicated by scattering maxima slightly shifted to higher azimuthal angles than  $90^\circ$  and  $270^\circ$  (Figure 6-3a). Typical two-dimensional scattering data obtained from the 25wt-%  $S_{33}B_{33}T_{34}^{160}$  solution in DOP, in the tangential configuration are shown in Figure 6-3.

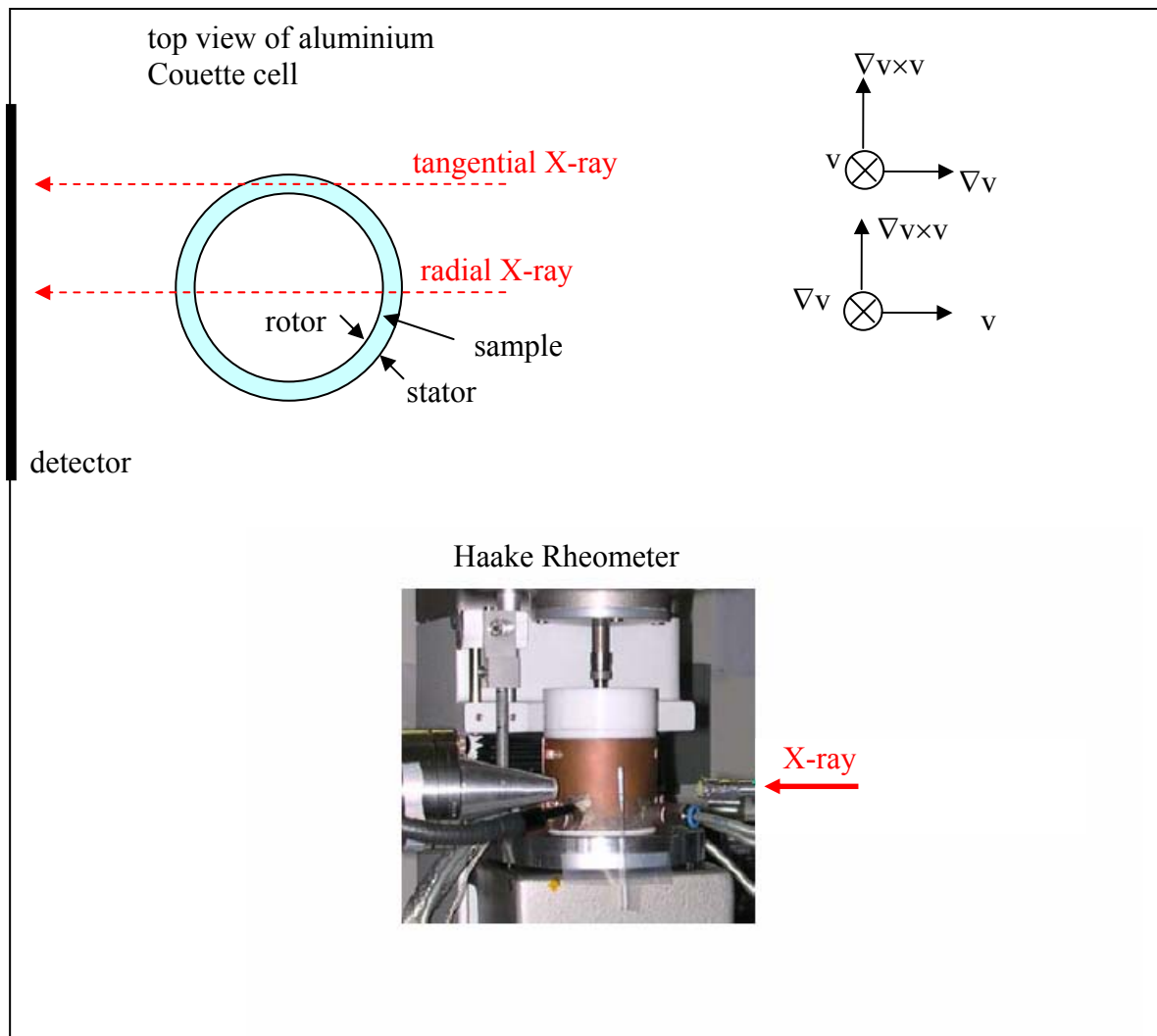


**Figure 6-2.** Schematic representation of the top view of the Couette shear cell in tangential and radial configurations within the defined coordinates:  $v$  - flow direction;  $\nabla v$  - velocity gradient;  $\nabla v \times v$  - vorticity. A Haake rheometer built into SAXS beam line has been used for the shear deformation.

Continuous shearing at  $T=40^\circ\text{C}$ ,  $\omega=10$  rad/s,  $\gamma=10\%$  after  $t=1380\text{s}$  led to a change of the alignment toward a coexistence of a predominantly parallel ( $15^\circ$  and  $195^\circ$ ) and slightly perpendicular orientation with a growth of the peaks at around  $90^\circ$  and  $270^\circ$  (Figure 6-3b). The coexistence of parallel and perpendicular alignment with increasing time is obvious from the interchangeable dominance of one of them until a single aligned state is reached after  $t=2074\text{s}$  (Figure 6-3c) with scattering maxima at  $150^\circ$  and  $330^\circ$ , respectively which may be called “mixed” alignment. It follows a shift toward a more parallel alignment at  $t=2287\text{s}$  with the corresponding angular dependence at  $170^\circ$  and  $350^\circ$  (not shown in Figure 6-3).

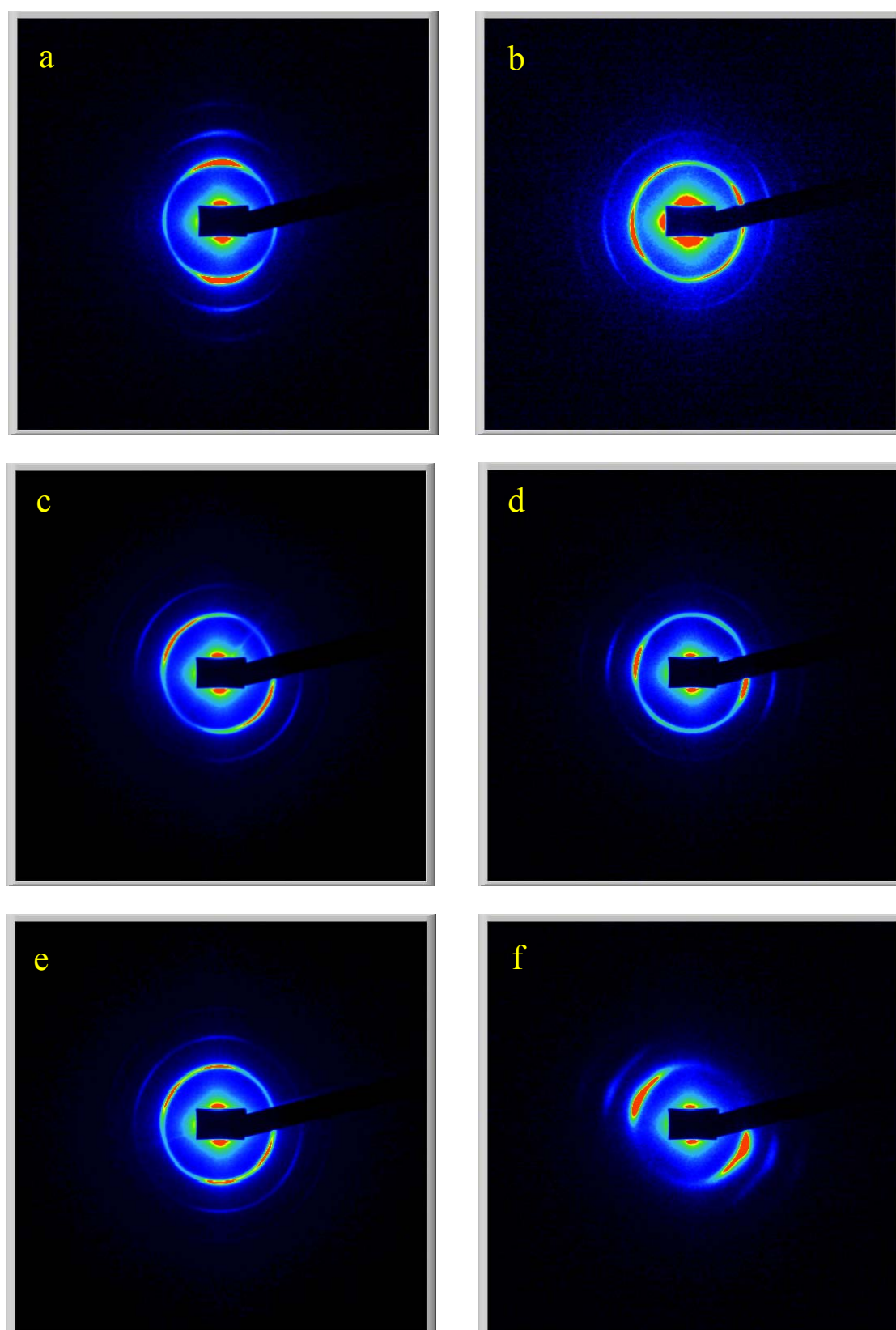


**Figure 6-3.** Evolution of alignment process in tangential view at various times and the corresponding type of alignment:(a)  $t=859\text{s}$ , perpendicular; (b)  $t=1380\text{s}$ , coexistence of mostly parallel and less perpendicular; (c)  $t=2074\text{s}$ , mixed alignment-single aligned state; (d)

$t=2517$ s, toward parallel; (e)  $t=2943$ s, coexistence of parallel and perpendicular with equal contribution; (f)  $t=3460$ s, so called “tilted” parallel.

An isotropization of the aligned state happens and surprisingly at larger time ( $t=2517$ s) the growth of parallel alignment was observed (Figure 6-3d), which was more developed than the previous one at  $t=2287$ s. After a very short time, at  $t=2592$ s the coexistence of both aligned states are present with a more parallel and less perpendicular or more perpendicular and less parallel state while between these states an isotropization takes place. At  $t=2943$ s an equal contribution from perpendicular ( $90^\circ$  and  $270^\circ$ ) and tilted parallel ( $150^\circ$  and  $330^\circ$ ) reflected by an almost same height of the peaks in the azimuthal dependence is shown in Figure 6-3e. A well aligned so-called “tilted” parallel state with an angular maxima at  $160^\circ$  and  $340^\circ$  arises after  $t=3460$ s and the 2D-pattern is illustrated in Figure 6-3f. A continuous shearing led to a reduction of alignment as seen from the decrease of the height of the peaks in the angular dependence and the alignment again is a coexistence of two states as found previously. The isotropic state appears always at interchanging from one dominant to the other dominant state (parallel or perpendicular). It may be concluded that after a yield behavior encountered after  $t=3460$ s the alignment process undergoes the same protocol in an opposite pathway since a non perfectly parallel aligned state was achieved (angular maximum at  $160^\circ$  and  $340^\circ$  than the expected values of  $180^\circ$  and  $360^\circ$  for a perfectly defined parallel state). The angular dependence during oscillatory shear with time is illustrated in Figure 6-4.

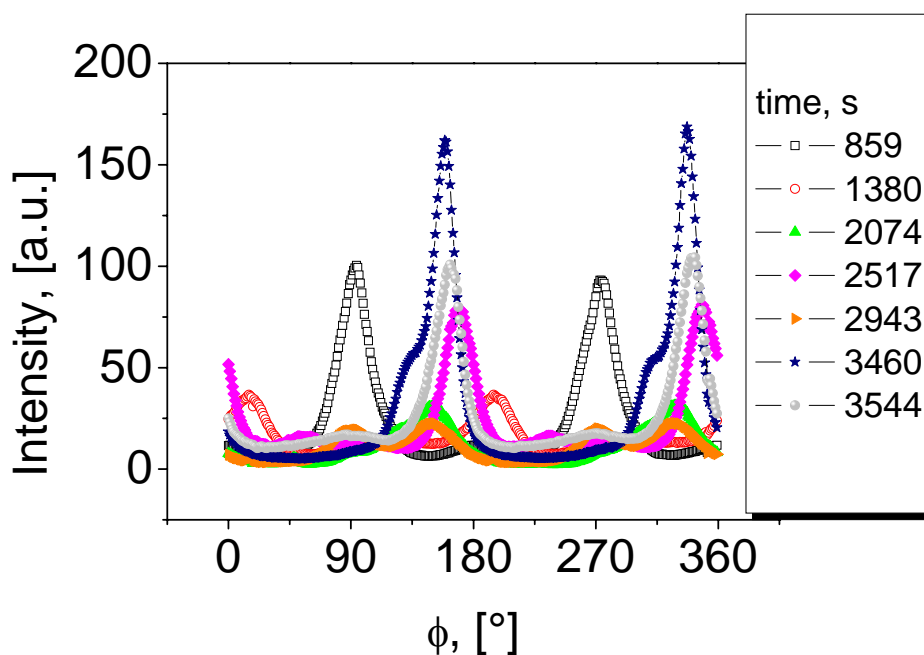


**Figure 6-4.** Intensity versus azimuthal angle in tangential view during oscillatory shear at temperature  $T=40^\circ\text{C}$ , frequency  $\omega=10$  rad/s, and strain amplitude  $\gamma=10\%$ .

As already illustrated by the 2D-patterns in Figure 6-3 the alignment undergoes from an initially induced perpendicular at short time scale  $t=859\text{s}$  toward a final tilted parallel state at  $t=3460\text{s}$  via intermediate of coexisting perpendicular and parallel states with a seldom isotropization step inbetween.

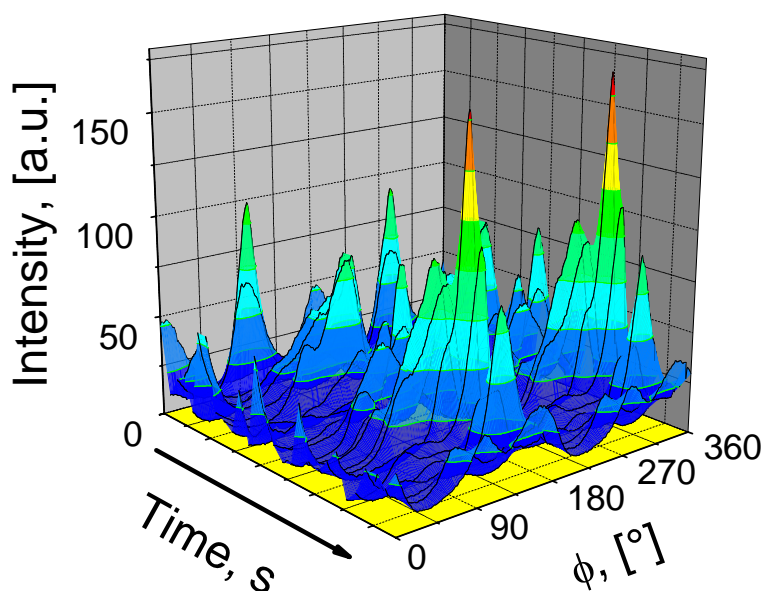


**Figure 6-5.** 3D azimuthal dependence within intensity and time scale.

A three dimensional plot illustrating the evolution of the alignment process is shown in Figure 6-5. The evidence of coexisting of two types of alignment is clearly evidenced in this map at the first stages of shearing by a multiangular dependence and obviously followed by the maximum of the single angular dependence (at  $160^\circ$  and  $340^\circ$ ) after a shearing time  $t=3460\text{s}$  where the so-called “tilted” parallel was shown. At longer times a loss of the alignment is encountered by less intense peaks at the end of shearing process ( $t=3544\text{s}$ , Figure 6-4).

Another pathway of quantitative evaluation of macroscopically aligned state with time is represented by the order parameter,  $P_2$ . In Figure 6-6 is represented the dependence of calculated order parameter of time. Depending on the type of alignment, two different ranges of the order parameter exist. For a parallel alignment in tangential view, the maximum scattering should be at  $\phi=180^\circ$  (the normals of lamellae along the gradient velocity axis,  $\nabla v$ ) and for a perpendicular alignment in tangential view the maximum scattering should be at  $\phi=90^\circ$  and  $270^\circ$  (the normals of lamellae along the vorticity axis,  $\nabla v \times v$ ), respectively in agreement with the axis definition for the Couette geometry (Figure 6-2). Thus, for a parallel

alignment,  $P_2$  ranges from 0 to 1 with  $P_2=1$  for a perfect parallel alignment with lamellae parallel to the plane formed between the axis  $v$  and  $\nabla v \times v$ .

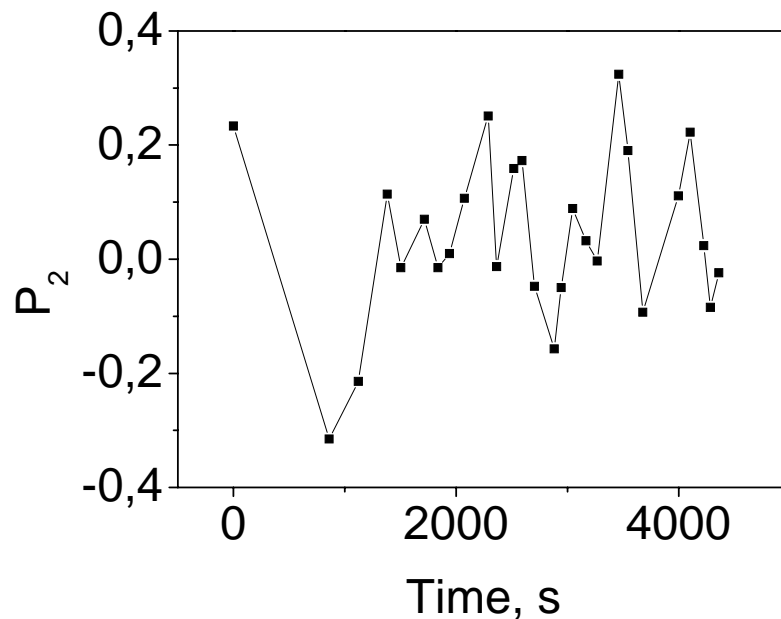


**Figure 6-6.** The order parameter,  $P_2$  versus time calculated by using eq 1-16 and eq 1-17 from section 1.2.2.

For a perpendicular alignment with the lamellae normals parallel to vorticity direction, the order parameter  $P_2$  ranges from 0 to -0.5 with  $P_2=-0.5$  corresponding to the case where all lamellae are aligned parallel to the plane formed by axis  $v$  and  $\nabla v$ .

In Figure 6-6 are depicted some values of the order parameter calculated while shearing has induced a valuable aligned state.

A strong influence from the surface effect which has induced an arrangement of lamellae parallel to the surface geometry, namely to the plane  $(v, \nabla v \times v)$  is evidenced before shearing by a value of the order parameter,  $P_2=0.23$  at  $t=0s$  illustrated as well in Figure 6-6. At the very early stages of shearing process after  $t=859s$ , the order parameter changes toward a negative value of  $P_2=-0.31$  due to the shear induced perpendicular alignment. With time the order parameter  $P_2$  will take negative and positive values depending of the type of alignment and sometimes  $P_2=0$  due to the isotropization between different aligned states. The most valuable parallel alignment encountered was characterized by a value of  $P_2=0.32$  at  $t=3460s$  followed by a decreasing of  $P_2$  value at longer times. Moreover a value of  $P_2=0.19$  after  $t=3544s$  proved as well some loss of alignment after the maximum encountered at  $t=3460s$ .

Therefore, after a shearing time of  $t=4360$ s a coexistence of mostly parallel and less perpendicular was accomplished similar to the one at  $t=2943$ s which may indicate a repeating of alignment process backwards following the same pathway as already illustrated in Figure 6-3. The stability of the aligned structure after cessation of shear and 10 min at rest was checked in both views as follows: in the tangential view the aligned state seems to present a coexistence of more perpendicular and less parallel state while in the radial view a slightly remaining perpendicular state was observed as well evidenced in the plot of intensity versus azimuthal angle from Figure 6-7.

According to the above discussed statements, we may conclude that a strain amplitude of  $\gamma=10\%$  has induced a coexistence of parallel and perpendicular alignment for small time scale and at larger time scale, after  $t=3460$ s, a pure parallel alignment is induced but still not well defined (maximum scattering intensity at  $\phi=160^\circ$  and  $340^\circ$ , respectively).

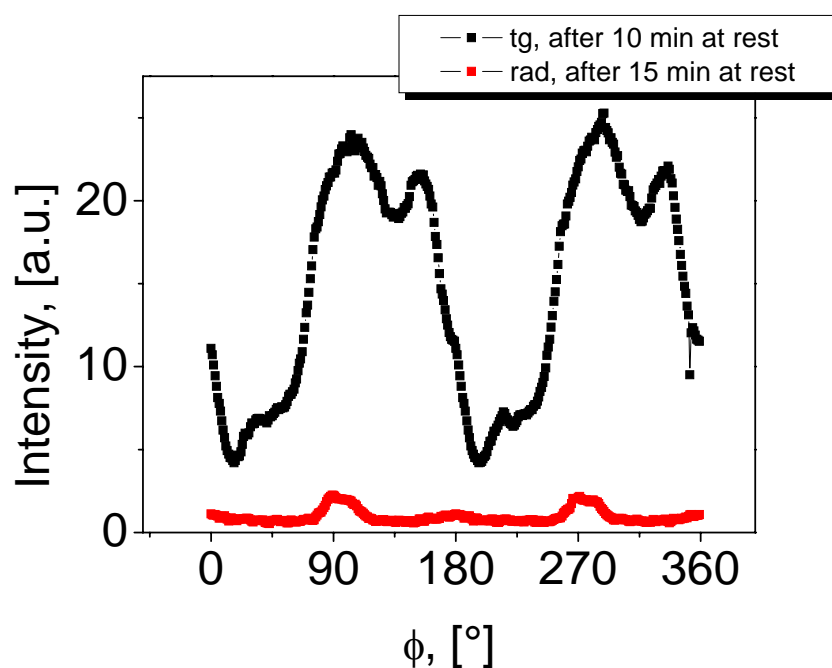
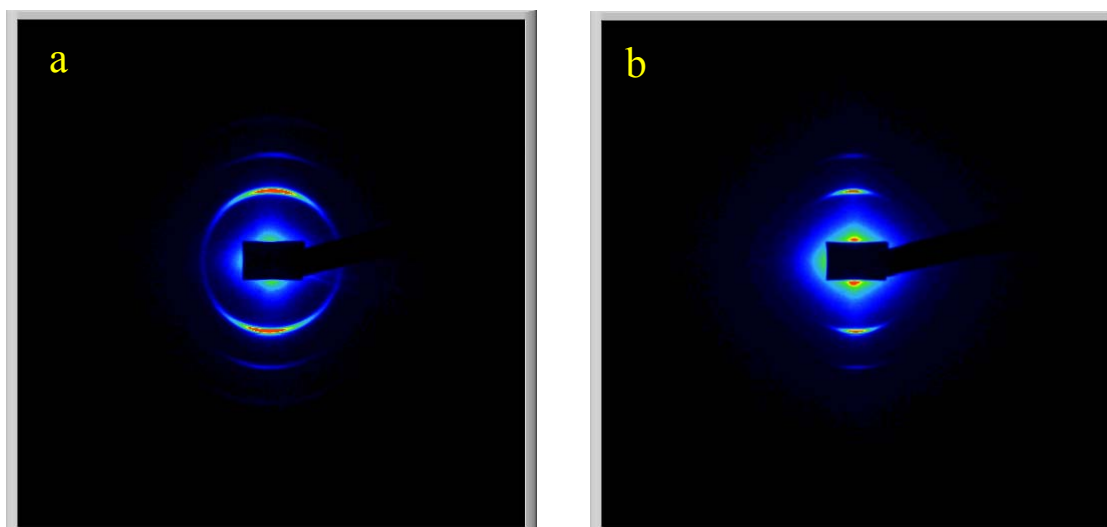


**Figure 6-7.** Azimuthal dependence in tangential and radial configurations after cessation of shear.

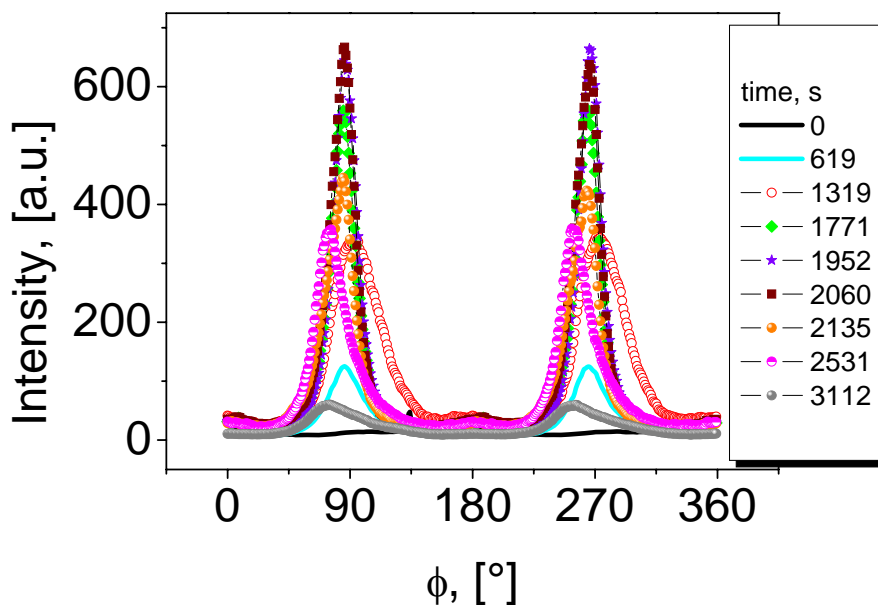
*Alignment kinetics for 25 wt-%  $S_{33}B_{33}T_{34}^{160}$  in DOP,  $T=40^\circ\text{C}$ ,  $\omega=10$  rad/s,  $\gamma=25\%$ .*

Due to the coexistence of parallel and perpendicular aligned states obtained at the low strain amplitude  $\gamma=10\%$ , an attempt was made to increase the strain amplitude to  $\gamma=25\%$  in order to improve the selectivity for one type of alignment (parallel or perpendicular). Before shearing the microphase separation was checked in the tangential and radial views, showing a yield

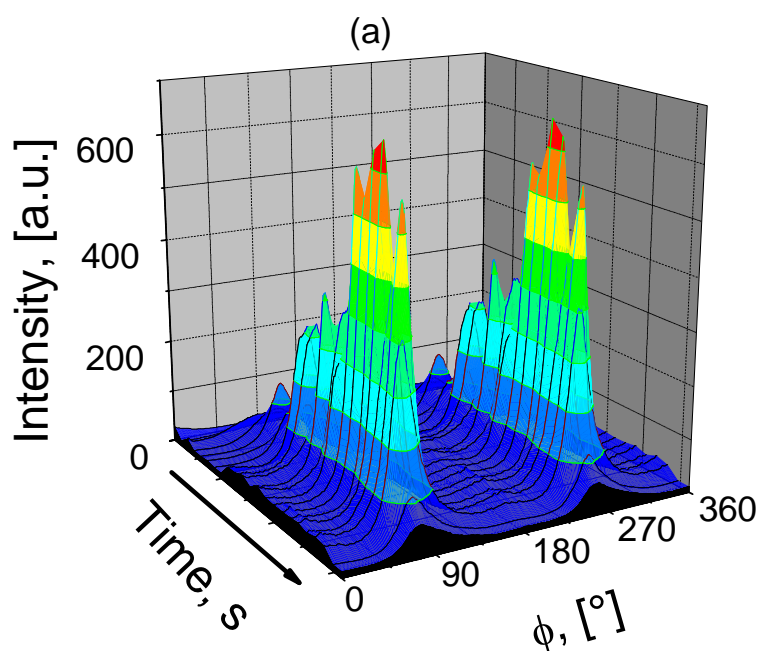
behavior in the tangential view with the ratio of correlation peaks 1 : 1.5 : 2 and poorly developed peaks in the radial view. Thus, mostly the alignment has been monitored in the tangential view. Shearing at a strain amplitude of  $\gamma=25\%$  induced a perpendicular alignment after an initial parallel alignment due to surface effects, as seen in the tangential view after  $t=619\text{s}$ . The maximum scattering intensity was shown at azimuthal angles of  $\phi=85^\circ$  and  $265^\circ$  as illustrated in Figure 6-8a. After it was achieved this perpendicular state a continuous shearing led to the same perpendicular alignment which appeared with  $\pm 7^\circ$  tilted from the initial first scattering maximum. The perpendicular alignment is perfected after  $t=1952\text{s}$  afterwards it is continuously decreasing showing less scattering intensity. Few scattering patterns were monitored as well in the radial view showing the same perpendicular alignment evidenced through much less scattering intensity than in tangential view (Figure 6-8 b). The evolution of the alignment process is shown as well in the overlay plot of intensity versus azimuthal angle in Figure 6-9 where the continuous increasing of intensity with time is encountered as a consequence of a well aligned state while the azimuthal angles are oscillating around the values  $85^\circ \pm 10^\circ$ . The scattering intensity decreased after  $t=1952\text{s}$  which may be correlated with the loss in alignment from a well aligned state toward weak aligned state following the same pathway backwards as the one leading to a well aligned state. Thus, it may be defined a critical shear time of  $t=1952\text{s}$ : until this time the aligned state developed gradually and after the well aligned state was obtained, it decayed toward a less aligned state characterized as well by a lower scattering intensity (Figure 6-9). Some of the most significant scattering profiles were plotted in Figure 6-9 indicating the evolution of alignment process. Moreover, a more detailed information about the alignment developed with time scale is given by the 3D map shown in Figure 6-10a.



**Figure 6-8.** 2D-patterns illustrating a perpendicular alignment in tangential (a) and radial (b) views.



**Figure 6-9.** The evolution of angular dependence for the solution 25 wt-%  $S_{33}B_{33}T_{34}^{160}$  in DOP at  $T=40^{\circ}\text{C}$ ,  $\omega=10$  rad/s,  $\gamma=25\%$  in tangential view. The maximum scattering intensity is shown at  $t=1952\div 2060$ s afterwards the intensity is decreased due to the loss in the alignment through a continuously shear with time scale.



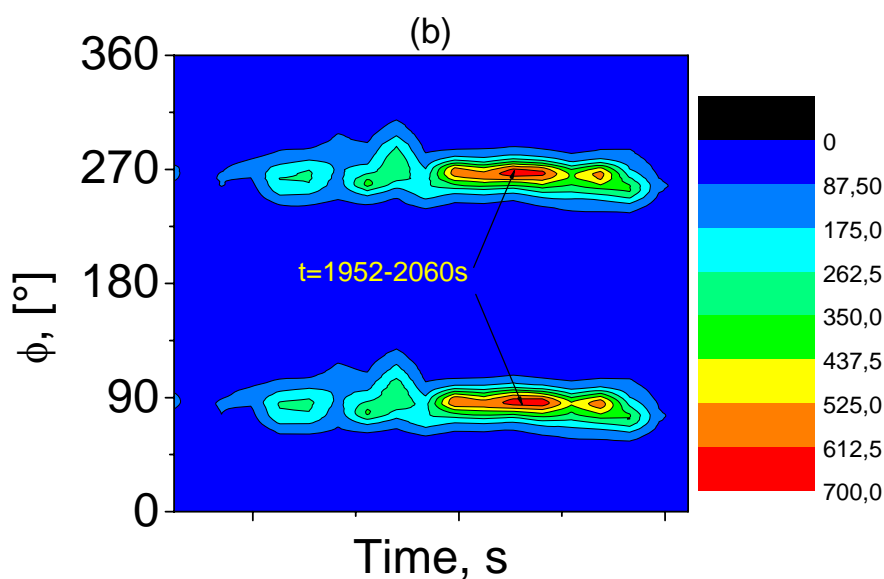


**Figure 6-10.** (a) 3D map of the angular dependence within time scale and scattering intensity; (b) top view of the azimuthal angle dependence with time scale.

The slight oscillation of the azimuthal angle around  $90^\circ$  and  $270^\circ$  in Figure 6-9 is diminished with increasing shearing time toward a perfection of the perpendicular alignment shown at  $t=1952\div 2060$ s. During continuous shearing the 2D patterns were taken just for the most significant changes and for such reason the time scale in Figure 6-10 is just qualitatively illustrated. Thus, the maximum intensity in Figure 6-10 is assigned to the time range of  $t=1952\div 2060$ s.

As seen in the 3D map (Figure 6-10a) the evidence of perpendicular alignment is quite obvious, with the corresponding azimuthal angle at around  $\phi\sim 90^\circ$  and  $\phi\sim 270^\circ$ . The scattering intensity is gradually increased with time until a maximum achieved after  $t=1952$ s and as well a gradually decreasing of scattering intensity at longer time  $t>1952$ s is shown in Figure 6-10a. The islands from the top view of azimuthal angle versus time (Figure 6-10b) are developed at  $90^\circ$  and  $270^\circ$  as an evidence that higher strain amplitude such as  $\gamma=25\%$  has induced a selectivity of the type of alignment toward a perpendicular one.

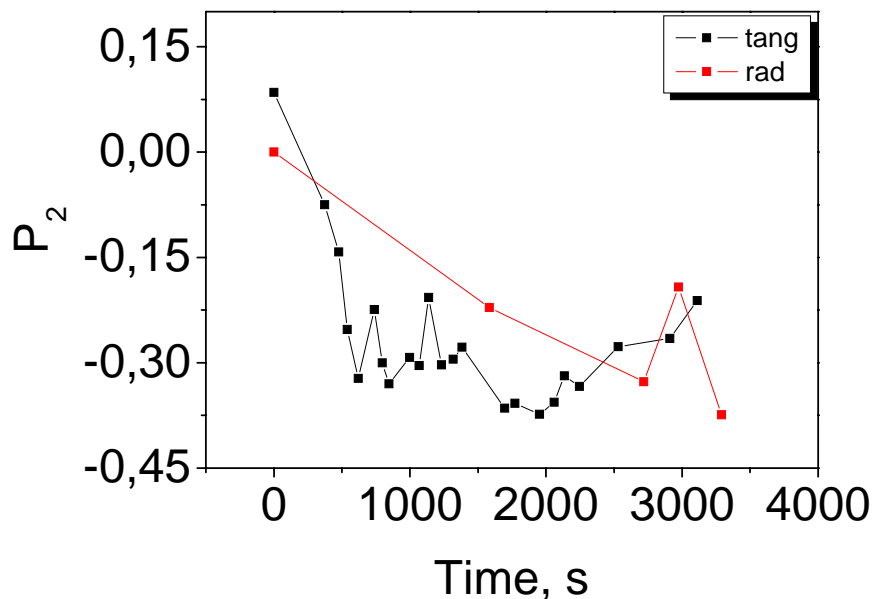


**Figure 6-11.** The calculated order parameter,  $P_2$  in tangential and radial views versus time.

The alignment has been quantified as well by the calculated order parameter,  $P_2$ , as illustrated in Figure 6-11. By increasing shear time the  $P_2$  values calculated for the tangential view were negative, indicative for the perpendicular alignment. The lowest value of order parameter was found,  $P_2 = -0.37$  at the corresponding time  $t = 1952$  s. Similarly, the few monitored experiments in the radial view encountered as well negative values of  $P_2$  with increasing shear time and at the end of shearing  $t = 3290$  s the maximum order was given by  $P_2 = -0.37$  while in the tangential view at the end of shearing order parameter undergoes  $P_2 = -0.21$  from the minimum value of  $P_2 = -0.37$ . Indeed, these order parameter values proved that by increasing the strain amplitude from  $\gamma = 10\%$  to  $\gamma = 25\%$  at a constant frequency,  $\omega = 10$  rad/s and temperature  $T = 40^\circ\text{C}$ , a selectivity toward an induced perpendicular alignment was shown.

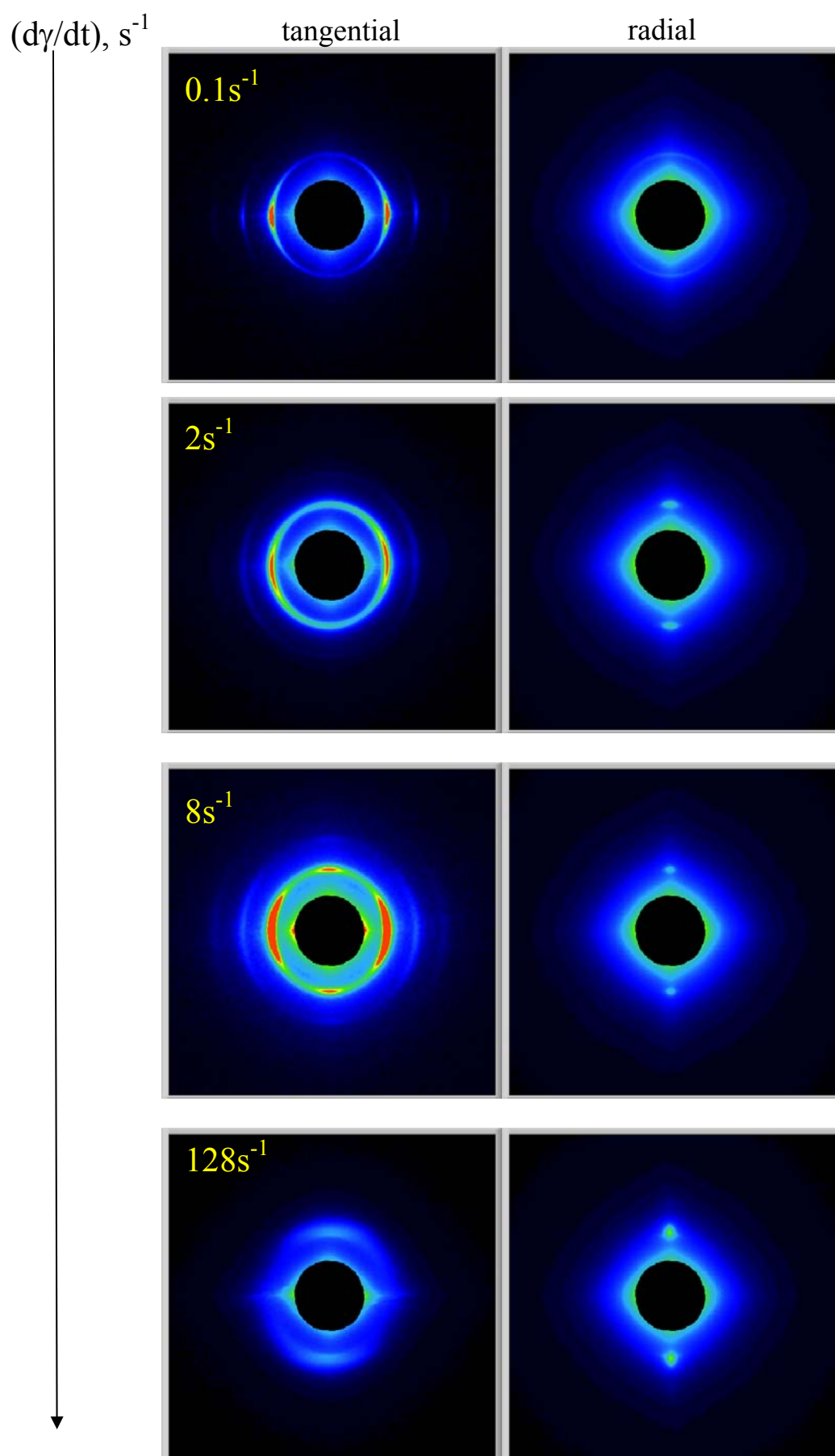
### 6.2.3 The alignment kinetics of block copolymer solution 25 wt-% S<sub>33</sub>B<sub>33</sub>T<sub>34</sub><sup>160</sup> in steady mode

According to the previous alignment tests performed in oscillatory shear mode which have demonstrated an induced perpendicular alignment of lamellae, an attempt was made to align the same system with a steady shear mode. Thus, in the following section will be presented the alignment kinetics at different shear rates in the tangential and radial views, summarized as 2D-patterns, angular dependencies plots, 3Dmaps and plot of order parameter,  $P_2$  versus shear rate,  $(d\gamma/dt)$ . The alignment was performed at  $T=40^\circ\text{C}$  where a microphase separated state was present. During the cooling process from the disordered state to  $T=40^\circ\text{C}$  a preferential alignment like a parallel one due to the surface effect has been detected.

Some of the 2D-patterns monitored during increasing shear rate, in tangential and radial views are illustrated in Figure 6-12. At low shear rate  $(d\gamma/dt)=0.1\text{s}^{-1}$  the initially parallel alignment of lamellae from tangential view was not changed and in the radial view an isotropic pattern was shown in agreement with only one type of lamellae parallel to the cell surface.

Subsequently, increasing the shear rate to  $(d\gamma/dt)=0.5\text{s}^{-1}$  and  $(d\gamma/dt)=1\text{s}^{-1}$ , have maintained the same pattern in tangential view with scattering maxima at  $\phi=0^\circ$  and  $180^\circ$ , respectively and in the radial view an isotropic pattern as shown in Figure 6-12. A slight tilting of lamellae in the tangential view from the parallel position has induced as well a slight trend toward isotropization which in radial view appeared as a weak scattering at  $\phi=90^\circ$  and  $270^\circ$ . A coexistence of parallel and perpendicular orientations as illustrated by four spots seems to appear in the tangential view at shear rate of  $(d\gamma/dt)=8\text{s}^{-1}$  and an improving of scattering in the radial view is encountered as well due to the growing of perpendicular aligned state in tangential view.

At higher shear rates following the sequence  $(d\gamma/dt)=16\text{s}^{-1}$ ,  $32\text{s}^{-1}$ ,  $64\text{s}^{-1}$  in the tangential view the perpendicular orientation disappears and only the parallel one remained as proved by an isotropic pattern in radial view, the same as shown previously for  $(d\gamma/dt)=0.1\text{s}^{-1}$ .



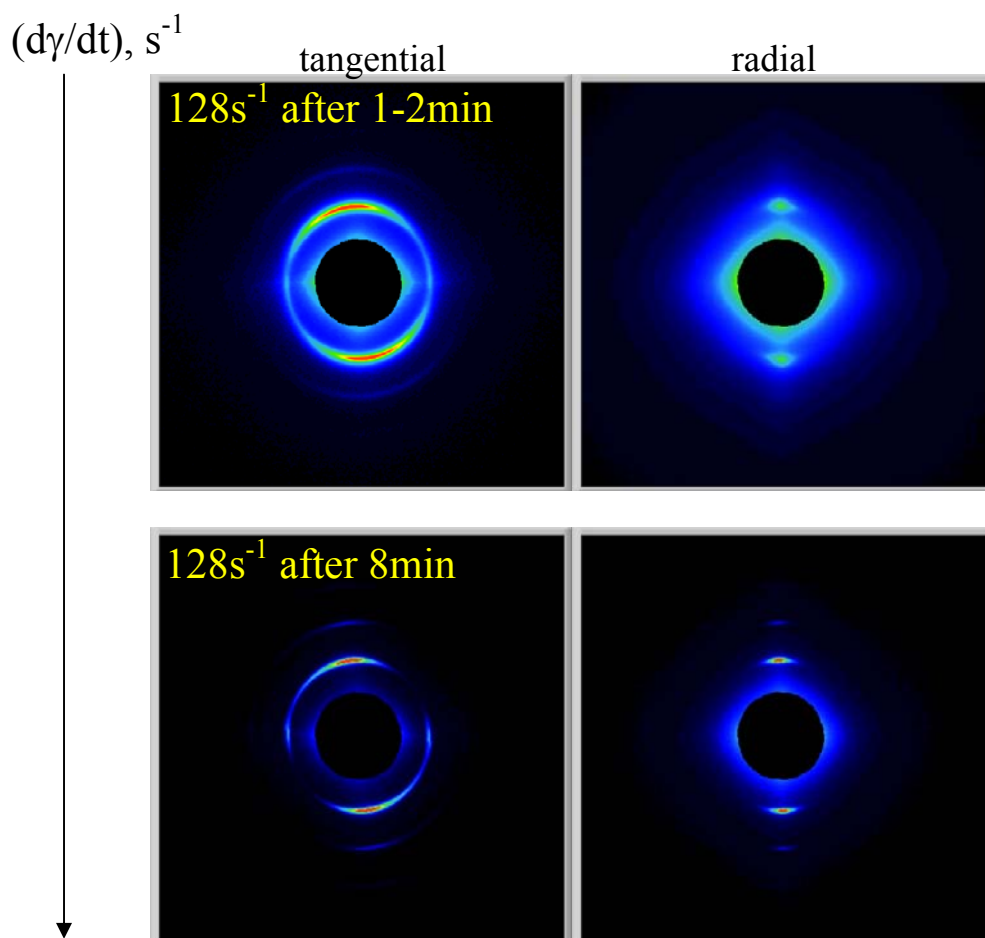


**Figure 6-12.** 2D-patterns of the alignment kinetics in steady shear mode at different shear rates.

A significant change takes place at shear rate  $(d\gamma/dt)=128s^{-1}$  when the parallel changed quantitatively toward perpendicular alignment. Thus, in tangential and radial configurations a weak scattering signal appeared around the azimuthal angles  $\sim 90^\circ$  and  $\sim 270^\circ$  which became stronger with time. The same scattering pattern without changes has been monitored at  $(d\gamma/dt)=256s^{-1}$  which allowed to conclude that this is the maximum shear rate possible to be applied for this system leading to a perpendicular alignment.

The presence of isotropization which accompanies the transition from parallel to perpendicular alignment during the shear process has been observed in the overlay plot of intensity (I) versus scattering vector, (q) as shown in Figure 6-13. In the plot I versus q at  $(d\gamma/dt)=128s^{-1}$  it corresponds to a broad peak which designates the transition from parallel to perpendicular state. With time the new aligned state develops and remains constant at higher shear rate,  $(d\gamma/dt) > 128s^{-1}$ . The correlation peaks are in the ratio 1 : 1.5 : 2 corresponding to the lamellar morphology.

In terms of angular dependence, the transition from parallel to perpendicular alignment in tangential view is shown in Figure 6-14 whereas the maximum scattering from azimuthal angle  $\phi=180^\circ$  disappears with increasing shear rate and the growth of perpendicular alignment is evidenced by scattering maxima at  $\phi=97^\circ$  and  $277^\circ$ , respectively.

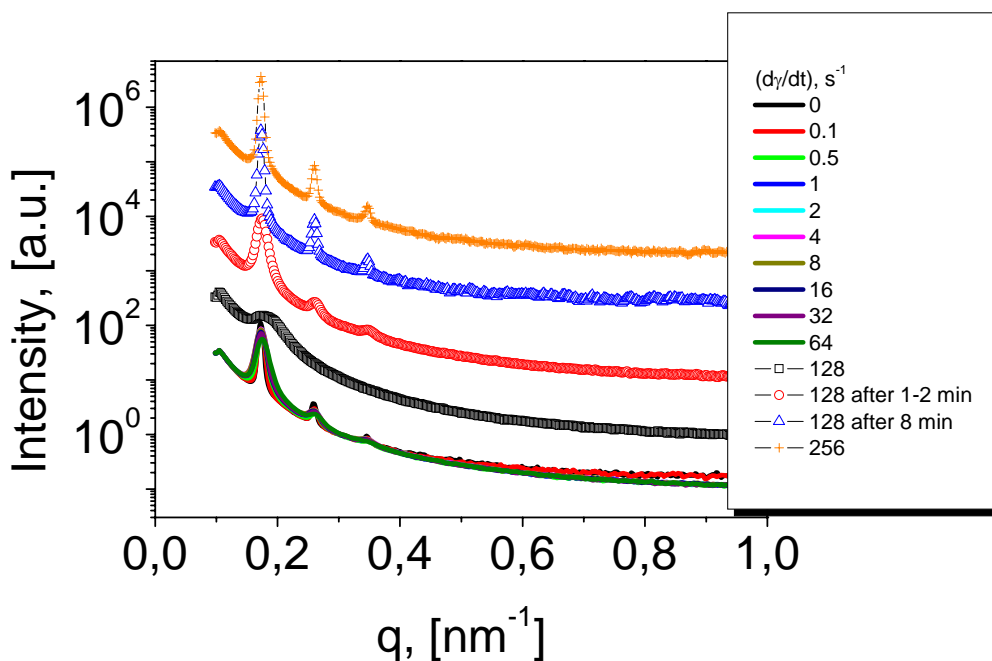


**Figure 6-13.** Monitoring the transition from parallel to perpendicular in the tangential view via isotropization and growing the new aligned state. The overlapped curves correspond to the range of shear rates  $(d\gamma/dt)=0\div 64\text{s}^{-1}$  and the other curves at  $(d\gamma/dt)=128\text{s}^{-1}$  and  $256\text{s}^{-1}$  were shifted vertically by a factor of 10.

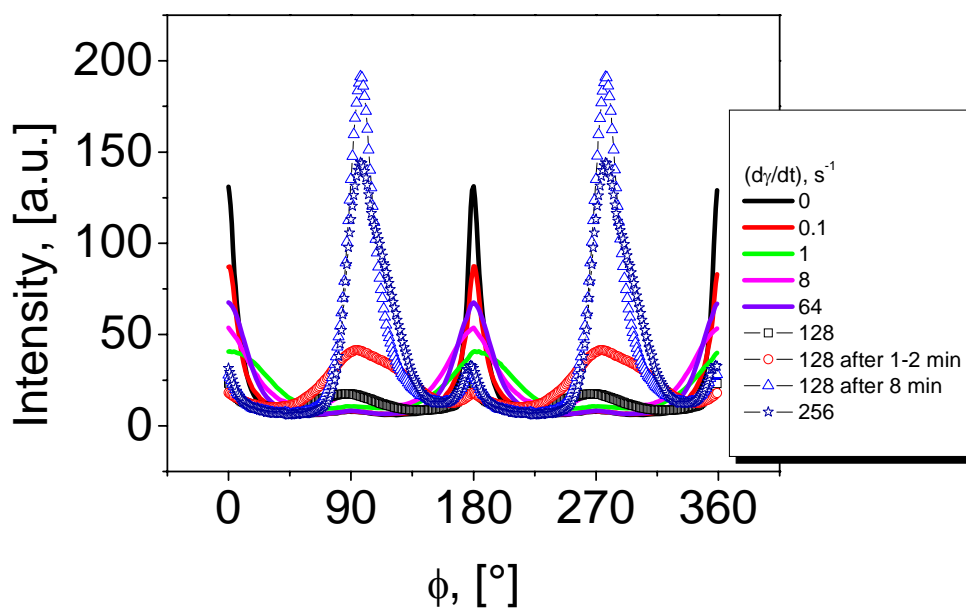


**Figure 6-14.** The evolution of scattering intensities with azimuthal angles illustrating the transition from parallel to perpendicular alignment in tangential view by increasing shear rate.

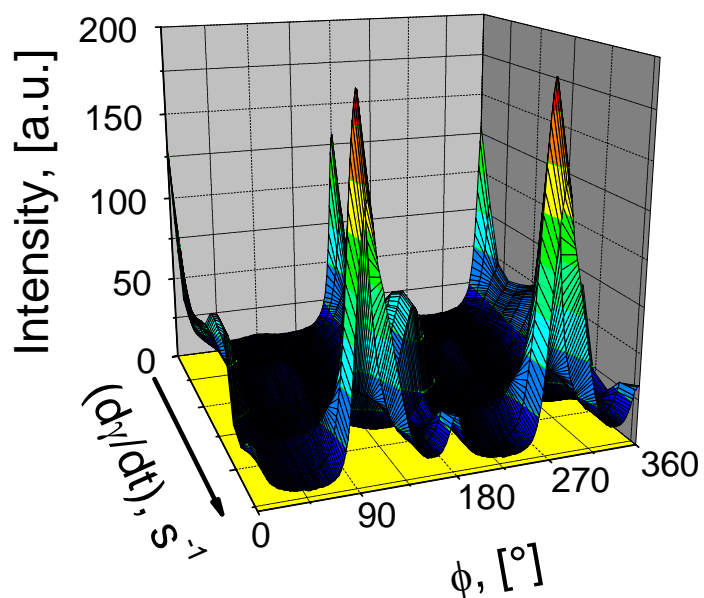


**Figure 6-15.** The three dimensional map in tangential view showing the growth of perpendicular alignment with increasing shear rate. The maximum in intensity corresponds to shear rate of  $(d\gamma/dt)=128s^{-1}$ .

A 3D-map in the tangential view of the evolution of scattering intensity with azimuthal angle and shear rate is given in Figure 6-15 where the occurrence of perpendicular alignment with increasing shear rate is quite obvious. Since the scattering profiles were monitored at certain shear rates and no data at intermediate shear rates were monitored, in Figure 6-15 it was not possible to assign a real scale for the shear rate.

However, at the critical shear rate, namely  $(d\gamma/dt)=128s^{-1}$ , the perpendicular alignment is quite well developed but tilted with  $+7^\circ$  from the usual  $90^\circ$  as an evidence of a remaining parallel alignment from the previous low shear rates. We may conclude that the perpendicular alignment is not perfected in the range of investigated shear rates.

In comparison with the tangential view the plot intensity versus scattering vector for the radial view shows as expected, only one peak for the range of shear rate  $0\div 64s^{-1}$  and at the critical shear rate of  $128s^{-1}$  three correlation peaks (ratio 1 : 1.5 : 2) are developed after 8 min, as seen in Figure 6-16. Simultaneously, after 8 min at this critical shear rate in the azimuthal dependence a scattering maximum at  $\phi=90^\circ$  and  $270^\circ$  accompanied by a weak peak at  $180^\circ$  as evidences the coexistence of mostly perpendicular and less parallel oriented lamellae (Figure 6-17).

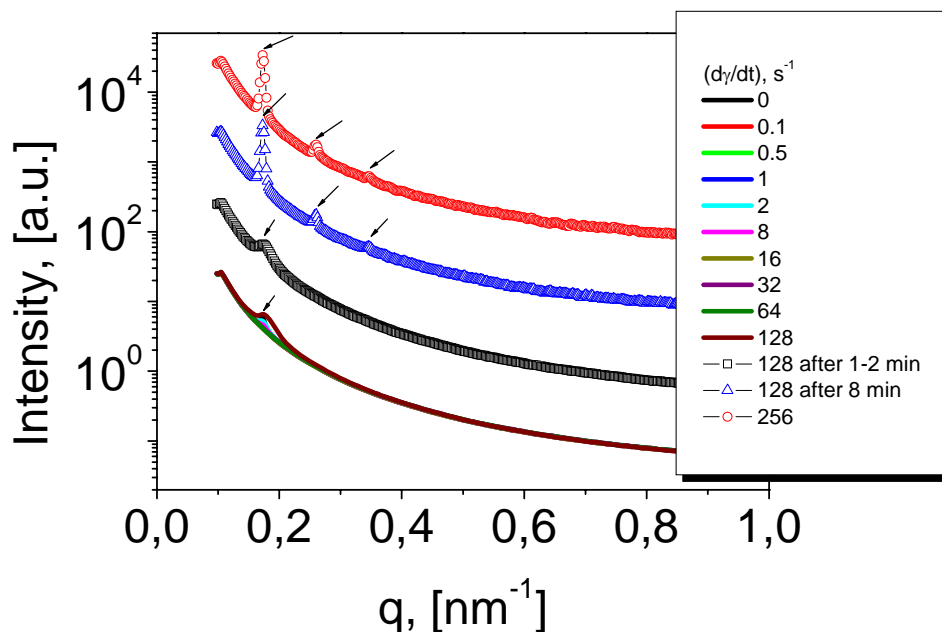


**Figure 6-16.** The induced isotropization in radial view at critical shear rate of  $128s^{-1}$ , at the transition from parallel toward perpendicular alignment. The overlapped lines correspond to the range of shear rate  $0\div 64s^{-1}$  illustrating only one peak which is in agreement with parallel

alignment from tangential view. The other curves ( $128\text{s}^{-1}$ ,  $256\text{s}^{-1}$ ) were shifted along vertically axis by a factor of 10. The arrows indicate the position of the correlation peaks.

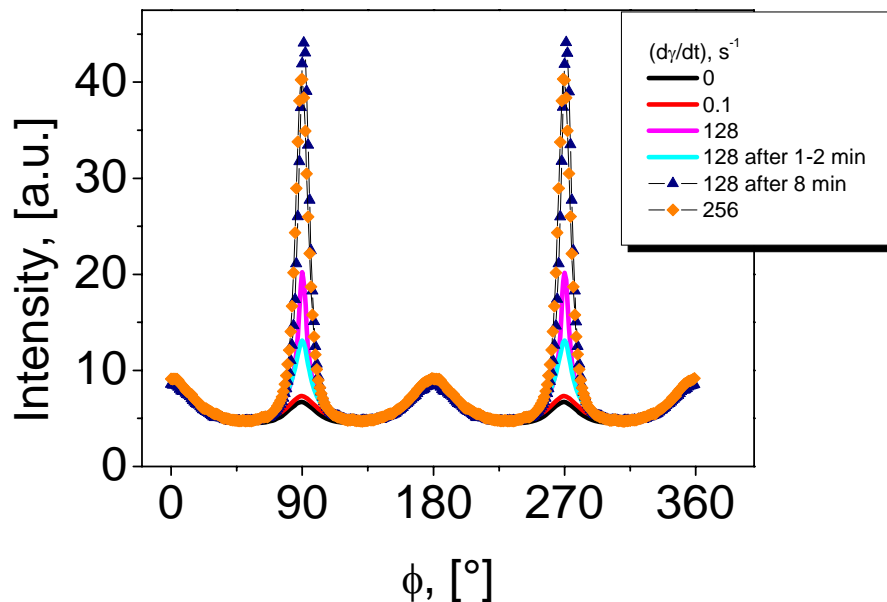


**Figure 6-17.** Azimuthal dependence in radial view illustrating a well developed perpendicular alignment and a weakly preserved parallel alignment.

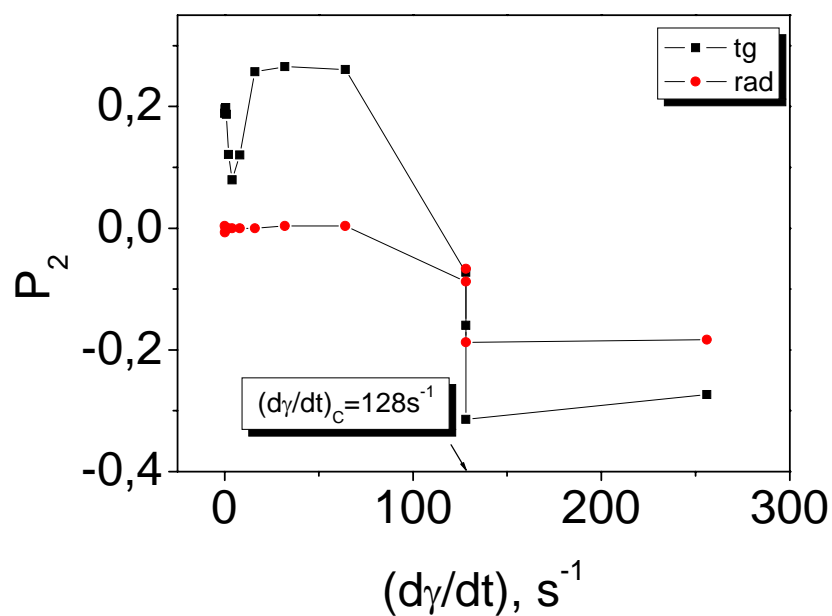


**Figure 6-18.** The dependence of order parameter,  $P_2$  with shear rate,  $d\gamma/dt$ , in tangential and radial views.

The alignment has been quantified for both configurations through the calculated order parameter as plotted in Figure 6-18.

In tangential view, in the range of shear rate  $(d\gamma/dt) = 0 \div 4 \text{ s}^{-1}$  the  $P_2$  decreases indicating the induced isotropization of the initially parallel arrangement (due to the surface effect) followed by a sharp increase in the range of shear rate  $(d\gamma/dt) = 4 \div 16 \text{ s}^{-1}$  as an evidence of parallel rearrangement of lamellae due to the shear effect. A plateau of order parameter values  $P_2 \sim 0.25 \div 0.26$  are shown for the range of shear rate  $(d\gamma/dt) = 16 \div 64 \text{ s}^{-1}$  illustrating the parallel alignment mostly due to the shear effect (less surface effect contribution) following a sudden change in the  $P_2$  toward negative values as evidence of change in alignment from parallel to perpendicular. A well developed perpendicular state is shown after 8 min at  $128 \text{ s}^{-1}$  characterized by an order parameter value,  $P_2 = -0.31$  and a slight decrease to  $P_2 = -0.27$  for  $256 \text{ s}^{-1}$  as a consequence of loss in alignment at high shear rates. Indeed, in radial view the  $P_2$  is in good agreement with the type of alignment for the parallel alignment in tangential view with approximately  $P_2 = 0$  in radial view (for a perfect achieved parallel in tangential view). The perpendicular alignment in tangential view is seen as well in radial view but less developed ( $P_2 = -0.18$ ) after 8 min at  $128 \text{ s}^{-1}$ . The advantage arising from the calculated  $P_2$  values is that they enable us to distinguish between parallel alignment induced due to the surface influence and the one induced due to the shear effect, which was not possible to differentiate from 2D-patterns.

The same but more diluted system (20 wt-%  $\text{S}_{33}\text{B}_{33}\text{T}_{34}^{160}$  in DOP) was investigated by rheo-optical method using oscillatory shear (Chapter 4). It showed parallel alignment by a declining birefringence toward zero. An often encountered problem by using the rheo-optical method was the impossibility to distinguish between the intermediate states (perpendicular with positive sign of birefringence or transverse with negative sign of birefringence) before approaching zero birefringence. One reason may be due to the coexistence of parallel and perpendicular at low strain amplitude ( $\gamma = 10\%$ ) with a higher contribution either from perpendicular or parallel states for which the birefringence showed negative sign. At higher strain amplitude ( $\gamma = 25\%$ ) the selectivity for one type of alignment is observed but still a tilted perpendicular would be responsible for different intermediate states as obtained from rheo-optical method. The coexistence of parallel and perpendicular aligned states with different contributions was proven as well in steady shear mode.

### 6.3 Conclusions

According to the alignment kinetics discussed above by using shear in oscillatory and steady mode, we may conclude that for 25 wt-% S<sub>33</sub>B<sub>33</sub>T<sub>34</sub><sup>160</sup> in DOP a perpendicular alignment was induced at short time scale (~1h). While a low strain amplitude such as  $\gamma=10\%$  has induced a coexistence of parallel and perpendicular alignment together with a tilted parallel alignment with scattering maxima at  $\phi=160^\circ$  and  $240^\circ$ , instead a higher strain amplitude such as  $\gamma=25\%$  has favored a selective alignment toward a perpendicular one. The parallel alignment induced at  $\gamma=10\%$  has been characterized through a calculated order parameter,  $P_2=0.32$ . The perpendicular alignment has been induced at higher strain amplitude,  $\gamma=25\%$  in oscillatory mode as well at a critical shear rate,  $d\gamma/dt=128s^{-1}$  in steady mode. A value of order parameter  $P_2=-0.37$  characterizes the perpendicular alignment achieved in oscillatory mode, and a value of  $P_2=-0.31$  was found for the steady mode. For a perfect perpendicular alignment the order parameter should be  $P_2=-0.5$  and thus the reached alignments are quite good.

## 7. In Situ Rheo-SAXS of a Block Copolymer Solution with Cylindrical Morphology in Couette geometry

### 7.1 Introduction

Lodge and co-workers have been conducted a broad study of the phase behavior of polystyrene-*b*-polyisoprene diblock copolymers in solvents of varying selectivity.<sup>212,213</sup> This work has suggested that block copolymer solutions may possess some advantages over melts in terms of studying order-order transition temperature. The use of solvents of different selectivity can provide access to several different order-order transition temperatures for a single polymer. Also, new phases can be accessed in solution such as face-centered-cubic (fcc) or hexagonally closed-packed array of spheres. For diblock copolymer melts some epitaxial relationships have been established as follows: i) cylinder  $\leftrightarrow$  bcc<sup>214,215</sup>; ii) lamellae  $\leftrightarrow$  cylinder<sup>216</sup>; iii) lamellae  $\leftrightarrow$  gyroid<sup>217,218</sup>; iv) cylinder  $\leftrightarrow$  gyroid.<sup>219</sup> Previous work<sup>211,220</sup> on polystyrene-*b*-polyisoprene (43K) diblock copolymer as a solution in selective solvent di-*n*-butyl phthalate has shown that a shear-oriented hexagonally packed cylinders transforms to cubic gyroid phase, as previously established in the melts. Using a combination of rheology and small-angle X-ray scattering a solution of 30 wt-% S<sub>34</sub>B<sub>19</sub>M<sub>47</sub><sup>65</sup> in DOP triblock terpolymer has been studied.

### 7.2 The monitored alignment of a block copolymer solution of 30 wt-% S<sub>34</sub>B<sub>19</sub>M<sub>47</sub><sup>65</sup> triblock terpolymer in DOP

#### 7.2.1 A preliminary SAXS investigation of block copolymer solution of 30 wt-% S<sub>34</sub>B<sub>19</sub>M<sub>47</sub><sup>65</sup> in DOP

The order-to-order and order-to-disorder transition temperatures for the system 30 wt-% S<sub>34</sub>B<sub>19</sub>M<sub>47</sub><sup>65</sup> in DOP have been studied by dynamic mechanical analysis in Chapter 5. A preliminary SAXS investigation for the cast film of S<sub>34</sub>B<sub>19</sub>M<sub>47</sub><sup>65</sup> from chloroform and its comparison with different solutions in DOP is presented in Figure 7-1. A *priori* TEM investigation (Chapter 5, Figure 5-1) has shown mostly a cylindrical morphology and some arrays assigned with a gyroid microstructure were presented as well. Thus, in Figure 7-1a the SAXS profile from a cast film from CHCl<sub>3</sub> showed a gyroid morphology (  $1 : (4/3)^{0.5} : (7/3)^{0.5} : (10/3)^{0.5}$  ) which was preserved as well for a concentration of 50 wt-% in DOP and at higher concentration of 70 wt-% the lamellar morphology was obtained. Varying the concentration

different morphologies were found (from gyroid toward lamellar) for the triblock terpolymer which may be related with a preferential swelling in DOP at room temperature. The 2D-SAXS pattern corresponding to the cast film is presented as well in Figure 7-1b and it may be interpreted as a coexistence of cylindrical and gyroid morphologies for this triblock terpolymer.

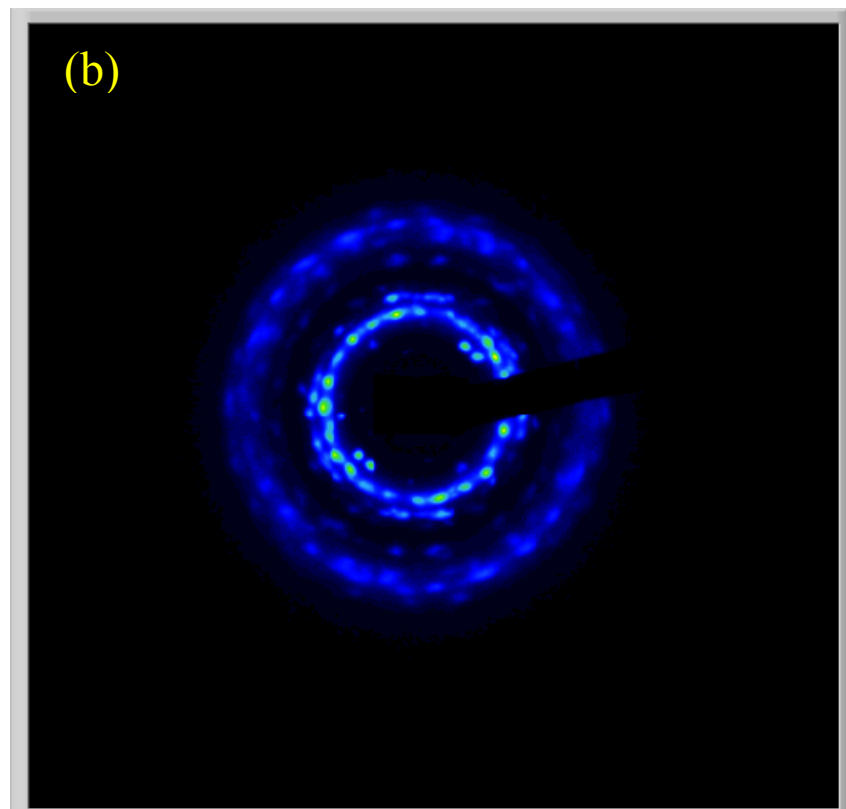
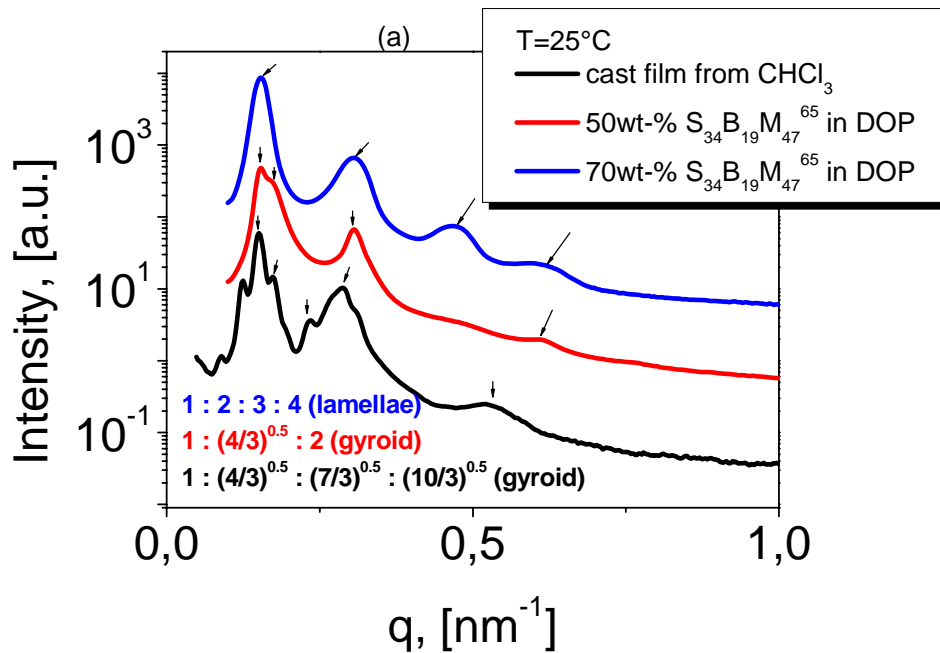


**Figure 7-1.** (a) SAXS profiles of  $S_{34}B_{19}M_{47}^{65}$  as cast film from  $CHCl_3$  and as solutions of 50wt-%, 70wt-% in DOP. The arrows indicate the position of correlation peaks. The curves corresponding to the solutions of 50wt-% and 70wt-%  $S_{34}B_{19}M_{47}^{65}$  in DOP were shifted vertically by a factor of 10. (b) SAXS-pattern for the cast film from  $CHCl_3$ .

The above mentioned SAXS experiments brought a clear indication about the selectivity of DOP as solvent for the  $S_{34}B_{19}M_{47}^{65}$  triblock terpolymer. While the TEM micrograph (Chapter 5) showed a coexistence of cylindrical and gyroid morphologies in the cast film, the SAXS profile from the cast film gave only evidence for the gyroid morphology. Taking into account the previous rheological investigation from Chapter 5 for 30wt%  $S_{34}B_{19}M_{47}^{65}$  in DOP, it can be concluded that a clear evidence for a morphological transition at  $T=114^\circ C$  is given and the SAXS experiments from the following sections will clarify and answer to the question: what type of morphology is involved within the morphological transition?

### 7.2.2 The alignment kinetics of block copolymer solution of 30 wt-% $S_{34}B_{19}M_{47}^{65}$ in oscillatory mode

The solution of 30wt-%  $S_{34}B_{19}M_{47}^{65}$  in DOP was filled into the Couette cell at high temperature  $T=110^\circ C$  annealed 40min at the same temperature to achieve a homogeneous state throughout the sample. Before applying shear, the scattering profiles were monitored at  $T=110^\circ C$  in the radial and tangential configurations as illustrated in Figure 7-2. This temperature of  $T=110^\circ C$  is considered as the onset temperature of the morphological transition observed at  $T=114^\circ C$  in the dynamic mechanical temperature sweep test (Chapter 5). Obviously at  $T=110^\circ C$  a cylindrical morphology is shown by SAXS profile in the tangential view with the cylinders lying along the Couette wall and perhaps a tilting of the cylinders gave in the radial view a body centered cubic morphology or it may be assumed the coexistence of cylindrical and spherical morphologies in equilibrium.

Under oscillatory shear at temperature  $T=110^\circ C$ , frequency  $\omega=10$  rad/s, strain amplitude  $\gamma=10\%$  the initially slight developed cylindrical morphology from the tangential view transformed into a well developed bcc microstructure.

While the monitored 2D-patterns did not show the transition from cylindrical to bcc microstructure in tangential view, the overlay of scattering profiles (intensity versus  $q$ ) showed this transition as depicted below in Figure 7-3.

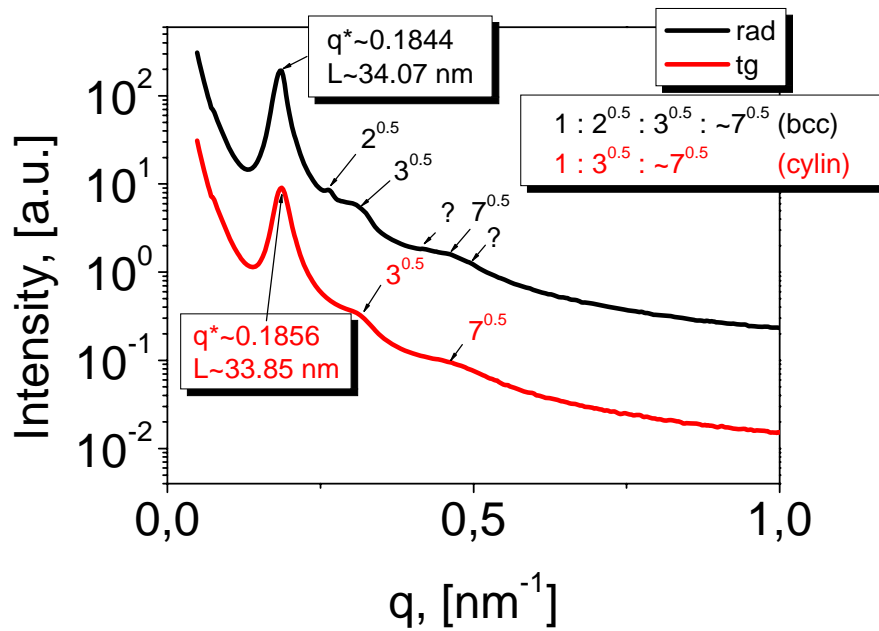


**Figure 7-2.** Scattering profiles at  $T=110^{\circ}\text{C}$  in tangential and radial configurations with the corresponding cylindrical and body centred cubic (bcc) morphologies. The long period is the same for the both views.

After shearing about  $t=174\text{s}$  at  $T=110^{\circ}\text{C}$ ,  $\omega=10\text{ rad/s}$ ,  $\gamma=10\%$  the same (weak) cylindrical morphology with the correlation peaks  $1 : 3^{0.5} : 7^{0.5}$  (missing the peak at  $4^{0.5}$ ) is shown. Further increase of shearing time, after  $t=670\text{s}$  lead to the appearance of a weak bcc morphology which develops with time. In tangential view the difference in the scattering profiles with shearing time is not due to the tilting and aligning of the cylindrical morphology in the flow direction, but it is due to the break up of cylinders into spheres. To prove this assumption further, in the scattering profiles from the radial view (Figure 7-4) between a weakly initial ( $t=0\text{s}$ , without shear) spherical and well developed spherical morphology with shear, the isotropic intermediate states are present at  $t=389\text{s}$  and  $t=516\text{s}$  which would not occur due to the alignment in the flow direction only.

It might be concluded for the oscillatory shear process that a morphological transition takes place at  $T=110^{\circ}\text{C}$ ,  $\omega=10\text{ rad/s}$ ,  $\gamma=10\%$  from coexisting spherical and weakly cylindrical morphologies toward a well developed spherical one.

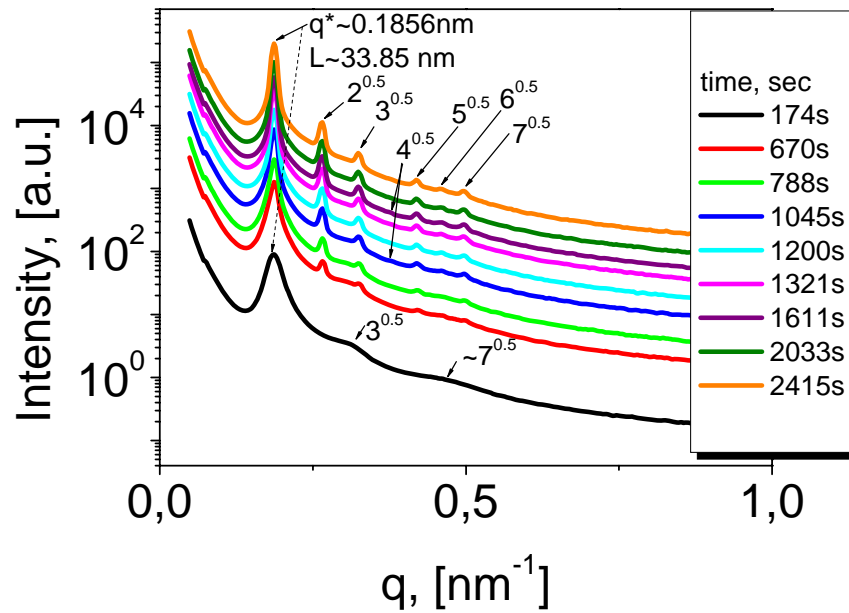


**Figure 7-3.** The shear-induced morphological transition in tangential view from an initially cylindrical microstructure toward a well developed body centered cubic morphology. Oscillatory shear has been applied at  $T=110^{\circ}\text{C}$ ,  $\omega=10$  rad/s,  $\gamma=10\%$ .

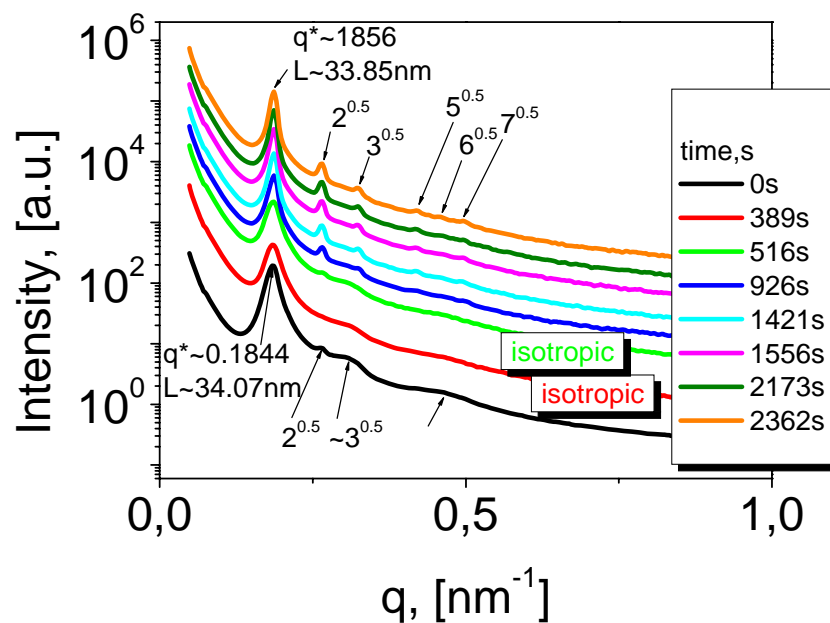


**Figure 7-4.** The shear-induced morphological transition in the radial view from an initially weak bcc morphology through an intermediate isotropic state before yielding the new bcc morphology. Oscillatory shear has been applied at  $T=110^{\circ}\text{C}$ ,  $\omega=10$  rad/s,  $\gamma=10\%$ .

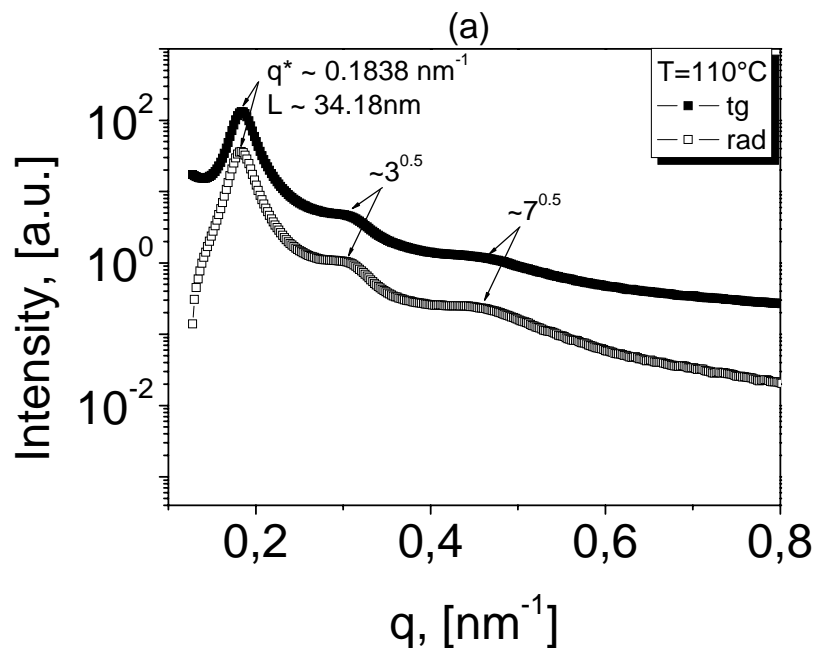
## 7.2.3 The alignment kinetics of the block copolymer solution 30 wt-%

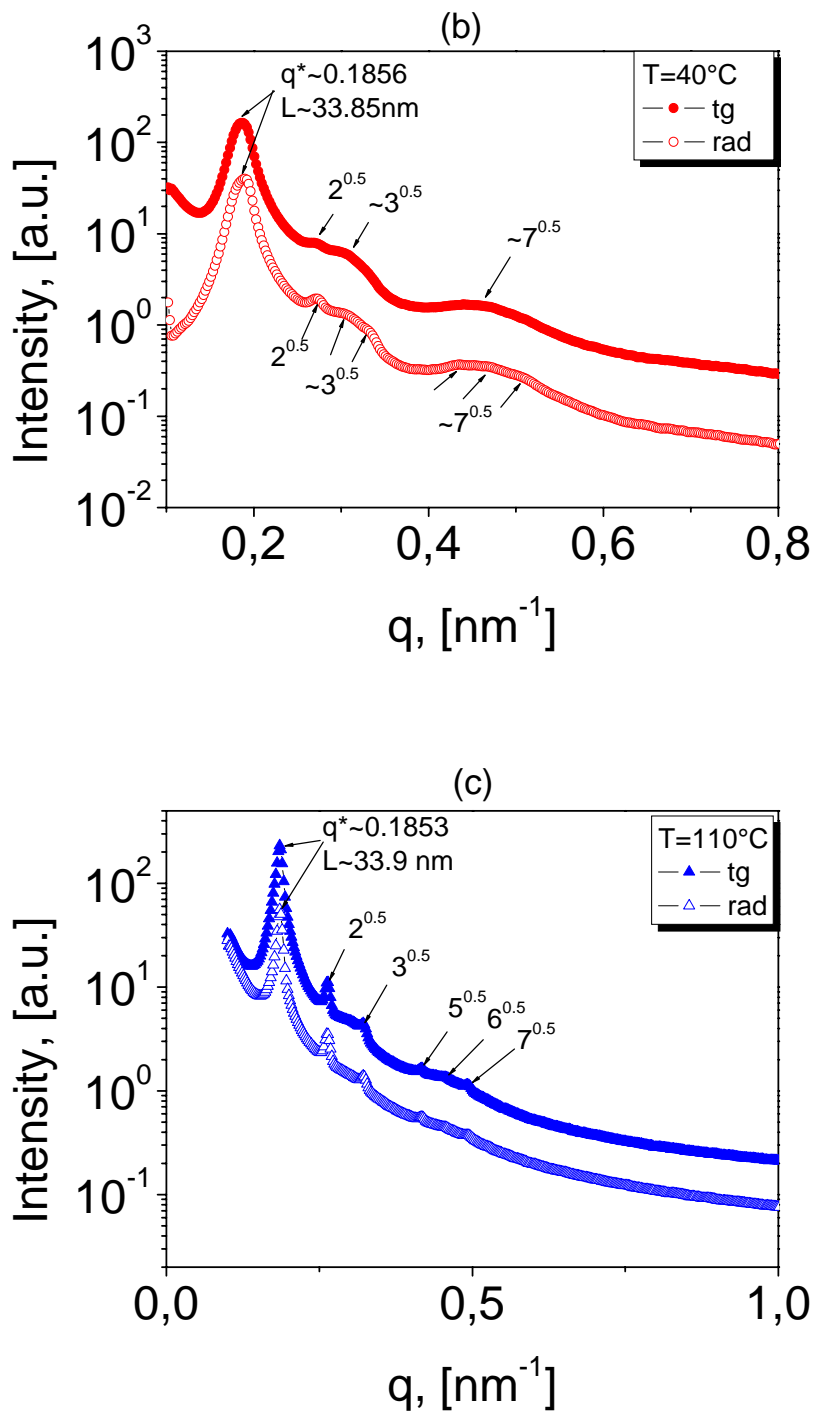
 $S_{34}B_{19}M_{47}^{65}$  in steady mode

A thermal treatment applied to the solution 30wt-%  $S_{34}B_{19}M_{47}^{65}$  in DOP has evidenced the following morphologies: i) after loading the sample into Couette geometry heated at 110°C and after 5 min equilibration at 110°C the scattering profiles in both views showed a cylindrical morphology (Figure 7-5a); ii) by loading of the sample at 110°C, equilibration for 8 min at 110°C, then cooling to 40°C and annealing for 5 min, the SAXS profiles at  $T=40^\circ\text{C}$  indicated a weak spherical morphology (Figure 7-5b); iii) loading at 40°C and subsequent heating to  $T=110^\circ\text{C}$ , equilibration for 30 min, the SAXS profiles indicate a well developed spherical morphology (Figure 7-5c). Depending on the annealing process the cylindrical or spherical morphologies are developed or a coexistence of both morphologies may be possible.

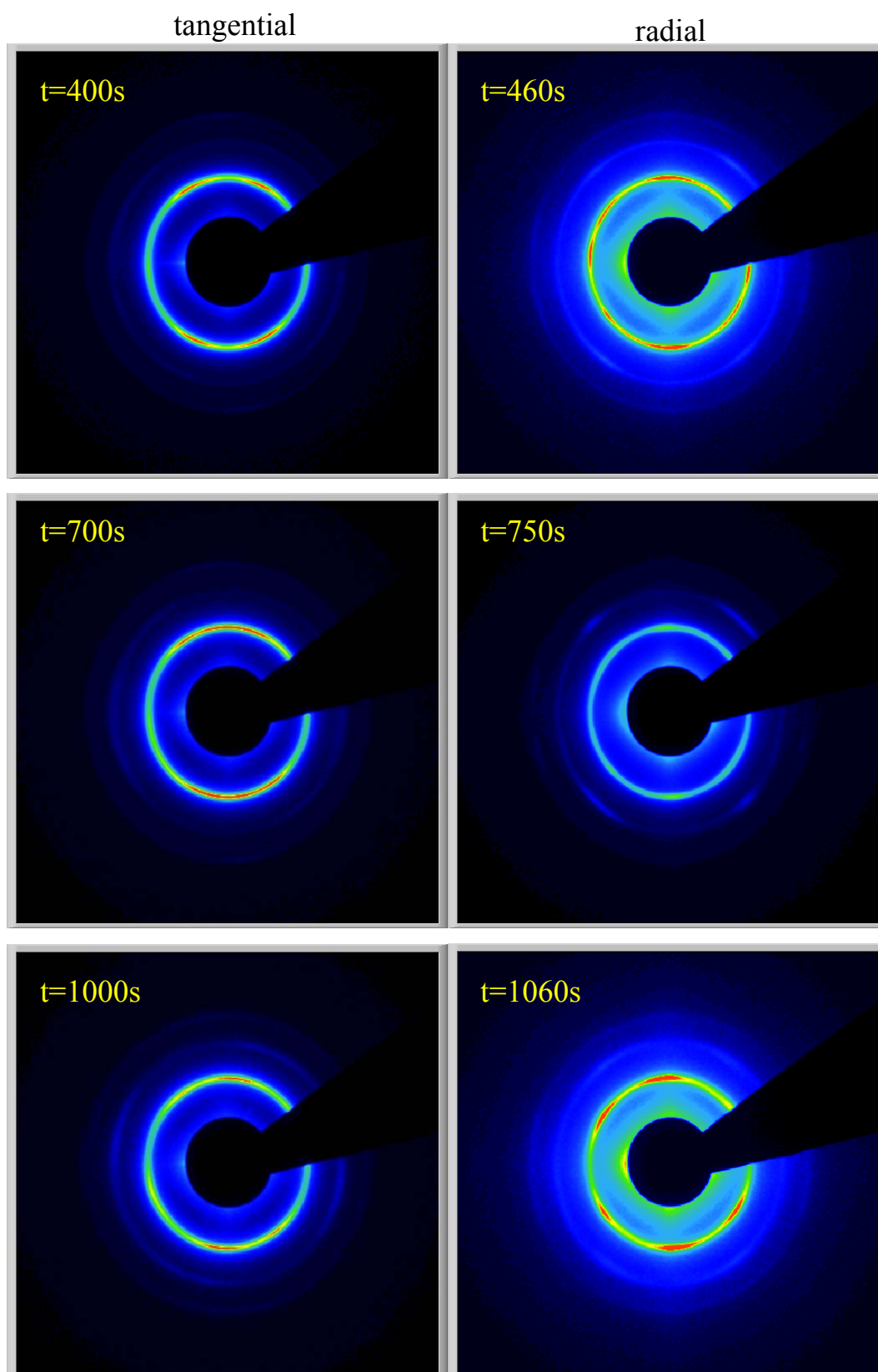
**Steady shear at  $(d\gamma/dt)=0.1\text{s}^{-1}$  and  $T=110^\circ\text{C}$** 

Before applying steady shear the initial morphology in both views was a well developed spherical (bcc) morphology as shown in Figure 7-5c. The alignment has been performed at low shear rate  $(d\gamma/dt)=0.1\text{s}^{-1}$ ,  $T=110^\circ\text{C}$  and the 2D-patterns were monitored in tangential and radial views. An insight into the morphological changes with time by monitoring the 2D-patterns is given in Figure 7-6.



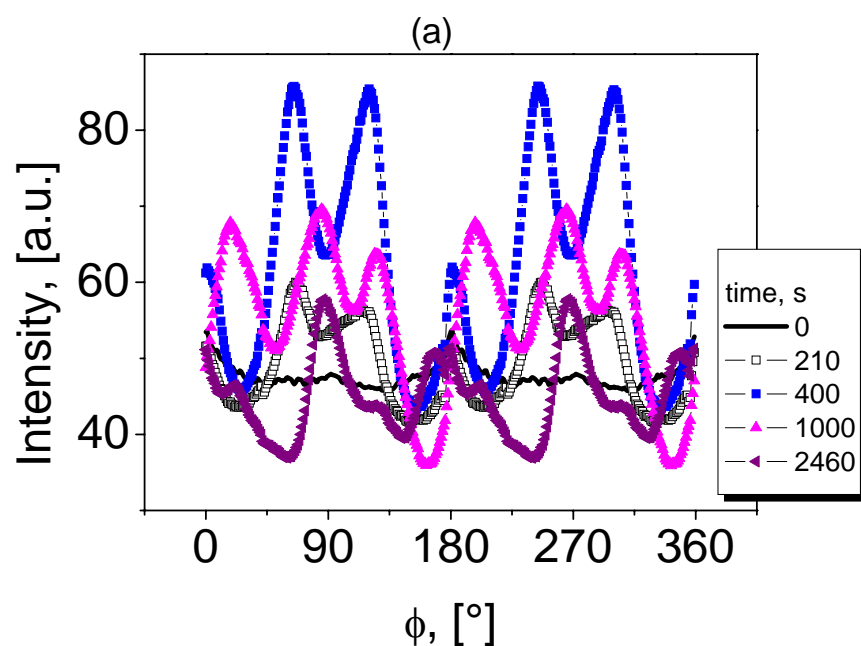


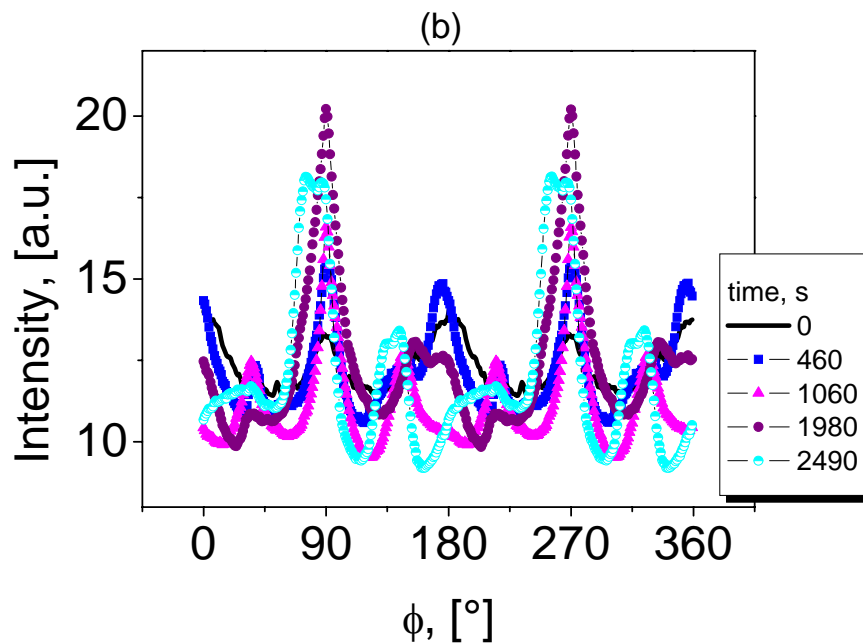
**Figure 7-5.** The influence of annealing process over the morphology: (a)  $T=110^\circ\text{C}$ , cylindrical morphology ; (b)  $T=40^\circ\text{C}$ , spherical morphology less developed; (c)  $T=110^\circ\text{C}$ , spherical morphology well developed.



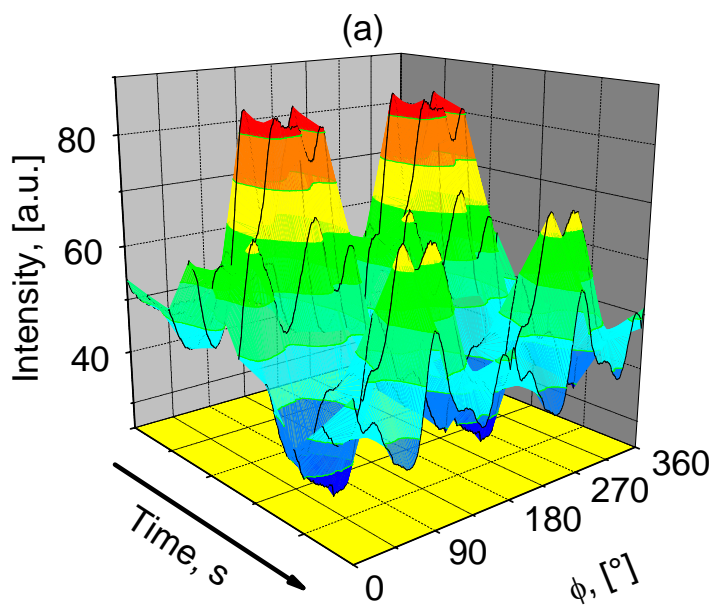
**Figure 7-6.** The 2D patterns monitored during steady shear at  $(d\gamma/dt)=0.1\text{ s}^{-1}$  and  $T=110^\circ\text{C}$  in tangential and radial views.

In terms of angular dependencies a detailed evolution of the process with the transition from a cubic toward hexagonal phase through an isotropic state is given in Figure 7-7. After shearing at  $(d\gamma/dt)=0.1s^{-1}$  at the first stages of shearing process (Figure 7-7 tangential (a) and radial (b) views), the angular dependencies are not significant for the both views. Continuous shearing at  $0.1s^{-1}$  will induce simultaneously changes in both views, like a well developed cubic arrangement in lamellae matrix after  $t=400s$  in tangential view (maxima scattering angles at  $65^\circ$ ,  $120^\circ$ ,  $245^\circ$ ,  $300^\circ$  and weak peak at  $182^\circ$ ) and corresponding in radial view, after  $t=460s$  a growth of a mixed cubic phase with the intense maxima scattering at  $0^\circ$ ,  $90^\circ$ ,  $180^\circ$ ,  $270^\circ$  and weak scattering at  $38^\circ$ ,  $150^\circ$ ,  $218^\circ$ ,  $330^\circ$  is shown as given in Figure 7-7b. Furthermore, in tangential view the well developed cubic phase changes into a well developed hexagonal phase after  $t=1000s$  (tangential view) and correspondingly after  $t=1060s$  in radial view. At the end of shear process a new cubic phase is shown in tangential view at  $t=2460s$  and in radial view at  $t=2490s$ , respectively, but it is less developed than previous ones. The detailed 3D representations for the both views are illustrated in Figure 7-8.





**Figure 7-7.** The angular dependencies with time in tangential (a) and radial (b) views at  $(d\gamma/dt)=0.1\text{s}^{-1}$  and  $T=110^\circ\text{C}$ .



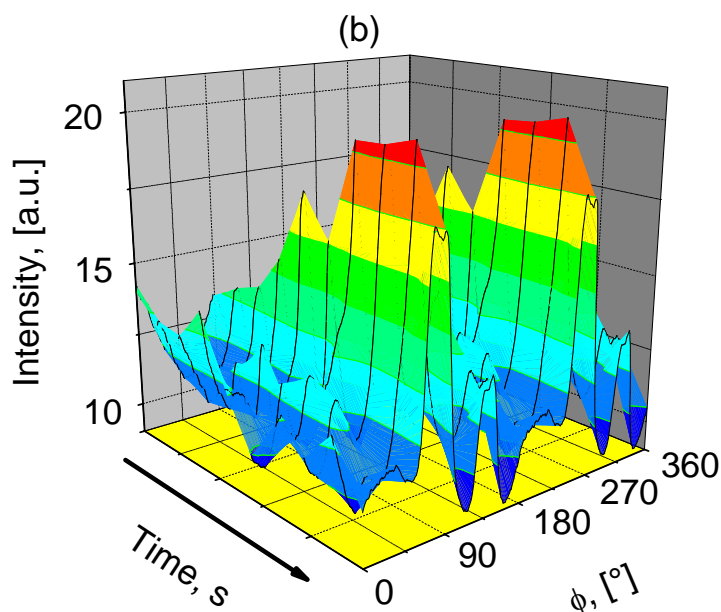


**Figure 7-8.** The three dimensional map in tangential view (a) and radial view (b) at  $(d\gamma/dt)=0.1s^{-1}$  and  $T=110^{\circ}C$  illustrating the evolution of the peaks as a function of azimuthal angle and time.

As already discussed for the plot of intensity versus azimuthal angle (Figure 7-7), as well in the three dimensional maps (Figure 7-8) it is quite obvious that in tangential view a maximum intensity of a cubic ordered structure is encountered at lower time scale  $t=400s$  followed by a gradually decreasing intensity as a consequence of appearance of a hexagonally new structure (Figure 7-7a), while in the radial view a maximum intensity of a cubic ordered structure is encountered at  $t=1980s$  (Figure 7-7b) followed by a gradually decreasing intensity toward stabilizing the cubic structure at the end of shearing process. Therefore, an interchangeability between cubic and hexagonal arrangements were achieved by shearing in steady mode at low shear rate ( $0.1s^{-1}$ ). Indeed, at the end of shearing process the cubic structure is present as well evidenced in both views.

**Step shear at  $T=115^{\circ}\text{C}$** 

A challenge of the shearing process in steady mode has been achieved by performing the tests at several shear rates ( $d\gamma/dt=1\text{s}^{-1}$ ,  $10\text{s}^{-1}$ ,  $50\text{s}^{-1}$ , incremental and decremental) and at  $T=115^{\circ}\text{C}$  where a certain spherical morphology is obviously accomplished. A similar bcc morphology as shown in Figure 7-5c is existent before applying shear. A rich behavior has been encountered in the radial view comparative with tangential view, behavior which has been improved with increasing shear rate. Thus, such pattern with the azimuthal dependence is presented in Figure 7-9.

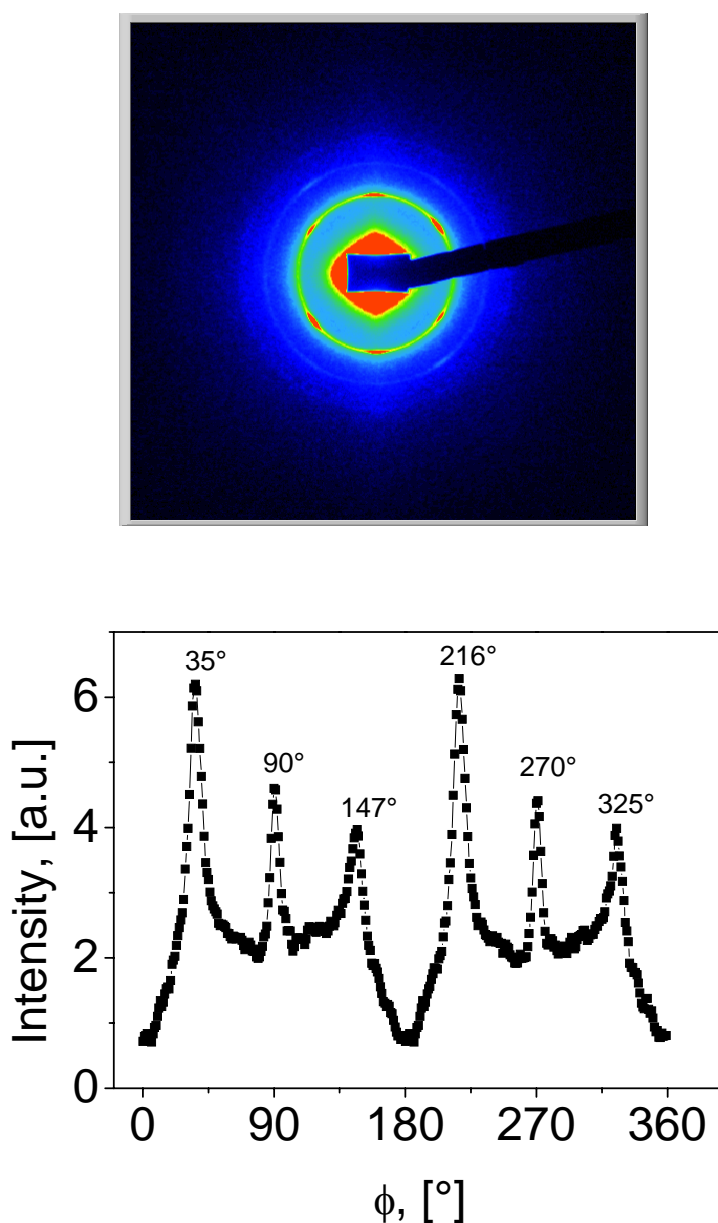


**Figure 7-9.** The shear-induced hexagonal arrangement with the azimuthal dependence monitored in the radial view at shear rate  $(d\gamma/dt)=50\text{s}^{-1}$ , after  $t=450\text{s}$  in the incremental step through the intermediate  $1\text{s}^{-1}$ , and  $10\text{s}^{-1}$ .

An overview on the steady shear experiments at different shear rates is summarized in the overlay plot intensity versus  $q$  given in Figure 7-10 for the tangential view. In the radial view the same scattering profiles at all shear rates with correlation peaks corresponding to the bcc morphology were monitored. In the tangential view only a poorly organized morphology has been shown with several isotropizations between shear rates and slightly developed bcc morphology in the incremental step, at shear rate  $1\text{s}^{-1}$  and time  $t=240\text{s}$ , followed by isotropization at  $10\text{s}^{-1}$ , and  $50\text{s}^{-1}$ . For continuous shear at  $50\text{s}^{-1}$  after  $t=510\text{s}$  a hexagonal array of bcc morphology is encountered similarly to the one shown in Figure 7-9. It follows isotropization in the decremental step at  $10\text{s}^{-1}$  and  $t=750\text{s}$  followed by a new formed bcc morphology after  $t=870\text{s}$  and shear rate  $10\text{s}^{-1}$  which persists after cessation shear.

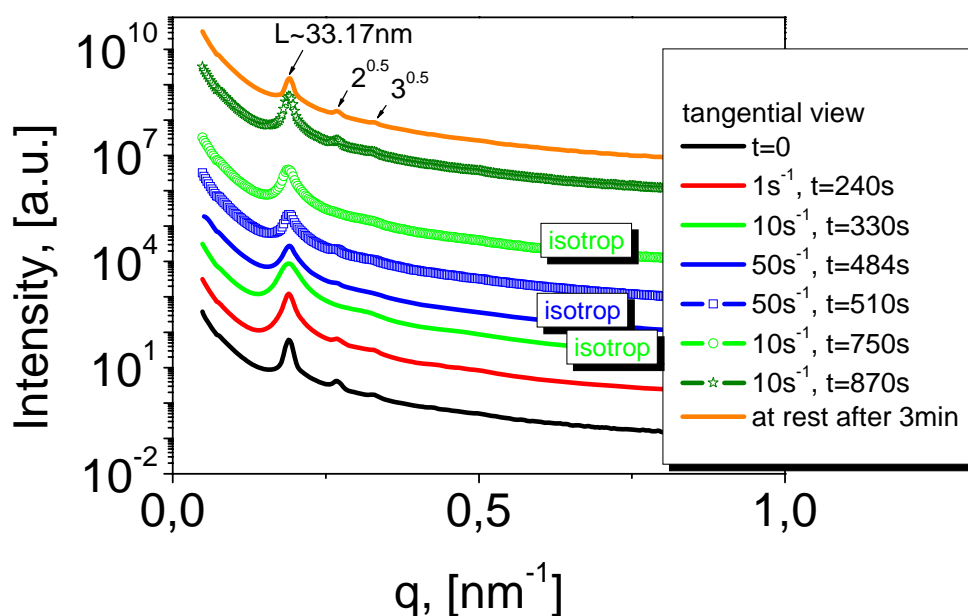


**Figure 7-10.** The scattering profiles monitored during steady shear at different shear rates incremental (from  $1\text{s}^{-1}$  to  $50\text{s}^{-1}$ ) and decremental (from  $50\text{s}^{-1}$  to  $1\text{s}^{-1}$ ). A vertically shifting up by a factor of 10 has been applied to avoid overlapping.

It might be concluded that a shear rate of  $50\text{s}^{-1}$  has induced a hexagonal array in the bcc morphology as clearly evidenced in radial and tangential views.

Previously an attempt of orienting such a solution as 30wt-%  $\text{S}_{34}\text{B}_{19}\text{M}_{47}$ <sup>65</sup> in DOP in oscillatory shear combined with a monitored optical retardation (following the calculated birefringence) has been made in Chapter 5. A wide range of low temperatures were employed in the alignment process in order to achieve an increase of microphase separation and to give

a significant form birefringence. A coexistence of cylindrical and spherical morphologies at  $T=110^{\circ}\text{C}$  at an applied shear in oscillatory mode and in situ monitoring of SAXS profiles proved a morphological transition toward a well developed bcc morphology. Thus, it may be assumed that at very low temperatures (below  $25^{\circ}\text{C}$ ) a coexistence of cylindrical and spherical morphologies could be possible since DOP is a  $\Theta$  solvent for PS block ( $T_{\Theta} \sim 7^{\circ}\text{C}$ ). Therefore, under oscillatory shear and at low temperature the cylindrical morphology transformed toward a spherical one (already proved by in situ rheo-SAXS at  $T=110^{\circ}\text{C}$ ) for which the form birefringence is very low in comparison with the lamellar one. This might be the reason for the very low values of birefringence (positive and negative depending on alignment temperature) monitored and presented in Chapter 5. While the birefringence method combined with LAOS was not an enough powerful tool to detect the morphological changes induced by shear, in situ rheo-SAXS at high temperatures detected the transition from mixed cylindrical and spherical morphologies toward a well developed spherical morphology.

### 7.3. Conclusions

By applying oscillatory shear to the solution of 30wt-%  $S_{34}B_{19}M_{47}^{65}$  in DOP under the following conditions: temperature  $T=110^{\circ}\text{C}$ , frequency  $\omega=10$  rad/s, strain amplitude  $\gamma=10\%$  it has been proved the shear-induced morphological transition from an initially coexisting cylindrical and spherical toward a well developed spherical morphology (bcc). While in oscillatory shear the 2D patterns have not been sensitive in illustrating the morphological changes, this was accomplished for the steady mode at the same temperature  $T=110^{\circ}\text{C}$  and low shear rate,  $(d\gamma/dt)=0.1\text{s}^{-1}$  where an interchange between cubic and hexagonal phase was shown (Figure 7-6). It should be remembered for the case of oscillatory shear at  $T=110^{\circ}\text{C}$  that according to the annealing process the initial morphology is a mixture of cylindrical and spherical phase while for the steady mode the initial morphology is an absolutely spherical one which allowed an alignment between a cubic and hexagonal array. A step shear mode at a temperature of  $T=115^{\circ}\text{C}$  and range of shear rates  $(d\gamma/dt)=1\div 50\text{s}^{-1}$  from an initial bcc morphology has been induced a well developed hexagonal array at  $50\text{s}^{-1}$  evidenced by the 2D-patterns and the azimuthal dependence.

## 8. In situ rheo-SAXS for a solution of polystyrene-b-poly(ethylene-co-butylene)-b-poly(methyl methacrylate) $S_{34}EB_{19}M_{47}^{65}$ in DOP in Couette geometry

### 8.1. Introduction

A previous investigation<sup>39</sup> on the “knitting pattern” formed by polystyrene-b-poly(ethylene-co-butylene)-b-poly(methyl methacrylate) SEBM triblock terpolymers proved a highly nonconstant mean curvature of the intermaterial dividing surface and a rather complicated SAXS pattern. The knitting pattern morphology was obtained only when chloroform was used as a casting solvent, while toluene as a casting solvent lead to a lamellar morphology. In this section a solution of a knitting pattern forming SEBM triblock terpolymer has been subjected to shear in order to align either this morphology or to monitor morphological changes.

### 8.2. The monitored alignment of a block copolymer solution of 30 wt-% $S_{34}EB_{19}M_{47}^{65}$ triblock terpolymer in DOP

#### 8.2.1. A preliminary rheological investigation of block copolymer solution of 30 wt-% $S_{34}EB_{19}M_{47}^{65}$

The “knitting pattern”  $S_{34}EB_{19}M_{47}^{65}$  has been obtained by hydrogenation of triblock terpolymer  $S_{34}B_{19}M_{47}^{65}$  (the cylindrical and gyroid morphologies seem to coexist for this polymer) and the detailed description of the procedure has been presented in Chapter 2. As expected an additional morphological change could appear due to the asymmetric composition which is depicted in Figure 8-1. At lower angular frequency,  $\omega=1$  rad/s an obvious minimum in the storage modulus at  $T\sim 36^{\circ}\text{C}$  is shown followed by an increase and stabilization of a new structure indicated by a plateau of the modulus prior to the order-disorder transition. Furthermore, higher frequencies  $\omega=10$  rad/s, and 100 rad/s have induced a shift in this minimum of storage modulus toward higher temperatures like  $T\sim 46^{\circ}\text{C}$  (at 10 rad/s) and  $T\sim 41^{\circ}\text{C}$  (at 100 rad/s) as well as a less pronounced decrease in modulus has been accomplished. According to the SCFT calculations for the intermediate segregation<sup>28</sup> in the phase diagram for symmetric diblock copolymers the sequence lamellar-gyroid-hexagonal-spheres-disordered is predicted for a certain range of compositions and/or temperatures. Other

more complex morphologies like perforated layer (PL) phase and ordered bicontinuous double diamond structure (OBDD) was found to be totally unstable. With regard to the knitting pattern there is not information about the stability limit as well as an evidence within a phase diagram, thus we cannot conclude by dynamic mechanical analysis about the kind of new morphology achieved through the morphological transition illustrated in Figure 8-1.

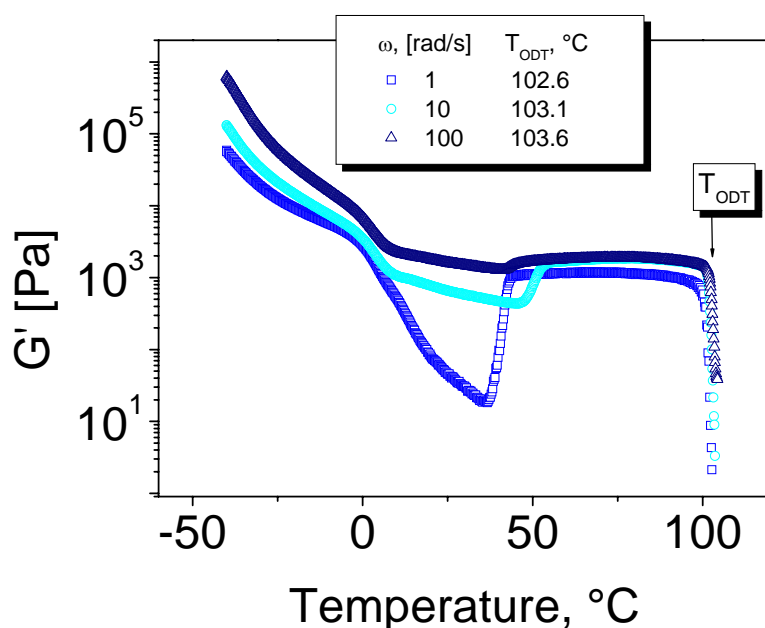


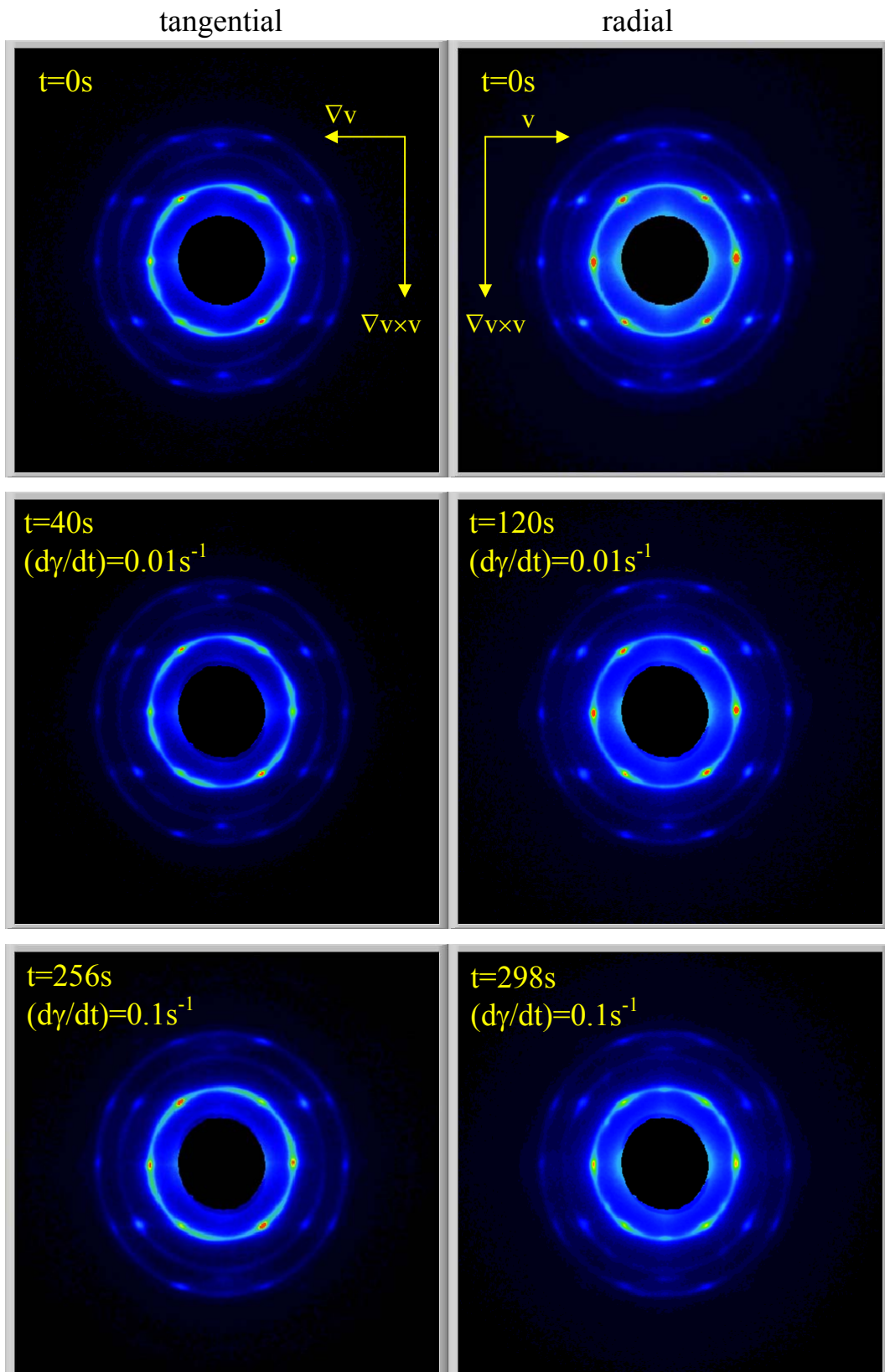
**Figure 8-1.** The moduli dependence within temperature by heating ( $1^\circ\text{C}/\text{min}$ ) and range of frequency ( $1\div 100\text{rad/s}$ ). The corresponding order-disorder transition temperatures were obtained: ( $\square$ )  $\omega=1\text{ rad/s}$  and  $T_{ODT}=102.6^\circ\text{C}$ ; ( $\circ$ )  $\omega=10\text{ rad/s}$  and  $T_{ODT}=103.1^\circ\text{C}$ ; ( $\triangle$ )  $\omega=100\text{ rad/s}$  and  $T_{ODT}=103.6^\circ\text{C}$ . The applied strain was  $\leq 1\%$  at overall frequencies.

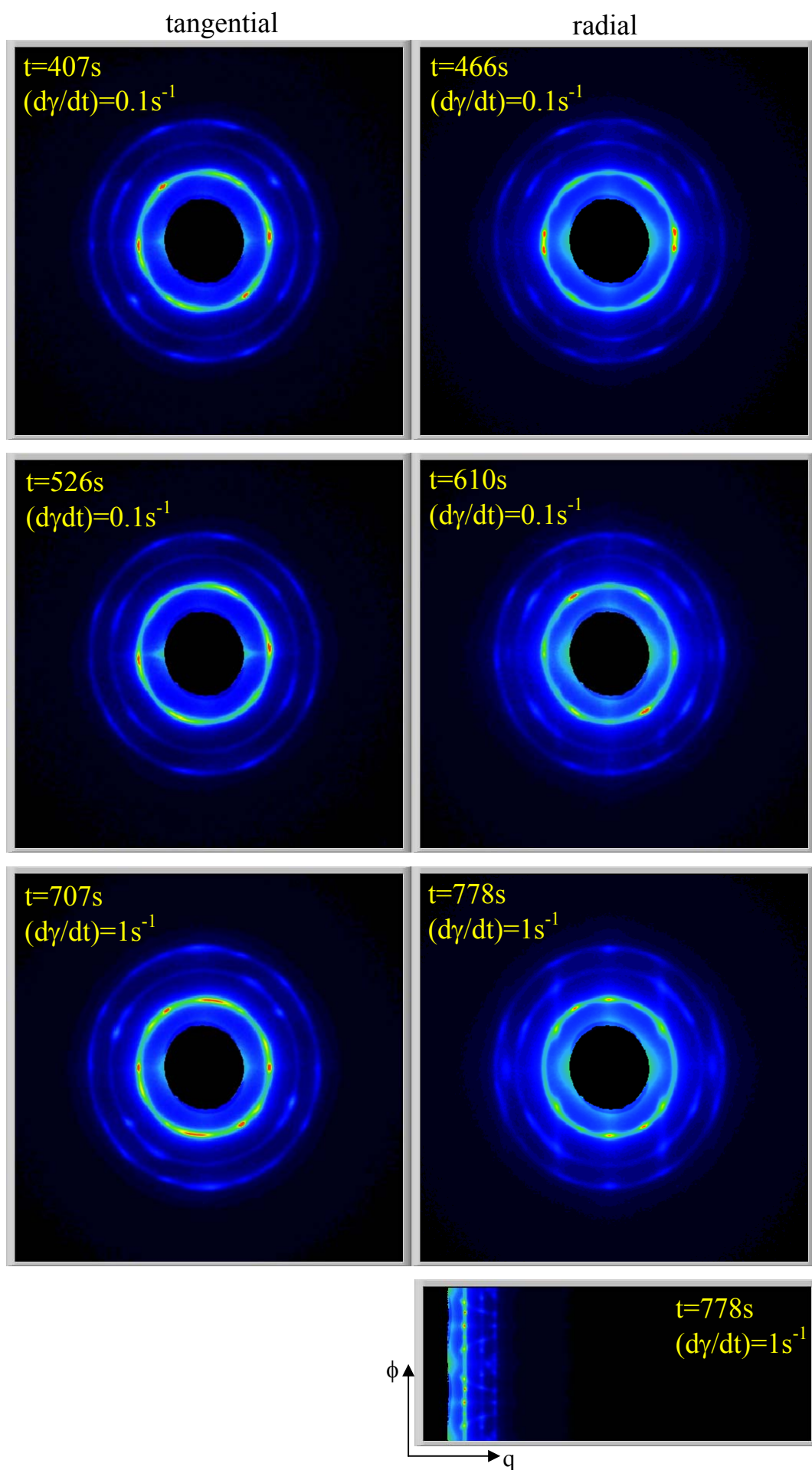
According to the previous work<sup>39</sup> the knitting pattern has been situated at the borderline between lamellar and lamellae-cylinder morphologies which might point to a transition between a lamellar-like and another morphology.

### 8.2.2. The alignment kinetics of the block copolymer solution of 30 wt-% $S_{34}EB_{19}M_{47}^{65}$ in steady mode

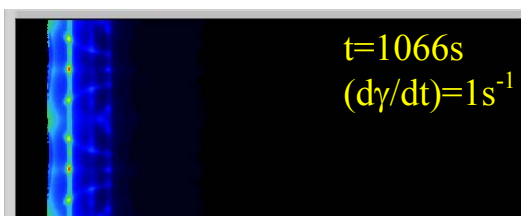
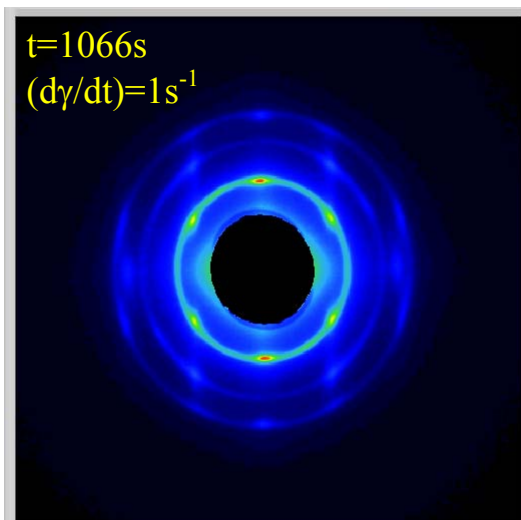
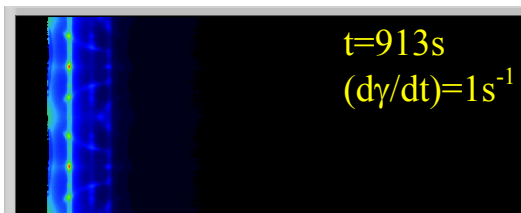
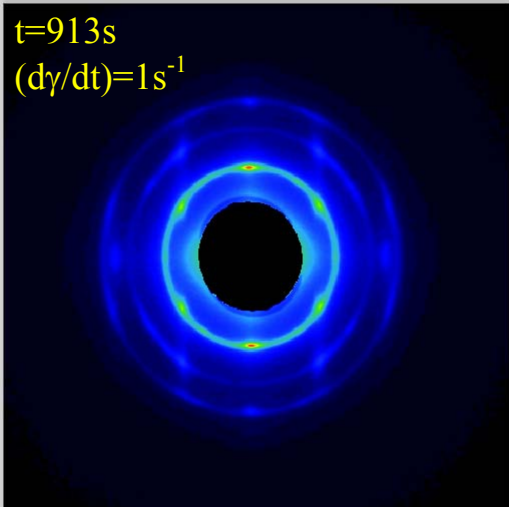
As discussed previously for the other investigated systems by in situ rheo-SAXS, the same setup has been used like Haake rheometer within an aluminium Couette cell built up in the synchrotron beam line. The loading of sample was performed at a temperature of  $T=80^\circ\text{C}$ . The SAXS profiles before shearing at  $T=80^\circ\text{C}$  revealed a spherical morphology (bcc) and this

will be presented together with the scattering profiles monitored during shearing process for comparison. A step shear experiment has been applied to the initial bcc morphology at temperature  $T=80^{\circ}\text{C}$  and the monitored 2D-patterns from tangential and radial views are presented in Figure 8-2.

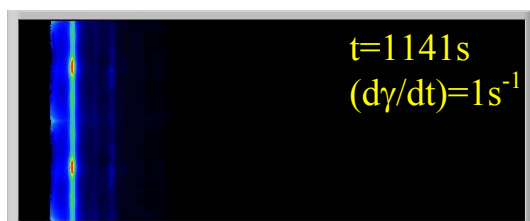
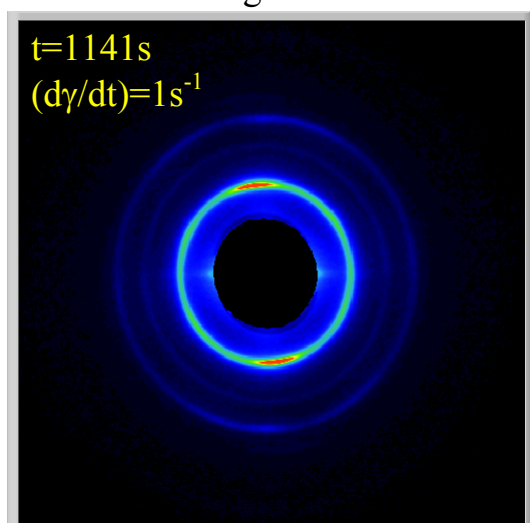




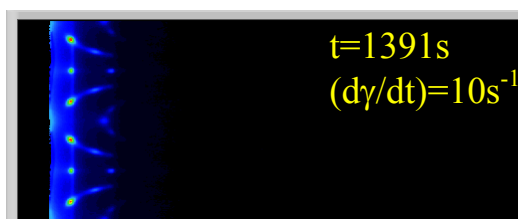
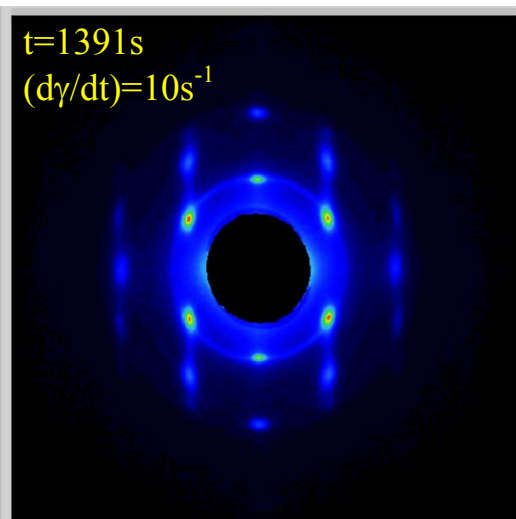
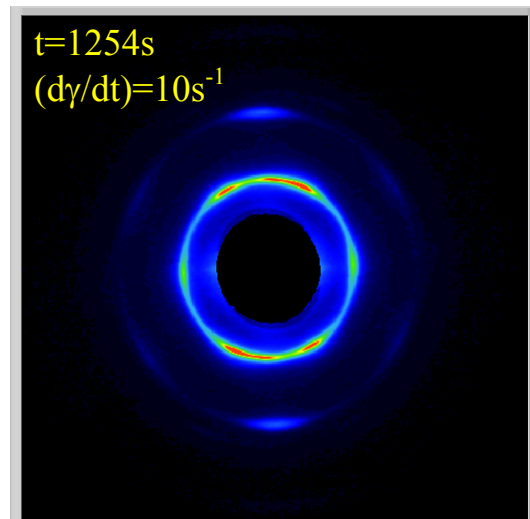
radial



tangential



radial



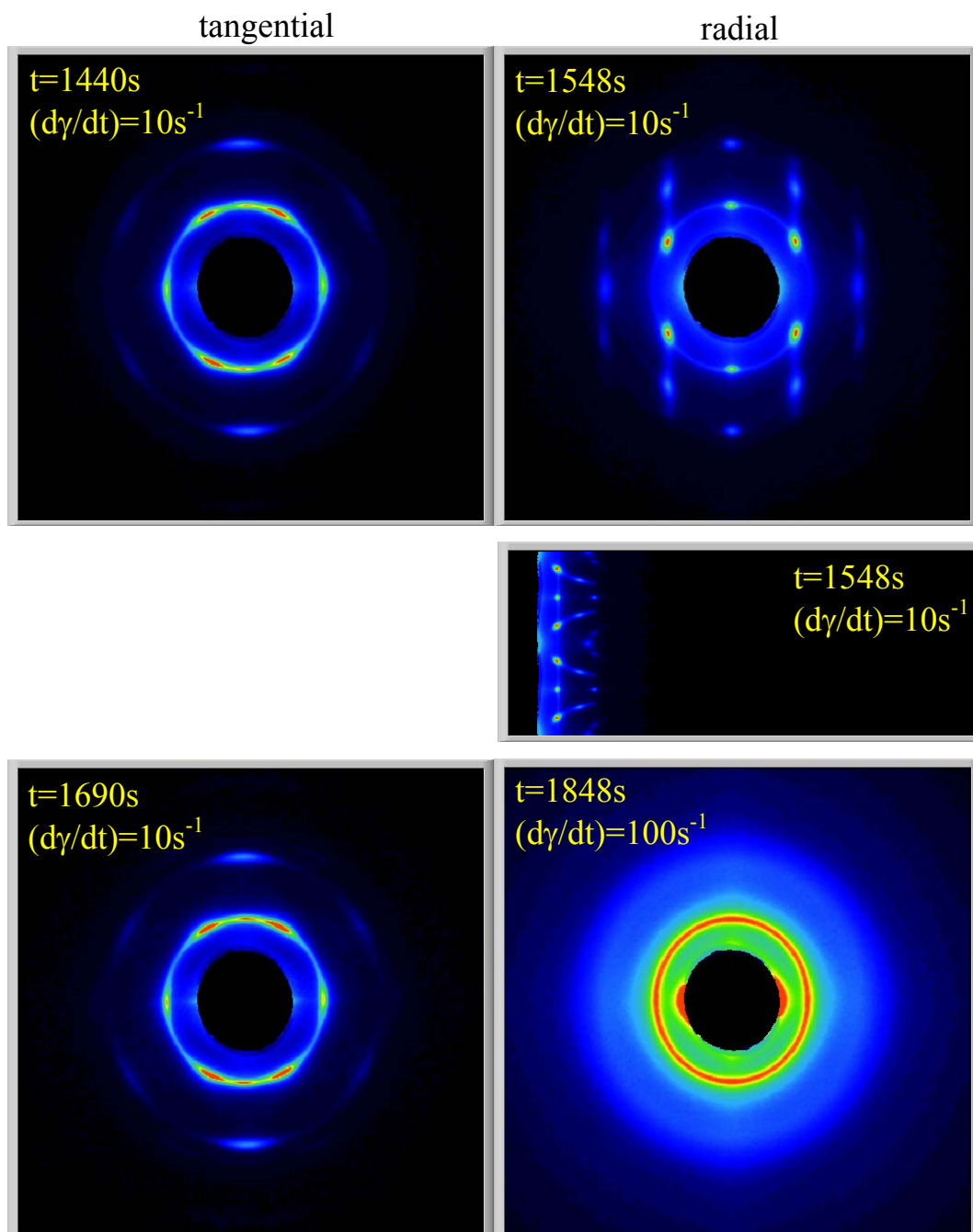
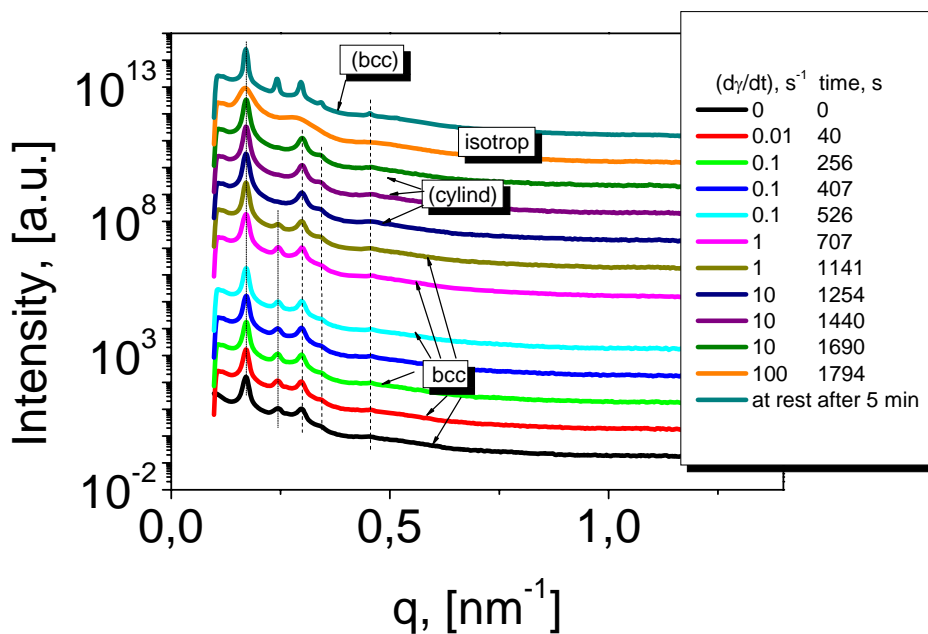


**Figure 8-2.** The 2D-patterns monitored at different shear rates and times in tangential and radial views. At some of the shear rates the patterns were monitored just in radial or tangential view where the meaningful changes took place.

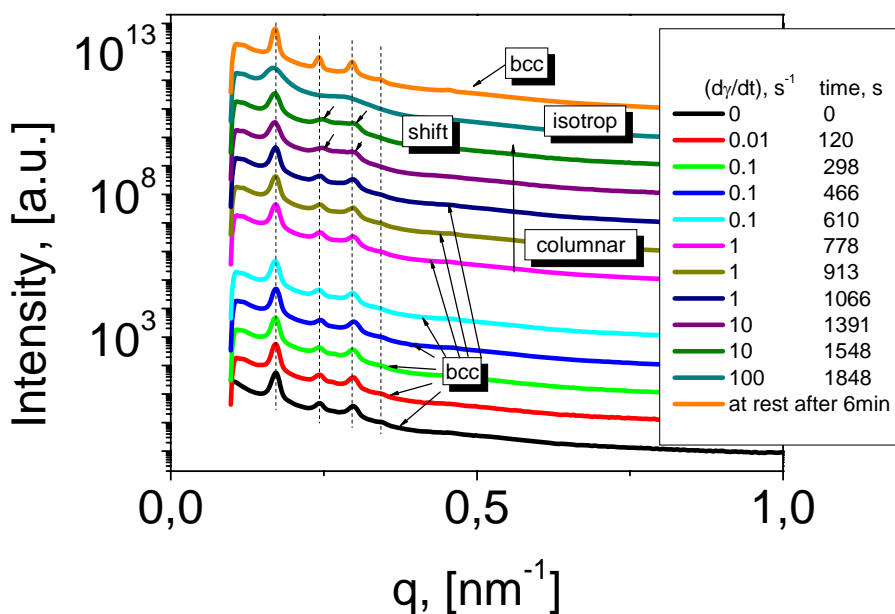
Before shearing a well developed spherical morphology (bcc) with an azimuthal dependence is existing as well evidenced by 2D-patterns from both views at time  $t=0s$  (Figure 8-2,  $t=0s$ ). Moreover, the bcc morphology illustrated in 2D-patterns and also through the radially averaged scattering profiles with the correlation peaks  $1:\sqrt{2}:\sqrt{3}:\sqrt{4}:\sqrt{7}$  at  $t=0s$  in both views (Figures 8-3 and 8-4) confirmed the assumption made previously regarding the

morphological transition taking place in the temperature sweep test (Figure 8-1). Since, for the monitored patterns has been used a temperature of  $T=80^{\circ}\text{C}$  which is above the order-order transition temperature of  $T\sim 40^{\circ}\text{C}$ , it may be concluded that a transition toward a spherical bcc morphology has been involved.

In the both views before applying shear at  $t=0\text{s}$  the bcc morphology involves different angular dependencies as follows:  $0^{\circ}$ ,  $17^{\circ}$ ,  $55^{\circ}$ ,  $72^{\circ}$ ,  $124^{\circ}$ ,  $142^{\circ}$ ,  $180^{\circ}$  in the tangential view and  $0^{\circ}$ ,  $55^{\circ}$ ,  $90^{\circ}$ ,  $125^{\circ}$ ,  $180^{\circ}$  in the radial view, which will imply different behavior regarding the alignment monitored in both views. By shearing at low shear rate  $(d\gamma/dt)=0.01\text{s}^{-1}$  in the tangential view after  $t=40\text{s}$  and in radial view after  $t=120\text{s}$  the 2D-patterns (Figure 8-2) together with scattering profiles (Figures 8-3, and 8-4) and angular dependencies (Figures 8-5, and 8-6) are unchanged in comparison with the initial state without shear ( $t=0\text{s}$ ). Increasing shear rate to  $(d\gamma/dt)=0.1\text{s}^{-1}$  lead to attenuation and appearance of new peaks due to the reorganization of the morphology as follows: in tangential view after  $t=526\text{s}$  the previous peaks from  $17^{\circ}$ ,  $72^{\circ}$  and  $142^{\circ}$  are less intense and shifted to  $14^{\circ}$ ,  $70^{\circ}$  and  $140^{\circ}$  while in radial view some peaks are growing at  $35^{\circ}$  and  $145^{\circ}$  and the one from  $90^{\circ}$  is more developed. A summarizing of the azimuthal dependence described above can be depicted in Figures 8-3 and 8-4 for the tangential and radial views. A bridge between the first order reflexion (110) and the second one (200) has been seen in the radial view at  $(d\gamma/dt)=1\text{s}^{-1}$ , at shearing time  $t=778\text{s}$  (Figure 8-2) and as well in the broadness of the peaks in the scattering profiles (tangential view, Figure 8-4). Besides the usual 2D-patterns  $(\nabla v \times v, \nabla v)$  or  $(\nabla v \times v, v)$ , the patterns as angular dependence  $\phi$  versus scattering vector  $q$  show also this bridge.



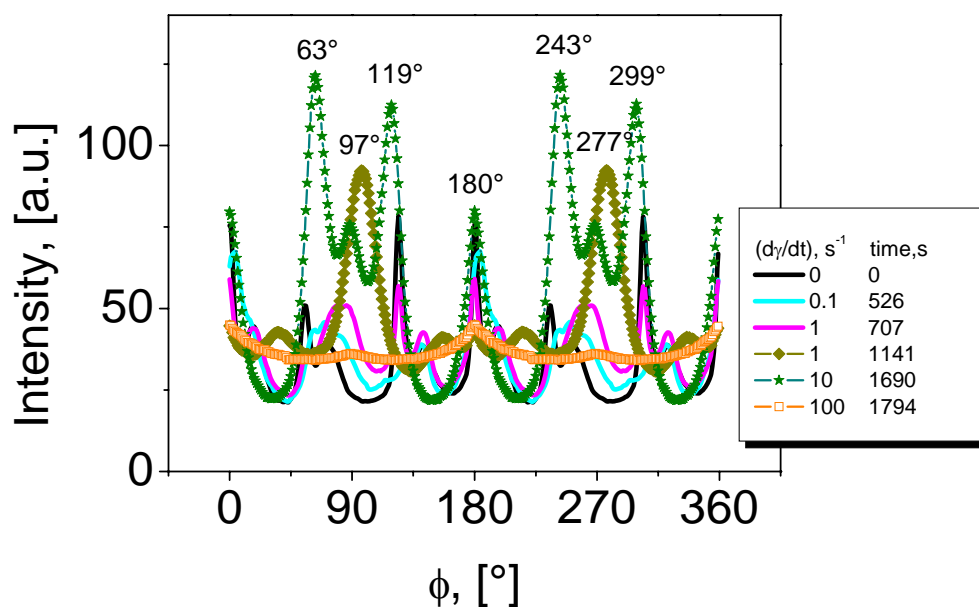
**Figure 8-3.** Scattering profiles in the tangential view at  $T=80^{\circ}\text{C}$  during increasing shear rate. At a critical shear rate of  $(d\gamma/dt)=10\text{s}^{-1}$  the transition from bcc to cylindrical morphology takes place.



**Figure 8-4.** Scattering profiles in the radial view at  $T=80^{\circ}\text{C}$  during increasing shear rate. The “columnar” structure achieved for a shear rate  $(d\gamma/dt)=10\text{s}^{-1}$  and corresponding time  $t=1391\text{s}$  and  $t=1548\text{s}^{-1}$  is evidenced through a broadness and slight shift (the set of four arrows) of the

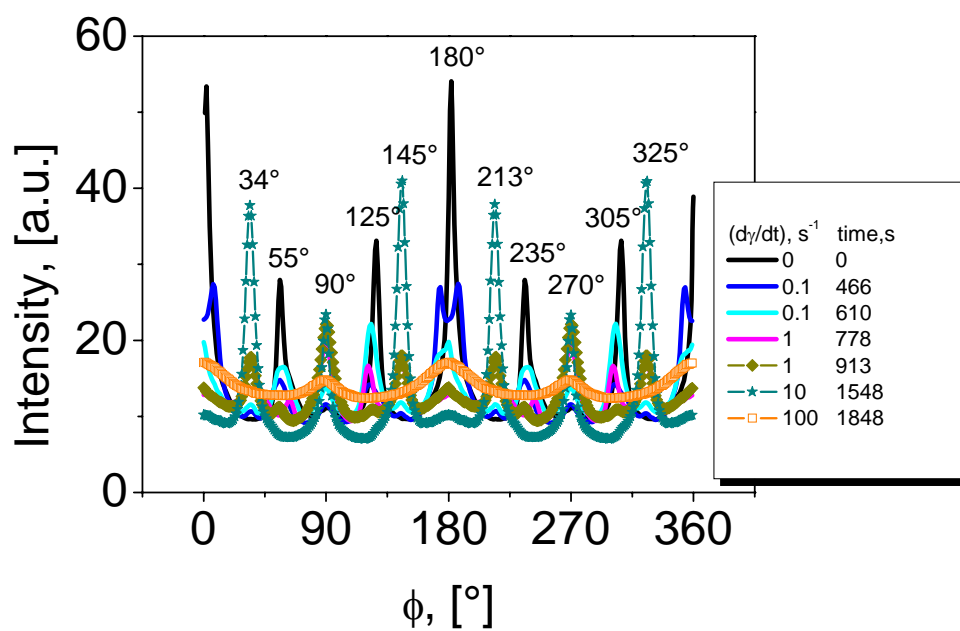
peaks toward higher  $q$  range. A vertical shifting by a factor of 10 has been applied to all curves.

While the hexagonal structure (so-called “columnar”) is seen in the radial view (2D-patterns), simultaneously in the tangential view after shearing time of  $t=1141$ s a scattering maxima appears at the azimuthal angles of  $97^\circ$  and  $277^\circ$  with additional peaks (Figure 8-5) as an indication of the columnar structure as already evidenced in the radial view. This angular dependence is similar to the one specific to a lamellar system and a order parameter of  $P_2 = -0.1$  has been calculated. It may be explained as a bridge appearing in the tangential view between the reflection planes along the flow direction which gave the maximum scattering at  $97^\circ$  and  $277^\circ$  and the slight reflections at the azimuthal angles of  $35^\circ$  and  $156^\circ$  according with the pathway of developing of the columnar structure. A well developed columnar structure appears in the radial view by increasing shear rate at  $(d\gamma/dt)=10\text{s}^{-1}$  after shearing time of  $t=1391$ s (Figure 8-2) and a clear map of the three connected planes (110, 200, 211) through the bridge inside the sample is illustrated via azimuthal angle versus scattering vector (2D-patterns). The columnar structure is characterized by sharpness of the peaks at  $34^\circ$ ,  $90^\circ$ , and  $145^\circ$  (Figure 8-6) which are maintained for longer shearing time such as after time  $t=1548$ s and shear rate of  $(d\gamma/dt)=10\text{s}^{-1}$  (Figure 8-2). In the meantime in the tangential view the previous maximum from  $97^\circ$  and  $277^\circ$  has been shifted at the following maxima  $64^\circ$ ,  $88^\circ$ ,  $119^\circ$  and  $180^\circ$  (Figure 8-5, at  $10\text{s}^{-1}$  and  $t=1690$ s) giving in the tangential view a hexagonal arrangement characterized by an order parameter of  $P_2 = -0.147$ . The interconnected planes giving rise to the columnar structure from the radial view are considered in the tangential view as lamellae initially showing the maxima at  $97^\circ$  and  $277^\circ$  while with increasing time the well developed columnar will lead to the transition of the maxima at  $97^\circ$  and  $277^\circ$  toward the multiple maxima distributed as hexagonally pattern (Figure 8-2, tangential view, at  $10\text{s}^{-1}$  and  $t=1690$ s). An isotropic pattern as a ring has been encountered at higher shear rate  $(d\gamma/dt)=100\text{s}^{-1}$  while after cessation of shear at rest the bcc morphology was reformed in both views as illustrated through the scattering profiles in Figures 8-3 and 8-4 after 5 min and 6 min, respectively. It should be mentioned that the bcc morphology formed at rest showed a final behavior with sharper correlation peaks than initially before shear.

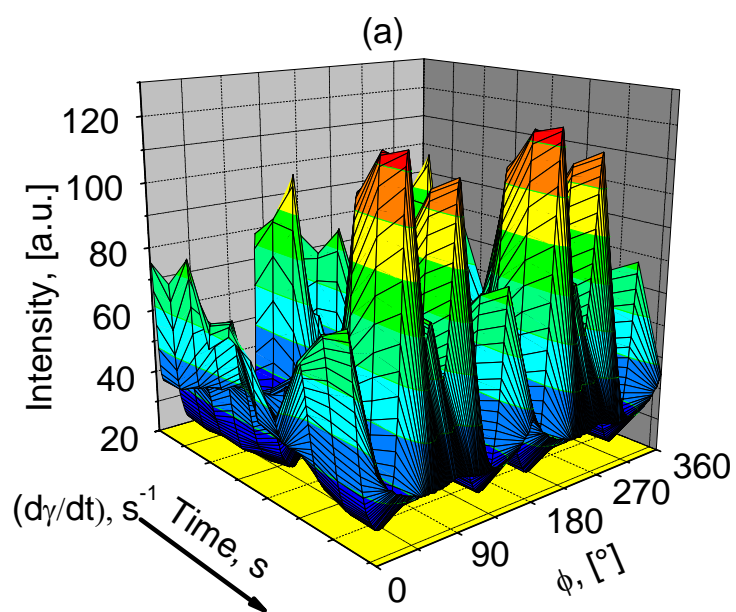


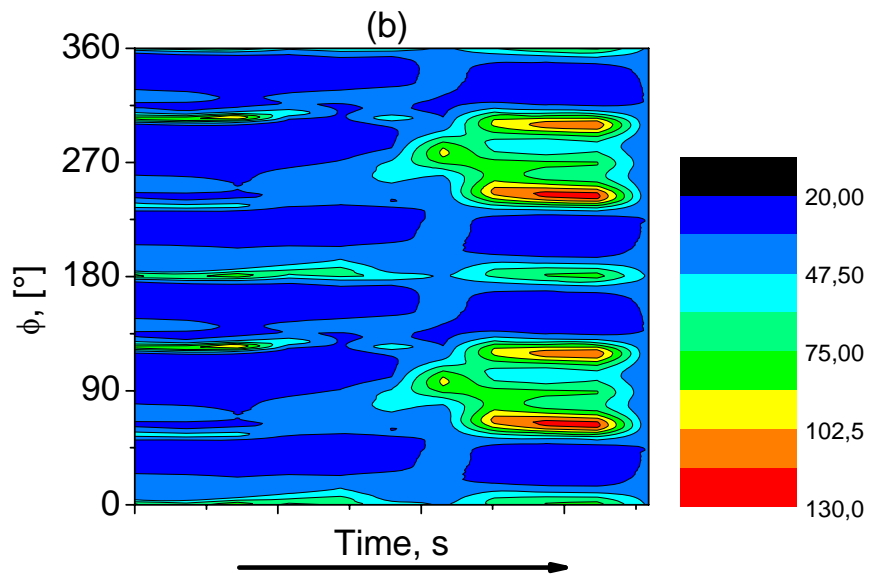
**Figure 8-5.** The angular dependence in tangential view at  $T=80^{\circ}\text{C}$  and different shear rates  $(d\gamma/dt), s^{-1}$  as follows: ( $\blackrightarrow$ )  $0s^{-1}$ , ( $\blackleftarrow$ )  $0.1s^{-1}$ ; ( $\blackrightarrow$ )  $1s^{-1}$ ; ( $\blackleftarrow$ )  $1s^{-1}$ ; ( $\blackrightarrow$ )  $10s^{-1}$ ; ( $\blackleftarrow$ )  $100s^{-1}$ .

The angular dependencies of the peaks with time in the tangential and radial views are illustrated in Figures 8-7 and 8-8. As seen in Figure 8-7a and b at larger time the peaks reached a maximum intensity around  $t\sim 1500s$  while in the radial view the peaks are less intense, both views illustrate the same supramolecular columns. In Figure 8-8a at the beginning of shear process the initial bcc morphology gave a maximum in peak intensity which decrease as a consequence of induced isotropization during shearing and furthermore at the end of shearing an average intensity has been found corresponding to the supramolecular columns. Thus, the supramolecular columns arising from the bcc morphology are well developed. Similarly, a qualitative representation of the evolution of supramolecular columns could be observed from the corresponding 3D-maps of the azimuthal dependence with time through the islands of maximum intensity for the tangential and radial views (Figures 8-7b and 8-8b).

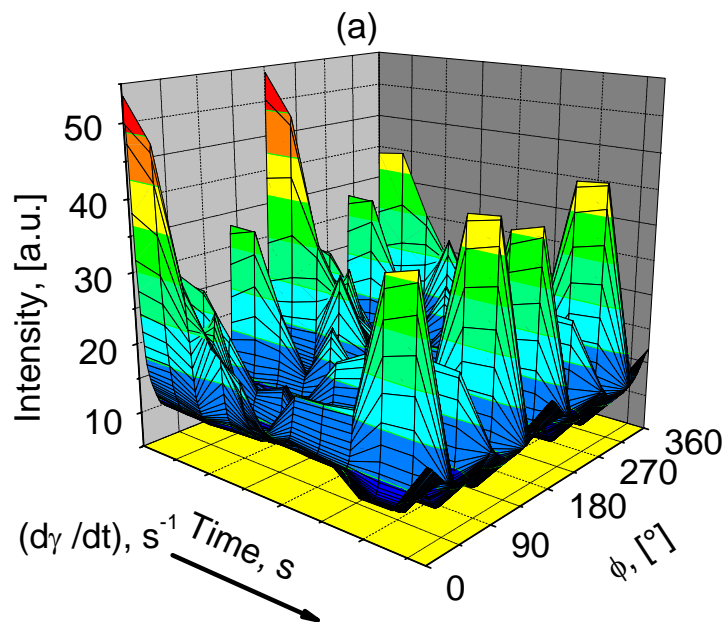


**Figure 8-6.** The angular dependence in radial view at  $T=80^{\circ}\text{C}$  and different shear rates,  $(d\gamma/dt), s^{-1}$  as follows: ( $\blackrightarrow$ )  $0s^{-1}$ ; ( $\color{blue}\rightarrow$ )  $0.1s^{-1}$ ; ( $\color{cyan}\rightarrow$ )  $0.1s^{-1}$ ; ( $\color{magenta}\rightarrow$ )  $1s^{-1}$ ; ( $\color{olive}\blacklozenge$ )  $1s^{-1}$ ; ( $\color{teal}\blackstar$ )  $10s^{-1}$ ; ( $\color{orange}\square$ )  $100s^{-1}$ .





**Figure 8-7.** (a) The evolution of intensity within time scale and azimuthal angle in tangential view at  $T=80^\circ\text{C}$ . (b) Top view of the azimuthal dependence with time.



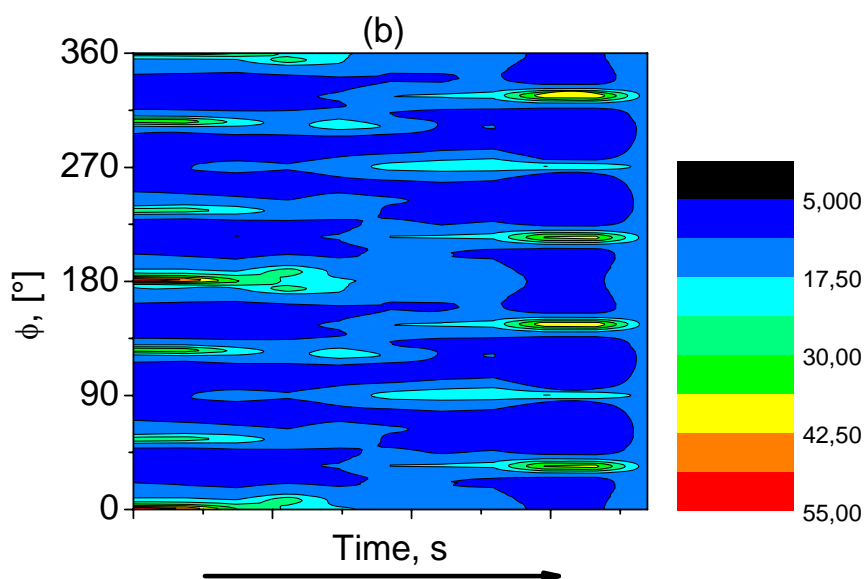


**Figure 8-8.** (a) The evolution of intensity with time and azimuthal angle in radial view at  $T=80^{\circ}\text{C}$ . (b) The azimuthal dependence with time in the radial view.

Previously it has been reported<sup>39</sup> by Stadler's group that the knitting pattern belongs to the two dimensional space group  $c2mm$ . The knitting pattern of polystyrene-*b*-polybutadiene-*b*-poly(methyl methacrylate) as swollen in DOP showed in the scattering profiles a bcc morphology  $Im\bar{3}m$  at the earlier stages of shearing which transformed into a hexagonal cylindrical structure with the correlation peaks as following:  $1:\sqrt{3}:\sqrt{4}:\sqrt{7}$  (Figure 8-3) corresponding to  $p6mm$  space group.

### 8.3. Conclusions

The morphological transition through a minimum in storage modulus has been detected via scanning of dynamic mechanical moduli in temperature sweeps and it was proved as well by scattering profiles monitored at a temperature above the morphological transition determined by DMA. Thus, the initial knitting pattern in bulk state after being swollen in DOP transforms by heating toward a well developed bcc morphology which has been investigated further by in situ rheo-SAXS.

It has been shown by in situ rheo-SAXS that by applying shear in steady mode the initial bcc morphology changed into a hexagonal morphology at a certain temperature. With increasing shear rate a well defined hexagonal cylindrical morphology was accomplished and developed at larger time scale. Above a critical shear rate the cylinders are erased and an isotropic state followed by the reformation of a better organized bcc morphology at rest after cessation of shear occurs.

While the pure spherical morphology such as 30wt-%  $S_{34}B_{19}M_{47}^{65}$  in DOP proved the shear-induced morphological transition in oscillatory shear mode together with a macroscopically aligned structure like hexagonal arrangement under steady shear mode, the solution of  $S_{34}EB_{19}M_{47}^{65}$  under applied steady shear generated a columnar structure which represents a novelty in terms of aligned state from block copolymer solutions. Similarly, bilayered supramolecular pyramidal columns were generated from semifluorinated dendritic benzamides<sup>221</sup> via hydrogen bonding while in the case of  $S_{34}EB_{19}M_{47}^{65}$  a shear-induced columnar structure of the three connected planes (110, 200, 211) evidenced in the 2D-pattern (Figure 8-2,  $\phi$  vs  $q$ ,  $t=913s$ ,  $(d\gamma/dt)=1s^{-1}$ ) has been achieved.

## 9. Summary

The alignment of the ordered microdomains of block copolymers in solution has been accomplished by using mechanical shear fields. Two pathways to monitor the achievement of aligned structures have been used: *rheo-optical* and in situ *rheo-SAXS* methods.

The AC diblock copolymer and ABC triblock terpolymer with high molecular weights and different morphologies were synthesized via anionic polymerization and the alignment has been monitored from the solutions of neat AC diblock, ABC triblock and their blend in a non-volatile solvent.

Before proceeding to the alignment protocols the thermodynamics of the diblock copolymer solutions has been studied by rheological means such as: temperature sweep, frequency sweep and master curve. The slightly asymmetric diblock copolymer polystyrene-*b*-poly(*t*-butyl methacrylate) (ST) as solutions at different concentrations was investigated by scanning of moduli over a range of temperatures and the morphological transitions were detected. This led us to conclude that dioctyl phthalate is a selective solvent for this diblock copolymer (ST) and a transition from the initially lamellar toward a cylindrical or spherical morphology takes place before order-disorder transition. The transition has been encountered via temperature sweep test through a minimum in storage modulus for two lamellar systems (ST), slightly asymmetric with different molecular weights,  $M \sim 72\text{K}$  and  $117\text{K}$ , respectively. These findings regarding to morphological transitions were in good agreement with the theoretical predictions made by Matsen for diblock copolymers. Since TEM investigations for these systems were not possible, a route to check the induced asymmetry due to the solvent selectivity was accomplished by applying the Leibler dilution approximation theory. While for the less asymmetric diblock copolymer ST(72K) the dilution approximation theory could be approached, for the higher asymmetric ST(117K) with a part contribution induced from the solvent selectivity a failure of the theory has been encountered. For the system ST(72K) where the theory was still valid, as a result an expression for the interaction parameter as a function of temperature has been developed.

The alignment kinetics were performed first by making use of the *rheo-optical method* and the monitored retardation was further used for calculation of birefringence. A perfectly symmetric diblock ST with high molecular weight (100K) as solution in dioctyl phthalate was used for the alignment protocols. Previous investigation of such system did not show any order-order transition, thus for this particular symmetric diblock the same lamellar morphology was preserved in the swollen state. Over a wide range of frequencies ( $\omega=0.1, 1,$

10 rad/s) and strain amplitudes (chosen accordingly with the instrumental limitation) the monitored birefringence was always positive meaning a perpendicular alignment with the normals of lamellae along the vorticity axis and perpendicular on the plane formed between flow direction and gradient velocity axes ( $v$ ,  $\nabla v$ ). This preferred alignment has been explained due to the low viscoelastic contrast between the polystyrene and poly(*t*-butyl methacrylate) blocks which did not allow the sliding toward a parallel alignment found for systems with a large viscoelastic contrast. Thus, it has been proved through an alignment of a solution of symmetric ST(100K) that choosing an appropriate chemical sequence of blocks a selective type of macroscopic alignment by LAOS can be achieved.

The introduction of the third elastomeric block as a middle block between the thermoplastic outer blocks (S and T), namely SBT triblock terpolymer, lead to significant changes in terms of alignment in the sense of tunable intermediate (perpendicular and transverse) aligned states which finally led to the same final parallel orientation in the diluted state. The in situ rheo-SAXS method applied to the same system elucidated the intermediate mechanism leading to a final parallel aligned state such as a coexistence of parallel and perpendicular states which gave rise to a transverse alignment in rheo-optical method. As a finally aligned state resulting from in situ rheo-SAXS in oscillatory mode the perpendicular one was found within a short time scale ( $\sim 1$ h), while the rheo-optical method revealed a perpendicular state at short time scale ( $\sim 1$ h) and parallel state at long time scale ( $\sim 10$ h).

Finally, the investigation of the lamellar non-centrosymmetric blend SBT:ST=60:40 allowed preferential parallel alignment above a critical strain amplitude,  $\gamma_C$  as follows: i)  $\gamma < \gamma_C$  only perpendicular alignment is achieved which was not perfected toward a saturated value within the time scale used in our experiments; ii)  $\gamma \cong \gamma_C$  a tendency toward a final parallel alignment via perpendicular was found; iii)  $\gamma > \gamma_C$  and together with an increased temperature from 10°C to 15°C showed an obvious parallel alignment through an intermediate perpendicular state.

While the rheo-optical method applied to a bcc morphology of a solution of SBM triblock terpolymer in DOP did not give evidence for an induced morphological transition, in situ rheo-SAXS was a powerful tool to illustrate such a transition.

Moreover, we have shown that more complicated morphologies like knitting pattern of SEBM (as cast film from chloroform) which reveals a bcc morphology as a solution in DOP could be investigated and macroscopically aligned via in situ rheo-SAXS while the rheo-optical method could not be used due to the non transparent system. The induced

columnar structure could be monitored in 2D SAXS patterns which have never been reported before.

In summary, it was demonstrated that mechanical field alignment of block copolymer domains in solution allowed to generate highly anisotropic structures even for block copolymers with high molecular weights under ambient conditions and for a large variety of morphologies.

## Zusammenfassung

Durch mechanische Scherfelder wurden geordnete Mikrodomänen von Blockcopolymeren ausgerichtet. Die Umwandlung zu ausgerichteten Strukturen wurde mit rheoptischen Methoden und in-situ Rheo-SAXS beobachtet.

Durch anionische Polymerisation wurden AC-Zweiblockcopolymere und ABC-Dreiblockterpolymere mit hohen Molekulargewichten und verschiedenen Morphologien hergestellt. Ihre Ausrichtung wurde in Lösungen der reinen Polymere und ihrer Mischungen in einem nichtflüchtigen Lösungsmittel untersucht.

Zuerst wurden die thermodynamischen Eigenschaften der Blockcopolymer-Lösungen mit rheologischen Methoden untersucht. Das geringfügig unsymmetrische Zweiblockcopolymer Polystyrol-block-Poly(t-butylmethacrylat) (ST) wurde in unterschiedlich konzentrierten Lösungen durch Messung der dynamischen Moduli bei verschiedenen Temperaturen untersucht, um die Übergänge zwischen den Morphologien festzustellen. Aus diesen Untersuchungen konnte geschlossen werden, dass Dioctylphthalat (DOP) ein selektives Lösungsmittel für das ST-Blockcopolymer ist und ein Übergang von anfänglich lamellarer zu zylindrischer oder Kugel-Morphologie vor dem Übergang vom geordneten in den ungeordneten Zustand stattfindet. Der Übergang wurde durch das Minimum des Speichermoduls als Funktion der Temperatur für zwei lamellare Systeme, einem leicht asymmetrischen ST-Zweiblockcopolymer mit 72 kg/mol bzw. 117 kg/mol, aufgezeichnet. Die Ergebnisse sind in guter Übereinstimmung mit den theoretischen Vorhersagen von Matsen. Da TEM-Untersuchungen für diese Systeme nicht möglich sind, wurde die Verdünnungstheorie von Leibler angewandt, um die Asymmetrie, die das Lösungsmittel hervorruft, zu beschreiben. Während für das weniger unsymmetrische Blockcopolymer die Anwendung dieser Theorie erfolgreich war, versagte sie für das stärker unsymmetrische Blockcopolymer. Für das kleinere ST-Zweiblockcopolymer, für das die Theorie gültig war, konnte ein Ausdruck für den segmentalen Wechselwirkungsparameter in Abhängigkeit von der Temperatur gefunden werden.

Die Kinetik der Ausrichtung wurde zuerst mit rheoptischen Methoden untersucht. Die aufgezeichnete Änderung des Polarisationszustandes des eingestrahnten Lichts wurde zur Berechnung der Doppelbrechung benutzt. Ein exakt symmetrisches ST-Zweiblockcopolymer

mit hohem Molekulargewicht (100 kg/mol) wurde in Dioctylphthalat untersucht. Frühere Untersuchungen solcher Systeme gaben keinen Hinweis auf einen Übergang von verschiedenen geordneten Morphologien. Für dieses spezielle Zweiblockcopolymer blieb die lamellare Morphologie in gequollenem Zustand erhalten. Über einen großen Bereich von Frequenzen ( $\omega = 0.1, 1, 10$  rad/s) und Dehnungen (innerhalb der Grenzen des Instruments) hatte die aufgezeichnete Doppelbrechung immer einen positiven Wert. Dies bedeutet eine senkrechte Ausrichtung, in der die Normale auf die Lamellen entlang der Drehachse und senkrecht zur Ebene zwischen Fließrichtung und den Achsen der Geschwindigkeit ( $v, \nabla v$ ) steht. Diese bevorzugte Ausrichtung kann durch den geringen viskoelastischen Kontrast zwischen den Polystyrol- und Poly(t-butylmethacrylat)-Blöcken erklärt werden. Dieser erlaubt kein Gleiten zu einer parallelen Ausrichtung, wie es in Systemen mit hohem viskoelastischen Kontrast gefunden wird. Es konnte somit durch die Ausrichtung einer Lösung des symmetrischen ST-Blockcopolymers (100 kg/mol) gezeigt werden, dass durch die geeignete chemische Abfolge der Blöcke eine bestimmte bevorzugte, makroskopische Orientierung durch LAOS erreicht werden kann.

Der Einbau eines dritten, elastischen Blocks als mittlerer Block zwischen den beiden thermoplastischen Blöcken S und T, also ein SBT Dreiblockterpolymer, führte zu einer wesentlichen Veränderung der Ausrichtung. Sie zeigte senkrecht und transversal orientierte Zwischenstufen, die am Ende zu der gleichen parallelen Orientierung im verdünnten Fall führten. Mit in-situ Rheo-SAXS konnte der Übergangsmechanismus in diesem System, wie zum Beispiel die Koexistenz von parallelen und senkrechten Zuständen, die zur transversalen Orientierung in der rheooptischen Methode führten, verfolgt werden. Mit in-situ Rheo-SAXS im oszillierenden Modus wurde in kurzen Zeitabständen (1 h) eine senkrechte Anordnung gefunden, während mit der rheooptischen Methode in kurzen Zeiten (1 h) ein senkrechter und nach langen Zeiten (10 h) ein paralleler Zustand gefunden wurde.

Schließlich wurde eine unsymmetrische Polymermischung SBT : ST = 60 : 40 mit lamellarer Morphologie untersucht, die oberhalb einer kritischen Dehnungsamplitude  $\gamma_C$  bevorzugt parallel ausgerichtet werden konnte. Für  $\gamma < \gamma_C$  konnte nur eine senkrechte Ausrichtung erhalten werden, die auf der Zeitskala der Experimente nicht vollständig erreicht wurde. Für  $\gamma \cong \gamma_C$  konnte eine Tendenz zu einer parallelen Ausrichtung über einen senkrechten Zwischenzustand beobachtet werden. Eine parallele Anordnung über einen senkrechten

Zwischenzustand konnte schließlich für  $\gamma > \gamma_c$  und bei von 10 °C auf 15 °C erhöhter Temperatur gefunden werden.

Während ein Übergang der bcc-Morphologie einer Lösung von SBM-Dreiblockcopolymer in DOP mit rheooptischen Methoden nicht gezeigt werden konnte, gelang dies mit in-situ Rheo-SAXS.

Weiterhin konnte gezeigt werden, dass kompliziertere Morphologien, wie bei einem aus einer Chloroform-Lösung gegossen SEBM-Film, der eine „Strickmuster“-Morphologie und in Lösung eine bcc-Morphologie zeigt, mit in-situ Rheo-SAXS untersucht und makroskopisch ausgerichtet werden können. Die rheooptische Methode kann dagegen nicht angewendet werden, da das System nicht transparent ist. Die erzeugte kolumnare Struktur konnte in 2D-SAXS-Mustern aufgezeichnet werden, was bisher noch nicht beschrieben wurde.

Zusammenfassend kann gesagt werden, dass bei Raumtemperatur durch mechanische Felder Blockcopolymer-Domänen in Lösung zu anisotropen Strukturen ausgerichtet werden können. Dies wurde für Blockcopolymere mit hohen Molekulargewichten und einer großen Bandbreite an Morphologien gezeigt.

## References

- (1) Gupta, V. K.; Krishnamoorti, R.; Kornfield, J. A.; Smith, S. D. *Macromolecules* **1995**, *28*, 4464-4474.
- (2) Gupta, V. K.; Krishnamoorti, R.; Chen, Z.-R.; Kornfield, J. A.; Smith, S. D.; Satkowski, M. M.; Grothaus, J. T. *Macromolecules* **1996**, *29*, 875-884.
- (3) Patel, S. S.; Larson, R. G.; Winey, K. I.; Watanabe, H. *Macromolecules* **1995**, *28*, 4313-4318.
- (4) Pinheiro, B. S.; Hajduk, D. A.; Gruner, S. M.; Winey, K. I. *Macromolecules* **1996**, *29*, 1482-1489.
- (5) Balsara, N. P.; Hammouda, B. *Phys. Rev. Lett.* **1994**, *72*, 360-363.
- (6) Balsara, N. P.; Hammouda, B.; Kesani, P. K.; Jonnalagadda, S. V.; Straty, G. C. *Macromolecules* **1994**, *27*, 2566-2573.
- (7) Wang, H.; Kesani, P. K.; Balsara, N. P.; Hammouda, B. *Macromolecules* **1997**, *30*, 982-992.
- (8) Albalak, R. J.; Capel, M. S.; Thomas, E. L. *Polymer* **1998**, *39*.
- (9) Bates, F. S.; Schulz, M. F.; Khandpur, A. K.; Förster, S.; Rosedale, J. H.; Almdal, K.; Mortensen, K. *Faraday Discussions* **1994**, *98*, 7-18.
- (10) Bates, F. S.; Fredrickson, G. H. *Annual Review of Physical Chemistry* **1990**, *41*, 525-557.
- (11) Matsen, M. W.; Schick, M. *Macromolecules* **1994**, *27*, 4014-4015.
- (12) Leibler, L. *Macromolecules* **1980**, *13*, 1602-1617.
- (13) Matsen, M. W.; Schick, M. *Physical Review Letters* **1994**, *72*, 2660-2663.
- (14) Spontak, R. J.; Smith, S. D.; Ashraf, A. *Macromolecules* **1993**, *26*, 956-962.
- (15) Thomas, E. L.; Anderson, D. M.; Henkee, C. S.; Hoffman, D. *Nature* **1988**, *334*, 598.
- (16) Alward, D. B.; Kinning, D. J.; Thomas, E. L.; Fetters, L. J. *Macromolecules* **1986**, *19*, 215-224.
- (17) Thomas, E. L.; Alward, D. B.; Kinning, D. J.; C., M. D.; Handlin, D. L., Jr.; Fetters, L. J. *Macromolecules* **1986**, *19*, 2197-2202.
- (18) Hasegawa, H.; Tanaka, H.; Yamasaki, K.; Hashimoto, T. *Macromolecules* **1987**, *20*, 1651-1662.
- (19) Hashimoto, T.; Yamasaki, K.; Koizumi, S.; Hasegawa, H. *Macromolecules* **1993**, *26*, 2895-2904.
- (20) Hashimoto, T.; Koizumi, S.; Hasegawa, H.; Izumitani, T.; Hyde, S. T. *Macromolecules* **1992**, *25*, 1433-1439.
- (21) Almdal, K.; Koppi, K. A.; Bates, F. S.; Mortensen, K. *Macromolecules* **1992**, *25*, 1743-1751.
- (22) Hamley, I. W.; Koppi, K. A.; Rosendale, J. H.; Bates, F. S.; Almdal, K.; Mortensen, K. *Macromolecules* **1993**, *26*, 5959-5970.
- (23) Disko, M. M.; Liang, K. S.; Behal, S. K.; Roe, R. J.; Jeon, K. J. *Macromolecules* **1993**, *26*, 2983-2986.
- (24) Helfand, E.; Wasserman, Z. R. *Macromolecules* **1976**, *9*, 879-888.
- (25) Helfand, E.; Wasserman, Z. R. *Macromolecules* **1978**, *11*; *13*, 960-966; 994-998.
- (26) Fredrickson, G. H.; Helfand, E. *Journal of Chemical Physics* **1987**, *87*, 697-705.
- (27) Whitmore, M. D.; Vavasour, J. D. *Acta Polymerica* **1995**, *46*, 341-360.
- (28) Matsen, M. W.; Bates, F. S. *Macromolecules* **1996**, *29*, 1091-1098.
- (29) Shull, K. R. *Macromolecules* **1992**, *25*, 2122-2133.
- (30) Hashimoto, T.; Shibayama, M.; Kawai, H. *Macromolecules* **1980**, *13*, 1237-1247.
- (31) Semenov, A. N. *Macromolecules* **1993**, *26*, 6617-6621.
- (32) Helfand, E.; Wasserman, Z. R. *Macromolecules* **1980**, *13*, 994-998.
- (33) Matsen, M. W. *J. Chem. Phys.* **2000**, *113*, 5539-5544.

- (34) Stadler, R.; Auschra, C.; Beckmann, J.; Krappe, U.; Voigt-Martin, I.; Leibler, L. In *Macromolecules*, 1995; Vol. 28, pp 3080-3097.
- (35) Breiner, U.; Krappe, U.; Abetz, V.; Stadler, R. *Macromol. Chem. Phys.* **1997**, *198*, 1051-1083.
- (36) Mogi, Y.; Kotsuji, H.; Kaneko, Y.; Mori, K.; Matsushita, Y.; Noda, I. *Macromolecules* **1992**, *25*, 5408-5411.
- (37) Mogi, Y.; Mori, K.; Kotsuji, H.; Matsushita, Y.; Noda, I.; Han, C. C. *Macromolecules* **1993**, *26*, 5169-5173.
- (38) Mogi, Y.; Nomura, M.; Kotsuji, H.; Ohnishi, K.; Matsushita, Y.; Noda, I. *Macromolecules* **1994**, *27*, 6755-6760.
- (39) Breiner, U.; Krappe, U.; Thomas, E. L.; Stadler, R. *Macromol. Rapid Commun.* **1998**, *31*, 135-141.
- (40) Herman, D. S.; Kinning, D. J.; Thomas, E. L.; Fetters, L. J. *Macromolecules* **1987**, *20*, 2940-2942.
- (41) Rosedale, J. H.; Bates, F. S. *Macromolecules* **1990**, *23*, 2329-2338.
- (42) Bates, F. S.; Rosedale, J. H.; Fredrickson, G. H.; Glinka, C. J. *Physical Review Letters* **1988**, *61*, 2229-2232.
- (43) Bates, F. S.; Rosedale, J. H.; Fredrickson, G. H. *J. Chem. Phys.* **1990**, *92*, 6255-6270.
- (44) Almdal, K.; Bates, F. S.; Mortensen, K. *J. Chem. Phys.* **1992**, *96*, 9122-9132.
- (45) Rosedale, J. H.; Bates, F. S.; Almdal, K.; Mortensen, K.; Wignall, G. D. *Macromolecules* **1995**, *28*, 1429-1443.
- (46) Fredrickson, G. H.; Helfand, E. *J. Chem. Phys.* **1988**, *89*, 5890-5897.
- (47) Fredrickson, G. H.; Larson, R. G. *J. Chem. Phys.* **1987**, *86*, 1553-1560.
- (48) Han, C. D.; Kim, J. *J. Polym. Sci., Polym. Phys.* **1987**, *25*, 1741.
- (49) Adams, J. L.; Graessley, W. W.; Register, R. A. *Macromolecules* **1994**, *27*, 6026-6032.
- (50) Sakamoto, N.; Hashimoto, T.; Han, C. D.; Kim, D.; Vaidya, N. Y. *Macromolecules* **1997**, *27*, 1621-1632.
- (51) Khandpur, A. K.; Förster, S.; Bates, F. S.; Hamley, I. W.; Ryan, A. J.; Bras, W.; Almdal, K.; Mortensen, K. *Macromolecules* **1995**, *28*, 8796.
- (52) Bates, F. S.; Rosedale, J. H.; Bair, H. E.; Russell, T. P. *Macromolecules* **1989**, *22*, 2557-2564.
- (53) Winey, K. I.; Gobran, D. A.; Xu, Z.; Fetters, L. J.; Thomas, E. L. *Macromolecules* **1994**, *27*, 2392-2397.
- (54) Han, C. D.; Kim, J.; Kim, J. K. *Macromolecules* **1989**, *22*, 383-394.
- (55) Choi, S.; Vaidya, N. Y.; Han, C. D.; Sota, N.; Hashimoto, T. *Macromolecules* **2003**, *36*, 7707-7720.
- (56) Owens, J. N.; Gancarz, I. S.; Koberstein, J. T.; Russell, T. P. *Macromolecules* **1989**, *22*, 3380-3387.
- (57) Roe, R.-J.; Fishkis, M.; Chang, J. C. In *Macromolecules*, 1981; Vol. 14, pp 1091-1103.
- (58) Hadziioannou, G.; Skoulios, A. *Macromolecules* **1982**, *15*, 267-271.
- (59) Schulz, M. F.; Bates, F. S.; Almdal, K.; Mortensen, K. *Physical review letters* **1994**, *73*, 86-89.
- (60) Spontak, R. J.; Fung, J. C.; Braunfeld, M. B.; Sedat, J. W.; Agard, D. A.; Kane, L.; Smith, S. D.; Satkowski, M. M.; Ashraf, A.; Hajduk, D. A.; Gruner, S. M. *Macromolecules* **1996**, *29*, 4494-4507.
- (61) Sakurai, S.; Irie, H.; Umeda, H.; Nomura, S.; Lee, H. H.; Kim, J. K. *Macromolecules* **1998**, *31*, 336-343.
- (62) Goldacker, T.; Abetz, V.; Stadler, R.; Erukhimovich, I.; Leibler, L. In *Nature*, 1999; Vol. 398, p 137.

- (63) Goldacker, T.; Abetz, V.; Stadler, R. *Macromolecular Symposia* **2000**, *149*, 93-98.
- (64) Lescanec, R. L.; Fetters, L. J.; Thomas, E. L. *Macromolecules* **1998**, *31*, 1680-1685.
- (65) Auschra, C.; Stadler, R. *Macromolecules* **1993**, *26*, 6364-6377.
- (66) Abetz, V.; Goldacker, T. *Macromolecular Rapid Communications* **2000**, *21*, 16-34.
- (67) Chen, Z.-R.; Issaian, A. M.; Kornfield, J. A.; Smith, S. D.; Grothaus, J. T.; Satkowski, M. M. In *Macromolecules*, 1997; Vol. 30, pp 7096-7114.
- (68) Vigild, M. E.; Chu, C.; Sugiyama, M.; Chaffin, K. A.; Bates, F. S. *Macromolecules* **2001**, *34*, 951-964.
- (69) Zryd, J. L.; Burghardt, W. R. *Macromolecules* **1998**, *31*, 3656-3670.
- (70) Chen, Z.-R.; Kornfield, J. A. *Polymer* **1998**, *39*, 4679-4699.
- (71) Keller, A.; Pedemonte, E.; Willmouth, F. M. *Colloid Polym. Sci.* **1970**, *238*, 385-389.
- (72) Folkes, M. J.; Keller, A.; Scalisi, F. P. *Colloid Polym. Sci.* **1973**, *251*, 1-4.
- (73) Zhang, Y.; Wiesner, U. *J. Chem. Phys.* **1995**, *103*, 4784-4793.
- (74) Leist, H.; Maring, D.; Thurn-Albrecht, T.; Wiesner, U. *Journal of chemical physics* **1999**, *110*, 8225.
- (75) Koppi, K. A.; Tirrell, M.; Bates, F. S.; Almdal, K.; Colby, R. H. *J. Phys. II* **1992**, *2*, 1941-1959.
- (76) Okamoto, S.; Saijo, K.; Hashimoto, T. *Macromolecules* **1994**, *27*, 5547-5555.
- (77) Polushkin, E.; Alberda van Ekenstein, G.; Dolbnya, I.; Bras, W.; Ikkala, O.; Brinke, G. *Macromolecules* **2003**, *36*, 1421.
- (78) Kitade, S.; Ochiai, N.; Takahashi, Y.; Noda, I.; Matsushita; Karim, A.; Nakatani, A. I.; Kim, H.; Han, C. C. *Macromolecules* **1998**, *31*, 8083.
- (79) Winey, K. I.; Patel, S. S.; Larson, R. G.; Watanabe, H. *Macromolecules* **1993**, *26*, 2542-2549.
- (80) Winey, K. I.; Patel, S. S.; Larson, R. G.; Watanabe, H. *Macromolecules* **1993**, *26*, 4373-4375.
- (81) Polis, D. L.; Winey, K. I. *Macromolecules* **1996**, *29*, 8180.
- (82) Gupta, V. K.; Krishnamoorti, R.; Kornfield, J. A.; Smith, S. D. *Macromolecules* **1996**, *29*, 1359.
- (83) Zhang, Y.; Wiesner, U.; Spiess, H. W. *Macromolecules* **1995**, *28*, 778-781.
- (84) Zhang, Y.; Wiesner, U.; Yang, Y.; Pakula, T.; Spiess, H. W. *Macromolecules* **1996**, *29*, 5427.
- (85) Maring, D.; Wiesner, U. *Macromolecules* **1997**, *30*, 660.
- (86) Macosko, C. W. *Rheology. Principles, Measurements, and Applications*, 1994.
- (87) Philippoff, W. *Trans. Soc. Rheol.* **1966**, *10*, 317-334.
- (88) MacSporran, W. C.; Spiers, R. P. *Rheologica Acta* **1982**, *21*, 193-200.
- (89) Onogi, S.; Matsumoto, T. *Polymer Engineering Reviews* **1981**, *1*, 45-87.
- (90) Dealy, J. M.; Petersen, J. F.; Tee, T. T. *Rheologica Acta* **1973**, *12*, 550-558.
- (91) Huang, Z.-F.; Drolet, F.; Vinals, J. *Macromolecules* **2003**, *36*, 9622.
- (92) Harada, T.; Bates, F. S.; Lodge, T. P. *Macromolecules* **2003**, *36*, 5440.
- (93) Balsara, N. P.; Perahia, D.; Safinya, C. R.; Tirrell, M.; Lodge, T. P. *Macromolecules* **1992**, *25*, 3896-3901.
- (94) Amundson, K.; Helfand, E.; Davis, D. D.; Quan, X.; Patel, S. S.; Smith, S. D. *Macromolecules* **1991**, *24*, 6546-6548.
- (95) Amundson, K.; Helfand, E.; Quan, X.; Smith, S. D. *Macromolecules* **1993**, *26*, 2698-2703.
- (96) Thurn-Albrecht, T.; DeRouchey, J.; Russell, T. P.; Jaeger, H. M. *Macromolecules* **2000**, *33*, 3250-3253.
- (97) Amundson, K.; Helfand, E.; Quan, X.; Hudson, S. D.; Smith, S. D. *Macromolecules* **1994**, *27*, 6559-6570.

- (98) Böker, A.; Knoll, A.; Elbs, H.; Abetz, V.; Müller, A. H. E.; Krausch, G. *Macromolecules* **2002**, *35*, 1319-1325.
- (99) Boeker, A.; Elbs, H.; Haensel, H.; Knoll, A.; Ludwigs, S.; Zettl, H.; Urban, V.; Abetz, V.; Mueller, A. H. E.; Krausch, G. *Polymer Preprints* **2002**, *43*, 350-351.
- (100) Bywater, S. *Encyclopedia of Polymer Science and Engineering*, second edition, Wiley-Interscience ed.; Kroschwitz, J. I.: New York, 1985; Vol. 2.
- (101) Morton, M. *Anionic Polymerization: Principles and Practice*; Academic Press: New York, 1983.
- (102) Szwarc, M.; Levy, M.; Milkovich, R. *Journal of the American Chemical Society* **1956**, *78*, 2656-2657.
- (103) Szwarc, M. *Nature* **1956**, *178*, 1168-1169.
- (104) Webster, O. W. *Science* **1991**, *251*, 887.
- (105) Fetters, L. J.; Thomas, E. L. *Material Science & Technology*; VCH Verlagsgesellschaft: Weinheim, 1993; Vol. 12.
- (106) Quirk, R. P.; Kinning, D. J.; Fetters, L. J. In *Comprehensive Polymer Science*; Pergamon, Ed.; S. L. Agarwal: Oxford, 1989; Vol. 7, p 1.
- (107) Quirk, R. P.; Kim, J. *Rubber Chem. Technol.* **1991**, *64*, 450.
- (108) Fontanille, M. *Comprehensive Polymer Science*, 1989; Vol. 3.
- (109) Kennedy, J. P.; Ivan, B. *Designed Polymers by Carbocationic Macromolecular Engineering: Theory and Practice*; Hanser Publishers, Munich, 1992.
- (110) Sawamoto, M.; Higashimura, T. *Encyclopedia of Polymer Science and Engineering*; J. I. Kroschwitz: New York, 1989.
- (111) Keii, T.; Doi, Y.; Soga, K. *Encyclopedia of Polymer Science and Engineering*; J. I. Kroschwitz: New York, 1989.
- (112) Doi, Y.; Keii, T. *Adv. Polym. Sci.* **1986**, *73/74*, 201.
- (113) Grubbs, R.; Novak, B. M. In *Encyclopedia of Polymer Science and Engineering*; Wiley-Interscience, Ed.; J. I. Kroschwitz: New York, 1989; p 420.
- (114) Georges, M. K.; Veregin, R. P. N.; Kazmaier, P. M.; Hamer, G. K. *Macromolecules* **1993**, *26*, 2987-2988.
- (115) Matyjaszewski, K.; Wang, J.-L.; Grimaud, T.; Shipp, D. A. *Macromolecules* **1998**, *31*, 1527-1534.
- (116) Rempp, P.; Franta, E.; Herz, J.-E. *Adv. Polym. Sci.* **1988**, *86*, 145.
- (117) Fetters, L. J. *Encyclopedia of Polymer Science and Engineering*; Wiley-Interscience: New York, 1985; Vol. 10.
- (118) Thomas, E. L. *Electron microscopy, Chap. 5 Encyclopedia of Polymer Science & Engineering*, 1986.
- (119) Tsuji, M. *Comprehensive Polymer Science*, 1989; Vol. VI.
- (120) Trent, J. S.; Scheinbeim, J. I.; Couchman, P. R. *Macromolecules* **1983**, *16*, 589-598.
- (121) Isaacson, M.; Johnson, D.; Crewe, A. V. *Radiation Research* **1973**, *55*, 205-224.
- (122) Murata, Y.; Fryer, J. R.; Baird, T.; Murata, H. *Acta Crystallographica* **1977**, *A33*, 198-200.
- (123) Glaeser, R. M.; Taylor, K. A. *Journal Microscopy* **1978**, *112*, 127.
- (124) Christ, B. *J. Polym. Sci., Polym. Phys.* **1973**, *11*, 635.
- (125) Todakoro, H. *Structures of Crystalline Polymers*; Wiley-Interscience: New York, 1979.
- (126) Hadjuk, D. A.; Harper, P. E.; Gruner, S. M.; Honeker, C. C.; Kim, G.; Thomas, E. L.; Fetters, L. J. *Macromolecules* **1994**, *27*, 4063-4075.
- (127) Oster, G.; Riley, D. P. *Acta Crystallogr.* **1952**, *5*, 272-276.
- (128) Glatter, O.; Kratky, O. In *Small-angle X-ray scattering*; Academic Press, 1981.
- (129) Fried, J. R. In *Polymer Science and Technology, 2nd ed.*; Prentice Hall, P., Ed., 2003.
- (130) Gedde, U. W. In *Polymer Physics*; Chapman & Hall, 1995; p 99.

- 
- (131) Hiemenz, P. C. In *Polymer Chemistry. The basic concepts*, 1984; p 133.
- (132) Gedde, U. W.; Chap.5. In *Polymer Physics*; Hall, C., Ed., 1995; p 77.
- (133) Pakula, T.; Floudas, G. *Block Copolymers*, Calleja F. J. B., Roslaniec Z. ed.; Marcel Dekker Inc.: New York, 2000.
- (134) Bullough, R. K. *Journal of Polymer Science* **1960**, *46*, 517-520.
- (135) Onuki, A.; Doi, M. *Journal of Chemical Physics* **1986**, *85*, 1190-1197.
- (136) Frisman, E. V.; Mao, H. *Vysokomolekulyarnye Soedineniya* **1964**, *6*, 193-196.
- (137) Fredrickson, G. H. *Macromolecules* **1987**, *20*, 3017-3020.
- (138) Janeschitz-Kriegl, H. *Polymer melt rheology and flow birefringence*; Springer-Verlag: Berlin, 1983.
- (139) White, J. L. *Principles of polymer engineering rheology*; Wiley: New York, 1990.
- (140) Treloar, L. R. G. *The physics of rubber elasticity*, 3rd ed.; Clarendon Press: Oxford, 1975.
- (141) Markgraf, K.; Abetz, V. *e-polymers* **2001**, *No15*.
- (142) Auschra, C.; Stadler, R. In *Polymer Bulletin*, 1993; Vol. 30, pp 257-264.
- (143) Mohammadi, N. A.; Rempel, G. L. *Macromolecules* **1987**, *20*, 2362-2368.
- (144) Hahn, S. F. *J. Polym. Sci., Part A: Polym. Chem.* **1992**, *30*, 397.
- (145) Helfand, E. *Macromolecules* **1975**, *8*, 552-556.
- (146) Hashimoto, T.; Kowsaka, K.; Shibayama, M.; Kawai, H. *Macromolecules* **1986**, *19*, 754-762.
- (147) Bates, F. S.; Hartney, M. A. *Macromolecules* **1985**, *18*, 2478-2486.
- (148) Chung, C. I.; Gale, J. C. *J. Polym. Sci., Polym. Phys. Ed.* **1976**, *14*, 1149-1156.
- (149) Bates, F. S. *Macromolecules* **1984**, *17*, 2607-2613.
- (150) Ohta, T.; Kawasaki, K. *Macromolecules* **1986**, *19*, 2621-2632.
- (151) Zyrd, J. L.; Burghardt, W. R. *Macromolecules* **1998**, *31*, 3656-3670.
- (152) Lodge, T. P.; Hanley, K. J.; Pudil, B.; Alahapperuma, V. *Macromolecules* **2003**, *36*, 816-822.
- (153) Barton, A. F. M. *CRC Handbook of Polymer-Liquid Interaction Parameters and Solubility Parameters*: Boston, 1990.
- (154) Han, C. D.; Baek, D. M.; Kim, J. K.; Ogawa, T.; Sakamoto, N.; Hashimoto, T. *Macromolecules* **1995**, *28*, 5043-5062.
- (155) Stangler, S.; Abetz, V. *e-polymers* **2002**, *018*.
- (156) Macosko, C. W. *Rheology. Principles, measurements, and applications*, pag. 398; VCH, 1994.
- (157) Saito, S.; Hashimoto, T.; Morfin, I.; Lindner, P.; Bouè, F.; Pine, D. J. In *Macromolecules*, 2003; Vol. 36, pp 3745-3748.
- (158) Rangel-Nafaile, C.; Metzner, A. B.; Wissbrun, K. F. *Macromolecules* **1984**, *17*, 1187-1195.
- (159) Yanase, H.; Moldenaers, P.; Mewis, J.; Abetz, V.; van Egmond, J.; Fuller, G. G. *Rheologica Acta* **1991**, *30*, 89-97.
- (160) Helfand, E.; Fredrickson, G. H. *Phys. Rev. Lett.* **1989**, *62*, 2468-2471.
- (161) Wu, X.-L.; Pine, D. J.; Dixon, P. K. *Phys. Rev. Lett.* **1991**, *66*, 2408-2411.
- (162) Minale, M.; Wissbrun, K. F.; Massouda, D. F. *Journal of Rheology* **2003**, *47*, 1-17.
- (163) Gehlsen, M. D.; Bates, F. S. *Macromolecules* **1993**, *37*, 4122-4127.
- (164) Arnold, K. R.; Meier, D. J. *J. Appl. Polym. Sci.* **1970**, *14*, 427.
- (165) Chung, C. I.; Lin, M. I. *J. Polym. Sci.* **1978**, *16*, 545-553.
- (166) Ferry, J. D. *Viscoelastic Properties of Polymers*, 1980; Vol. 3rd ed.; Wiley: New York.
- (167) Graessley, W. W.; Edwards, S. F. *Polymer* **1981**, *22*, 1329-1334.
- (168) Graessley, W. W. *J. Polym. Sci., Polym. Phys. Ed.* **1980**, *18*, 27-34.
- (169) Porter, R. S.; Johnson, J. F. *Chemical Reviews* **1966**, *66*, 1-27.

- (170) Fesko, D. G.; Tschögl, N. W. *International Journal of Polymeric Materials* **1974**, *3*, 51-79.
- (171) Fredrickson, G. H.; Leibler, L. *Macromolecules* **1989**, *22*, 1238-1250.
- (172) Olvera de la Cruz, M. *J. Chem. Phys.* **1989**, *90*, 1995-2002.
- (173) Krause, S. *Journal of Macromolecular Science, Reviews in Macromolecular Chemistry* **1972**, *7*, 251-314.
- (174) Cochran, E. W.; Bates, F. S. *Macromolecules* **2002**, *35*, 7368-7374.
- (175) Keller, A.; Pedemonte, E.; Willmouth, F. M. *Nature* **1970**, *225*, 538-539.
- (176) Hadziioannou, G.; Mathis, A.; Skoulios, A. *Colloid Polym. Sci.* **1979**, *257*, 136-139.
- (177) Pakula, T.; Saijo, K.; Kawai, H.; Hashimoto, T. *Macromolecules* **1985**, *18*, 1294-1302.
- (178) Balsara, N. P.; Dai, H. J.; Watanabe, H.; Sato, T.; Osaki, K. *Macromolecules* **1996**, *29*, 3507-3510.
- (179) Zhang, Y.; Wiesner, U. *J. Chem. Phys.* **1997**, *106*, 2961-2969.
- (180) Wiesner, U. *Macromolecular Chemistry and Physics* **1997**, *198*, 3319-3352.
- (181) Stangler, S. In *Macromoleculare Chemistry*; University of Bayreuth, 2002; p 157.
- (182) Folkes, M. J.; Keller, A. *J. Polym. Sci., Polym. Phys. Ed.* **1976**, *14*, 833-846.
- (183) Folkes, M. J.; Keller, A. *Polymer* **1971**, *12*, 222-236.
- (184) Amundson, K.; Helfand, E.; Patel, S. S.; Quan, X.; Smith, S. D. *Macromolecules* **1992**, *25*, 1935-1940.
- (185) Lodge, T. P.; Fredrickson, G. H. *Macromolecules* **1992**, *25*, 5643-5650.
- (186) Brandrup, J.; Immergut, E. H.; Grulke, E. A. *Polymer Handbook, 4th ed.*; Wiley: New York, 1999.
- (187) Rosendale, J. H.; Bates, F. S.; Almdal, K.; Mortensen, K.; Wignall, G. D. *Macromolecules* **1995**, *28*, 1429-1443.
- (188) Rachapudy, H.; Smith, G. G.; Raju, V. R.; Graessley, W. W. *Journal of Polymer Science, Polymer Physics* **1979**, *17*, 1211-1222.
- (189) Pakula, T.; Saijo, K.; Hashimoto, T. *Macromolecules* **1985**, *18*, 2037-2044.
- (190) Kulicke, W.-M.; Reinhardt, U.; Arendt, O. *Macromol. Rapid Commun.* **1998**, *19*, 219-222.
- (191) Kannan, R. M.; Kornfield, J. A. *Macromolecules* **1994**, *27*, 1177-1186.
- (192) Koppi, K. A.; Tirrell, M.; Bates, F. S. *Physical Review Letters* **1993**, *70*, 1449-1452.
- (193) Larson, R. G.; Winey, K. I.; Patel, S. S.; Watanabe, H.; Bruinsma, R. *Rheologica acta* **1993**, *32*, 245-253.
- (194) Hadziioannou, G.; Mathis, A.; Skoulios, A. *Macromolecules* **1982**, *15*, 258-262.
- (195) Auschra, C.; Stadler, R. *Macromolecules* **1993**, *26*, 2171-2174.
- (196) Zheng, W.; Wang, Z.-G. *Macromolecules* **1995**, *28*, 7215-7223.
- (197) Brandrup, J.; Immergut, E. H. *Polymer Handbook, 3rd ed.*; J. Wiley&Sons: New York, 1989.
- (198) Kambour, R. P.; Bandler, J. T.; Bopp, R. C. *Macromolecules* **1983**, *16*, 753-757.
- (199) Silvestre, C.; Martuscelli, E.; Karasz, F. E.; MacKnight, W. J. *Polymer* **1987**, *28*, 1190-1199.
- (200) Ten Brinke, G.; Karasz, F. E.; MacKnight, W. J. *Macromolecules* **1983**, *16*, 1827-1832.
- (201) Mayes, A. M.; Olvera de la Cruz, M. *J. Chem. Phys.* **1989**, *91*, 7228-7235.
- (202) Dobrynin, A. V.; Erukhimovich, I. Y. *Macromolecules* **1993**, *26*, 276-281.
- (203) Hajduk, D. A.; Tepe, T.; Takenouchi, H.; Tirrell, M.; Bates, F. S.; Almdal, K.; Mortensen, K. *J. Chem. Phys.* **1998**, *108*, 326-333.
- (204) Tepe, T.; Hajduk, D. A.; Hillmyer, M. A.; Wiemann, P. A.; Tirrell, M.; Bates, F. S.; Almdal, K.; Mortensen, K. *J. Rheology* **1997**, *41*, 1147-1171.
- (205) Neumann, C.; Abetz, V.; Stadler, R. *Colloid Polym. Sci.* **1998**, *276*, 19-27.

- (206) Clasen, C.; Kulicke, W.-M. *Progress in polymer science* **2001**, *26*, 1839-1919.
- (207) Clasen, C.; Kulicke, W.-M. *Journal of rheology* **2003**, *47*, 321-335.
- (208) Goldacker, T.; Abetz, V. *Macromol. Rapid Commun.* **1999**, *20*, 415-418.
- (209) Breiner, U.; Krappe, U.; Stadler, R. *Macromol. Rapid Commun.* **1996**, *17*, 567-575.
- (210) Shin, G.; Sakamoto, N.; Saijo, K.; Suehiro, S.; Hashimoto, T.; Ito, K.; Amemiya, Y. *Macromolecules* **2000**, *33*, 9002-9014.
- (211) Wang, C.-Y.; Lodge, T. P. *Macromolecules* **2002**, *35*, 6997-7006.
- (212) Hanley, K. J.; Lodge, T. P.; Huang, C.-I. *Macromolecules* **2000**, *33*, 5918-5931.
- (213) Lodge, T. P.; Pudil, B.; Hanley, K. J. *Macromolecules* **2002**, *35*, 4707-4717.
- (214) Sakurai, S.; Hashimoto, T.; Fetters, L. J. *Macromolecules* **1996**, *29*, 740-747.
- (215) Kim, J. K.; Lee, H. H.; Ree, M.; Lee, K.-B.; Park, Y. *Macromolecular Chemistry and Physics* **1998**, *199*, 641-653.
- (216) Sakurai, S.; Umeda, H.; Taie, K.; Nomura, M. *Journal of chemical physics* **1996**, *105*, 8902-8908.
- (217) Hajduk, D. A.; Takenouchi, H.; Hillmyer, M. A.; Bates, F. S.; Vigild, M. E.; Almdal, K. *Macromolecules* **1997**, *30*, 3788-3795.
- (218) Hamley, I. W.; Fairclough, J. P. A.; Ryan, A. J.; Mai, S.-M.; Booth, C. *Physical chemistry, chemical physics* **1999**, *1*, 2097-2101.
- (219) Vigild, M. E.; Almdal, K.; Mortensen, K.; Hamley, I. W.; Fairclough, J. P. A.; Ryan, A. J. *Macromolecules* **1998**, *31*, 5702-5716.
- (220) Wang, C.-Y.; Lodge, T. P. *Macromolecular rapid communications* **2002**, *23*, 49-54.
- (221) Percec, V.; Imam, M. R.; Bera, T. K.; Balagurusamy, V. S. K.; Peterca, M.; Heiney, P. A. *Angewandte Chemie* **2005**, *44*, 4739-4745.
- (222) Due to the lack of literature data regarding the poly(*t*-butyl methacrylate) homopolymer, its polarizability anisotropy has been calculated using the expression<sup>197</sup>  
$$\alpha = 3M(n^2 - 1) / 4\pi N_A d(n^2 + 2)$$
. The polarizability anisotropy of DOP has been calculated with the same expression.

# Acknowledgements

This work would not have been possible without support which I have received during the course of my Ph.D. study.

Especially I would like to thank Prof. Dr. Volker Abetz for his interest in providing me an interesting topic. I appreciate his supervision, suggestions and fruitful discussions.

Prof. Dr. Axel H. E. Müller is acknowledged for the support during my last year of Ph.D as well as for his friendly discussions.

Dr. Alexander Böker thank you for the collaboration concerning SAXS experiments in Grenoble and for giving the opportunity to join for the first time and become familiar with such exciting experiments. As well the fruitful and kind discussions on Grenoble data were of a great help for me.

Dr. Sandie Auffret and Dr. Holger Schmalz were the first persons which have introducing me the technique of anionic polymerization for which I would like to thank. Also a great help I have received from Dr. Sandie Auffret for the daily life for which I really thank a lot.

Thanks Xavier Àndre for the fruitful collaboration concerning synthesis of block copolymers by anionic polymerization which I have used during my Ph.D work.

As well, I would like to thank Gunther Jutz for helping me with many things and advices, as well for translating the summary to Zusammenfassung. Thanks to Chih-Cheng Peng and Felix Plamper for the help concerning computer stuff and network. Thanks to Dr. Stefan Stangler for explaining the rheoptical method and for the help in the evaluation of the primary results from my Ph.D work. For the first introduction concerning the rheology laboratory I would like to thank Kerstin Matussek.

The people from microscope-team: Astrid Göpfert, Dr. Markus Drechsler are great acknowledged due to their patience to search for nice TEM images.

A nice collaboration have been arised with Physikalische Chemie II people like : Kristin Schmidt, Dr. Frank Schubert and Dr. Helmut Hänsel due to closed projects and especially concerning the evaluation of Grenoble data for which I would like to say “thanks a lot”. Without their help would be difficult a proper and reliable evaluation of Grenoble data. Due

to the LabView program developed by Dr. Helmut Hänsel an easy and complete evaluation of synchrotron experiments was possible therefore I thank him a lot.

Thanks to Dr. Pierre Panine from European Synchrotron Radiation Facility (ESRF, Grenoble, France) for providing the opportunity to use ID02 beam line and guiding throughout the synchrotron SAXS experiments.

Furthermore, a lot of understanding and friendly discussions I have found to persons like Sharmila Mutukrishnan and Clarissa Abetz which have encouraged and motivated me during my work.

A nice atmosphere has been provided by the former members of the MCII group like Dr. Yanfei Liu, Dr. Shimei Jiang, Dr. Nemesio Martinez Castro, Dr. Markus Hartenstein, Hans Lechner, and as well entertained by the actual colleagues: Evis Penott, Manuela Fink, Markus Burkhardt, Annette Krökel, Cornelia Lauble.

A great “Thank you” I would like to address to Gaby Oliver for her help in handling with all my documents written in German which would have been a big problem for me.

At the end I would like to thank to my family for encouragement during my Ph.D study.

## **Erklärung**

Die vorliegende Arbeit wurde von mir selbstständig verfasst und ich habe dabei keine anderen als die angegebenen Hilfsmittel und Quellen benutzt.

Ferner habe ich nicht versucht, anderweitig mit oder ohne Erfolg eine Dissertation einzureichen oder mich der Doktorprüfung zu unterziehen.

Bayreuth, den 14.10.2005

Gabi Cantea